Synthesis of Mesoporous Pd and PdCu Alloy in Micellar Solutions

ミセル溶液を用いたメソポーラス Pd, PdCu 合金の合成

February 2019

Muhammad IQBAL

イクバル ムハンマド

Synthesis of Mesoporous Pd and PdCu Alloy in Micellar Solutions

ミセル溶液を用いたメソポーラス Pd, PdCu 合金の合成

February 2019

Waseda University

Graduate School of Advanced Science and Engineering

Department of Nanoscience and Nanoengineering

Research on Synthetic Chemistry of Nanomaterials

Muhammad IQBAL

イクバル ムハンマド

Preface

Noble metals are important materials that increase the efficiency of chemical reactions in organic chemistry and electrocatalysis. Palladium (Pd) in particular is an essential component in various reactions including the electrocatalytic oxidation of hydrogen and other small molecules, and the electrocatalytic reduction of oxygen. Controlling the shapes, compositions, and sizes of Pd nanoparticles enables beneficial tuning of their properties and interfacial surface effects for suitable applications. In general, ultra-small Pd nanoparticles (2~10 nm) are most often utilized as catalysts in industry. However, they tend to suffer performance degradation because their chemical and thermal stabilities are very poor, and they easily undergo structural transformations under reaction conditions. Recently, researchers have been exploring more cost-effective electrocatalysts based on alloys of Pd metal with non-noble metals including copper, Cu. The presence of the second element can increase the electrocatalytic activity and stability of Pd catalysts. To further improve the catalytic properties of Pd-based materials, it is important to introduce novel nanostructures. Among previously reported nanostructures, mesoporous architectures are quite promising due to their high specific surface areas and exposed catalytically active sites. This PhD thesis is focused on the development of new kinds of Pd-based nanostructures and mesoporous materials by combining shape- and structure-directing agents with wet-chemical and electrochemical synthetic approaches. This thesis establishes a new platform for the facile synthesis of mesoporous Pd-based nanoparticles and films, which can be extended to other metallic nanostructures for a wide range of applications.

In **Chapter 1**, the properties of Pd and literature reviews on the synthetic methods reported previously are presented. In **Chapter 2**, an electrochemical method to prepare continuous mesoporous Pd films from micellar solutions is reported. **Chapter 3** describes the extension of the above approach to prepare bimetallic standing mesochannels PdCu films. **Chapters 4-6** demonstrate a synthesis of mesoporous nanoparticles via chemical reduction. **Chapter 4** demonstrates a synthesis of a three-dimensional (3D) super-branched PdCu nanoparticles with controlled particular facets. **Chapter 5** describes a method to prepare of mesoporous Pd nanoparticles and hybridize them with functionalized reduced graphene oxide (FrGO) sheets. In **Chapter 6,** how to synthesize large-sized mesoporous PdCu alloy spheres via chemical reduction on soft polymeric micelle templates is reported. **Chapter 7** presents the general conclusions and prospective directions of this thesis.

Table of Contents

Chapter 1

1. General Introduction

1.1. Palladium as Nanocatalyst

Noble metals (*e.g.,* Pt, Pd, Ag, and Au) play significant roles in many catalytic reactions, including organic catalysis and electrocatalysis. Among noble metals, Pd is well-known to be highly active for various surface reactions, such as electrocatalysis of hydrogen oxidation, oxidation of small organic molecules, oxygen reduction, hydrogenation, coupling reactions and carbon monoxide oxidation.[1-9] Pd shows a remarkable activity toward the dissociation of hydrogen gas as well as small organic molecules (such as ethanol, methanol, formic acid, *etc.*). Furthermore, Pd is also capable of catalyzing the reduction reaction of oxygen with the presence of electrons and protons. In addition, Pd is known for its high selectivity for some heterogeneous (*e.g.,* the hydrogenation of acetylene) and homogeneous catalytic reactions (*e.g.,* Suzuki reaction, Sonogashira reaction, *etc.*). The high catalytic performance of Pd for these reactions renders them highly promising for several applications, such as fuel cells, pharmaceutical, automotive (catalytic converters) and electrochemical sensors.[10-19] In recent years, Pd has gained increasing attention as a substitute for Pt in many electrocatalytic applications. This is because Pd and Pt possess a number of similarities, for example, they belong to the same group in the periodic table and they both exhibit face-centered cubic (*fcc*) structure. Although the economical price of Pd has risen in the last three years due to the high demand from automotive industries (catalytic converters),[19] Pd remains as a promising substitute for Pt in electrocatalysis as it is fifty times more abundant on earth than Pt.[20-22]

The nature of catalytic reactions catalyzed by Pd atoms involves a good understanding of the underlying chemistry at a molecular level. For this purpose, various techniques (such as Auger electron spectroscopy, low-energy electron diffraction, mass spectrometry and thermal desorption spectrometry) have been employed to characterize the surface chemistry of Pd.[23] Pd has three low Miller-index surfaces, *i.e.,* (111), (100) and (110). The Pd(111) surface is a preferential site for CO adsorption, as proven by theoretical and experimental approaches.[24,25] In fact, Pd is the preferred catalyst for the oxidation of hydrogen or liquid fuels, rather than the reduction of oxygen.[26] However, CO is often

found as an intermediate product during the electrochemical oxidation of hydrogen and liquid fuels and similar to Pt, Pd is also sensitive to CO poisoning.[27,28]

Proper control over the shape and size of Pd nanoparticles can enable effective tuning of their properties and characteristics for the desired applications.[29-31] The size of the catalyst particles essentially determines the specific surface-active area.[32] The smaller the size of the particles, the larger the specific surface-active area and *vice versa*. The catalytic performance of an electrooxidation catalyst is proportional to its specific surface-active area. In the early development stage of Pd-based electrocatalysts, many scientists focused on the preparation of the smallest yet optimum size of Pd nanoparticles. However, to further enhance the stability of electrocatalysts upon chemical and mechanical deformations, recent studies have been aimed toward controlling not only the size, but also the morphology of Pd by creating various nanostructures from 0D to 3D and exposing the active facets.[33-37]

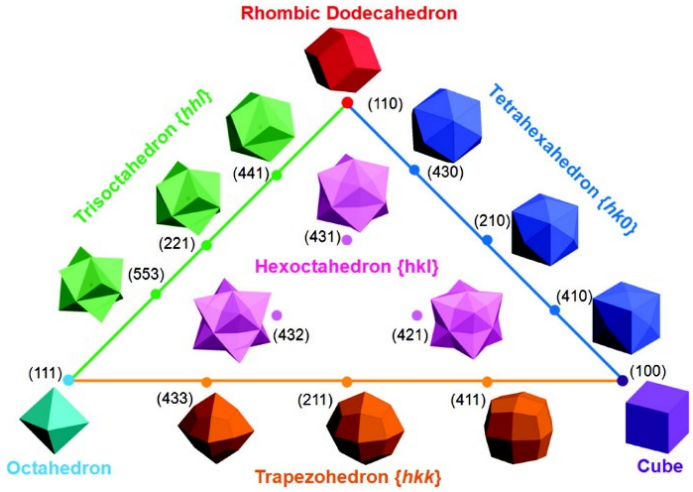

Figure 1.1 Triangular diagram showing the correlations between convex polyhedron with different crystallographic facets. Reproduced with permission.[38] Copyright 2014, The Royal Society of Chemistry.

To date, many groups have reported the preparation of various Pd polyhedrons with specifically exposed facets: cubes with {100} facets, rhombic dodecahedron with {110} facets, and octahedron with {111} facets (**Figure 1.1**).[38] For instance, Hoshi *et al.*

carefully investigated the shape effect of Pd single crystal with different surface structure toward ethanol (MOR).[39] Their experiments revealed that the Pd(111) surface showed the lowest activity, while the Pd(100) surface showed the highest activity for MOR. Furthermore, the Pd(100) surface also exhibited the highest activity toward formic acid oxidation reaction (FAOR) compared to the other low-index planes.[2] From a theoretical point of view, Wang and co-workers demonstrated for the first time that the activity and selectivity of Pd for ethanol oxidation reaction (EOR) were highly structure-dependent and that the Pd(100) surface was best at promoting the dissociation of an ethanol molecule with a rather low energy barrier.[40] Furthermore, their DFT study also showed that complete ethanol oxidation could be achieved on the active Pd (100) surface in the presence of hydroxide (OH) group.

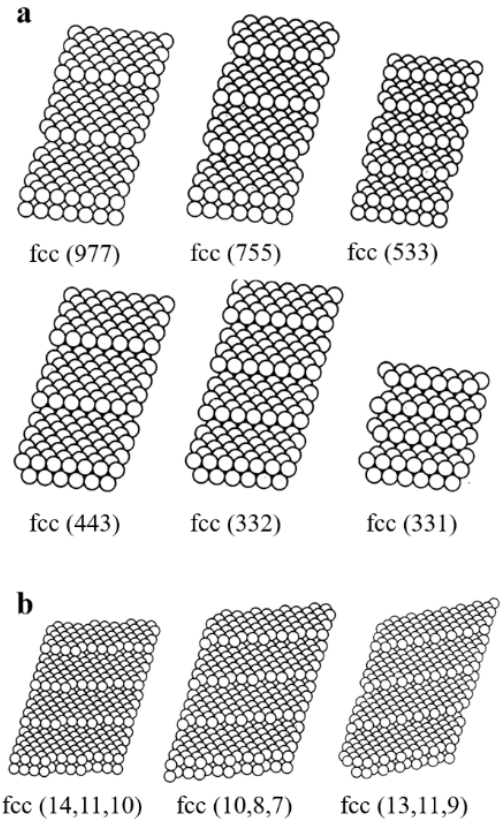

Figure 1.2 Various (a) stepped and (b) kinked surfaces in close-packed *fcc* lattice. Reproduced with permission.[44] Copyright 1985, US National Academy of Sciences.

Even though the control over the morphology of Pd nanocrystals with low-index planes has been widely explored, recent studies have expanded into the fabrication of 0D, 1D, 2D and 3D Pd nanoarchitectures enclosed with high-index facets.[41,42] In the case of electrooxidation of small organic molecules, catalyst particles with rough surface are preferred. This is because the rough surface of the particles can be translated as having high-index facets, which improve the density of low-coordinated atoms, such as steps, terrace, and kinks.[43] The schematic illustration of low-coordinated atoms is given in **Figure 1.2**.[44] The presence of a high density of low-coordinated atoms is beneficial for enhancing the amount of active sites available for surface catalytic reactions. Noble metal nanoparticles enclosed with high-index facets have been shown to exhibit better stability and possess a higher density of dangling bonds on the surface, which are preferential for catalysis.[45]

In addition to high activity, the design of highly stable Pd-based nanoarchitectures is also of significant interest. A good catalyst should possess excellent chemical, thermal and mechanical stabilities during the catalytic reactions. Therefore, some strategies have been developed to enhance the stability of Pd-based nanoarchitectures. The functionalization of Pd by forming alloys or intermetallics with non-noble metals or by dispersing it on support materials is often necessary to improve the stability of Pd. For example, the introduction of a secondary metal (*e.g.,* Au, Ir, Cu, *etc.*) at a certain concentration to form alloys or intermetallics can improve not only the activity but also the chemical stability of the Pd-based catalysts through ensemble and electronic effects.[46-48] The improvement of thermal and mechanical stabilities can be achieved through the fabrication of Pd-based nanoarchitectures with higher dimensions (1D, 2D and 3D), since they have lower vulnerability to dissolution, the Ostwald ripening and aggregation during the reactions compared to 0D nanoparticles.[42,49,50] Apart from alloying, the incorporation of Pd-based nanoarchitectures into support materials, such as carbon and oxides, have also been utilized as a lucrative strategy to enhance their chemical, thermal and mechanical stabilities.[51]

As of now, several synthetic strategies have been developed to create a wide variety of Pd-based nanoarchitectures for catalytic applications. However, This chapter will focus on the fabrication of various Pd-based nanoarchitectures through chemical reduction and electrochemical deposition methods due to their simplicity and cost-effectiveness.[33,52,53]

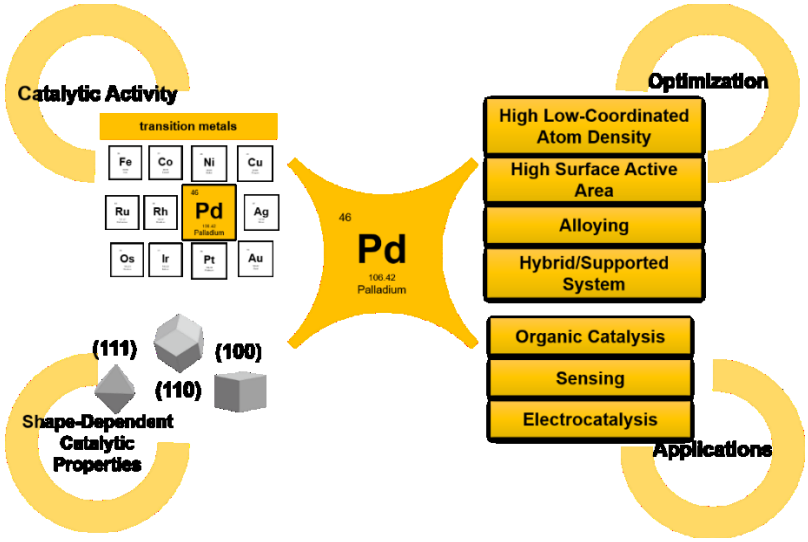

Figure 1.3 Schematic diagram of the basic concept of Pd as nanocatalyst. Pd belongs to the *d*-block transition metals and its high catalytic activity arises from the incompletely-filled subshell in the *d*-orbital. The catalytic performance of Pd-based catalysts has been shown to be dependent on the shape and size of the Pd nanocatalyst. The optimization to meet the demand for high performance Pd catalyst can be achieved by creating nanoarchitectures which possess a high density of low-coordinated atoms, high surface-active area, and high stability by combining Pd with other elements to provide synergistic effects. Various Pd nanoarchitectures are promising for many applications, such as organic catalysis, non-enzymatic sensing and electrocatalysis.

The fundamental concepts of this chapter are illustrated in **Figure 1.3**. The Chapter 1 is divided into several sections. The first section deals with the nanoarchitectures of Pd catalysts with zero-dimensional to two-dimensional structures, including discussions on the shape and size effects toward some catalytic applications. The second section focuses on the creation of various 3D Pd-based nanoarchitectures, such as aerogels, dendritic and mesoporous structures. The third section explores the functionalization of Pd nanocatalysts

(intermetallic, alloys and hybrid structures). Finally, the last section discusses the PhD thesis direction related to the fabrication of Pd and PdCu nanoarchitectures in micellar solutions.

1.2. 0D to 2D Pd Nanoarchitectures

In this section, various types of Pd nanostructures from zero-dimensional (0D) to two-dimensional (2D) nanoarchitectures are discussed. Basically, the 0D morphology refers to unsupported Pd nanoparticles with sizes less than 100 nm on each axis. Meanwhile, 1D morphology refers to Pd particles in which one axis dimension has a size greater than 100 nm (*e.g.*, nanowires, nanotubes, and nanorods). Pd nanoplates, nanosheets, and nanodiscs are classified as 2D Pd nanoarchitectures. The preparation procedures of each kind of morphology and their corresponding properties toward some catalytic applications are discussed.

1.2.1. 0D – Nanoparticles

The rational design of Pd nanoparticles with exposed facets has been well-reported in the literatures.[54] The synthesis of unsupported colloidal 0D Pd nanoparticles is typically done through seed-mediated or direct (seedless) synthesis. The seed-mediated approach generally consists of two steps: the preparation of small Pd nanocubes as seeds, followed by the growth of polyhedral Pd nanoparticles *via* thermodynamically or kinetically-controlled reactions.[55] The synthesis of Pd seeds typically involves the reduction or decomposition of the Pd metal precursor, followed by nucleation and growth of a single-crystal structure with a particular facet. Directive seed nucleation is commonly assisted by the presence of bromide ions (Br^-) in the reaction solution. For example, in a typical synthesis, Pd precursor (H_2PdCl_4) aqueous solution is added into the CTAB solution and heated at 95 ^oC under stirring. Then, the reduction of the Pd precursor into Pd(0) is achieved with the use of a mild reducing acid, such as ascorbic acid. This reaction then yields cubic Pd seeds which can be used to grow polyhedral Pd particles.[55] To control the growth of the cubic Pd seeds into the desired polyhedron structure, some key factors should be taken into consideration. Niu *et al.* suggested that there were three factors which governed spontaneous nucleation: 1) the amount of seeds added to the growth solution; 2) the

reaction temperature and 3) the presence of halide ions (KI) in the growth solution. In particular, adsorbates, such as surfactants or halide anions are often used to alter the surface energy by selectively interacting with different metal crystal facets during the reaction.[56] The strong binding of halides on metallic Pd surfaces suggests that halides could potentially play an important role in the chemical synthesis of Pd nanocrystals by changing the surface energy of different Pd facets, which led to the formation of different final morphology of the Pd nanocrystals. For instance, the presence of Br^- in the synthesis of Pd nanocrystals reported by Xia *et al.* led to the formation of Pd nanocubes and nanobars enclosed by {100} facets, while in the absence of Br^-, only Pd cubocathedrals enclosed by a mix of {111} and {100} facets were obtained.[57]

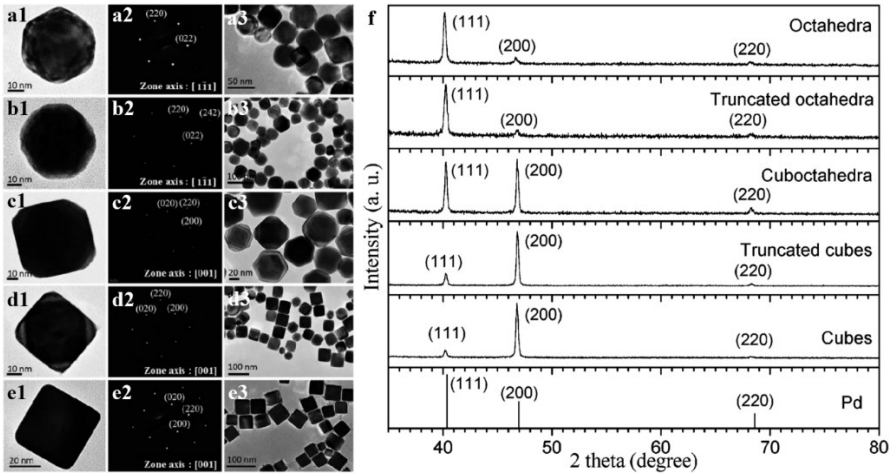

Figure 1.4 TEM images of single Pd nanocrystals, their corresponding SAED patterns and TEM images of the particles over larger areas: (a1-a3) Pd octahedra, (b1-b3) truncated octahedra, (c1-c3) cuboctahedra, (d1-d3) truncated cubes, and (e1-e3) cubes. The respective diffraction patterns for the various Pd nanocrystals are shown in panel (f). Reproduced with permission.[58] Copyright 2015, American Chemical Society.

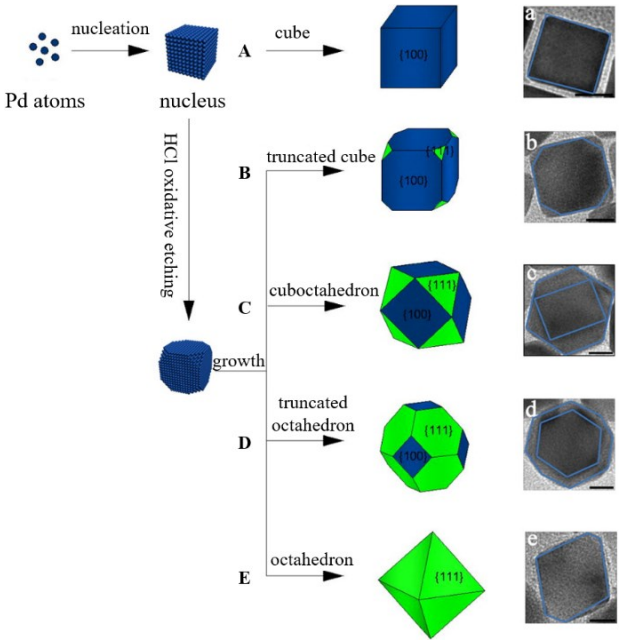

Figure 1.5 Schematic illustration of shape evolution of the Pd nanocrystals and (a-e) the corresponding TEM images for various morphologies, respectively (scale bars, 10 nm), where slight truncation at the corner of cubic Pd was induced by HCl oxidative etching in the early stage and then, continuous atomic addition to {100} facets promotes the enlargement of {111} facets, resulting in the formation of octahedral Pd bounded by {111} facets. Reproduced with permission.[59] Copyright 2014, The Royal Society of Chemistry.

The fabrication of well-defined Pd nanocrystals with various exposed facets can also be achieved by direct (seedless) approaches. Unlike seed-mediated methods, the seedless methods require fewer steps and are easier to perform. For instance, Liu *et al.* employed a halide additive (KBr) to control the shape of Pd nanoparticles from cubic to octahedra (**Figure 1.4**).[58] Another direct approach to synthesize shape-controlled Pd nanocrystals was demonstrated by Zhang and co-workers through oxidative etching with hydrochloric acid (HCl).[59] They demonstrated that the concentration of HCl added to the reaction solution was crucial for controlling the morphology of the resulting Pd nanocrystals (**Figure 1.5**). In their report, Pd nanocubes were obtained in the absence of HCl due to the fast reduction rate. However, with the addition of a small quantity of HCl to the precursor solution, truncated nanocubes were formed instead. In contrast, the excessive addition of HCl slowed down the reaction rate even further, leading to the formation of Pd cuboctahedrons. The obtained Pd nanocrystals with three different morphologies were utilized as catalysts for formic acid oxidation. The results revealed that

Pd nanocubes with {100} exposed facets showed the best catalytic activity, which was in good agreement with a previous report.[60]

Pd nanoparticles with high-index facets (HIFs) have also been reported in past literatures, including concave nanocubes[61], concave disdyakis triacontahedra[62], concave tetrahedra[63], concave nanocubes[64] and arrow-headed tripods.[65] Pd concave nanocubes enclosed with {730} facets were previously synthesized by Xie *et al.* through a one-pot liquid method. According to their report, Pd nanoarchitectures with various high-index facets could be synthesized by tuning the reaction kinetics, such as temperature and concentration of reducing agent and capping agent.[61,66] At high reaction temperatures (75-80 ^{o}C), Pd nanocubes were obtained. On the contrary, at lower reaction temperatures and high concentration of the reducing agent (ascorbic acid), well-defined Pd concave nanocubes were achieved. The obtained Pd nanocubes and concave nanocubes were employed as catalysts toward MOR. It was shown that Pd nanocubes with exposed {100} facets exhibited the best catalytic activity for electrooxidation of alcohols or formic acid compared to other low-Miller index Pd nanocrystals. However, Pd nanocrystals enclosed with HIFs (concave nanocubes) displayed a significantly higher catalytic activity toward MOR by about 2.8 and 50 times compared to Pd nanocubes and commercial Pd/C, respectively.

Well-defined concave tetrahedra Pt nanocrystals were previously obtained through a simple solvothermal process with high yield. Zhang and co-workers used polyvinylpyrrolidone (PVP) as a surfactant and both iron(II) acetylacetonate ($Fe(acac)_2$) and ascorbic acid as shape-directing agents.[63] The palladium precursor ($Pd(acac)_2$) and all the other reagents were dissolved in *N*, *N*-dimethylformamide (DMF), which also served as a reducing agent. Following solvothermal reaction at 120 ^{o}C for 10 h and consecutive washing, concave tetrahedra Pd nanocrystals were obtained. Interestingly, the concave tetrahedra Pd nanocrystals exhibited 3 times higher activity than commercial PdB for formic acid oxidation.

Concave disdyakis triacontahedra Pd nanocrystals (C-DTH Pd NCs) enclosed with {631} facets were prepared through electrochemical deposition on a working electrode from deep eutectic solvent (DES).[62] The time-dependent experiments revealed that the unique C-DTH structure was evolved from octahedral and icosahedral structures (**Figure 1.6**). The adsorbed urea in the solvent at the upper limit potential (E_U) of the square-wave potential applied during the electrochemical deposition played a crucial role in the formation of C-DTH Pd NCs. When tested for electrooxidation of ethanol, the C-DTH Pd

NCs exhibited a superior specific activity than the Pd nanocrystals with mixed octahedron and icosahedron structure. The high activity of C-DTH Pd NCs was attributed to the presence of high-index facets with high density of low-coordinated atoms, steps and kinks. Controlling the shape of nanoparticles can lead to a change in their molecule-sorption energies, and hence, their catalytic performance. This change typically arises from the modified *d*-band center of a metal nanoparticle as a result of lattice strain.[67] A lattice strain is typically introduced by crystal twinning during the synthesis of metal nanoparticles, and this can lead to various distinct morphologies, such as decahedra and icosahedra.

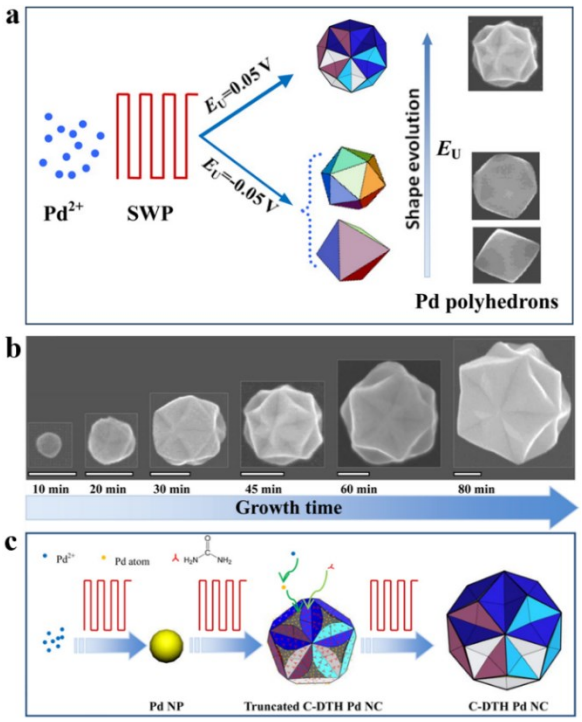

Figure 1.6 (a) Illustration of shape evolution of polyhedral Pd NCs by adjusting upper limit potential (E_U). (b) SEM images of Pd NPs electrodeposited on GCE for different time, showing the growth process of C-DTH Pd NCs. Scale bars are 100 nm. (c) Schematic illustration of the proposed growth mechanism of C-DTH Pd NCs. Reproduced with permission.[62] Copyright 2016, American Chemical Society.

1.2.2. 1D – Nanorods, Nanotubes, Nanowires

1D nanostructures possess several advantages for catalytic applications, due to the enhanced electron and mass transport and improved chemical stability compared to 0D nanoparticles.[49,68-70] Previously, Xu *et al.* reported the fabrication of highly ordered array of Pd nanowires *via* electrochemical deposition.[71] The array deposition was carried out on

the glassy carbon electrode (GCE) assisted by the anodized aluminum oxide (AAO) template. The deposited Pd nanowire array was well-isolated, standing vertically toward the electrode surface, and had a uniform diameter (*ca.* 80 nm) and length (*ca*. 800 nm). When tested for EOR, the Pd nanowire array showed both enhanced activity and stability compared to PtRu/C. It is worth noting that upon increasing the length of the nanowires (6 μm), the mass activity was significantly reduced. This was attributed to the increased diffusion resistance of reactant and product to and from the Pd nanowire array electrode. In contrast to Xu's work, Wang and co-workers successfully prepared ultrathin Pd nanowires through a polyol method.[72] In the initial growth stage of the nanowires, Pd nanoparticles with diameters around 2-3 nm were created. To obtain such ultrathin nanowires, proper control of the reaction kinetics during this initial stage was critical for ensuring the formation of small and thermodynamically unstable nanoparticles and then, the nanowires v*ia* attachment growth (**Figure 1.7**). Although the Pd/C particles and ultrathin Pd nanowires have nearly similar geometrical size (2 nm in width for ultrathin Pd nanowires and 2-3 nm in diameter for Pd/C), the ultrathin Pd nanowires displayed 2.5 times higher catalytic activity than the commercial Pd/C catalyst for electrooxidation of formic acid due to the unique wire-like structure and abundance of twin defects.

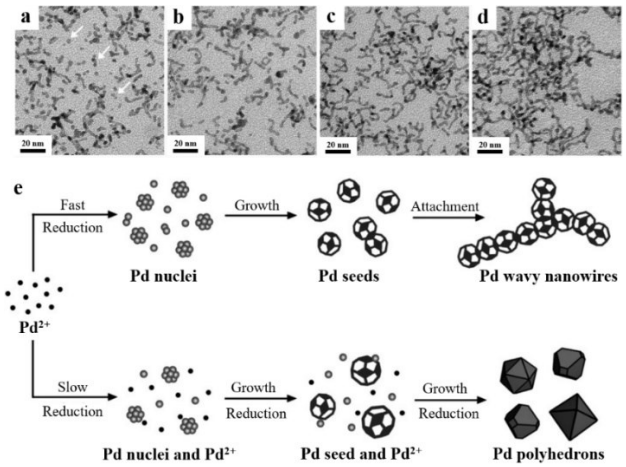

Figure 1.7 TEM images showing the attachment and time-dependent growth of Pd nanoparticles into wavy nanowires at 140 °C after the precursor had been injected: a) 1 min, b) 10 min, c) 30 min, and d) 3 h. The white arrows in (a) mark a few typical small Pd nanoparticles formed in the early stage of the synthesis. (e) A schematic illustration showing how the reaction kinetics (as mediated by precursor) affect the nucleation, growth, attachment, and thus, the final morphology of Pd nanostructures in polyol synthesis. Reproduced with permission.[72] Copyright 2014, Wiley-VCH Verlag GmbH.

The synthesis of 1D Pd nanorods with exposed {110} facets *via* electrochemical deposition has previously been reported by Xiao and co-workers.[73] When employed as an oxygen reduction reaction (ORR) catalyst, these Pd nanorods were as catalytically active as bulk Pt. The superior ORR activity of these Pd nanorods was contributed by the exposed {110} facets, as also indicated by their theoretical study (DFT calculations), in which the O adatom was shown to weakly interact with Pd(110). The morphology-controlled growth of such nanorods was governed by the presence of appropriate halide ions, concentration of Pd precursors, and applied deposition potential. In this case, the anisotropic growth of the Pd crystal during the synthesis process occurred due to the fast reduction rate. Das group has also reported the synthesis Pd nanorods with an average rod length of 150 nm *via* electrochemical deposition in the presence of nicotinamide adenine dinucleotide (NAD^+) as a shape regulating agent.[74] The selection of appropriate applied pulse width during the electrochemical deposition and concentration Pd precursors in the electrolyte solution were important for ensuring the formation of the nanorods. These Pd nanorods were demonstrated to be highly sensitive and selective for hydrazine detection with low detection limit (LDL) of 5 nM, high sensitivity of 0.78 ± 0.02 μA mM^{-1} cm^{-2} and stable response without any interference from potential interferents, such as Na^+, K^+, NO^{2-}, BrO^{3-}, or Pb^{2+} ions.

As highlighted in this section, 1D Pd nanoarchitectures possess good electronic conductivity. Aside from their intrinsic capability to oxidize several biological substances molecules, such as glucose, lactic acid, *etc*., these 1D Pd nanostructures have also shown excellent performance as non-enzymatic biosensors.[75] For instance, Wang *et al.* had examined porous Pd nanotubes synthesized through *in situ* galvanic replacement reaction on glassy carbon electrode (GCE) for non-enzymatic glucose sensing.[76] In this work, Cu nanowires were used as a template, however after the galvanic replacement reaction, only pure Pd (no CuPd alloy) was detected in the product, indicating the complete removal of the template. Using amperommetric technique, the Pd nanowire sensor was found to generate a wide linear response range from 5 μM to 10 mM for non-enzymatic glucose sensing, with a maximum sensitivity of 6.58 μA mM^{-1} cm^{-2} and a detection limit of 1 μM.

1.2.3. 2D – Nanoplates, Nanosheets

In recent years, 2D metal nanostructures have attracted increasing attention for catalytic applications.[50,77] This is because they possess abundant low-coordinated atoms at the perimeters, which provide many active sites for enhancing the catalytic activity. To date, several groups have successfully synthesized 2D Pd nanostructures with various distinct structures, such as nanoplates[78-80] and nanosheets[81-92]. For example, 2D Pd nanoplates have previously been fabricated using two different methods: templated self-assembly and template-free electrochemical deposition methods. Nadagouda *et al.* employed vitamin B_1 as a capping agent for the synthesis of Pd nanoplates, motivated by the use of green chemistry.[78] Apart from its capping properties, vitamin B_1 (reduction potential 0.4 V *vs.* Ag/AgCl) was also considered to be suitable for the reduction of Pd (0.915 V *vs.* SCE). Upon the appropriate selection of solvent and Pd precursor concentration, Pd nanoplates were successfully grown on a single nanorod backbone, generating a leaf-like structure with an average length of several microns. The resulting Pd nanoplates were utilized as effective catalysts for carbon-carbon cross-coupling reactions, such as Suzuki, Heck, and Sonogashira reactions.

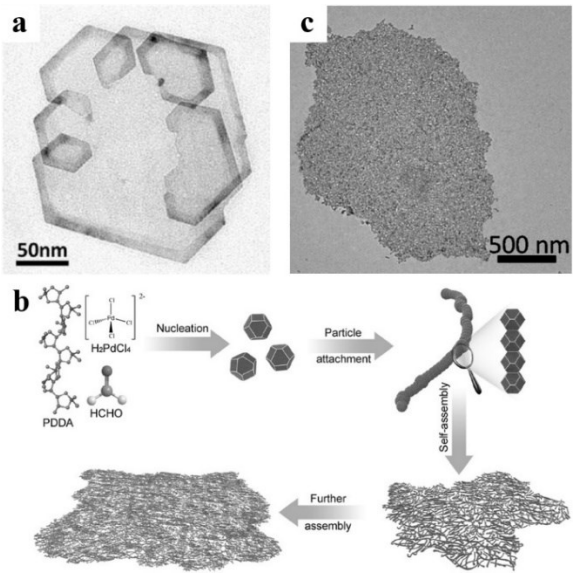

Figure 1.8 (a) TEM image of Pd nanosheets. Reproduced with permission.[63] Copyright 2015, American Chemical Society. (b) Schematic illustration of the possible formation mechanism and (c) TEM image of the free-standing 2D porous Pd nanosheets through particle attachment and self-assembly processes. Reproduced with permission.[91] Copyright 2017, Wiley-VCH Verlag GmbH.

On the other hand, Jia group had successfully prepared Pd nanoplate array using an electrochemical route in the absence of any template.[79] The Pd nanoplate array was electrodeposited on a gold substrate by employing a constant potential or current. The key factors which determined the successful growth of these Pd nanoplates were the applied potential and the amount of CTAB surfactant. According to their report, the CTAB used in the electrolyte solution could influence the anisotropic growth of the Pd nanocrystals due its selective adsorption. Hence, with the assistance of uniform electric field between the working and counter electrodes, the initially deposited nanoparticles were able to grow into Pd nanoplates. Furthermore, the obtained Pd nanoplates were found to be superior compared to the flat Pd film electrode for MOR with several times higher catalytic activity. The roughness of the Pd nanoplates was suggested to greatly contribute toward their high surface-active area and consequently, their high catalytic activity for MOR.

Compared to nanoplates, nanosheets are expected to possess higher specific surface area per mass due to their smaller thickness. Therefore, many research groups have reported the successful preparation of ultrathin nanosheets. For example, Zhang and co-workers reported the controllable synthesis of Pd nanocrystals with various structures ranging from tetrahedral, concave tetrahedral to 2D nanosheets through a direct wet-chemical method.[63] This innovative approach did not require the use of any toxic and/or explosive compounds, such as carbon monoxide or metal carbonyls to assist with the formation of the nanosheets. The fabricated Pd nanosheets had an average length of 124 nm and thickness of only 2.3 nm (**Figure 1.8a**). Their additional experiments revealed that several key factors governed the formation of these nanosheets, including the H_2O/DMF ratio and the strength of the reducing agent (mild reducing agents, such as ascorbic acid were preferred compared to very strong ones, such as citric acid due to their weaker effect on the nucleation of the nanosheets) and the presence of $Fe(acac)_2$ in the reaction solution. Formic acid electrooxidation and catalytic hydrogenation of styrene were selected as model reactions to showcase the excellent catalytic performance of these Pd nanosheets. From the electrooxidation tests, these Pd nanosheets were found to exhibit 3.5 times higher mass activity than the commercial PdB. Furthermore, even after 200 sweeping CV cycles, the mass activity remained as high as 54% of the initial catalytic activity. In addition, these Pd nanosheets also displayed superior performance toward the hydrogenation of styrene with a high conversion rate of 88%, compared to only 38% for commercial PdB.

Later, Qiu and co-workers synthesized free-standing porous Pd nanosheets through a facile one-pot chemical method.[91] Quite similar to Sial's work,[77] the free-standing porous

Pd nanosheets were constructed by the interweaving of long ultrathin nanowires (**Figure 1.8b**). The interweaving of these nanowires was achieved with the assistance of poly(diallyldimethylammonium chloride) (PDDA) and the obtained Pd nanosheets had a dimension of 2.5 μm in lateral length and 10 nm in thickness (**Figure 1.8c**). Interestingly, by changing the pH of the reaction solution, the sheet-like morphology was transformed into nanoflowers and nanochains at pH 9-10 and pH 12-13, respectively. Therefore, the electrostatic charge distribution on PDDA, hydrogen-bonding forces, electrostatic repulsion, steric forces, PDDA-PDDA interactions, and binding affinity of PDDA-Pd nanoparticles were affected by the variation in pH value of the reaction solution. The model formic acid oxidation reaction was carried out to probe the superiority of these 2D Pd nanosheets compared to commercial PdB. As expected, the as-obtained Pd nanosheets exhibited a higher mass activity by almost two-fold compared to commercial PdB. Moreover, they also displayed a high stability upon chronoamperommetry (CA) test for 3000 s and accelerated durability test for 1000 cycles. SEM analysis of these Pd nanosheets after the stability test revealed that they successfully maintained the morphology without noticeable changes. In contrast, the commercial PdB particles suffered from severe aggregation after the stability test. The above examples clearly demonstrate the superiority of 2D Pd nanoarchitectures for such electrocatalytic reactions due to: (1) their lower vulnerability to dissolution, Ostwald ripening and aggregation during the reactions compared to Pd nanoparticles and (2) their high density of coordinatively unsaturated atoms and (3) high active surface area.[50]

1.3. 3D Pd Nanoarchitectures

In this section, the synthetic methods for the preparation of 3D Pd nanoarchitectures (aerogels, dendritic and mesoporous) will be discussed. Pd aerogels are typically comprised of self-supported metallic backbone nanonetworks. The nanonetworks generally consist of a high density of (111) and (100) crystal facets. The interconnected nanonetwork allows Pd aerogels to have a large specific surface area, excellent conductivity, and hierarchical porosity.[93-95] In comparison, the dendritic structure typically shows a branched structure resembling a tree. This unique structure typically possesses large surface area, high mass transport and high density of low-coordinated atoms at their dendritic branches.[96]

Furthermore, mesoporous Pd particles have a 3D structure (mostly spherical) with highly-ordered pores and pore size ranging from 2 to 50 nm.[97,98] In addition, for certain applications, such as micro fuel cells, mesoporous films constructed by metallic frameworks are generally preferred.[99] In such fuel cells, the catalyst film (porous Pd films) and the current collector (gold layer substrate) are embedded together to form the anode. Moreover, mesoporous films with metallic framework structures are also highly desirable for non-enzymatic electrochemical sensing of specific biomolecules (*e.g.*, glucose, dopamine, lactic acid, *etc*.) with high sensitivity and selectivity.[100]

1.3.1. Aerogels

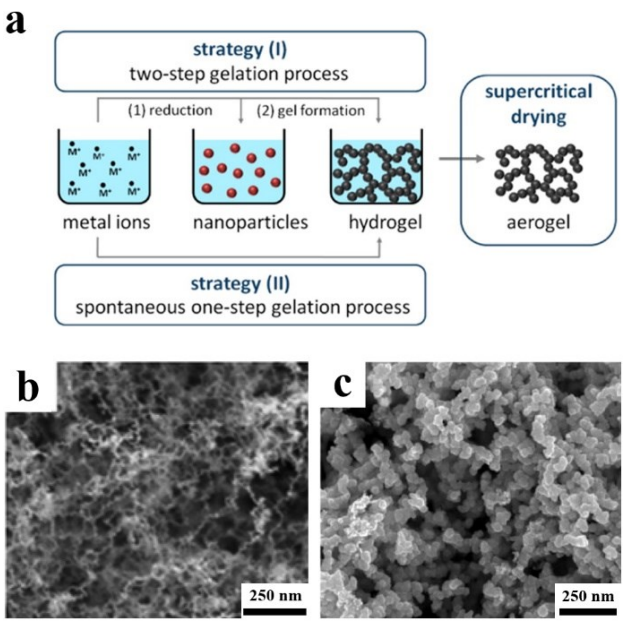

Figure 1.9. (a) Schematic illustration of noble metal aerogel preparation *via* gelation of pre-formed nanoparticles (Strategy (I)) and *via* an *in-situ* spontaneous gelation process (Strategy (II)). Reproduced with permission.[95] Copyright 2015, American Chemical Society. SEM images of Pd aerogels prepared using (b) Strategy I (Reproduced with permission.[104] Copyright 2014, American Chemical Society) and (c) Strategy II. Reproduced with permission.[105] Copyright 2017, Cambridge University Press.

Analogous to carbon aerogels, metal aerogels possess both high electrical conductivity and high surface area.[101] Furthermore, due to their intrinsically high catalytic activity, noble metal aerogels are desirable for many electrochemical applications.[102,103] Generally, the preparation of metal aerogels can be achieved through two different strategies (**Figure**

1.9a), nonetheless both strategies require the formation of a hydrogel. To obtain the hydrogel, the first step involves the gelation of pre-formed noble metal nanoparticles. Next, the hydrogel is spontaneously formed from the metal ions *via* an *in-situ* gelation process.[95] For example, Wen and co-workers reported the controlled growth of porous Pd aerogels through a facile assembly induced by calcium ions (Ca^{2+}) (**Figure 1.9**).[104] In their report, Ca^{2+} ions were employed as a destabilizing agent for the preparation of Pd aerogels. Prior to the addition of Ca^{2+} ions, the Pd precursors were reduced with sodium borohydride ($NaBH_4$) in hot water and capped with citrate. Here, citrate was used to impart electrostatic and steric repulsions to the metal nanoparticles. The addition of Ca^{2+} ions to the concentrated citrate-coated Pd nanoparticles then induced the formation of hydrogels. The aerogels were then formed after subjecting the hydrogels to supercritical drying. According to their report, the concentration of Ca^{2+} could control the volume (porosity) of the hydrogels. The Pd aerogels prepared using higher Ca^{2+} concentration were much denser and exhibited numerous mesopores. When tested for glucose oxidation in the range of 2 to 20 mM, the Pd aerogels with large pore size displayed a high sensitivity of 1.11 $\mu A\ mM^{-1}$, which was 125 and 3 times higher than those of GCE and Pd NPs, respectively.

Later, Burpo *et al.* prepared Pd aerogels through a direct solution-based reduction by employing several combinations of Pd precursors (Na_2PdCl_4 and $Pd(NH_3)_4Cl_2$) and reducing agents (sodium borohydride/$NaBH_4$, dimethylamine borane/DMAB, and sodium hypophosphite/$NaHPO_2$).[105] From their screening, the combination which provided the best aerogel was Na_2PdCl_4 (concentration threshold of 5 mM) and $NaBH_4$ (0.1 M). The effectiveness of reducing agents in terms of forming aerogel was in the order of $NaBH_4$ > DMAB > $NaHPO_2$. The well-formed Pd aerogels had an average ligament diameter of 34.5 ± 9.5 nm and an average pore size of 82.7 ± 57.7 nm (**Figure 1.9c**). More recently, Yazdan-Abad and Douk group successfully prepared Pd aerogels with electrochemical surface-active area as high as 133.3 $m^2\ g^{-1}$, respectively.[106,107] Moreover, their mass activity toward the electrooxidation of ethanol was 6-7 times higher than that of commercial Pd/C. The superior catalytic performance of these Pd aerogels was attributed to their hierarchical porosity (macropores and mesopores), improved structural stability and enhanced transport of electrons. Here, the mesopores could provide more active sites and high surface-active area, while the macropores could ensure easier access for reactants to the active sites. The above examples clearly highlight the benefits of Pd aerogels for electrocatalytic applications.

1.3.2. Dendritic Structures

By nature, most metals, such as Ni, Pd, Pt, Cu, Ag and Au have a *fcc* crystal structure. As such, to form 3D dendritic structure from these metals, surfactants are usually required as shape-directing agents by preferentially adsorbing on specific crystal planes. Zhou *et al.* proposed the formation of Pd dendrites *via* a polyglycol-assisted oriented attachment process.[108] The polyglycol played a crucial role as a structure-directing agent by promoting the structural evolution of small urchin-like particles formed during the initial growth stage into dendrite-like particles. In addition, hydrazine hydrate ($N_2H_4.H_2O$) and ammonia (NH_3) were also utilized to reduce the Pd precursor ($PdCl_2$) and to regulate the pH value of the reaction solution, respectively.

Patra and co-workers previously synthesized Pd dendrites with a high density of surface steps by controlling the growth along the (110) direction.[109] In their work, electrodeposition method (using AC impedance technique) was used to deposit branched Pd dendrites on the carbon paper electrode. The growth of these dendrites was greatly contributed by the instabilities induced by sinusoidal potential applied during the electrodeposition process, as such dendrites were not observed when DC potential was applied under similar conditions. The presence of many surface steps on these dendrites greatly contributed toward their enhanced activity for formic acid oxidation. It is believed that the high step density provided many active sites for the adsorption of formic acid molecules. In other report, Pd dendrites had also been grown on carbon fiber cloth *via* electrochemical deposition with potential pulse technique in the presence of perchloric acid.[110] Moreover, Zhao and co-workers have also successfully synthesized Pd dendrites from the electrolyte solution (containing Pd precursor and hydrochloric acid) using electrodeposition technique.[111] It is worth noting that in both reports, acid was used to increase the ionic conductivity of the electrolyte solution as high ionic conductivity was essential for ensuring good transport of ions from the electrolyte to the working electrode.[112]

More recently, Bai and co-workers prepared dendritic Pd nanoparticles through a facile chemical reduction process.[113] In their synthesis, CTAB was used as a shape-directing agent and ascorbic acid was used as a mild reducing agent. Interestingly, the presence of a small amount of nickel ions (Ni^{2+}) was necessary to ensure the formation of these Pd dendrites, although their exact role is still unclear. A spectroscopy study (*i.e.*, X-ray photoelectron spectroscopy or XPS study) on the electronic coordination state of dendritic Pd nanoparticles revealed that the binding energies of Pd^0 and $Pd^{II}O$ were negatively

shifted by *ca*. 0.86 eV compared to those of commercial Pd catalyst.[114] This implies that the dendritic morphology affected the electronic structure of Pd, leading to better electrocatalytic activity, enhanced stability and superior CO tolerance compared to the commercial Pd catalyst.

1.3.3. Mesoporous Structures

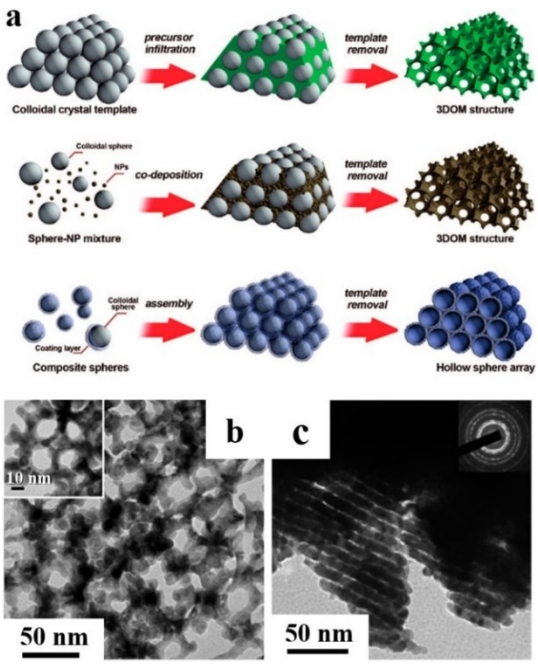

Figure 10. (a) Three different approaches for synthesizing ordered porous structures using colloidal crystal templating. Reproduced with permission.[120] Copyright 2015, American Chemical Society. TEM images of (b) silica-free 3DOM Pd networks recorded along zone axis ⟨100⟩ with an enlarged image (inset in b) Reproduced with permission.[121] Copyright 2011, The Royal Society of Chemistry, and (c) as-prepared silica-free hexagonally packed Pd nanoarray with the SAED pattern (inset in c). Reproduced with permission.[122] Copyright 2008, American Chemical Society.

In general, the fabrication of well-ordered mesoporous metals can be performed through two main methods: hard-templating and soft-templating methods.[115-120] In the hard-templating method, mesoporous silica or mesoporous carbon is commonly used as a hard template. Generally, the hard-templating method involves multiple steps: (1) the preparation of the template; (2) the deposition of metallic materials on the template and (3) the removal of the template (**Figure 10a**).[120] For instance, Ye *et al.* previously reported

the preparation of 3D ordered mesoporous (3DOM) Pd network templated by silica super crystal.[121] The silica nanoparticles were self-assembled into super crystal by centrifugation. Then, the silica super crystal was impregnated with metal ions by adding the dried silica super crystal into the Pd precursor solution and hydrazine was used to reduce the Pd salt to metallic Pd. In the final step, the siliceous template was removed by dissolution in hydrofluoric acid (HF). The 3DOM Pd network replicated from the silica template exhibited pore wall thickness of *ca.* 3-8 nm and pore diameter of *ca.* 40 nm (**Figure 1.10b**). In their report, several parameters, such as the concentration of the Pd precursor, volume ratio of the Pd precursor to the pore size of the silica super crystal template and the reduction rate could influence the formation of the 3DOM Pd network. Since hydrazine could induce fast reduction of Pd, interconnected Pd network was observed. However, the 3DOM Pd network was not observed when the reduction process was carried out using either dimethylamine borane (DMAB) or H_2. When tested as an electrocatalyst for formic acid oxidation, the 3DOM Pd network displayed both higher electroactivity and better electrochemical stability than commercial PdB.

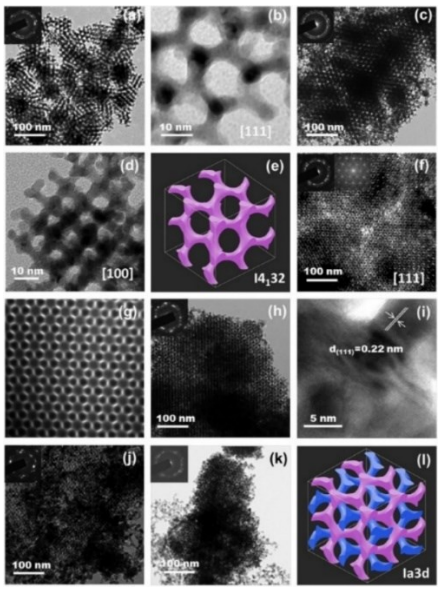

Figure 1.11 TEM images of silica-free mesoporous Pd network catalysts. Various KIT-6 templates were used: (a, b) Pd-308-KBH_4, (c, d) Pd-353-KBH_4, (e) skeletal model of a fragment of single gyroid with $I4_132$ symmetry, (f) Pd-373-KBH_4, (g) TEM image simulation of Pd-373-KBH_4, (h, i) Pd-403-KBH_4, (j) Pd-373-H_2, (k) Pd-373-$N_2H_4{\cdot}H_2O$ and (l) skeletal model of a fragment of double gyroid with *Ia*3*d* symmetry. Insets are the corresponding SAED patterns and Fourier diffractograms. Reproduced with permission.[125] Copyright 2014, Elsevier, Ltd.

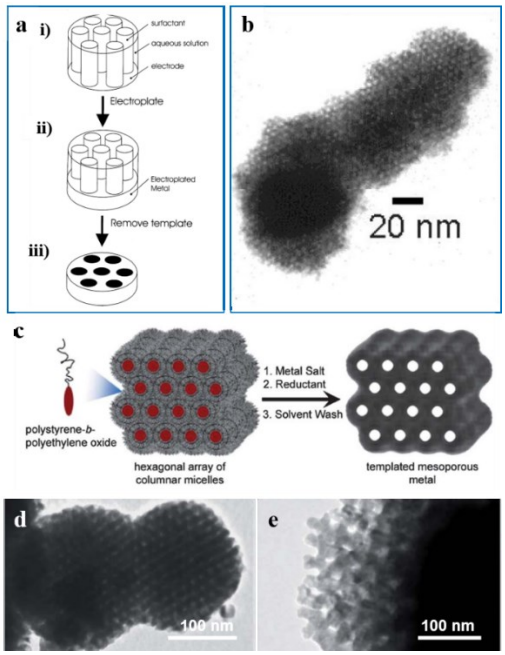

Figure 1.12 (a) Schematic representation of the templating process used to deposit the H_1-e films. The cylinders represent the micellar rods in the lyotropic liquid-crystalline phase. (b) TEM image of H_1-e palladium. Reproduced with permission.[129] Copyright 2003, American Chemical Society. (c) Scheme for the formation mechanism of PS-*b*-PEO templated mesoporous Pd. (d) Low- and (e) high-magnification TEM images of nanoporous Pd particles prepared using PS_{2300}-*b*-PEO_{3100} and PS_{3800}-*b*-PEO_{5000}, respectively. Reproduced with permission.[130] Copyright 2013, The Royal Society of Chemistry.

Pd nanoarrays with hexagonally-closed mesoporous structures were previously fabricated using SBA-15 as a template (**Figure 1.10c**).[122] These nanoarrays exhibited an average pore size of *ca.* 3.2 nm and a moderate surface area of 29.5 m^2 g^{-1}. It is worth noting that the use of different template will lead to different arrangement of mesoporous Pd structure. SBA-15-templated mesoporous Pd structure typically consists of hexagonally-arranged cylindrical Pd nanowires (the exact inverse replica of SBA-15) interconnected by self-supported shorter wires. This is because of the occupation of Pd in the channel-interconnecting micropores within the SBA-15 wall.[123,124] The mesoporous silica KIT-6 has also been employed as a hard template for the synthesis of mesoporous Pd networks, as reported by Wang *et al.* (**Figure 1.11**).[125] The catalytic properties of these mesoporous Pd networks varied with the different topology in the enantioselective hydrogenation of acetophenone and its derivatives. The enantioselectivity over the

mesoporous Pd catalysts increased in the sequence of double gyroid structure (*Ia*3*d*) > single gyroid structure ($I4_132$) > 2D hexagonal structure (P6mm) > ultrafine Pd black. The double gyroid structure was obtained with the KIT-6 template treated at 130 ^oC and KBH_4 was identified to be the best reducing agent. The double gyroid mesoporous Pd network showed an excellent performance in the enantioselective hydrogenation test due to the unique spatial arrangement with the optimum pore size. Moreover, the desired lattice structure formed by the KBH_4 reduction provided the appropriate micro-environment for improving the enantio-differentiation. Hence, the enantioselectivity could be tuned by manipulating the confinement effect in the catalyst structure.[126]

The fabrication of mesoporous metals using soft-templated method typically relies on the use of lyotropic liquid crystals (LLCs) [127-129] and micelle assembly[130-139]. In the LLC approach, there are several lyotropic phases, including cubic *Ia*3*d*, lamellar, and hexagonal phase. Bartlett and co-workers reported the synthesis of mesoporous Pd layers with a hexagonal pore arrangement using the hexagonal LLC template (**Figure 1.12a**).[129] The thickness of the metallic layers could be controlled by adjusting the total charge. The obtained mesoporous Pd layer had an average pore diameter of 3 nm and pore to pore distance of 6 nm (**Figure 1.12b**), with a relatively high electrochemical surface-active area (ECSA) of 39 $m^2 g^{-1}$. Interestingly, the pores were found to run continuously from the outer surface to the inner pore walls. Thus, by carrying out the deposition in several stages, continuous pore structure could be achieved, which lead to the high ECSA.

Compared to LLCs, the utilization of block copolymers as soft templates can enable the attainment of mesoporous Pd with larger pore size. Cappillino *et al.* successfully demonstrated the fabrication of mesoporous Pd with tunable porosity by changing the block size of the block copolymer, poly(styrene-*b*-ethylene oxide) (PS-*b*-PEO).[130] Two block copolymers, PS_{2300}-*b*-PEO_{3100} and PS_{3800}-*b*-PEO_{5000} were utilized as soft templates and the prepared mesoporous Pd particles were denoted as Pd_S and Pd_L, respectively. The formation mechanism of the mesoporous Pd can be described as follows (**Figure 1.12c**). The block copolymer arranged hexagonal array of cylindrical micelles. The hydrophobic PS block and the hydrophilic PEO block formed the core and shell of the micelles, respectively. The PEO block solvated the metallic ions in aqueous phase. The pores were formed on the regions which were previously occupied by the templates following their removal. In this case, the pore walls or backbones were constructed by metallic Pd. Interestingly, the use of different molecular weight of the block copolymer PS-*b*-PEO generated different average pore size for the resulting mesoporous Pd particles. The

average pore sizes of Pd_S and Pd_L were 7 nm and 13 nm, respectively, consistent with the pore sizes observed by TEM (**Figure 1.12d,e**).

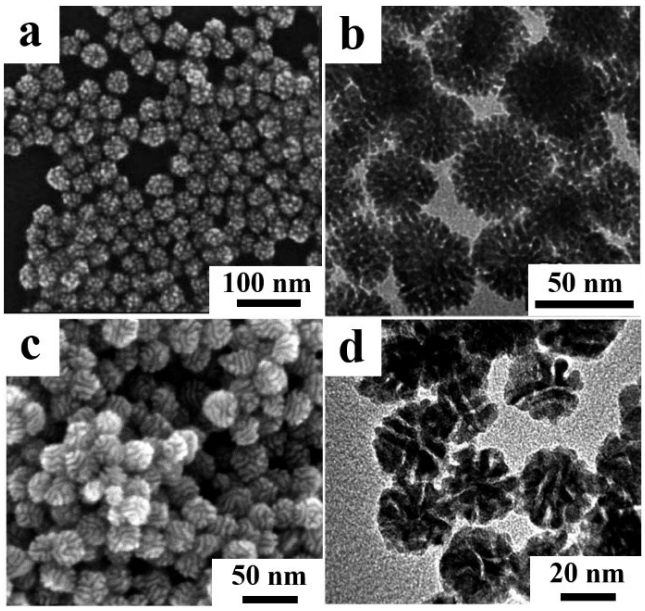

Figure 1.13 (a, c) SEM and (b, d) TEM images of mesoporous Pd particles prepared *via* chemical reduction with different structure-directing agents: (a, b) CTAC (Reproduced with permission.[132] Copyright 2011, The Royal Society of Chemistry) and (c, d) HDPC (Reproduced with permission.[134] Copyright 2014, The Royal Society of Chemistry)

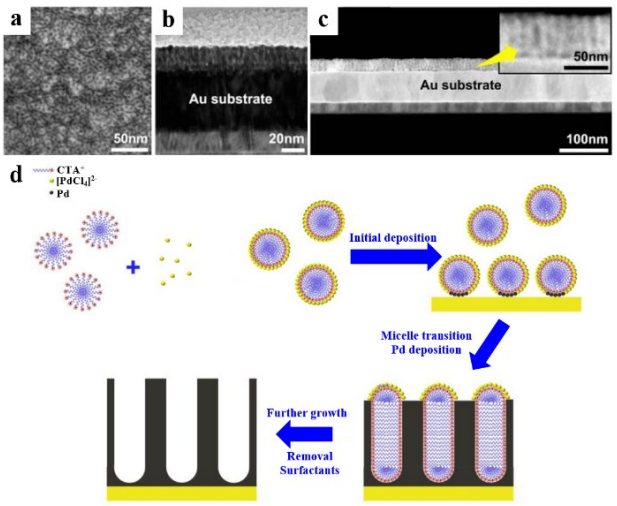

Figure 14. (a) Top view SEM image, cross-sectional (b) TEM and (c) HAADF-STEM images of mesoporous Pd film with vertically-aligned mesochannels. Schematic diagram illustrating the formation of mesoporous Pd film is shown in panel (d). Reproduced with permission.[136] Copyright 2015, American Chemical Society.

Cationic surfactants, such as cetyltrimethyl ammonium bromide (CTAB), cetyltrimethyl ammonium chloride (CTAC), hexadecylpyridinium chloride (HDPC), cetylpyridinium chloride (CPC) and non-ionic surfactants, such as Pluronic F127 and P123, can assist the formation of mesoporous Pd *via* chemical reduction. For example, Zhang and co-workers successfully prepared spherical mesoporous Pd particles with an average diameter of *ca.* 33 nm and rough surface by utilizing CTAC as a structure-directing agent (**Figure 1.13a**).[132] An in-depth structural analysis of an individual sphere by TEM revealed that each sphere is actually composed of smaller nanoparticles with an average size of 7 nm (**Figure 1.13b**). Later, Li *et al.* reported the successful size-controlled synthesis of spherical mesoporous Pd particles by employing dual surfactants, HDPC and F127 (**Figure 1.13c, d**).[134] In their report, the reaction solution consisted of HPDC, F127, Na_2PdCl_4 and ascorbic acid, which acted as shape-directing agent, protecting agent, Pd source and reducing agent, respectively. The size of the mesoporous Pd particles could be easily controlled by tuning the amount of F127 in the reaction solution. The rough surface of these particles was caused by the oxidative etching process as a result of the sufficient amount of Cl^- ions derived from the cationic surfactant. When tested for formic acid oxidation, the mesoporous Pd catalyst exhibited more than double the activities of commercial Pd black and Pd nanoparticles, along with better electrochemical stability. The superior activity and stability were attributed to the mesoporous nature of these particles with high-index facets, which provided a high density of active sites. Apart from spherical mesoporous Pd particles, mesoporous Pd film has also been fabricated *via* electrodeposition with the assistance of CTAC.[136] The applied deposition potential was fixed at a constant value to attract metallic ion complexes in the electrolyte solution toward the working electrode and to ensure successful reduction of the metallic ion complexes to the metallic state. Interestingly, the deposited Pd film formed vertical mesochannels with pore channel size of 2.1 ± 0.2 nm and channel wall size of 3.3 ± 0.2 nm (**Figure 1.14**). The presence of these vertical mesochannels ensured easier access for the reactant and product to and from inner side of the pores, owing to the lower diffusion resistance.[118] Although various surfactants have been successfully utilized as pore-directing agents in the fabrication of mesoporous metals, achieving mesoporous Pd particles with controllable pore size and orientation using surfactants is still challenging and further studies are needed to resolve this issue in the future.

1.4. Functionalization of Pd-Based Nanocatalyst

1.4.1. Pd-Based Alloys and Intermetallics

Despite its high catalytic activity, pure Pd cannot exceed the performance of Pt in many catalytic reactions. Furthermore, the intermediates produced during the oxidation of small organic molecules, such as carbon monoxide (CO) are often strongly adsorbed on the Pd surface, thereby lowering its catalytic performance. In the case of oxygen oxidation reaction, the oxygenated species tend to adsorb on the surface of pure Pt or Pd catalyst. In addition, pure Pt or Pd catalysts suffer from poor alcohol tolerance when employed in direct alcohol fuel cells. Therefore, the development of intermetallics or Pd alloys with non-noble metals has gained significant momentum in the last ten years to produce cheaper high-performance catalysts with enhanced stability.[140-149] The tolerance of Pd to poisoning species in direct alcohol fuel cells can be enhanced by combining or alloying it with other transition metals (*e.g.*, Ni, Co, Fe, Cu, Cr, Sn, Mo, and W). Such enhancement is believed to have arisen from two possible mechanisms: 1) the neighbor sites of Pd atoms from the second element provide oxygenated species which induce a surface reaction with the Pd-adsorbed poisoning species and 2) the alloy structure shift the energy of Pd electronic states, thus resulting in a weakening of Pd-poisoning species interaction.[150-156] In the case of electrooxidation of ethanol, incomplete oxidation of ethanol sometimes occurs due to the decreased capability of Pd to break the C−C bond when the ethanol oxidation goes through the C_2 pathway.[157] Therefore, by alloying Pd with other element(s), it becomes possible to completely oxidize ethanol into CO_2.[158-160] Meanwhile, in the case of cathode catalyst, the alcohol cross-over tolerance enhancement can be achieved by weakening the bond strength of the oxygenated species on the catalyst surface.

To date, numerous Pd-based intermetallics and alloys have been reported in the literatures.[161-190] **Table 1.1** lists an exhaustive summary of previously reported Pd-based alloys and intermetallics, including their synthetic approach, application and properties. The most common solution-based methods for generating Pd-based alloys or intermetallics are chemical reduction, galvanic replacement reaction and polyol method. With regard to the chemical reduction method, the reduction and deposition of the secondary element on the Pd to prepare the bimetallic alloys are typically achieved through underpotential deposition (UPD). For instance, Pd-Cu bimetallic alloys with tripod architectures were

previously reported by Zhang and co-workers.[176] To generate such alloys, the Cu atoms were deposited on the Pd surface after the preferential reduction of $PdBr_4^{2+}$ into Pd metal (**Figure 1.15a**). The Pd ions could be directly reduced to metallic Pd by ascorbic acid. Meanwhile, in the absence of Pd precursors in the reaction solution, no Cu particles were obtained, indicating that the Cu UPD could only occur on the metal surface with a higher redox potential than its standard reduction potential. The formation of the tripod Pd-Cu bimetallic alloys was governed by the presence of Cu precursor and the amount of KBr in the reaction solution. In the absence of Cu precursor, only Pd nanoparticles with cubic morphology were obtained. When a small amount of Cu precursor was introduced in the reaction solution, the cubic Pd nanoparticles were transformed into Pd-Cu alloy with a mixture morphology of cubic and tripods. Upon the addition of more Cu precursor, Pd-Cu tripods with clear branched arms were observed (**Figure 1.15b**). In the early stage of the synthesis (t = 10 min), the small plate-like particle seeds of *ca.* 4 nm in size with a triangular shape were formed, together with very short arms. The branched tripod structures grew along three <211> directions as the synthesis proceeded. The atomic arrangement on the side face of the arm branches was characterized by the alternation of {111} and {100} atom steps (**Figure 1.15d and 1.15e**). In addition, the formation of the tripod morphology was also facilitated by the Br^- ions. Here, the growth direction was affected by the strongly bonded Br^- ions to the three of the {100} side faces of a triangular plate, which forced the Pd atoms to grow on the three corners of the plate-like seed to generate the tripod structure (**Figure 1.15c**). The bimetallic PdCu catalyst was found to exhibit almost 9 times higher mass activity for formic acid oxidation than the commercial Pdb as well as better stability due to the contribution from the high-index facets.

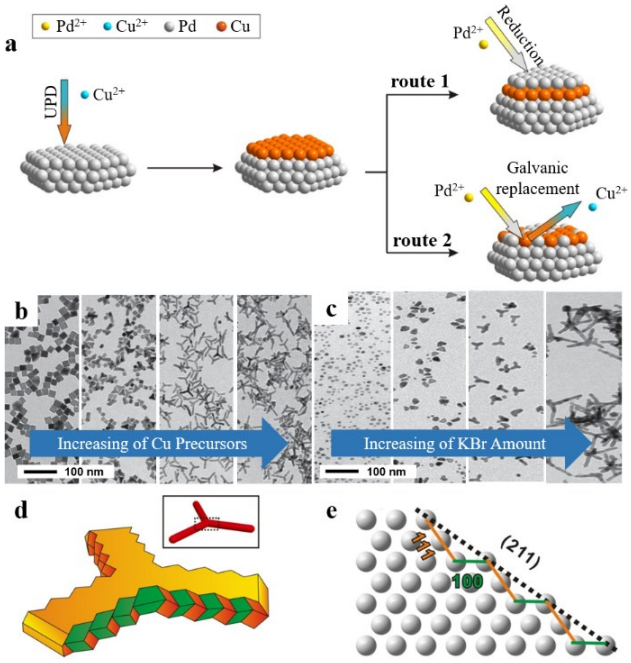

Figure 1.15. (a) A schematic illustration showing the Cu under potential deposition (UPD) process during the formation of Pd-Cu nanocrystals. TEM images showing the structural variations of the Pd-Cu bimetallic alloy by (b) increasing the amount of Cu precursor (0, 1, 3, and 5 mg, respectively) and (c) increasing the amount of KBr involved in the reaction solution (0, 50, 100, and 300 mg, respectively). (d) A model of the Pd-Cu tripod in the central region marked in the inset, indicating that the side faces are consisted of alternating {100} and {111} steps. (e) An illustration of the atomic arrangement for the side face, showing the alternation of {100} and {111} atom steps. Reproduced with permission.[176] Copyright 2014, Wiley-VCH Verlag GmbH.

Table 1.1 Various Pd-based intermetallic and alloy nanocatalysts synthesized through solution-phase and electrochemical deposition methods reported in the literatures.

Compound	Morphology	Intermetallic or Alloy	Synthetic Approach	Features	Applications	Ref.
Pd_2Ge	3D Networks	Intermetallic	Solvothermal	▪ High activity toward ethanol oxidation and better stability compared to Pd/C	Electrooxidation of ethanol	[161]
Pd_3Pb	Nanowire networks	Intermetallic	One-pot reduction	▪ Bifunctional catalyst ▪ Superior long-term stability ▪ Higher activity toward ethanol oxidation and oxygen reduction ▪ Better methanol- and CO-tolerance than PdB	Electrooxidation of methanol and electroreduction of oxygen	[162]
Pd_3Pb	Flower-like nanoparticles	Intermetallic	Polyol method	▪ The synthetic method can be extended for the formation of other Pd and group IV metal-based intermetallics ▪ Higher activity toward ethanol oxidation and formic acid compared to Pd/C	Electrooxidation of formic acid and ethanol	[163]
PdBi	Nanowires	Alloy	Solvothermal	▪ Superior mass activity toward formic acid oxidation in comparison with Pd/C	Electrooxidation of formic acid	[164]
PdCo	Nanoparticles	Alloy	Chemical reduction	▪ Final product composition can be tuned by metal molar ratios ▪ High activity in the order of $Co_{50}Pd_{50}$ > $Co_{60}Pd_{40}$ > $Co_{10}Pd_{90}$ > Pd.	Electrooxidation of formic acid	[165]
PdCo	Mesoporous	Alloy	Electrochemical deposition and de-alloying	▪ Final product composition can be tuned by changing the applied potential deposition ▪ Exhibit higher activity compared to conventional nanoparticle-based catalyst	Electroreduction of oxygen	[166]
PdCo, PdNi	Dendritic	Alloy	One-pot solvothermal	▪ More negative onset potential for CO oxidation ▪ Higher catalytic activity for CO oxidation ▪ High activity toward methanol and ethylene glycol oxidation in the order of PdCo > PdNi > Pd dendritic > PdB	Electrooxidation of methanol and ethylene glycol	[167]
PdCoP	3D Networks	Alloy	Chemical reduction	▪ Large BET surface area ▪ Higher hydrazine oxidation activity than PdCo	Electrooxidation of hydrazine	[168]
PdCu	Branched nanopods	Alloy	Galvanic replacement reaction	▪ More negative onset potential for CO oxidation ▪ High activity toward formic acid oxidation and oxygen reduction ▪ Good stability	Electrooxidation of formic acid Electroreduction of oxygen	[169]
PdCu	Nanowire networks	Alloy	One-pot reduction	▪ High surface area and mass activity toward ethanol oxidation	Electrooxidation of ethanol	[170]
PdCu	Concave tetrahedra	Alloy	One-pot hydrothermal	▪ Stable and tolerance toward CO poisoning ▪ Higher mass activity than PdB toward formic acid oxidation	Electrooxidation of formic acid	[171]
PdCu	Aerogels	Alloy	One-pot reduction	▪ High activity toward ethanol oxidation and better stability compared to Pd/C	Electrooxidation of ethanol	[172]

Compound	Morphology	Intermetallic or Alloy	Synthetic Approach	Features	Applications	Ref.
PdCu	Porous nanoparticles	Alloy	Hydrothermal	▪ High ECSA due to the porous structure ▪ Higher activities for methanol and formic acid oxidation compared to Pd/C ▪ Good stability	Electrooxidation of methanol and formic acid	[173]
PdCu	Hollow nanocubes	Alloy	Solvothermal	▪ High ECSA due to the hollow structure ▪ Higher activity for formic acid oxidation compared to Pd nanoparticles ▪ Good stability	Electrooxidation of formic acid	[174]
PdCu	Nanodendrites	Alloy	Chemical reduction	▪ Tunable Cu to Pd composition ratio ▪ Higher activity and better stability toward methanol oxidation than Pd/C	Electrooxidation of methanol	[175]
PdCu	Nanotripods	Alloy	Chemical reduction	▪ Encased by high-index facets ▪ Mass activity toward formic acid about 8.7 times higher than PdB ▪ Better stability	Electrooxidation of formic acid	[176]
PdCu	Nanosheets	Alloy	Solvothermal	▪ Superior activity about 10 times higher than PdB ▪ Excellent ECSA ▪ Better CO tolerance due to the modulated *d*-band electrons	Electrooxidation of methanol	[177]
PdCu	Spherical, cubic, and dendritic nanoparticles	Alloy	Galvanic replacement reaction	▪ High Faradaic efficiency for CO conversion	Electroreduction of CO_2	[178]
PdCu	3D Branched	Alloy	One-pot reduction	▪ High activity and better stability toward formic acid oxidation compared to PdB and Pd/C	Electrooxidation of formic acid	[179]
PdCuCo, PdCuNi, PdCu	Nanoparticles	Intermetallic	One-pot reduction and thermal annealing	▪ Bifunctional catalyst ▪ Ordered intermetallic phase ▪ Activity increase in the order of Pd/C < Pt/C < ordered PdCu < ordered PdCuNi < ordered PdCuCo	Electrooxidation of ethanol and electroreduction of oxygen	[180]
PdCuCr	Nanoparticles	Alloy	Chemical reduction	▪ Higher activity and selectivity than bimetallic PdCu, PdCr and monometallic Pd	Dehydrogenation of Formic Acid	[181]
PdNi	Nanowire networks	Alloy	Chemical reduction	▪ Higher activity for formic acid oxidation compared to Pd/C ▪ Good stability	Electrooxidation of formic acid	[182]
PdNi	Aerogels	Alloy	One-pot reduction	▪ Superior mass activity toward ethanol oxidation about 5 times higher than Pd/C ▪ Excellent stability	Electrooxidation of ethanol	[183]
PdNi	3D Networks	Alloy	Chemical reduction	▪ Hierarchical pore structure ▪ Superior ORR performance in comparison with PdNi nanoparticles and PdB	Electroreduction of oxygen	[184]
PdNi	3D Networks	Alloy	One-pot reduction	▪ High surface area due to hierarchical porous structure ▪ High activity toward methanol oxidation and better stability compared to Pd/C	Electrooxidation of methanol	[185]
PdNi	Nanowires	Alloy	Electrodeposition	▪ Consist of mesopores (an average diameter of 3-6 nm) ▪ Higher activity for formic acid oxidation compared to Pd/C ▪ Better stability	Electrooxidation of formic acid	[186]
Pd-P	3D Networks	Alloy	Hydrothermal	▪ More negative onset potential for CO oxidation	Electrooxidation of formic acid	[187]

Compound	Morphology	Intermetallic or Alloy	Synthetic Approach	Features	Applications	Ref.
PdPb	Aerogels	Intermetallic	One-pot reduction	▪ High activity toward formic acid oxidation and oxygen reduction ▪ Good stability ▪ Ordered intermetallic phase ▪ Mass activity toward ethylene glycol oxidation about 6 times higher than PdB ▪ Better stability than PdB	Electrooxidation of ethylene glycol	[188]
PdSn	Dendritic	Alloy	Electrochemical deposition	▪ More negative onset potential for CO oxidation ▪ Higher catalytic activity for CO oxidation ▪ High activity toward ethanol	Electrooxidation of ethanol	[189]
PdTe	Nanowires	Alloy	Hydrothermal	▪ Mass activity toward ethylene glycol oxidation about 4.5 times higher than Pd/C ▪ Good stability	Electrooxidation of methanol and ethylene glycol	[190]

More recently, Fan *et al.* successfully created ultrathin PdCu nanosheets with average thickness of 2.71 ± 0.48 nm and lateral size of 33.8 ± 8.3 nm through a solvothermal method (**Figure 1.16a**).[177] In their synthesis, CO molecules and *n*-butylamine were used as capping agents by promoting anisotropic growth. In addition, *n*-butylamine also assisted the reduction of Cu^{2+} by creating complexes between Cu^{2+} and ammonium. In addition, the wrinkle-free nanosheet morphology was also affected by the presence of PVP and CTAB in the reaction solution, which acted as stabilizing agent (to prevent aggregation) and shape-directing agent, respectively. By changing the ratio of the initial Pd and Cu precursors, the final composition of the PdCu alloy could be tuned (**Figure 1.16c**). Interestingly, these bimetallic nanosheets exhibited a modulated electronic structure of Pd atoms, as evidenced by theoretical and experimental observations. The theoretical study by density functional theory (DFT) calculations showed that the *d*-band center of PdCu nanosheets (−2.44 eV) was further away from the Fermi level, as compared to that of PdCu nanoparticles (−2.25 eV). The XPS results also supported the DFT calculations, as indicated by the shift of the core-level XPS peak of Pd in PdCu nanosheets by about 0.25 eV toward higher binding energy relative to that of PdCu nanoparticles, indicating a down-shift of the *d*-band of PdCu nanosheets (**Figure 1.16b**). These findings suggested that the introduction of Cu atoms could effectively decrease the bonding between the adsorbate and Pd surface which in turn, improved the catalytic activity and stability of the bimetallic PdCu nanosheets.

The intermetallic structure differs from its counterparts (alloy and bimetallic) in terms of its ordered structure which leads to some unique advantages, such as uniform surrounding of the active sites and therefore, the number as well as the distance between neighboring sites can be easily identified both experimentally and theoretically. However, the ordered structure is typically achieved by post-synthetic heating at a very high temperature (1000 °C). Previously, two different groups reported the intermetallic Pd_3Pb and Pd_2Ge nanonetworks *via* one-pot reduction and solvothermal methods, respectively, at low reaction temperatures (170 °C and 220 °C). The ordered Pd_2Ge nanonetwork was firstly reported by Sarkar and co-workers.[161] To synthesize this intermetallic nanonetwork, K_2PdCl_4 and $GeCl_4$ were used as the metal precursors, superhydride ($Li(Et_3BH)$) was employed as the reducing agent and tetraethylene glycol (TEG) was utilized as the solvent. Their TEM analysis revealed that in the initial stage of the reaction, Pd_2Ge was formed as small nanoparticles. Then, after 24 h, the as-formed intermetallic particles grew larger and became joined together (**Figure 1.17a**). Through further reaction (36 h), the joined particles

formed a large connected network (**Figure 1.17b**) *via* oriented attachment (**Figure 1.17c**). The covalent bonding strength between Pd and the secondary element in the intermetallic structure was studied by XPS. As seen in **Figure 1.17d-g**, the binding energies of the core-level Ge peaks were shifted down by 0.7 eV compared to elemental Ge, indicating the existence of a strong covalent bond between Pd and Ge. When tested for EOR, the ordered Pd_2Ge nanonetwork exhibited not only higher activity but also better stability than the commercial Pd/C catalyst. The superior electroactivity of the intermetallic Pd_2Ge nanonetwork was attributed to the perfect balance between the adsorption energies of the reaction intermediate species, such as CH_3CO and OH. Their theoretical simulations revealed that the intermetallic Pd_2Ge could bond strongly to OH, however it was only weakly bonded to CH_3CO.

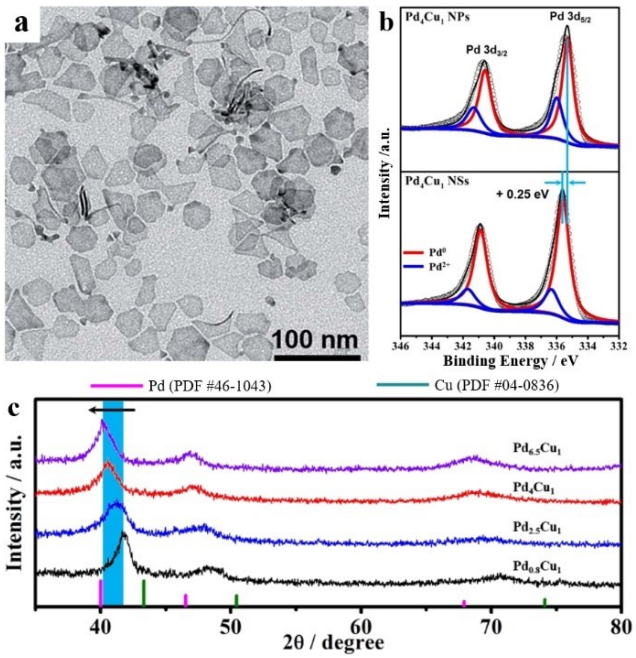

Figure 1.16 (a) TEM image of Pd_4Cu_1 nanosheets (NSs). (b) The Pd 3d XPS spectra of Pd_4Cu_1 nanoparticles (NPs) and Pd_4Cu_1 NSs. The core-level XPS peak of Pd in Pd_4Cu_1 NSs was shifted by about 0.25 eV toward higher energy compared to that of Pd_4Cu_1 NPs, indicating a down-shift of the *d*-band in Pd_4Cu_1 NSs. (c) X-ray diffraction patterns of PdCu nanostructures obtained with different Pd/Cu ratio. Reproduced with permission.[177] Copyright 2018, The Royal Society of Chemistry.

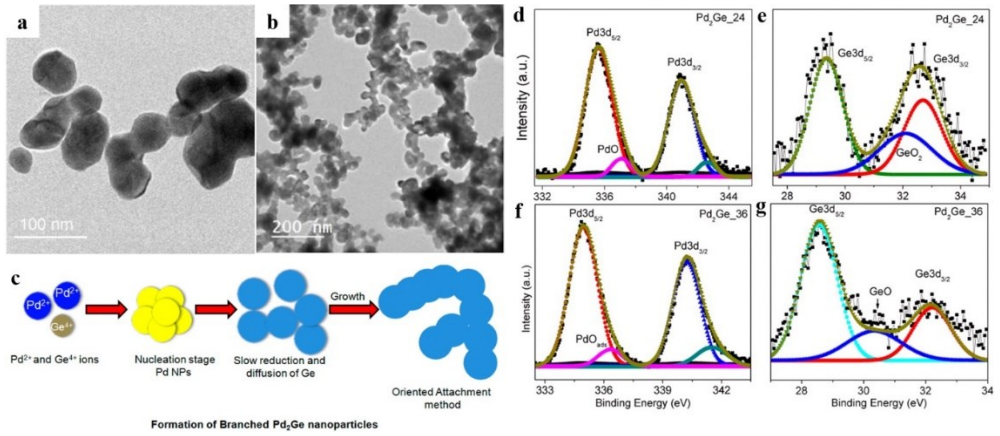

Figure 1.17 TEM images of (a) Pd_2Ge_24 nanoparticles grown from ellipsoidal particles from small nanoparticles (<15 nm) to smaller joined structures and (b) highly connected network of Pd_2Ge_36 nanoparticles. (c) Mechanism of formation of branched Pd_2Ge nanoparticles by oriented attachment. XPS data of Pd_2Ge_24 and Pd_2Ge_36 for (d, f) Pd3d and (e, g) Ge3d orbitals, respectively. Reproduced with permission.[161] Copyright 2015, The Royal Society of Chemistry.

Ordered Pd_3Pb nanonetwork has previously been prepared by Shi *et al.* through a one-pot reduction method at low temperatures.[162] The metal precursors (Na_2PdCl_4 and $Pb(acac)_2$) were co-reduced by citric acid and the solvent, ethylene glycol. In addition, the anisotropic growth of the nanonetwork was dictated by the capping agent PVP. The XRD pattern of the ordered Pd_3Pb nanonetwork showed the typical five peaks assigned to (111), (200), (220), (311), and (222) along with six additional peaks (so-called "ordering peaks") assigned to (100), (110), (210), (211), (300) and (310) planes of Pd_3Pb cP4 crystalline type (space group $Pm\bar{3}m$(221)), thereby confirming the formation of the intermetallic phase. The inter-diffusion of Pb atoms for creating structurally ordered and chemically stable intermetallic phase was important for optimizing the electronic and geometric effects (rough surfaces with abundance of opening channels within the nanonetwork) by downshifting the *d*-band center. This in turn, weakened the adsorption energy of the reaction intermediate products, accelerated the desorption rate and enhanced the catalytic activity, CO tolerance and stability.

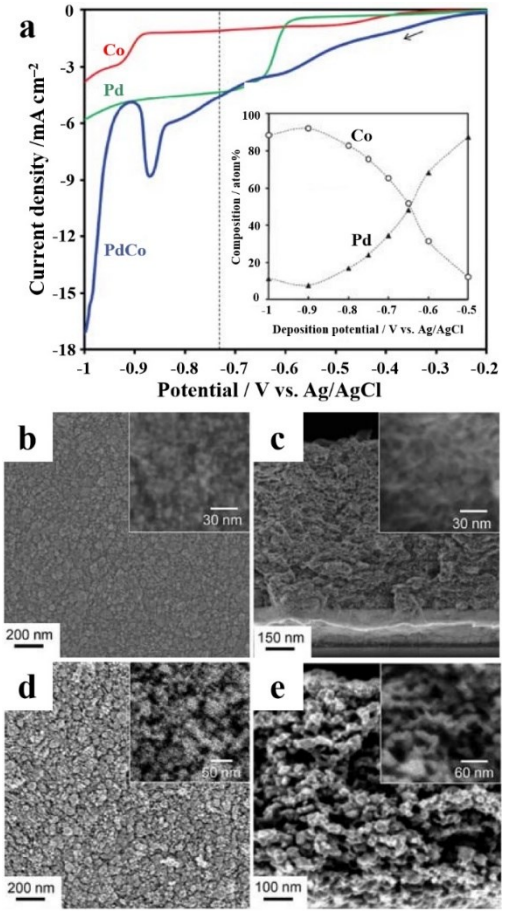

Figure 18. (a) Linear sweep voltammogram (LSV) profiles of mesoporous Co, Pd and PdCo films at 10 mV s^{-1} with a negative scan potential. The vertical dotted line shows the hydrogen evolution potential, 0.73 V *vs.* Ag/AgCl. The inset shows the compositions of the films deposited at different constant potentials (0.5, 0.6, 0.65, 0.7, 0.75, 0.8, 0.9 and 1.0 V vs. Ag/AgCl) for 10 min. (b, d) Top-view and (c, e) cross-sectional SEM images of (b, c) as-deposited and (d, e) de-alloyed mesoporous PdCo films. Reproduced with permission.[166] Copyright 2010, The Royal Society of Chemistry.

Apart from chemical reduction, electrochemical deposition has also been shown to be effective for creating nanoarchitectures of Pd-based alloys. For instance, Tominaka *et al.* reported the fabrication of mesoporous PdCo sponge-like film using electrochemical deposition and de-alloying techniques. The aqueous electrolyte solution consisted of the mixture of $[Pd(NH_3)_4]Cl_2$, NH_4Cl, $CoCl_2$ and malonic acid.[166] Electrochemical deposition of the mesoporous PdCo film was carried out at a constant potential of -0.9 V *vs.* Ag/AgCl for 10 min at 14 ± 2 °C. The mesoporous structure was formed through a subsequent electrochemical de-alloying process by applying a potential of 0.6 V in nitrogen-saturated 0.5 M H_2SO_4 for 6 h at room temperature. The determination of the applied deposition

potential through linear sweep voltammogram (LSV) of the electrolyte solution consisting more than single metal complexes cannot be determined as a simple summation of those individual voltammogram profiles. The linear sweep voltammogram (LSV) profile of the PdCo electrolyte solution showed a unique profile, in which the deposition current increased as the potential was decreased from −0.2 to −0.8 V (**Figure 1.18a**). Comparison of the LSV profiles of PdCo and Co revealed that the reduction and deposition of Co atoms in PdCo occurred through underpotential co-deposition. The quality of the as-deposited mesoporous PdCo film could be enhanced by de-alloying technique, which further improved the porosity by *ca.* 62%, but also reset the Pd and Co composition ratio to 92:8. Such a high level of porosity was beneficial for ensuring good oxygen diffusion and the Pd:Co composition ratio of 92:8 was reported to be the optimum composition for obtaining the best ORR activity (**Figure 1.18b-e**). More importantly, the mesoporous PdCo film displayed a higher ORR activity than the typical Pt electrode, owing to their unique geometric features and enhanced electronic properties.

1.4.2. Supported Pd Nanoparticles

The use of support materials which have larger particle size than the actual catalyst can enable the catalyst particles to be well-dispersed on the support.[191] Good dispersion of the catalyst particles will increase the catalyst contact area with the reactant(s), leading to better catalytic activity, while also reducing the loading of catalyst.[192] To date, numerous materials have been utilized as support materials for noble metal catalysts, including carbons[193-195], oxides[196-198], carbides[199-201] and electroconductive polymers [202-206]. For electrocatalytic applications, some requirements should be fulfilled by the support materials to ensure their successful utilization.[207] These requirements are: (1) high surface area for ensuring good dispersion of metallic catalyst particles; (2) high electrical conductivity; (3) good interaction with the metallic catalyst particles, either through electrostatic, van der Waals, or covalent bonding and (4) high tolerance to poisoning, corrosion and mechanical deformation.

Strong electronic interaction between the metallic catalyst particles and the support material is crucial for achieving high catalytic activity.[208] Several analytical techniques (XPS and Raman spectroscopy) and DFT calculations can be employed to characterize and predict the interaction and charge transfer distribution at the Pd-support interface.[209] For instance, Rao *et al.* revealed the correlation between support functionalization and charge

distribution at the Pd-carbon interface. It was shown that carbon support could modify the electronic properties of Pd and therefore, enhanced the catalytic activity.[210]

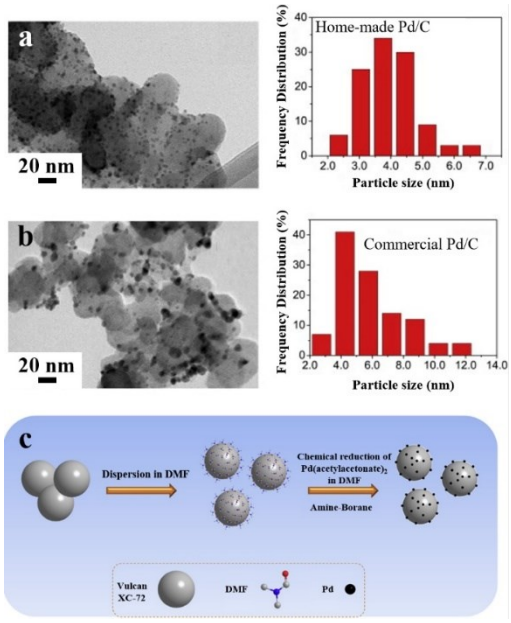

Figure 1.19. TEM image (left) and particle size distribution histograms (right) of (a) home-made Pd/C and (b) commercial Pd/C catalysts. (c) Schematic illustration of the synthesis process of Pd/C catalyst in DMF. Reproduced with permission.[213] Copyright 2015, Elsevier, Ltd.

Carbon black is commonly employed as a carbonaceous support for electrocatalysts due to their high surface area and electrical conductivity. However, its high surface area is mostly contributed by the large density of micropores (<1 nm), which is not good for the dispersion of the metallic catalyst particles and the flow of the reactant(s). In contrast, ordered mesoporous carbon (OMC) and carbon gels are preferred host materials for the deposition of metallic catalyst particles.[211] Furthermore, emerging graphitic carbon materials (*e.g.*, graphene and carbon nanotubes) have also drawn significant attention as catalyst support due to their unique structures and properties, which can affect the chemical stability of the catalyst.[212]

Although commercial carbon black-supported Pd catalysts are widely available on the market, recent studies have been aimed at synthesizing small-sized Pd particles on the carbon support with better size uniformity and improved dispersion. For example, Wang *et al.* successfully prepared monodisperse small-sized Pd particles with an average size of *ca.* 3.8 nm on Vulcan XC-72 through a one-pot reduction method at room temperature.[213]

The size of these Pd particles was more uniform compared to the commercial Pd/C particles (**Figure 1.19a** and **1.19b**). The deposition of the Pd nanoparticles on the carbon surface was achieved through a mild reduction process in the presence of DMF and *N*, *N*-diethylaniline borane (**Figure 1.19c**). In this process, DMF provided a free pair of electrons which could interact with the carbon surface and assisted the formation of monodisperse Pd atoms/cluster on the carbon support. Furthermore, the use of *N*, *N*-diethylaniline borane enabled alkyl substitution to nitrogen, which could prevent the overgrowth of Pd nanoparticles. The resulting carbon-supported monodisperse Pd catalyst exhibited 2.5 times higher ECSA than the commercial Pd/C particles, as investigated by CO-stripping experiments.[214] Correspondingly, they displayed around 2.6 and 4 times higher mass activity than the commercial Pd/C catalyst toward formic acid and ethanol oxidation, respectively. Pd nanoparticles supported on OMC for electrooxidation catalyst have been reported by Hu *et al.*[215] OMC possesses larger pore size and hence, it can host more Pd nanoparticles as well as provide more accessible channels for the reactants and products. Pd nanoparticles with an average size of 3 nm were easily decorated on the highly ordered mesoporous structure with an average pore diameter size of 4.7 nm (**Figure 1.20a-c**). The agglomeration of Pd nanoparticles during self-assembly and growth could be prevented by adding dimethylamine hydrolyzed from DMF as the solvent, as illustrated in **Figure 1.20d**. A significant fraction of Pd nanoparticles inside the porous structure was investigated from the decrease in mean surface area (around 22.4%) of non-decorated OMC and Pd-decorated-OMC through the analysis of nitrogen adsorption isotherms (**Figure 1.20e and 1.20f**). Pd-decorated-OMC showed significant improvement in catalytic activity toward ethanol and methanol oxidation compared to PdB and Pd/C. Hollow graphitic carbon nanocages synthesized using magnesium oxide (MgO) as a sacrificial template have been utilized as support for Pd nanoparticles (*i.e.,* Pd/CN catalyst).[216] Owing to its large surface area, uniform dispersion and excellent electrical conductivity, the Pd/CN catalyst could outperform commercial Pd/C catalyst in EOR.

Emerging carbonaceous materials, such as carbon nanotubes (CNTs), carbon nanofibers (CNFs), graphene and reduced graphene oxide (rGO) are widely used as support materials for Pd nanoparticles.[217-220] Recently, Mondal and co-workers reported a new approach to unzip single-walled CNTs (SWCNTs) simultaneously with the formation of small-sized Pd nanoparticles encapsulated with a graphitic carbon layer. This approach could ensure the successful integration of the metallic catalyst with the honeycomb carbon network, leading to high electrocatalytic activity toward oxidation of formic acid.[221] There

are still some challenges with regard to the deposition of small-sized Pd nanoparticles on the carbon support: (1) How to avoid the agglomeration of Pd nanoparticles; (2) How to prevent the overgrowth of Pd nanoparticles; (3) How to maintain the original carbon structure during growth and/or attachment of Pd and (4) how the Pd nanoparticles can be anchored/attached well on the support surface. A natural polymer, such as deoxyribonucleic acid (DNA), was recently employed to promote the growth of small-sized Pd clusters and to modify the surface of CNTs to prevent aggregation and provide sufficient binding sites.[222] The effect of the size of Pd nanoparticles on the ECSA was studied by Yang *et al.* and Zhang *et al.* Their studies revealed that larger-sized Pd nanoparticles (average size of *ca.* 20 nm) exhibited lower ECSA than smaller-sized ones (average size of *ca*. 4.2 nm).[223] Pd nanoparticles supported on helical carbon nanofibers (Pd/HCNFs) have been reported by two different groups.[224,225] Hu and co-workers utilized a specific type of functional group (phenyl groups) to anchor uniform small-sized Pd nanoparticles (an average size of 4.5 nm) on the surface of HCNFs through π- π interaction.

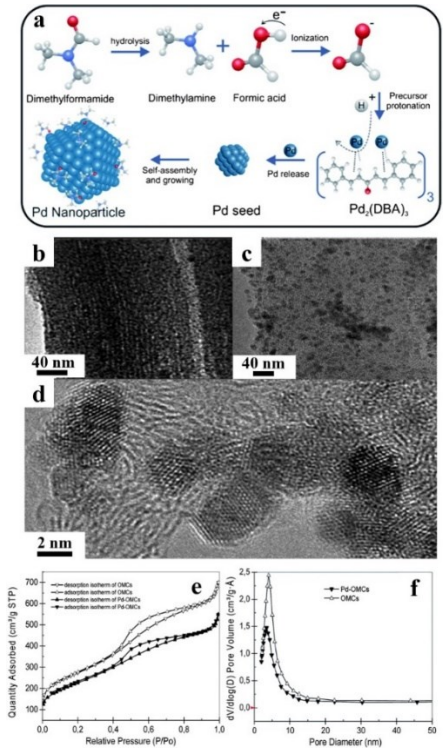

Figure 1.20. (a) An illustration of the formation mechanism of Pd nanoclusters *via* the decomposition of $Pd_2(DBA)_3$ in DMF solution. (b) TEM and (c, d) HRTEM images of Pd–OMCs. (e) Nitrogen adsorption-desorption isotherms and (f) pore size distribution of OMCs (white triangle) and Pd–OMCs (black triangle). Reproduced with permission.[215] Copyright 2014, The Royal Society of Chemistry.

Graphene sheets have also been utilized as support for Pd nanoparticles.[226-228] However, their restacking property, aggregation of metal particles on the pristine sheet surface, and insufficient binding sites present major problems for graphene sheets. To solve these problems, chemical functionalization and chemical doping with heteroatoms should be performed prior to attaching Pd nanoparticles on the sheet surface.[229,230] Kiyani *et al.* Have successfully synthesized uniform small-sized Pd nanoparticles with good dispersion on the surface of nitrogen-doped graphene (NG) sheets. The N-doped graphene sheets exhibited many surface defects which provided good deposition sites for metal nanoparticles.[231] The anchoring of Pd nanocatalysts with exposed high-index facets on 2D support materials, such as graphene sheets is still rarely reported. The successful anchoring of Pd nanoparticles with multi-edges and corners on graphene support was previously reported by Liu and co-workers.[232] The preparation of these graphene-supported Pd nanoparticles comprised of three steps: (1) the preparation of graphene oxide (GO) by modified Hummers‘ method followed by the reduction of GO into reduced graphene oxide (RGO); (2) the preparation of Pd nanoparticles and (3) the assembly of Pd nanoparticles on the RGO support. In this work, ascorbic acid was employed as both reducing and structure-directing agents. Interestingly, the incorporation of the Pd nanoparticles on the RGO support did not alter the morphology as well as the uniformity of the Pd nanoparticles. Such incorporation however, has successfully prevented the agglomeration of the Pd nanoparticles and improved their dispersion on the RGO surface**.** The covalent bond strength of the Pd nanoparticles and RGO support has been calculated theoretically and according to their report, the Pd adatoms on graphene preferred B-site bonding than T-site or H-site. Multi-edges and corners are expected to provide enhanced charge transfer efficiency as these structures can promote the spontaneous formation of localized electric field. The corresponding mechanism of electron transfer from the corner of the Pd nanoparticles to the RGO occurred through strong covalent interaction between Pd nanoparticles and RGO. In comparison to Pd nanoparticles and commercial Pd/C catalyst, the electrocatalytic performance of the Pd/RGO hybrid was higher. This enhancement was attributed to the novel morphology of the nanoparticles with multi-edges and corners, the enhanced conductivity, and the higher surface area contributed by the RGO.

1.5. Thesis Directions

Chemical synthesis, both solution-phase and electrochemical deposition methods, offer a simple process yet high yield and tailored design to produce mesoporous Pd nanomaterials with the presence of surfactant/pore directing agent. Despite a various kind of zero-dimensional (0D) Pd nanocatalyst with well-defined shape: cube, tetrahedral, octahedral, and dodecahedral have been developed through chemical synthesis to achieve the high catalytic performance demand, they are vulnerable towards dissolutions, the Ostwald ripening, and aggregations thus would result in the performance degradation. Hence, the facile synthesis of higher dimensional Pd nanocatalyst which possesses a high density of active sites and enhanced stability by creating mesoporous structure, alloying with the second metal and hybridization with the support materials is still challenging issues to overcome.

1.6. References

[1] Y.-Y. Yang, J. Ren, Q.-X Li, Z.-Y Zhou, S.-G Sun, W.-B. Cai, *ACS Catal.* **2014**, *4*, 798-803.

[2] K. Jiang, H.-X Zhang, S. Zou, W.-B. Cai, *Phys. Chem. Chem. Phys.* **2014**, *16*, 20360-20376.

[3] L. Guczi, Á. Molnár, D. Teschner, in *Comprehensive Inorganic Chemistry II (Second Edition): From Elements to Applications*, Vol. 7 (Eds: J. Reedijk, K. R. Poeppelmeier), Elsevier Ltd., **2013**.

[4] L. Liu, A. Corma, *Chem. Rev.* **2018**, *118*, 4981-5079.

[5] Q.-A. Chen, Z.-S. Ye, Y. Duan, Y.-G. Zhou, *Chem. Soc. Rev.* **2013**, *42*, 497-511.

[6] B. Cai, S. Henning, J. Herranz, T. J. Schmidt, A. Eychmüller, *Adv. Energy Mater.* **2017**, *7*, 1700548.

[7] P. B. Kettler, *Org. Proc. Res. Dev.* **2003**, *7*, 342-354.

[8] E. J. Peterson, A. T. DeLaRiva, S. Lin, R. S. Johnson, H. Guo, J. T. Miller, J. H. Kwak, C. H. F. Peden, B. Kiefer, L. F. Allard, F. H. Ribeiro, A. K. Datye. *Nat. Commun.* **2014**, *5*, 4885.

[9] M. Shao, *J. Power Sources* **2011**, *196*, 2433-2444.

[10] Y. Qiao, C. M. Li, *J. Mater. Chem.* **2011**, *21*, 4027-4036.

[11] C. Bianchini, P. K. Shen, *Chem. Rev.* **2009**, *109*, 4183-4206.

[12] W. Li, in *Materials for Low- Temperature Fuel Cells*, (Eds: B. Ladewig, S. P. Jiang, Y. Yan), Wiley- VCH Verlag GmbH & Co. KGaA, **2014**, Ch. 4.

[13] K. E. Toghill, R. G. Compton, *Int. J. Electrochem. Sci.* **2010**, *5*, 1246-1301.

[14] K. Dhara, D. R. Mahapatra, *Microchim Acta* **2018,** *185,* 49.

[15] L. Wang, A. Lavacchi, M. Bevilacqua, M. Bellini, P. Fornasiero, J. Filippi, M. Innocenti, A. Marchionni, H. A. Miller, F. Vizza, *ChemCatChem* **2015**, *7*, 2214-2221.

[16] Y. Lu, X. Feng, B. S. Takale, Y. Yamamoto, W. Zhang, M. Bao, *ACS Catal.* **2017**, *7*, 8296-8303.

[17] C. Chen, Q. Xie, D. Yang, H. Xiao, Y. Fu, Y. Tana, S. Yaoa, *RSC Adv.* **2013**, *3*, 4473-4491.

[18] S. Golunski, *Platinum Metals Rev.* **2007**, *51*, 162.

[19] E. Antolini, *Energy Environ. Sci.* **2009**, *2*, 915–931.

[20] E. Antolini, S. C. Zignani, S. F. Santos, E. R.Gonzalez, *Electrochim. Acta* **2011**, *56*, 2299-2305.

[21] B. D. Adams, A. Chen, *Mater. Today* **2011**, *14*, 282-289.

[22] G. A. Somorjai, *Chemistry in Two Dimensions: Surfaces,* Cornell University Press, Ithaca, NY, USA **1981**.

[23] X. Huang, S. Tang, X. Mu, Y. Dai, G. Chen, Z. Zhou, F. Ruan, Z. Yang and N. Zheng, *Nat. Nanotech.* **2011**, *6*, 28-32.

[24] P.-Y. Yang, S.-P. Ju, Z.-M. Lai, J.-S. Lin, J.-Y. Hsieh, *Nanoscale* **2016**, *8*, 2041-2045.

[25] A. Chen, C. Ostrom, *Chem. Rev.* **2015**, *115***,** 11999-12044.

[26] P. Ferrin, A. U. Nilekara, J. Greeley, M. Mavrikakis, J. Rossmeisl, *Surf. Sci.* **2008**, *602*, 3424-3431.

[27] W. Vogel, L. Lundquist, P. Ross, P. Stonehart, *Electrochim. Acta* **1975**, *20*, 79-93.

[28] J. Pala, T. Pal, *Nanoscale* **2015**, *7*, 14159-14190.

[29] J. Solla-Gullón, F. J. Vidal-Iglesiasa, J. M. Feliu, *Annu. Rep. Prog. Chem., Sect. C: Phys. Chem.* **2011**, *107*, 263-297.

[30] M. Crespo-Quesada, A. Yarulin, M. Jin, Y. Xia, L. Kiwi-Minsker, *J. Am. Chem. Soc.* **2011**, *133*, 12787–12794.

[31] E. Antolini, J. Perez, *J. Mater. Sci.* **2011,** *46,* 4435-4457.

[32] B. Lim, M. Jiang, J. Tao, P. H. C. Camargo, Y. Zhu, Y. Xia, *Adv. Funct. Mater.* **2009**, *19*, 189-200.

[33] Y. Li, Q. Liu, W. Shen, *Dalton Trans.* **2011**, *40*, 5811-5826.

[34] J. W. Hong, Y. Kim, Y. Kwon, S. W. Han, *Chem.-Asian J.* **2016**, *11*, 2224-2239.

[35] Y. Xia, X. Xia, H.-C. Peng, *J. Am. Chem. Soc.* **2015**, *137*, 7947–7966.

[36] H. Zhang, M. Jin, Y. Xiong, B. Lim, Y. Xia, *Acc. Chem. Res.* **2013**, *46*, 1783–1794.

[37] Z. Yin, L. Lin, D. Ma, *Catal. Sci. Technol.* **2014**, *4*, 4116-4128.

[38] N. Hoshi, M. Nakamura, H. Haneishi, *Electrochemistry* **2017**, *85*, 634–636.

[39] E. D. Wang, J. B. Xu, T. S. Zhao, *J. Phys. Chem. C* **2010**, *114*, 10489–10497.

[40] Z. Quan, Y. Wang, J. Fang, *Acc. Chem. Res.* **2013**, *46*, 191-202.

[41] J. N. Tiwari, R. N. Tiwari, K. S. Kim, *Prog. Mater. Sci.* **2012**, *57*, 724–803.

[42] D. Y. Chung, H. Shin, J. Y. Yoo, K.-S. Lee, N.-S. Lee, K. Kang, Y.-E. Sung, *J. Power Sources* **2016**, *334*, 52-57.

[43] L. M. Falicov, G. A. Somorjai, *Proc. Natl. Acad. Sci. USA* **1985**, *82*, 2207-2211.

[44] R. Huang, Y.-H Wen, Z.-Z. Zhua, S.-G. Sun, *J. Mater. Chem.* **2011**, *21*, 11578-11584.

[45] D. Yuan, X. Gong, R. Wu, *Phys. Rev. B* **2007**, *75*, 233401-233404.

[46] E. Pizzutilo, S. J. Freakley, S. Geiger, C. Baldizzone, A. Mingers, G. J. Hutchings, K. J. J. Mayrhofer, S. Cherevko, *Catal. Sci. Technol.* **2017**, *7*, 1848-1856.

[47] D. A. Slanac, W. G. Hardin, K. P. Johnston, K. J. Stevenson, *J. Am. Chem. Soc.* **2012,** *134*, 9812–9819.

[48] W. Wang, F. Lv, B. Lei, S. Wan, M. Luo, S. Guo, *Adv. Mater.* **2016**, *28*, 10117-10141.

[49] D. Deng, K. S. Novoselov, Q. Fu, N. Zheng, Z. Tian, X. Bao, *Nat. Nanotechnol.* **2016**, *11*, 218-230.

[50] C. Wen, Y. Wei, D. Tang, B. Sa, T. Zhang, C. Chen, *Sci. Rep.* **2017**, *7*, 1-11.

[51] Q. Li, S. Sun, *Nano Energy* **2016**, *29*, 178-197.

[52] Y. Xia, Y. Xiong, B. Lim, S. E. Skrabalak, *Angew. Chem. Int. Ed.* **2008**, *48*, 60-103.

[53] H. You, S. Yang, B. Dinga, H. Yang, *Chem. Soc. Rev.* **2013**, *42*, 2880-2904.

[54] W. Niu, L. Zhang, G. Xu, *ACS Nano* **2010**, *4*, 1987-1996.

[55] S.-H. Yoo, J.-H. Lee, B. Delley, A. Soon*, Phys. Chem. Chem. Phys*. **2014**, *16*, 18570-18577.

[56] Y. Xiong, Y. Xia, *Adv Mater.* **2007,** *19*, 3385-3391.

[57] S.-Y. Liu, Y.-T. Shen, C.-Y. Chiu, S. Rej, P.-H. Lin, Y.-C. Tsao, M. H. Huang, *Langmuir* **2015**, *31*, 6538−6545.

[58] J. Zhang, C. Feng, Y. Deng, L. Liu, Y. Wu, B. Shen, C. Zhong, W. Hu, *Chem. Mater*. **2014**, *26*, 1213−1218.

[59] F. J. Vidal-Iglesias, R. M. Arán-Ais, J. Solla-Gullón, E. Garnier, E. Herrero, A. Aldaz, J. M. Feliu, *Phys. Chem. Chem. Phys.* **2012**, *14*, 10258-10265.

[60] X. Xie, G. Gao, Z. Pan, T. Wang, X. Meng, L. Cai, *Sci. Rep.* **2015**, *5*, 1-5.

[61] L. Wei, C.-D. Xu, L. Huang, Z.-Y. Zhou, S.-P. Chen, S.-G. Sun, *J. Phys. Chem. C* **2016**, *120*, 15569-15577.

[62] Y. Zhang, M. Wang, E. Zhu, Y. Zheng, Y. Huang, X. Huang, *Nano Lett.* **2015**, *15*, 7519-7525.

[63] W. Niu, W. Zhang, S. Firdoz, X. Lu, *Chem. Mater.* **2014**, *26*, 2180-2186.

[64] N. Su, X. Chen, Y. Ren, B. Yue, H. Wang, W. Cai, H. He, *Chem. Commun.* **2015**, *51*, 7195-7198.

[65] Y. Wang, H.-C. Peng, J. Liu, C. Z. Huang, Y. Xia, *Nano Lett.* **2015**, *15*, 1445-1450.

[66] C.-H. Kuo, L. K. Lamontagne, C. N. Brodsky, L.-Y. Chou, J. Zhuang,B. T. Sneed, M. K. Sheehan, C.-K. Tsung, *ChemSusChem* **2013**, *6*, 1993-2000.

[67] D. A. Gilbert, E. C. Burks, S. V. Ushakov, P. Abellan, I. Arslan, T. E. Felter, A. Navrotsky, K. Liu, *Chem. Mater.* **2017**, *29*, 9814-9818.

[68] C. Koenigsmann, S. S. Wong, *Energy Environ. Sci.* **2011**, *4*, 1161-1176.

[69] H. Meng, C. Wang, P. K. Shen, G. Wu, *Energy Environ. Sci.* **2011**, *4*, 1522-1526.

[70] C. Xu, H. Wang, P.K. Shen, S. P. Jiang, *Adv. Mater.* **2007**, *19*, 4256-4259.

[71] Y. Wang, S.-I. Choi, X. Zhao, S. Xie, H.-C. Peng, M. Chi, C. Z. Huang, Y. Xia, *Adv. Funct. Mater.* **2014**, *24*, 131-139.

[72] L. Xiao, L. Zhuang, Y. Liu, J. Lu, H. D. Abruña, *J. Am. Chem. Soc.* **2009**, *131*, 602-608.

[73] A. K. Das, N. H. Kim, D. Pradhan, D. Hui, J. H. Lee, *Composites, Part B* **2018**, *144*, 11-18.

[74] S. Y. Tee, C. P. Teng, E. Ye, *Mater. Sci. Eng., C* **2017**, *70*, 1018-1030.

[75] Q. Wang, Q. Wang, K. Qi, T. Xue, C. Liu, W. Zheng, X. Cui, *Anal. Methods* **2015**, *7*, 8605-8610.

[76] M. A. Z. G. Sial, M. A. U. Din, X. Wang, *Chem. Soc. Rev*. **2018**, *47*, 6175-6200,

[77] M. N. Nadagouda, V. Polshettiwar, R. S. Varma, *J. Mater. Chem*. **2009**, *19*, 2026-2031.

[78] F. Jia, K.-w. Wong, R. Du, *Electrochem. Commun.* **2009**, *11*, 519-521.

[79] X. Yin, M. Shi, K. S. Kwok, H. Zhao, D. L. Gray, J. A. Bertke, H. Yang, *Nano Res.* **2018**, *11*, 3442–3452.

[80] D. Xu, Y. Liu, S. Zhao, Y. Lu, M. Han, J. Bao, *Chem. Commun.* **2017**, *53*, 1642-1645.

[81] X. Yin, X. Liu, Y.-T. Pan, K. A. Walsh, H. Yang, *Nano Lett.* **2014**, *14*, 7188-7194.

[82] W. Zhu, L. Zhang, P. Yang, C. Hu, Z. Luo, X. Chang, Z. Zhao, J. Gong, *Angew. Chem. Int. Ed.* **2018**, *57*, 1-6.

[83] X. Zhang, C. Lian, Z. Chen, C. Chen, Y. Li, *Nano Res.* **2018,** *11*, 4142-4148.

[84] H. Shan, L. Liu, J. He, Q. Zhang, W. Chen, R. Feng, C. Chang, P. Zhang, P. Tao, C. Song, W. Shang, T. Deng, J. Wu, *CrystEngComm* **2017**, *19*, 3439-3444.

[85] H. Wang, X. He, Y. Zhao, J. Li, T. Huang, H. Liu, *CrystEngComm* **2017**, *19*, 4304-4311.

[86] K. Gu, X. Pan, W. Wang, J. Ma, Y. Sun, H. Yang, H. Shen, Z. Huang, H. Liu, *Small* **2018**, *14*, 1801812.

[87] M. Farsadrooh, J. Torrero, L. Pascual, M. A. Peña, M. Retuerto, S. Rojas, *Appl. Catal., B* **2018**, *237*, 866-875.

[88] D. Xu, X. Liu, H. Lv, Y. Liu, S. Zhao, M. Han, J. Bao, J. He, B. Liu, *Chem. Sci.* **2018**, *9*, 4451-4455.

[89] X. Qiu, H. Zhang, P. Wu, F. Zhang, S. Wei, D. Sun, L. Xu, Y. Tang, *Adv. Funct. Mater.* **2017**, *27*, 1603852.

[90] M. Davi, D. Keßler, A. Slabon, *Thin Solid Films* **2016**, *615*, 221-225.

[91] B. Cai, V. Sayevich, N. Gaponik, A. Eychmüller, *Adv. Mater.* **2018***, 30,* 1707518.

[92] N. C. Bigall, A.-K. Herrmann, M. Vogel, M. Rose, P. Simon, W. Carrillo-Cabrera, D. Dorfs, S. Kaskel, N. Gaponik, A. *Eychmüller, Angew. Chem. Int. Ed.* ***2009,*** 48*, 9731-9734.*

[93] W. Liu, A.-K. Herrmann, N. C. Bigall, P. Rodriguez, D. Wen, M. Oezaslan, T. J. Schmidt, N. Gaponik, A. Eychmüller, *Acc. Chem. Res.* **2015**, *48*, 154-162.

[94] A. Mohanty, N. Garg, R. Jin, *Angew. Chem. Int. Ed.* **2010**, *49*, 4962-4966.

[95] V. Malgras, H. Ataee-Esfahani, H. Wang, B. Jiang, C. Li, K. C.-W. Wu, J. H. Kim, Y. Yamauchi, *Adv. Mater.* **2016**, *28*, 993-1010.

[96] J. Zhang, C. M. Li, *Chem. Soc. Rev.* **2012**, *41*, 7016-7031.

[97] S. Tominaka, S. Ohta, H. Obata, T. Momma, T. Osaka, *J. Am. Chem. Soc.* **2008**, *130*, 10456-10457.

[98] X. Niu, M. Lan, H. Zhao, C. Chen, *Anal. Chem.* **2013**, *85*, 3561-3569.

[99] S.A. Al-Muhtaseb, J.A. Ritter, *Adv. Mater.* **2003**, *15*, 101-114.

[100] S. D. Minteer, B. Y. Liaw, M. J. Cooney, *Curr. Opin. Biotechnol.* **2007**, *18*, 228-234.

[101] Y. Kamitaka, S. Tsujimura, N. Setoyama, T. Kajino, K. Kano, *Phys. Chem. Chem. Phys.* **2007**, *9*, 1793-1801.

[102] D. Wen, A.-K. Herrmann, L. Borchardt, F. Simon, W. Liu, S. Kaskel, A. Eychmüller, *J. Am. Chem. Soc.* **2014**, *136*, 2727-2730.

[103] F. J. Burpo, E. A. Nagelli, L. A. Morris, J. P. McClure, M. Y. Ryu, J. L. Palmer, *J. Mater. Res.* **2017**, *32*, 4153-4165.

[104] M. Z. Yazdan-Abad, M. Noroozifar, A. R. M. Alam, H. Saravani, *J. Mater. Chem. A* **2017**, *5*, 10244-10249.

[105] A. S. Douk, H. Saravani, M. Noroozifar, *Electrochim. Acta* **2018,** *275*, 182-191.

[106] P. Zhou, Z. Dai, M. Fang, X. Huang, J. Bao, J. Gong, *J. Phys. Chem. C* **2007**, *111*, 12609-12616.

[107] S. Patra, B. Viswanath, K. Barai, N. Ravishankar, N. Munichandraiah, *ACS Appl. Mater. Interfaces* **2010**, *2*, 2965-2969.

[108] F. Yang, K. Cheng, Y. Mo, L. Yu, J. Yin, G. Wang, D. Cao, *J. Power Sources* **2012**, *217*, 562-568.

[109] Y. Zhao, S.-J. Qin, Y. Li, F.-X. Deng, Y.-Q. Liu, G.-B. Pan, *Electrochim. Acta* **2014**, *145*, 148-153.

[110] A. J. Bard, L. R. Faulkner, *Electrochemical Methods: Fundamental and Applications*, 2nd ed., John Wiley & Sons, Hoboken, NJ, **2001**.

[111] J. Bai, L. Shen, D. Sun, Y. Tang, T. Lu, *CrystEngComm* **2014**, *16*, 10445-10450.

[112] W. Du, K. E. Mackenzie, D. F. Milano, N. A. Deskins, D. Su, X. Teng, *ACS Catal.* **2012**, *2*, 287-297.

[113] Y. Liu, J. Goebla, Y. Yin, *Chem. Soc. Rev.* **2013**, *42*, 2610-2653.

[114] S. Yang, X. Luo, *Nanoscale* **2014**, *6*, 4438-4457.

[115] X.-Y. Yang, L.-H. Chen, Y. Li, J. C. Rooke, C. Sanchez, B.-L. Su, *Chem. Soc. Rev.* **2017**, *46*, 481-558.

[116] N. Menzel, E. Ortel, R. Kraehnert, P. Strasser, *ChemPhysChem* **2012**, *13*, 1385-1394.

[117] J.-G. Li, C.-Y. Tsai, S.-W. Kuo, *RSC Adv.* **2015**, *5*, 42798-42803.

[118] C. Zhu, D. Du, A. Eychmüller, Y. Lin, *Chem. Rev.* **2015**, *115*, 8896-8943.

[119] L. Ye, Y. Wang, X. Chen, B. Yue, S. C. Tsang, H. He, *Chem. Commun.* **2011**, *47*, 7389-7391.

[120] X. Chen, Z. Lou, M. Qiao, K. Fan, S. C. Tsang, H. He, *J. Phys. Chem. C* **2008**, *112*, 1316-1320.

[121] D. Y. Zhao, J. L. Feng, Q. S. Huo, N. Melosh, G. H. Fredrickson, B. F. Chmelka, G. D. Stucky, *Science* **1998**, *279*, 548-552.

[122] K. K. Zhu, B. Yue, W. Z. Zhou, H. Y. He, *Chem. Commun.* **2003**, *1*, 98-99.

[123] Y. Wang, N. Su, L. Ye, Y. Ren, X. Chen, Y. Du, Z. Li, B. Yue, S. Chi, E. Tsang, Q. Chen, H. He, *J. Catal.* **2014**, *313*,113-126.

[124] N. Su, X. Chen, B. Yue, H. He, *Catal. Sci. Technol.* **2015**, *5*, 638-649.

[125] C. Wang, D. Chen, X. Jiao, *Sci. Technol. Adv. Mater.* **2009**, *10,* 023001.

[126] Y. Yamauchi, K. Kuroda, *Chem.-Asian J.* **2008**, *3*, 664-676.

[127] P. N. Bartlett, J. Marwan, *Chem. Mater.* **2003**, *15*, 2962-2968.

[128] P. J. Cappillino, K. M. Hattar, B. G. Clark, R. J. Hartnett, V. Stavila, M. A. Hekmaty, B. W. Jacobs, D. B. Robinson, *J. Mater. Chem. A* **2013**, *1*, 602-610.

[129] K. Qi, Q. Wang, W. Zheng, W. Zhang, X. Cui, *Nanoscale* **2014**, *6*, 15090-15097.

[130] L. Zhang, J. Zhang, Z. Jiang, S. Xie, M. Jin, X. Han, Q. Kuang, Z. Xie, L. Zheng, *J. Mater. Chem*. **2011**, *21*, 9620-9625.

[131] Y. Wu, G. Li, L. Zou, S. Lei, Q. Yu, B. Ye, *Sens. Actuators, B* **2018**, *259*, 372-379.

[132] C. Li, T. Sato, Y. Yamauchi, *Chem. Commun.* **2014**, *50*, 11753-11756.

[133] C. Li, B. Jiang, M. Imura, N. Umezawa, V. Malgras, Y. Yamauchi, *Chem.-Eur. J.* **2015**, *21*, 18671-18676.

[134] C. Li, B. Jiang, N. Miyamoto, J. H. Kim, V. Malgras, Y. Yamauchi, *J. Am. Chem. Soc.* **2015**, *137*, 11558-11561.

[135] B. Jiang, C. Li, H. Qian, M. S. A. Hossain, V. Malgras, Y. Yamauchi, *Angew. Chem. Int. Ed.* **2017**, *56*, 7836-7841.

[136] Y. Li, B. P. Bastakoti, Y. Yamauchi, *APL Mater.* **2016**, *4*, 040703-1-8.

[137] S. J. Ye, D. Y. Kim, S. W. Kang, K. W. Choi, S. W. Han, O O. Park, *Nanoscale* **2014**, *6*, 4182-4187.

[138] E. Antolini, *Appl. Catal., B* **2017**, *217*, 201–213.

[139] N. Kakati, J. Maiti, S. H. Lee, S. H. Jee, B. Viswanathan, Y. S. Yoon, *Chem. Rev.* **2014**, *114*, 12397-12429.

[140] K. D. Gilroy, A. Ruditskiy, H.-C. Peng, D. Qin, Y. Xia, *Chem. Rev.* **2016**, *116*, 10414-10472.

[141] B. J. Plowman, I. Najdovski, A. Pearson, A. P. O'Mullane, *Faraday Discuss.* **2013**, *164*, 199-218.

[142] M. Sankar, N. Dimitratos, P. J. Miedziak, P. P. Wells, C. J. Kielye, G. J. Hutchings, *Chem. Soc. Rev.* **2012**, *41*, 8099-8139.

[143] S. Shan, J. Luo, J. Wu, N. Kang, W. Zhao, H. Cronk, Y. Zhao, P. Joseph, V. Petkov, C.-J. Zhong, *RSC Adv.* **2014**, *4*, 42654-42669.

[144] H.-l. Liu, F. Nosheen, X. Wang, *Chem. Soc. Rev.* **2015**, *44*, 3056-3078.

[145] Y. Xu, L. Chen, X. Wang, W. Yao, Q. Zhang, *Nanoscale* **2015**, *7*, 10559-10583.

[146] L. Zhang, Q. Chang, H. Chen, M. Shao, *Nano Energy* **2016**, *29*, 198-219.

[147] C. Ray, T. Pal, *J. Mater. Chem. A* **2017**, *5*, 9465-9487.

[148] M. H. Seo, S. M. Choi, D. U. Lee, W. B. Kim, Z. Chen, *J. Power Sources* **2015**, *300*, 1-9.

[149] L. Chen, L. Lu, H. Zhu, Y. Chen, Y. Huang, Y. Li, L. Wang, *Nat. Commun.* **2016**, *8*, 14136.

[150] Y. Yazawa, H. Yoshida, N. Takagi, S. Komai, A. Satsuma, T. Hattori, *Appl. Catal., B* **1998**, *19*, 261-266.

[151] W. Xiao, W. Lei, M. Gong, H. L. Xin, D. Wang, *ACS Catal.* **2018**, *8*, 3237-3256.

[152] J. Xue, G. Han, W. Ye, Y. Sang, H. Li, P. Guo, X. S. Zhao, *ACS Appl. Mater. Interfaces* **2016**, *8*, 34497-34505.

[153] A. K. Singh, Q. Xu, *ChemCatChem* **2013**, *5*, 652-676.

[154] N. Lopez, J. K. Nørskov, *Surf. Sci.* **2001**, *477*, 59-75.

[155] Z. X. Liang, T. S. Zhao, J. B. Xu, L. D. Zhu, *Electrochim. Acta* **2009**, *54*, 2203–2208.

[156] E. A. Monyoncho, S. N. Steinmann, C. Michel, E. A. Baranova, T. K. Woo, P. Sautet, *ACS Catal.* **2016**, *6*, 4894-4906.

[157] E. A. Monyoncho, S. N. Steinmann, P. Sautet, E. A. Baranova, C. Michel, *Electrochim. Acta* **2018**, *274*, 274-278.

[158] M. Li, W. Guo, R. Jiang, L. Zhao, H. Shan, *Langmuir* **2010**, *26*, 1879-1888.

[159] S. Sarkar, R. Jana, Suchitra, U. V. Waghmare, B. Kuppan, S. Sampath, S. C. Peter, *Chem. Mater.* **2015**, *27*, 7459-7467.

[160] Q. Shi, C. Zhu, C. Bi, H. Xia, M. H. Engelhard, D. Du, Y. Lin, *J. Mater. Chem. A* **2017**, *5*, 23952-23959.

[161] R. Jana, U. Subbarao, S. C. Peter, *J. Power Sources* **2016**, *301*, 160-169.

[162] H. Liao, J. Zhu, Y. Hou, *Nanoscale* **2014**, *6*, 1049-1055.

[163] V. Mazumder, M. Chi, M. N. Mankin, Y. Liu, Ö. Metin, D. Sun, K. L. More, S. Sun, *Nano Lett.* **2012**, *12*, 1102-1106.

[164] S. Tominaka, T. Hayashi, Y. Nakamura, T. Osaka, *J. Mater. Chem.* **2010**, *20*, 7175-7182.

[165] J.-N. Zheng, L.-L. He, F.-Y. Chen, A.-J. Wang, M.-W. Xue, J.-J. Feng, *J. Mater. Chem. A* **2014**, *2*, 12899-12906.

[166] Y. Ma, R. Wang, H. Wang, J. Key, S. Ji, *RSC Adv.* **2015**, *5*, 9837-9842.

[167] D. Chen, P. Sun, H. Liu, J. Yang, *J. Mater. Chem. A* **2017**, *5*, 4421-4429.

[168] J. Liu, Z. Huang, K. Cai, H. Zhang, Z. Lu, T. Li, Y. Zuo, H. Han, *Chem.-Eur. J.* **2015**, *21*, 17779-17785.

[169] Y. Chen, Y. Yang, G. Fu, L. Xu, D. Sun, J.-M. Lee, Y. Tang, *J. Mater. Chem. A* **2018**, *6*, 10632-10638.

[170] C. Zhu, Q. Shi, S. Fu, J. Song, H. Xia, D. Du, Y. Lin, *Adv. Mater.* **2016**, *28*, 8779-8783.

[171] B. Yan, C. Wang, H. Xu, K. Zhang, S. Li, Y. Du, *ChemPlusChem* **2017**, *82*, 1121-1128.

[172] L. Yang, C. Hu, J. Wang, Z. Yang, Y. Guo, Z. Bai, K. Wang, *Chem. Commun.* **2011**, *47*, 8581-8583.

[173] Y. Xiong, W. Ye, W. Chen, Y. Wu, Q. Xu, Y. Yan, H. Zhang, J. Wu, D. Yang, *RSC Adv.* **2017**, *7*, 5800-5806.

[174] L. Zhang, S.-I. Choi, J. Tao , H.-C. Peng, S. Xie, Y. Zhu, Z. Xie, Y. Xia, *Adv. Funct. Mater.* **2014**, *24*, 7520-7529.

[175] J. Fan, S.Yu, K. Qi, C. Liu, L. Zhang, H. Zhang, X. Cui, W. Zheng, *J. Mater. Chem. A* **2018**, *6*, 8531-8536.

[176] D. Chen, Q. Yao, P. Cui, H. Liu, J. Xie, J. Yang, *ACS Appl. Energy Mater.* **2018**, *1*, 883-890.

[177] B. Jiang, C. Li, V. Malgras, Y. Bando, Y. Yamauchi, *Chem. Commun.* **2016**, *52*, 1186-1189.

[178] K. Jiang, P. Wang, S. Guo, X. Zhang, X. Shen, G. Lu, D. Su, X. Huang, *Angew. Chem.* **2016**, *128*, 9176-9181.

[179] K. Mori, K. Naka, S. Masuda, K. Miyawaki, H. Yamashita, *ChemCatChem* **2017**, *9*, 3456-3462.

[180] D. Bin, B. Yang, F. Ren, K. Zhang, P. Yang, Y. Du, *J. Mater. Chem. A* **2015**, *3*, 14001-14006.

[181] B. Cai, D. Wen, W. Liu, A.-K. Herrmann, A. Benad, A. Eychmüller, *Angew. Chem. Int. Ed.* **2015**, *54*, 13101-13105.

[182] Z. Liu, X. Yang, L. Cui, Z. Shi, B. Lu, X. Guo, J. Zhang, L. Xu, Y. Tang, Y. Xiang, *Part. Part. Syst. Charact.* **2017**, *35*, 1700366.

[183] C. Zhu, D. Wen, M. Oschatz, M. Holzschuh, W. Liu, A.-K. Herrmann, F. Simon, S. Kaskel, A. Eychmüller, *Small* **2015**, *11*, 1430-1434.

[184] C. Du, M. Chen, W. Wang, G. Yin, *ACS Appl. Mater. Interfaces* **2011**, *3*, 105-109.

[185] J. Zhang, Y. Xu, B. Zhang, *Chem. Commun.* **2014**, *50*, 13451-13453.

[186] C. Zhu, Q. Shi, S. Fu, J. Song, D. Du, D. Su, M. H. Engelhard, Y. Lin, *J. Mater. Chem. A* **2018**, *6*, 7517-7521.

[187] L.-X. Ding, A.-L. Wang, Y.-N. Ou, Q. Li, R. Guo, W.-X. Zhao, Y.-X. Tong, G.-R. Li, *Sci. Rep.* **2013**, *3*, 1-7.

[188] W. Hong, J. Wang, E. Wang, *CrystEngComm* **2015**, *17*, 9011-9015.

[189] X. Wang, S. Wang, in *Materials for Low-Temperature Fuel Cells*, (Eds: B. Ladewig, S. P. Jiang, Y. Yan), Wiley-VCH Verlag GmbH & Co. KGaA, **2014**, Ch. 3.

[190] Q.-L. Zhu, Q. Xu, *Chem*. **2016**, *1*, 220-245.

[191] E. Pérez-Mayoral, V. Calvino-Casildaa, E. Soriano, *Catal. Sci. Technol.* **2016**, *6*, 1265-1291.

[192] H. Ali, S. Zaman, I. Majeed, F. K. Kanodarwala, M. A. Nadeem, J. A. Stride, M. A. Nadeem, *ChemElectroChem* **2017**, *4*, 3126–3133.

[193] S. Hu, F. Munoz, J. Noborikawa, J. Haan, L. Scudiero, S. Ha, *Appl. Catal., B* **2016**, *180*, 758-765.

[194] X. Liu, P. Ning, L. Xu, Q. Liu, Z. Song, Q. Zhang, *RSC Adv.* **2016**, *6*, 41181-41188.

[195] H. Yan, Z. Bai, S. Chao, L. Yang, Q. Cui, K. Wang, L. Niu, *RSC Adv.* **2013**, *3*, 20332-20337.

[196] Z. Zhang, C. Zhang, J. Sun, T. Kou, Q. Bai, Y. Wang, Y. Ding, *J. Mater. Chem. A* **2013**, *1*, 3620-3628.

[197] A. L. Bugaev, A. A. Guda, A. Lazzarini, K. A. Lomachenko, E. Groppo, R. Pellegrini, A. Piovano, H. Emerich, A. V. Soldatov, L. A. Bugaev, V. P. Dmitriev, J. A. van Bokhoven, C. Lamberti, *Catal. Today* **2017**, *283*, 119-126.

[198] J. Yang, Y. Xie, R. Wang, B. Jiang, C. Tian, G. Mu, J. Yin, B. Wang, H. Fu, *ACS Appl. Mater. Interfaces* **2013**, *5*, 6571-6579.

[199] C. He, J. Tao, Y. Kea, Y. Qiu, *RSC Adv.* **2015**, *5*, 66695-66703.

[200] S. Ghosh, A.-L. Teillout, D. Floresyona, P. de Oliveira, A. Hagège, H. Remita, *Int. J. Hydrog. Energy* **2015**, *40*, 4951-4959.

[201] R. K. Pandey, V. Lakshminarayanan, *J. Phys. Chem. C* **2010**, *114*, 8507-8514.

[202] S. Ghosh, S, Bera, S. Bysakh, R. N. Basu, *ACS Appl. Mater. Interfaces* **2017**, *9*, 33775-33790.

[203] S. Siwal, S. Matseke, S. Mpelane, N. Hooda, D. Nandi, K. Mallick, *Int. J. Hydrog. Energy* **2017**, *42*, 23599-23605.

[204] L. A. Fard, R. Ojani, J. B. Raoof, E. N. Zare, M. M. Lakouraj, *Energy* **2017**, *127*, 419-427.

[205] Z. Łodziana, J. K. Nørskov, *Surf. Sci.* **2002**, *518*, 577–582.

[206] Y.-J. Wang, D. P. Wilkinson, J. Zhang, *Chem. Rev.* **2011**, *111*, 7625-7651.

[207] S. Ch. Sarma, S. C. Peter. *Dalton Trans.* **2018**, *47*, 7864-7869.

[208] R. G. Rao, R. Blume, T. W. Hansen, E. Fuentes, K. Dreyer, S. Moldovan, O. Ersen, D. D. Hibbitts, Y. J. Chabal, R. Schlögl, J.-P. Tessonnier, *Nat. Commun.* **2017**, *8*, 340.

[209] W. Xin, Y. Song, *RSC Adv.* **2015**, *5*, 83239-83285.

[210] M. Khan, M. N. Tahir, S. F. Adil, H. U. Khan, M. R. H. Siddiqui, A. A. Al-warthan, W. Tremel, *J. Mater. Chem. A* **2015**, *3*, 18753-18808.

[211] Q. Wang, Y. Liao, H. Zhang, J. Li, W. Zhao, S. Chen, *J. Power Sources* **2015**, *292*, 72-77.

[212] M. Shao, J. H. Odell, S.-I. Choi, Y. Xia, *Electrochem. Commun.* **2013**, *31*, 46–48.

[213] G. Z. Hu, F. Nitze, X. Jia, T. Sharifi, H. R. Barzegar, E. Gracia-Espino, T. Wågberg, *RSC Adv.* **2014**, *4*, 676-682.

[214] Q. Zhang, L. Jiang, H. Wang, J. Liu, J. Zhang, Y. Zheng, F. Li, C. Yao, S. Hou, *ACS Sustainable Chem. Eng.* **2018**, *6*, 7507-7514.

[215] H. Huang, X. Wang, *J. Mater. Chem.* **2012**, *22*, 22533-22541.

[216] D. Liu, Q. Guo, H. Hou, O. Niwa, T. You, *ACS Catal.* **2014**, *4*, 1825-1829.

[217] Z. Yan, W. Yao, L. Hu, D. Liu, C. Wang, C.-S. Lee, *Nanoscale* **2015**, *7*, 5563-5577.

[218] R. D. Morgan, A. Salehi-khojin, R. I. Masel, *J. Phys. Chem. C* **2011**, *115*, 19413-19418.

[219] S. Mondal, S. Ghosh, C. R. Raj, *ACS Omega* **2018**, *3*, 622-630.

[220] L. Y. Zhang, C. X. Guo, H. Pang, W. Hu, Y. Qiao, C. M. Li, *ChemElectroChem* **2014**, *1*, 72-75.

[221] H. Yang, X. Zhang, H. Zou, Z. Yu, S. Li, J. Sun, S. Chen, J. Jin, J. Ma, *ACS Sustainable Chem. Eng.* **2018**, *6*, 7918−7923.

[222] G. Hu, F. Nitze, T. Sharifi, H. R. Barzegar, T. Wågberg, *J. Mater. Chem.* **2012**, *22*, 8541-8548.

[223] X. Jia, G. Hu, F. Nitze, H. R. Barzegar, T. Sharifi, C.-W. Tai, T. Wågberg, *ACS Appl. Mater. Interfaces* **2013**, *5*, 12017-12022.

[224] B. F. Machadoab, P. Serp, *Catal. Sci. Technol.* **2012**, *2*, 54-75.

[225] M. Liu, R. Zhang, W. Chen, *Chem. Rev.* **2014**, *114*, 5117-5160.

[226] M. Sawangphruk, A. Krittayavathananon, N. Chinwipas, P. Srimuk, T. Vatanatham, S. Limtrakul, J. S. Foord, *Fuel Cells* **2013**, *13*, 881-888.

[227] H. Chang, H. Wu, *Energy Environ. Sci.* **2013**, *6*, 3483-3507.

[228] F. Ren, K. Zhang, D. Bin, B. Yang, H. Wang, P. Yang, Z. Fei, Y. Du, *ChemCatChem* **2015**, *7*, 3299-3306.

[229] R. Kiyani, M. J. Parnian, S. Rowshanzamir, *Int. J. Hydrog. Energy* **2017**, *42*, 23070-23084.

[230] Z. Liu, Y. Feng, X. Wu, K. Huang, S. Feng, X. Dong, Y. Yanga, B. Zhao, *RSC Adv.* **2016**, *6*, 98708-98716.

Chapter 2

2. Continuous Mesoporous Pd Films

2.1. Continuous Mesoporous Pd Films Using Pluronic P123

2.1.1. Introduction

Because of their unique structural features, such as high surface area, large pore volume, and uniform pore size, mesoporous materials have shown great potential in many important applications (e.g., catalysis, drug delivery, sensing).[1-5] In particular, mesoporous metals combining catalytic activity and high surface area provide more opportunities for enhancing electrocatalytic performances, including small molecule oxidation reaction, oxygen reduction reaction, or oxygen/hydrogen evolution reaction.[6-10] To date, several applications using mesoporous noble metals (e.g., Pt, Pd, Au) have been demonstrated. Mesoporous Pt films[6] and mesoporous Pt/Ru nanoparticles[8] exhibit strong catalytic activity and stability for the electrocatalysis of methanol oxidation reactions. Furthermore, mesoporous Pd films show enhanced electrocatalytic performance for formic acid oxidation reaction by fully taking advantage of their large surface area.10 Various synthetic methods, including hard templating from mesoporous silica or alumina,[11-13] dealloying,[14-16] and soft-templating,[6,10,17,18] have been developed to prepare mesoporous/nanoporous metals. Micelle assembly, typically involved in soft-templates, is flexible and convenient for the preparation of mesoporous metals under different conditions and greatly outperforms other methods.[6,10] It is, however, difficult to control, and the ordering can be destroyed during the metal deposition process, which is detrimental when it comes to designing precisely mesostructured materials. Therefore, techniques involving micelle assembly must be improved to obtain desired mesoporous structures with fine precision.

In the previous study, Yamauchi's group successfully synthesized mesoporous Pd films by using cetyltrimethylammonium chloride (CTAC) as pore-directing agent, which participates in the formation of intermediate $CTA^+/[PdCl_4]^{2-}$ during the reaction process.[10] For well-constructed mesoporous metallic structures to be achieved, micelles based on different categories of surfactants (e.g., cationic, nonionic, anionic) have been selected for their specific affinities with the target materials.[19-23] Until now, only cationic surfactants have been employed to direct the fabrication of mesoporous palladium (Pd), which is more

abundant than platinum (Pt) and represents a promising candidate for several applications.[24-26] Although mass transport is already facilitated by making the metal mesoporous, it can be further improved by expanding the pore size. The diameter of the obtained mesopores is limited to less than 5 nm due to the small molecular weight of the pore-directing molecules, thereby greatly hindering its practical application. Nonionic surfactants with a large molecular weight have been specifically employed for tailoring the synthesis of large pore mesoporous metal oxides and carbon-based materials.[27,28] If nonionic surfactants could be appropriately utilized for the preparation of mesoporous Pd, it would undoubtedly contribute to enhance its catalytic performance. Herein, an electrochemical method is used to finely control the growth of mesoporous Pd using nonionic surfactants to finally obtain mesoporous Pd films (**Scheme 2.1**). The resulting mesoporous Pd film with large pores is promising for the electrocatalysis of the ethanol oxidation reaction.

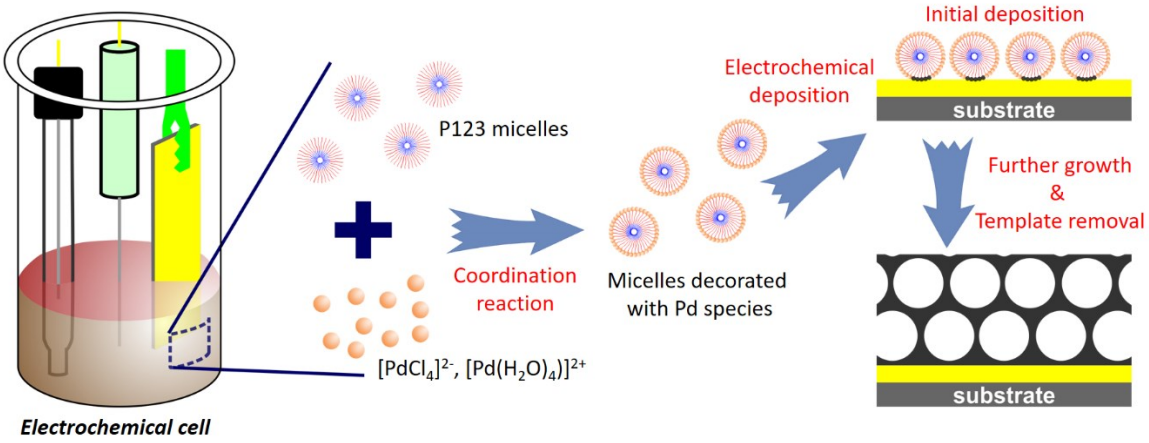

Scheme 2.1 Schematic illustration of the electrochemical deposition of mesoporous Pd film from aqeuous solution assisted by nonionic surfactant P123.

2.1.2. Experimental Section

Materials

Pluronic P123, Pluronic F127, Brij 58, and Nafion perfluorinated resin solutions were obtained from Sigma. Block copolymers, polystyrene-*b*-poly(ethylene oxide) with three

different molecular weights, were purchased from Polymer Source. Tetrahydrofuran (THF), palladium(II) chloride, and ethanol were received from Nacalai Tesque, Inc. Hydrochloric acid, sulfuric acid, and potassium hydroxide were purchased from Wako Chemicals. Palladium black was purchased from Alfa Aesar. The double distilled water was obtained through a water purification system Merck Milli-Q®. All chemicals were used without further purification.

Synthesis of Mesoporous Pd Films

Electrochemical deposition of mesoporous Pd films was conducted by utilizing an electrochemical station (CHI 842B electrochemical analyzer, CHI Instruments, USA) with a standard three-electrodes cell system, including a Ag/AgCl (3.0 M KCl), a platinum wire and a gold-coated silicon wafer substrate as the reference, counter and working electrodes, respectively. The electrolyte used during electrochemical deposition was prepared by dissolving 2.5wt% Pluronic P123 in 40 mM $PdCl_2$ aqueous solution. The electrodeposition of the Pd films was carried out at 0.0 V potential (*vs.* Ag/AgCl) for 600 s without stirring at room temperature. Since P123 are water-soluble surfactant (solubility in water > 10wt% at 25^{o}C), they can be easily removed from the films by rinsed with water. The as-deposited Pd films then were thoroughly rinsed with deionized water and dried under nitrogen gas flow for further characterization.

Characterizations

Morphological scanning electron microscope (SEM) imaging of the deposited Pd films were obtained using a Hitachi FESEM SU-8000 microscope at an accelerating voltage of 5 kV. Transmission electron microscopy (TEM) was carried out using JEOL JEM-2100F microscope at an accelerating voltage of 200 kV. Grazing incidence small-angle X-ray scattering (GI-SAXS) pattern was recorded by using a Rigaku NANO-Viewer (Microfocus rotating anode, Cu Kα radiation) equipped with a camera length of 700 mm, an operation voltage of 40 kV and a current of 30 mA. Small angle neutron scattering was employed to characterize the micellar structure using the Bilby instrument at ANSTO.[30a] The instrument was used in time-of-flight mode using neutrons with wavelengths between 3.0 and 18.0 Å, ($\Delta\lambda/\lambda$ = 12.0-16.0 %) with detectors positioned at 8.030 (rear), 2.030 (horizontal curtains) and 1.030 m (vertical curtains) from the sample. Two series of samples were measured, with and without the addition of $PdCl_2$, at 0.5 wt% of P123 and at 40%, 60%, 80% and 100% D_2O. Round Hellma cells were used (1 mm pathlength for 40

and 60% D_2O or 2 mm for 80 and 100% D_2O) and samples were measured at 25, 30 and 35°C. Data were reduced and put on an absolute scale relative to the direct beam using Mantid[30b] and then solvent subtracted. The Ultraviolet-Visible (UV-Vis) spectra of the aqueous electrolyte solution used for electrochemical deposition were obtained with a JASCO V-7200. Low- and wide-angle X-ray diffraction (XRD) pattern of as-deposited Pd films was obtained by Rigaku SmartLab XRD with Cu Kα radiation. X-ray photoelectron spectroscopy (XPS) was utilized by using a PHI Quantera SXM (ULVAC-PHI) with Al Kα radiation to determine the composition and electronic coordination state of the as-prepared Pd films. All XPS spectra were calibrated to the C 1*s* peak at 285.0 eV.

Electrochemical Measurement

All electrochemical measurements were recorded with a CHI 842B electrochemical analyzer (CHI Instruments, USA). A conventional three-electrode set up was employed to carry out the electrochemical measurement. A gold-coated silicon wafer substrate further coated with the Pd films, a Pt wire and Ag/AgCl or Hg/HgO electrodes were employed as the working, counter and reference electrodes, respectively. The geometric area of the deposited Pd films on the gold-coated silicon wafer working electrode was 3 mm × 6 mm. As for electrochemical measurement of commercially available Pd black (denoted as PdB), a glassy carbon electrode (GCE) with a diameter of 3 mm was used as the working electrode. Prior to the PdB surface coating, the GCE was polished with 1.0 and 0.05 μm alumina powder, rinsed with deionized water and dried under nitrogen gas flow. Then, 5.0 μg of PdB was coated on the surface of the GCE. After drying under atmospheric conditions, a Nafion® solution (5.0 μL, 0.5 wt%) was subsequently coated on the GCE surface and dried at room temperature before further electrochemical measurements. Cyclic voltammograms were recorded in 0.5 M H_2SO_4 electrolyte at a scan rate of 50 mV s^{-1} between -0.2 and +1.2 V (*vs.* Ag/AgCl). The electrocatalytic performance towards the ethanol oxidation reaction was recorded in 1.0 M KOH containing 1.0 M C_2H_5OH in the potential range from -0.8 to 0.3 V (*vs.* Hg/HgO). Amperometric *i-t* curves were recorded at a potential of -0.3 V (*vs.* Hg/HgO) for 1,500 s in 1.0 M KOH containing 1.0 M C_2H_5OH to study the stability test.

2.1.3. Characterization of Mesoporous Pd Films

The electrodeposition was carried out in aqueous solution containing 2.5 wt% Pluronic P123 and 40 mM $PdCl_2$, without stirring, at room temperature for 600 s and at a constant potential of 0.0 V *vs.* Ag/AgCl (see Experimental Section for more details). Both the top-surface and the cross-section of the obtained films are imaged by SEM and TEM after carefully removing the surfactants. From the top-view, pores uniformly distributed over the entire film can be clearly observed (**Figure 2.2a**). The average pore diameter is measured to be 10.9 nm (calculated from over 200 pores) (**Figure 2.2b** and **Figure 2.1a-b**). The periodicity of the pore organization is studied by using low-angle XRD clear peak centered at 0.62°, corresponding to a pore-to-pore distance of 14.2 nm (**Figure 2.3b**). From these results, the average wall thickness is estimated to be 3.3 nm which is consistent with the average wall thickness analyzed statistically from the TEM image (**Figure 2.1c**). A cross-section prepared by focused ion beam (FIB) was further studied by high-angle annular dark-field (HAADF) scanning transmission electron microscopy (STEM), suggesting that the porous structure is uniform through the entire thickness of the film (**Figures 2.2c** and **2.3a**). The typical arc-like 2D GI-SAXS pattern suggests that the uniformly-sized spherical mesopores are randomly packed inside the film (**Figure 2.4a**). Furthermore, the plot profile derived from the arc pattern clearly shows a peak centered at q = 0.4 nm^{-1} (**Figure 2.4b**), which corresponds to a pore-to-pore distance of 15.7 nm. Although the pore-to-pore distances obtained from low-angle XRD and GI-SAXS are slightly different, this fact has been often observed in mesoporous films and is due to distortion of the mesoporous film along the perpendicular direction to the substrate.[31] All the results fully support the formation of highly uniform mesoporous Pd film.

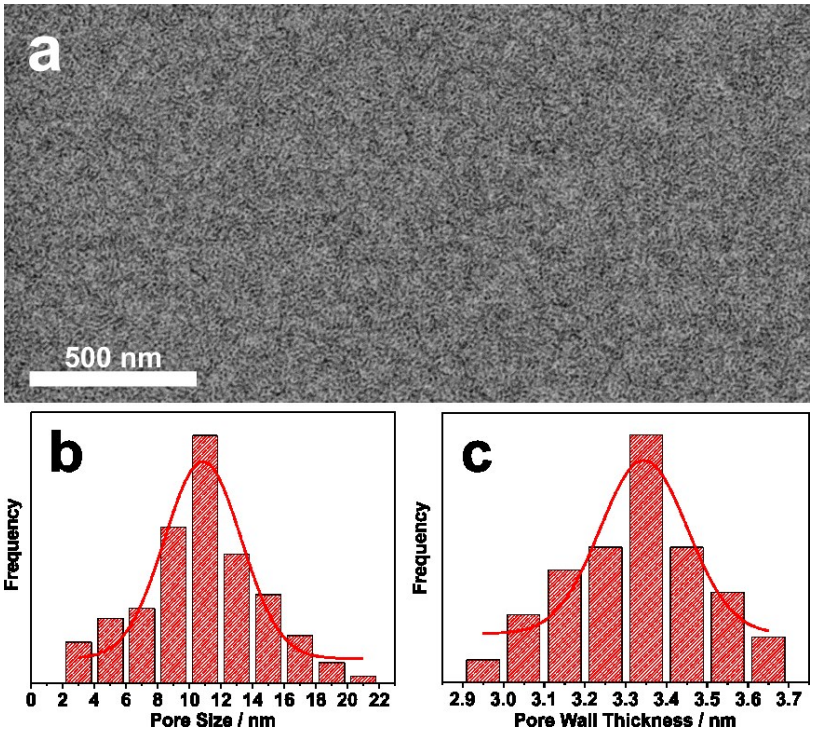

Figure 2.1 (a) Low-magnification SEM image of the film surface, (b-c) histograms of (b) pore sizes and (c) pore wall thickness of mesoporous Pd film prepared under the typical condition.

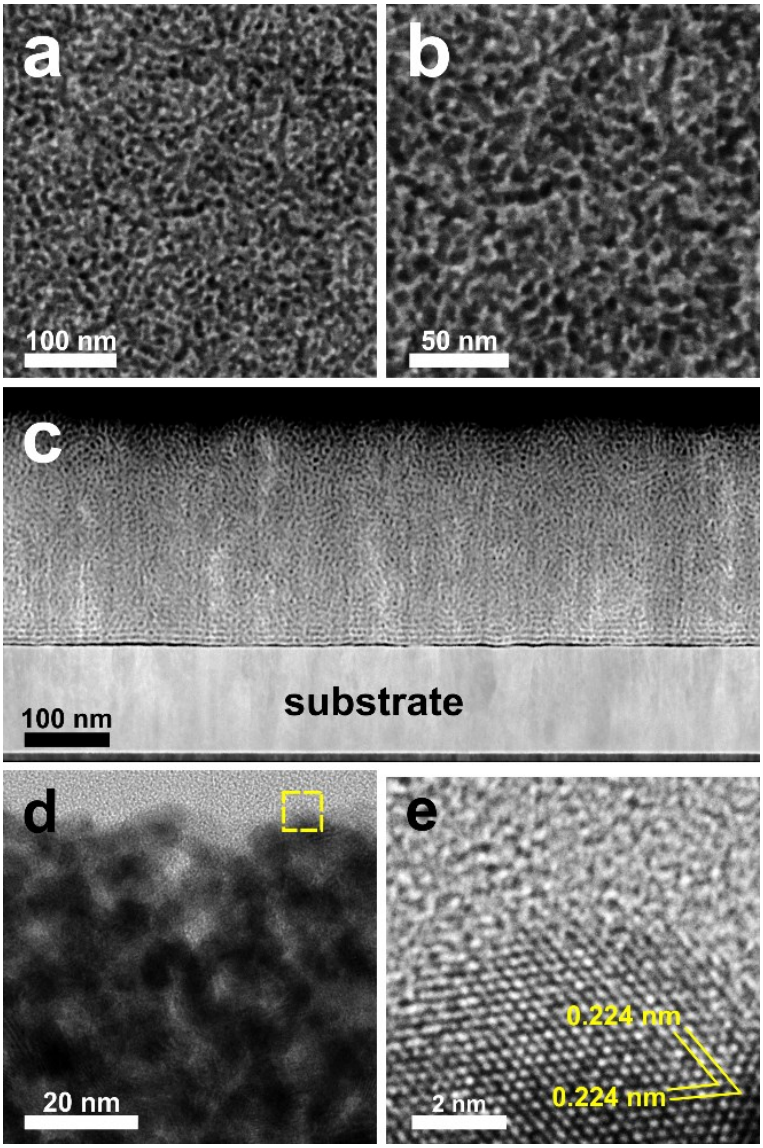

Figure 2.2 (a) Low- and (b) high-magnification SEM images to show the top-surface structure of the obtained film. (c) Cross-sectional HAADF STEM image to show the cross-sectional structure of the obtained film. (d) TEM and (e) HRTEM images to show the crystallinity of the obtained film. HRTEM image shown in panel (e) is derived from the rectangle area marked in panel (d) which is located on the top-edge of the Pd films.

The difference in contrast in the cross-sectional TEM image highlights the porous nature of the film and suggests that the pore walls are interconnected (**Figure 2.2d**). A typical HRTEM image observed on the edge of the obtained film clearly shows the lattice fringes with a constant *d*-spacing of 0.224 nm, which can be ascribed to the (111) lattice planes of face-centered cubic (*fcc*) Pd crystals (**Figure 2.2e**). The lattice fringes are shown to be aligned on the particle to particle interface (**Figure 2.5)**. The XRD pattern of the mesoporous film contains diffraction peaks located at 40.18º, 46.72º, 68.16º, 82.18º and

86.82° (**Figure 2.3c**), which can be assigned to the (111), (200), (220), (311) and (222) diffraction planes of Pd with a *fcc* structure, respectively (JCPDS Card No. 05-0681), thus supporting the previous HRTEM observations. **Figure 2.6a** shows the survey spectra recorded from mesoporous Pd film surface. The high-resolution spectra of Pd 3*d* clearly shows the two peaks at 335.7 eV and 341 eV which belong to metallic Pd $3d_{5/2}$ and Pd $3d_{3/2}$, respectively (**Figure 2.6b**).

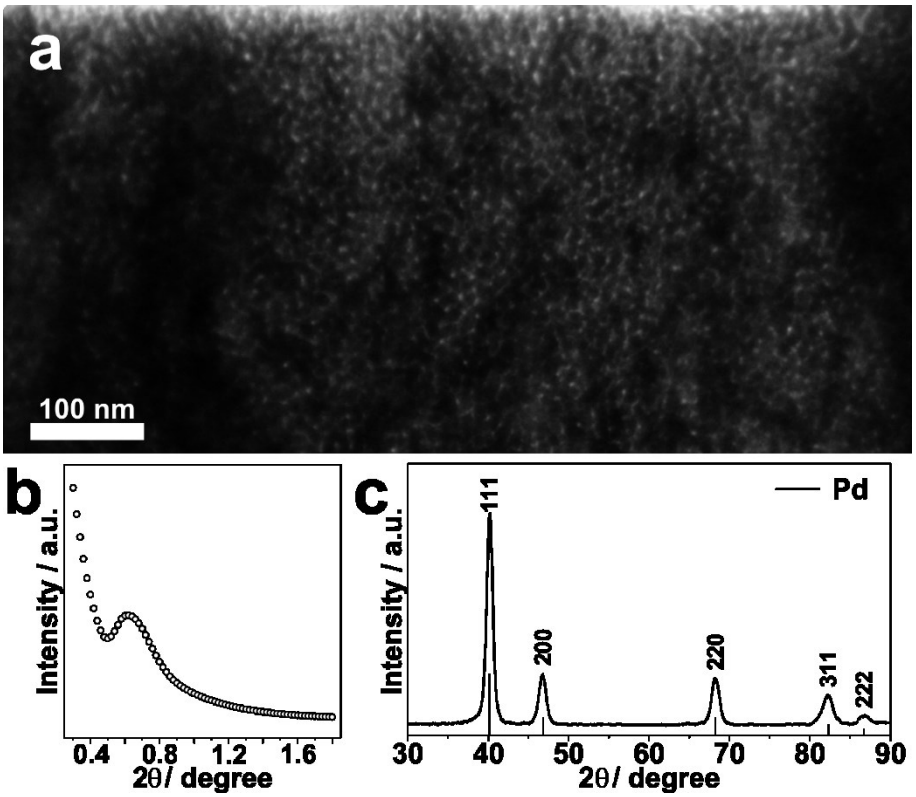

Figure 2.3 (a) Bright-field cross-sectional TEM image, (b) low- and (c) wide-angle X-ray diffraction patterns of mesoporous Pd film prepared under the typical condition.

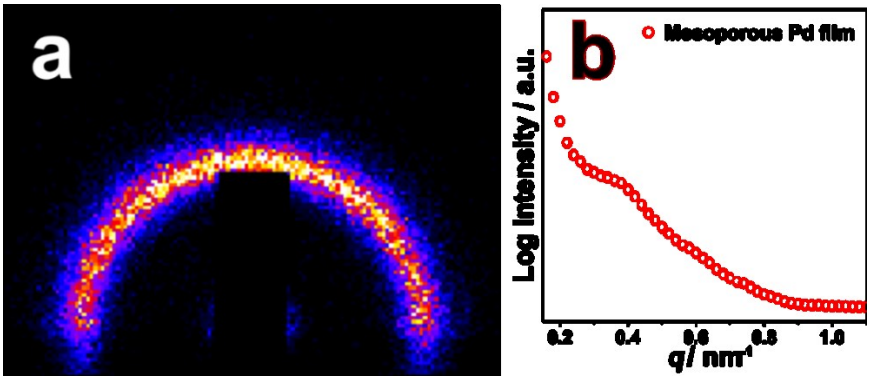

Figure 2.4 (a) GI-SAXS pattern and (b) in-plane profile of mesoporous Pd film prepared under the typical condition.

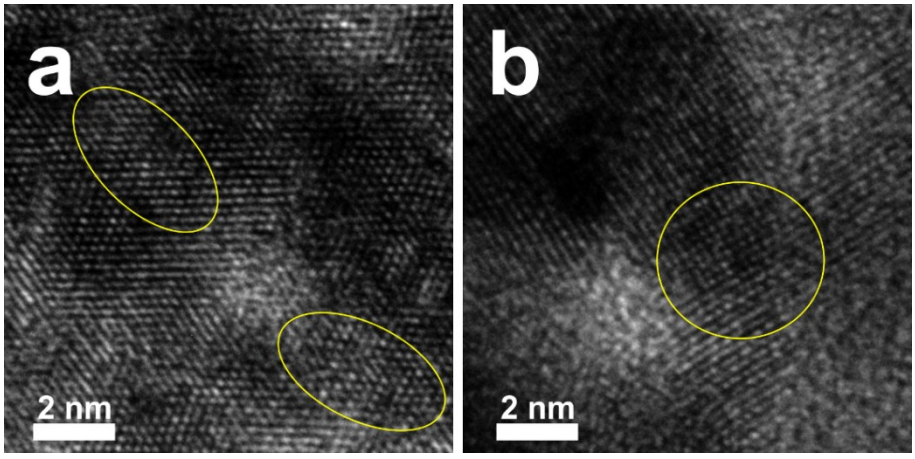

Figure 2.5 Low-magnification high-resolution TEM (HRTEM) images within the mesoporous Pd film. The yellow circle/ellipses showing the lattice fringes along particle to particle interface.

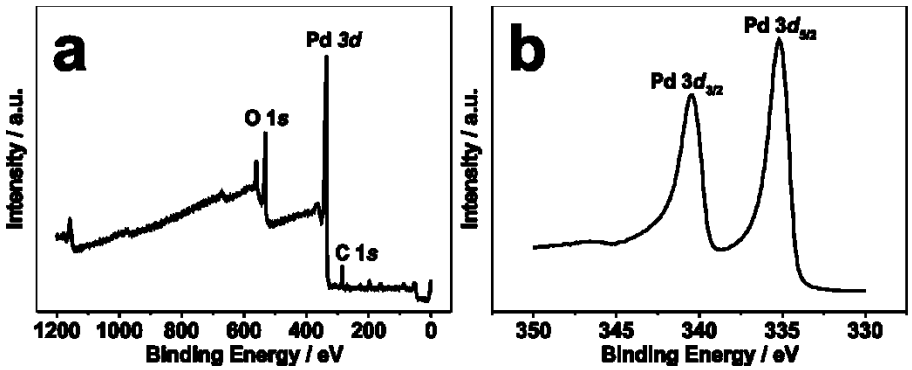

Figure 2.6 XPS spectra for mesoporous Pd film prepared under the typical condition. [(a) Full spectrum and (b) Pd3*d* spectrum]

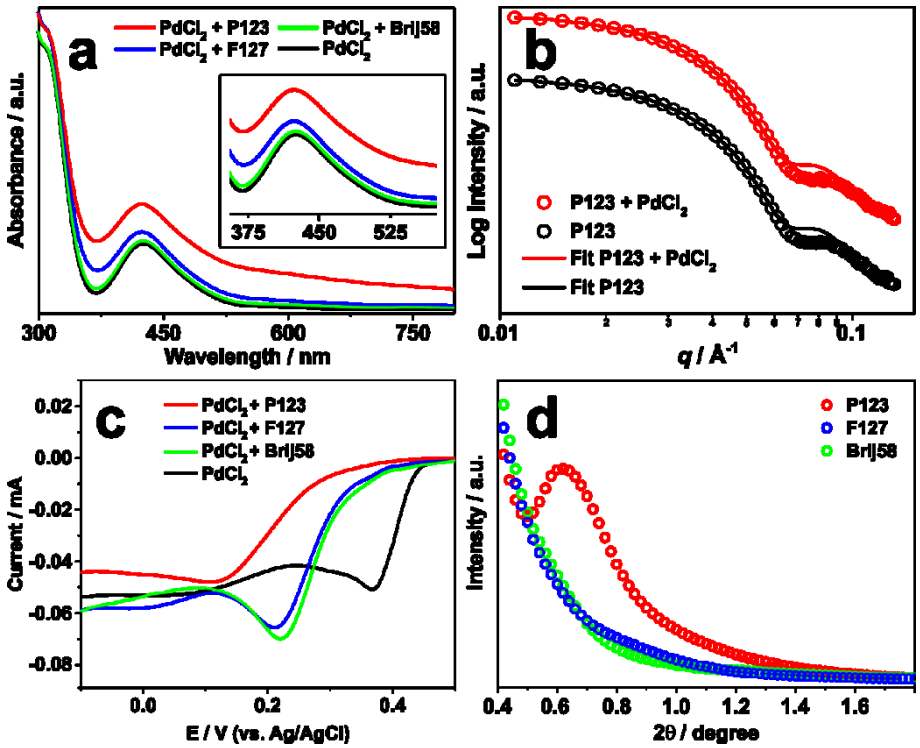

Figure 2.7 (a) UV-Vis spectra and (c) LSV plot recorded at the scan rate of 10 mV s^{-1} from electrolyte solution consisting various mixture of nonionic surfactant and $PdCl_2$. (b) SANS data of P123 micelles in solution with fits to a polydisperse spherical model. (d) Low-angle XRD pattern form the Pd film prepared by different surfactant.

Previously reported mesoporous Pd films are usually obtained by using cationic surfactants as pore-directing agents, because of the suitable interactions between their positive functional group and the Pd species.[10] Therefore, the interaction between the nonionic micelles and the Pd species is investigated by using UV-Vis spectroscopy and SANS. For the UV-Vis investigation, three nonionic surfactants, *i.e.* Pluronic P123, Pluronic F127 and Brij 58, are mixed with the $PdCl_2$ solution. $PdCl_2$ in an aqueous solution form $[PdCl_x(H_2O)_{4-x}]^{2-n}$ species that has been investigated in 1970s and 1980s in the establishment of ligand field theory. These species have been experimentally investigated using UV-vis absorption spectroscopic data, as well as DFT calculations that all these species suggested in this study are thermodynamically stable, equilibrium species in the aqueous media.[32a-d] All the UV-Vis spectra exhibit the typical *d-d* transition of an aqueous solution of $PdCl_2$, consisting of $[Pd(H_2O)_4]^{2+}$ and $[PdCl_4]^{2-}$ ions by Cl^- exchange with water molecules (**Figure 2.7a**). The *d-d* transitions blue shifts with increasing H_2O in the coordination sphere. The high energy side of the peak around 400 nm in the UV-Vis spectra is due to water rich and the low energy side (shoulder) is due to Cl^- rich species.

Interestingly, whichever ion goes into the micelle domains it also pulls the other ion ($[Pd(H_2O)_4]^{2+}$ and $[PdCl_4]^{2-}$) for the charge balance. The water coordinated species are interacting with the ethylene oxide moiety of the micelles to keep Pd(II) species to get at the working electrode surface effectively. The only species on the cathode side is Cl^- ion that was produced from the media.

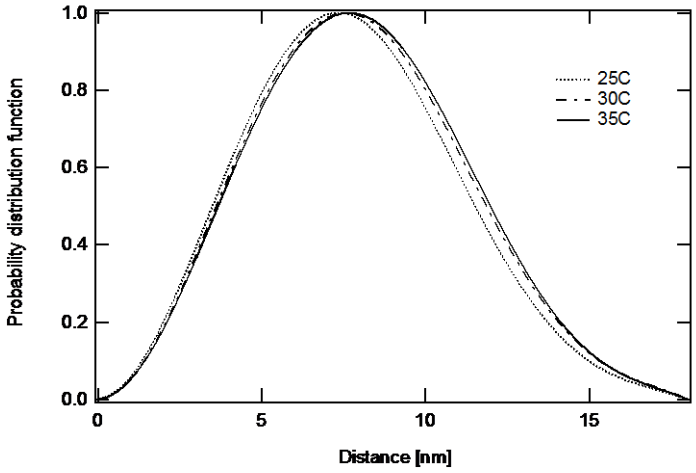

Figure 2.8 Probability distribution functions as a function of temperature for P123 samples at 0.5 wt% in 100 % D_2O.

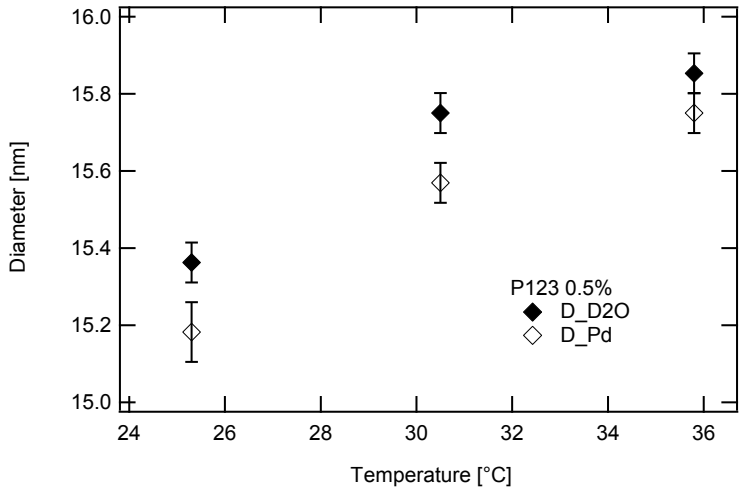

Figure 2.9 Temperature dependence of the diameter of P123 micelles in solution, extracted from the *P(r)* analysis, assuming a spherical particle, with and without metal precursor.

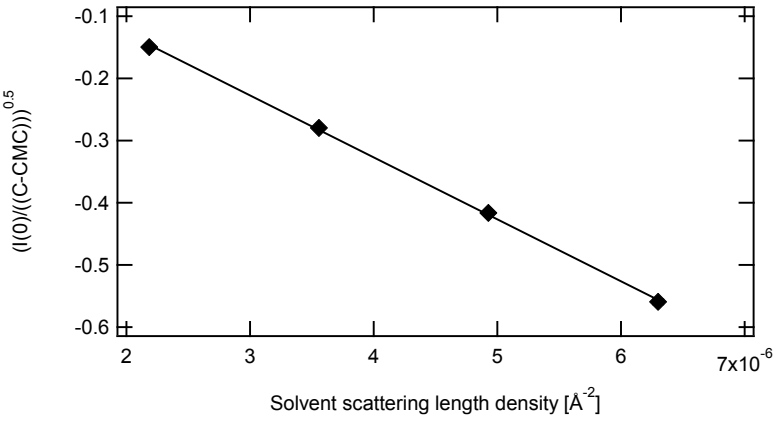

Figure 2.10 Linear fit of $\left(\frac{I(0)}{(C-CMC)}\right)^{0.5}$ versus solvent scattering length density at 25°C.

Two typical samples (pure P123 and P123 in 40 mM $PdCl_2$) were measured using small angle neutron scattering (**Figures 2.8-2.10**). The Fourier transforms to real space of the SANS data provided in **Figure 2.8** are consistent with P123 forming spherical shaped micelles as reported previously.[33] The scattering data were therefore fit to polydisperse spheres using Igor Pro macros provided by NIST[34] assuming the scattering length density to be uniform throughout the micelle (**Figure 2.7b**). The diameters of the scattering particles extracted from the spherical fit to the full scattering curves are 13.78 and 13.84 nm (±0.04) for P123 with and without the metal precursor respectively, with a polydispersity of 12%. An average diameter of ~14 nm for P123 micelles in both solvent conditions indicates that the addition of the metal ions (herein, $PdCl_2$) does not significantly modify the micelle structure, which is the essence of the micelle assembly approach. Furthermore, the average micelles size and pore diameter observed in the present study are almost consistent with the average pore size reported previously for mesoporous materials synthesized with Pluronic P123. Temperature dependent data recorded showed a small increase, less than 1 nm, in the diameter of the micelles between 25 and 35°C (**Figure 2.9**). The linear fit presented in **Figure 2.10** allows the determination of a P123 unimer volume and the aggregation number of the micelles in solution. At 25°C the volume of the unimer was calculated to be 5520 $Å^3$ and an aggregation number of 309 was determined.

The surfactant concentration takes a critical role in optimizing the final porous structures as the micelles are be formed when the surfactant concentration is higher than its critical micelle concentration (CMC). In the present synthesis, the concentration of P123 is fixed at 2.5 wt% (4.3 mM), which is higher than its CMC value (0.03 wt% or 0.052 mM at 25°C).[35] In the absence of nonionic surfactant, bulk Pd with a relatively large size was

formed (**Figure 2.11a**). If the concentration of P123 (*i.e.*, 0.025 wt%) is lower than its CMC value, no porous structure could be obtained (**Figure 2.12a**). When its concentration is further increased to be 2.5 wt%, a well-defined porous structure is obtained (**Figure 2.12c**) and it becomes irregular at the concentrations of 1.0 and 5.0 wt% (**Figures 2.12b** and **2.12d**, respectively).

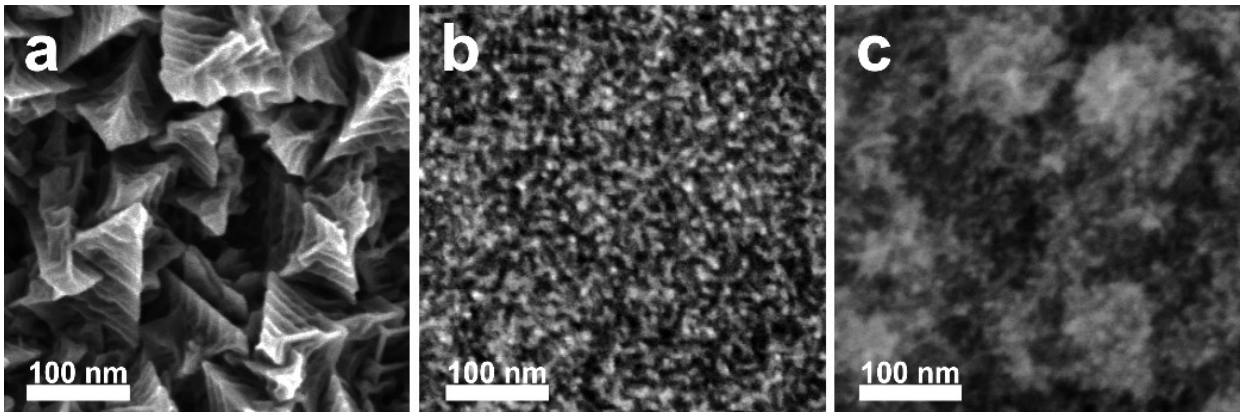

Figure 2.11 Top view SEM images of Pd films prepared (a) without surfactant, (b) 2.5 wt% F127, and (c) 2.5 wt% Brij 58.

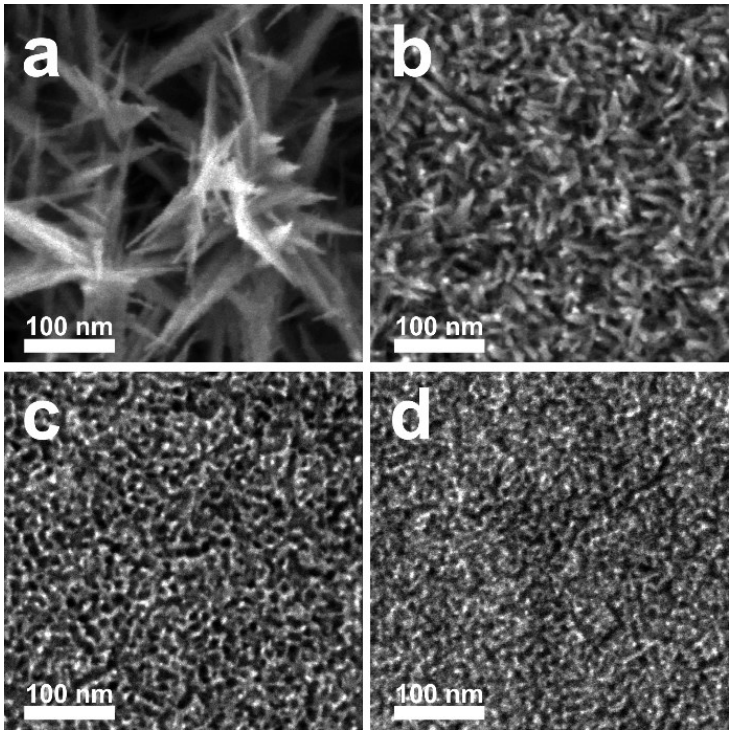

Figure 2.12 SEM images of Pd films prepared by the typical procedure but with different concentration of P123, *i.e.* (a) 0.025wt% (b) 1.0wt%, (c) 2.5wt% and (d) 5.0wt%.

The formation mechanism of mesoporous Pd films are described as follows. As the electrolyte solution prepared by dissolution of P123 in water with the concentration above its CMC, P123 micelles were formed in the aqueous solution. The presence of P123 micelles was confirmed by SANS as previously explained. Then some amount of metal precursor, $PdCl_2$ solution, was added into the electrolyte. Even after the addition of metal precursor, the micelles structure still exist. This indicated that in the electrolyte solution, the water coordinated Pd ions in the form of metal-aqua complex interact with the ethylene oxide moiety of surfactant (adsorbed) as proved by the UV-Vis absorption spectroscopic study. The feature at around 400 nm of UV-Vis spectra has been assigned to *d-d* transition (assigned to $^1A_{1g}$ to $^1A_{2g}$ transition that gradually blue shifts with decreasing *x*, number of Cl^- in the coordination sphere).[32a] The tail on the low energy site of the peak at around 400 nm originate from the Cl^- rich species (**inset Figure 2.7a**). This is reasonable, because Cl^- is a relatively weaker field ligand than H_2O. Presence of coordinated water is important for the assembly and interaction with the micelle domains, because the charge of the complex varies from 2- to 2+ with increasing water in the coordination sphere (Pd(II) in all complexes). The complexes interact with the ethylene oxide domains of the surfactant through coordinated water by hydrogen-bonding. Notice that the water-rich complexes are positively charged and attracted by the micelles and therefore the negatively charged Cl^--rich complexes are attracted by the positively charged water-rich complexes through electrostatic interactions to enhance the Pd(II) species in and around the micelles for electrodeposition of Pd(0). During electrodeposition process, the Pd ions along with the micelles are attracted to the gold-coated silicon wafer substrate (working electrode) by the applied potential voltage (0.0 V *vs.* Ag/AgCl or -0.045 V *vs.* SCE). From these descriptions, it is supposed that the Pd films were electrochemically deposited on the working electrode by surfactant micelles assembly.

To check whether other surfactants may be used to form a porous Pd film, control experiments were carried out under the same condition only replacing P123 by nonionic surfactants with different molecular weights: F127 (EO_{100}-PO_{65}-EO_{100}) and Brij 58 (C_{16}-EO_{20}). The obtained films, which were electrodeposited under the similar condition to the P123 one, were firstly studied by SEM. To my surprise, the structures of the obtained films were highly sensitive to the type of the surfactants used. Interconnected Pd nanowires were obtained when F127 was used as the surfactant, and irregular structures were obtained when Brij 58 was used (**Figure 2.11b** and **2.11c**, respectively). Therefore, linear sweep

voltammetry (LSV) was then employed to carefully study the electrodeposition process of the electrolytes with different surfactants. The LSV plots obtained at a slow scan rate of 10 mV s^{-1} based on the electrolytes with $PdCl_2$ and different surfactants are shown in **Figure 2.7c**. As clearly seen from the plots, the electrolyte containing P123 shows a negatively shifted reduction peak in comparison to the electrolytes containing F127 or Brij 58. It indicates the stabilization of Pd(II) in the electrolyte containing P123 was occurred. Both F127 and Brij 58 has a large ethylene oxide units compared to P123 thus the micelles should be more uniform in the P123 case than F127 and Brij 58. Hydrophobic core (PO block) of P123 stabilize the micelles and likely the metal species which are interacting with the micelles are causing the different morphological structure. The low-angle XRD patterns show no peaks for the Pd films prepared by F127 and Brij 58 (**Figure 2.7d**). All these results indicate that only P123 can act as the pore-directing agent in the preparation of mesoporous Pd films.

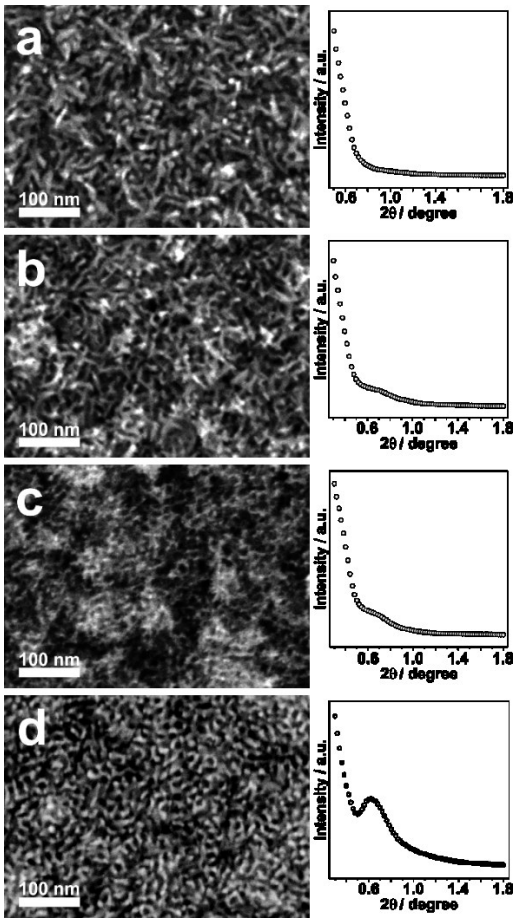

Figure 2.13. Top-surface SEM images (left) and low-angle XRD pattern (right) of Pd film prepared with the use of P123 at various electrodeposition potential, *i.e.* (a) -0.3 V, (b) -0.2 V, (c) -0.1 V and (d) 0.0 V *vs*. Ag/AgCl.

Here the effect of the applied potentials on the mesoporous structure ordering of the Pd film was investigated. In the present study, various constant potentials in the range of -0.3 and 0.0 V (*vs*. Ag/AgCl) were employed for the electrodeposition of Pd films. The deposition potential applied in the electrodeposition process affected to the current passed through the working electrode.[36a,b] The lower applied deposition potential (more negative) lead to the higher current which can promotes higher reduction speed of metal ions associated with the surfactant micelles. The reduction speed is quite important to get porous structures. Because a high reduction speed will break down the micelle structures, however, a very low reduction speed may kick away the micelles.[37] The structures in the obtained films were studied by SEM and low-angle XRD (**Figure 2.13**). The structures of the obtained Pd films were gradually changed from the dendritic structure (-0.3 V *vs*. Ag/AgCl) to the porous structure (0.0 V *vs*. Ag/AgCl). The peaks shown in the low-angle XRD patterns gradually increased when the potential changed to a larger value, and a highly intense diffraction peak was clearly observed for the mesoporous Pd film prepared by using a potential of 0.0 V, indicating the porous ordering was optimized at a deposition potential of 0.0 V. Furthermore, when the applied potential was higher than 0.0 V *vs.* Ag/AgCl, *i.e.* at 0.1 V, the mesoporous structure ordering was decreased due the slower rate of reduction (**Figure 2.14**). Therefore, the optimized surfactant concentration as well as the applied electrodeposition potential were the important factors to ensure the high quality of mesoporous structure ordering.

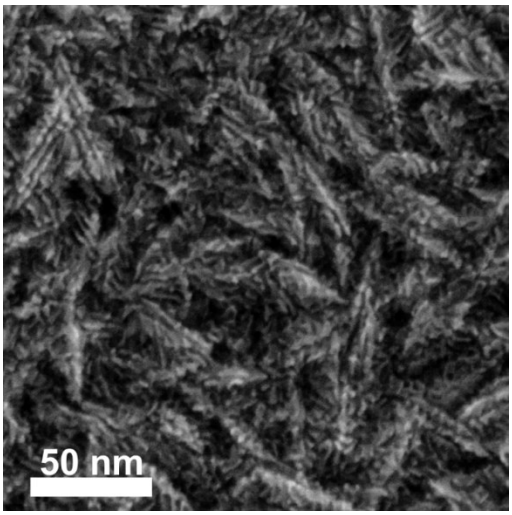

Figure 2.14 SEM images of Pd film prepared at applied potential of 0.1 V (*vs.* Ag/AgCl).

Not only the pore size but also the film thickness influences the catalytic activity of the film catalysts, even for the porous films. The electrochemical approach is sophisticated at controlling the film thickness by easily changing the deposition time. The film thickness was carefully checked based on the cross-sectional SEM observation (**Figure 2.15**). The dotted plot derived from the film thickness of mesoporous Pd films *versus* the deposition time reveals that the film thickness linearly increased with the increase of the deposition time with a growth rate of 100 nm min^{-1} (**Figure 2.15f**) which is lower than that of nonporous Pd films (*ca.* 210 nm min^{-1}). The film thickness could linearly increase until the metal sources was used up. The amount of metallic Pd that were deposited on the working electrode can be calculated theoretically by Faraday's first law of electrolysis and would be informative to describe its linear relationship with the applied deposition time. According to this law, the amount of the deposited substance is directly proportional to the quantity of electricity passed ($m \propto Q$).[38] The current density passed through the working electrode at a certain applied deposition potential was similar though the deposition time was varied. Furthermore, the estimated mass of deposited Pd can be estimated through **Equation (1).**

$$m = \left(\frac{Q}{F}\right)\left(\frac{M}{z}\right) \quad (1)$$

where *m* is the mass of substance deposited at an electrode in grams, *Q* is the total electric charge passed through the substance in coulombs, *F* is the Faraday constant (96485 C mol^{-1}), *M* is the molar mass of the substance in grams per mol, and *z* is the valence number of ions involved in the reduction reaction. Note that the reduction step of Pd species are assumed as follows,

$$PdCl_4^{2-}(aq) + 2e^- \rightarrow Pd(s) + 4Cl^-(aq)$$
$$[Pd(H_2O)_4]^{2+}(aq) + 2e^- \rightarrow Pd(s) + 4H_2O(aq)$$

While the total reaction is,

$$PdCl_4^{2-}(aq) + [Pd(H_2O)_4]^{2+}(aq) + 4e^- \rightarrow 2Pd(s) + 4Cl^-(aq) + 4H_2O(aq)$$

According to the reduction step of Pd as described above, the number of electrons involved in the total reaction is 4. The relationship plot between applied deposition time and theoretical amount (mass) of deposited substance is presented in **Figure 2.16**. In addition,

the actual mass of deposited Pd which measured by precision scale also presented in **Figure 2.16** and showing that the deposition efficiency was around 99%. The morphology of mesoporous Pd films prepared by various applied deposition time are also observed by SEM (**Figure 2.17**). There is no difference of the Pd films morphology with the variation of applied deposition time which suggested the efficiency of electrodeposition process. Linear relationship between of deposited film thickness towards applied deposition time was commonly occurred as reported in some literatures.[6,10]

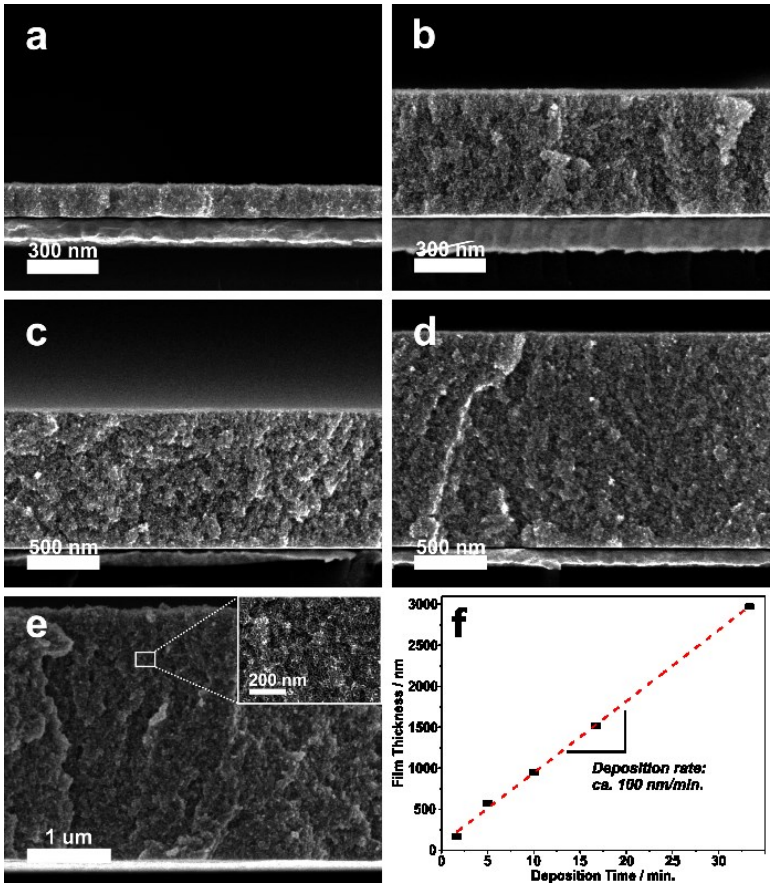

Figure 2.15 Cross-sectional SEM images of mesoporous Pd films prepared with different applied deposition time, *i.e.* (a) 100 s, (b) 300 s, (c) 600 s, (d) 1000 s and (e) 2000 s. (f) Relation between the film thickness of deposited mesoporous Pd films and the applied deposition time.

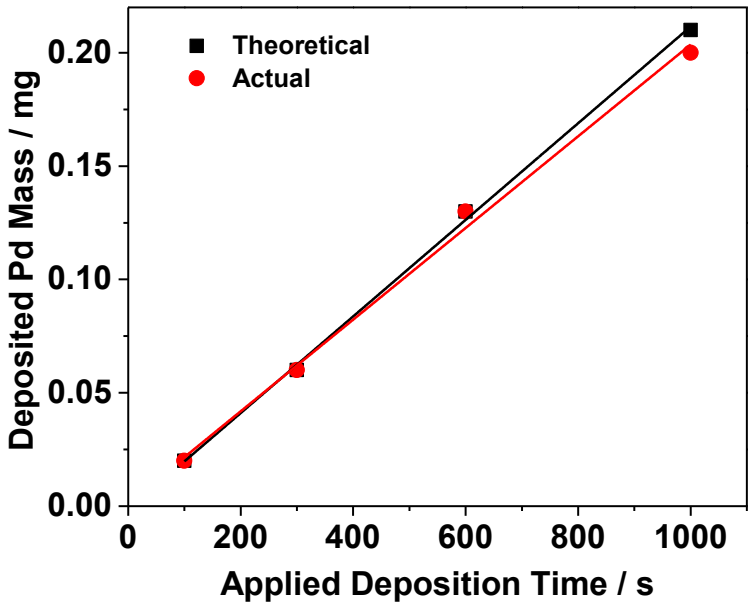

Figure 2.16 Relationship between Pd mass deposited on the working electrode and applied deposition time calculated by theoretical approach and measured by precision scale.

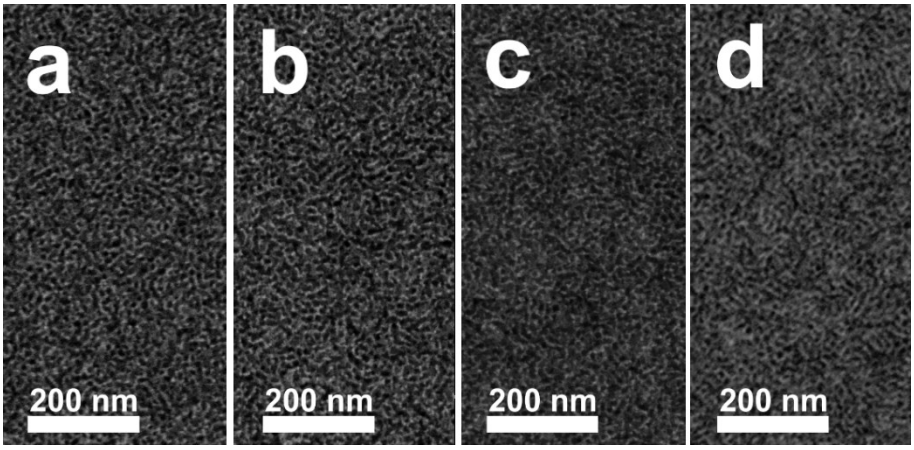

Figure 2.17 Time-evolution of mesoporous Pd films morphology prepared at various applied deposition time: (a) 6 s, (b) 16 s, (c) 100 s and (d) 600 s.

2.1.4. Electrocatalytic Activity of Mesoporous Pd Films

The influence of the film thickness to the mass transport was then studied by using the electrochemical surface area (ECSA). Four typical samples with a deposition time of 100,

300, 600, and 1000 s were selected for the study. The ECSA investigation was carried out by cyclic voltammetric (CV) approach in 0.5 H_2SO_4 with a scan rate of 50 mV s^{-1} in a potential range of -0.2 and 1.2 V (*vs.* Ag/AgCl). The ECSA was estimated by calculating the oxide reduction charge assuming that the conversion factor for an oxide monolayer reduction was 420 μC cm^{-2} on the smooth surface of Pd.[39] With film thicknesses increase, the reduction peak of PdO which located between potential 0.3 to 0.7 V (*vs.* Ag/AgCl) obviously increase (**Figure 2.18a**). The ECSA values are 7.17, 14.66, 30.28, and 60.95 cm^2 for the mesoporous Pd films with deposition time of 100, 300, 600, and 1000 s, respectively. The ECSA linearly increase with the film thickness increase (**Figure 2.18b**, black line). Interestingly, even when the ECSA values of mesoporous Pd films with various thickness were divided by their respective geometric volume, the volume-normalized ECSA shows a relatively similar value (**Figure 2.18b**, blue line), indicating that the large surface area derived from the mesoporous structure inside the film are fully accessible. The mass-normalized ECSA of mesoporous Pd film was calculated to be 37.85 m^2 g^{-1} which is obviously higher than those of Pd film without mesopores (3.56 m^2 g^{-1}) and commercial PdB (3.43 m^2 g^{-1}).

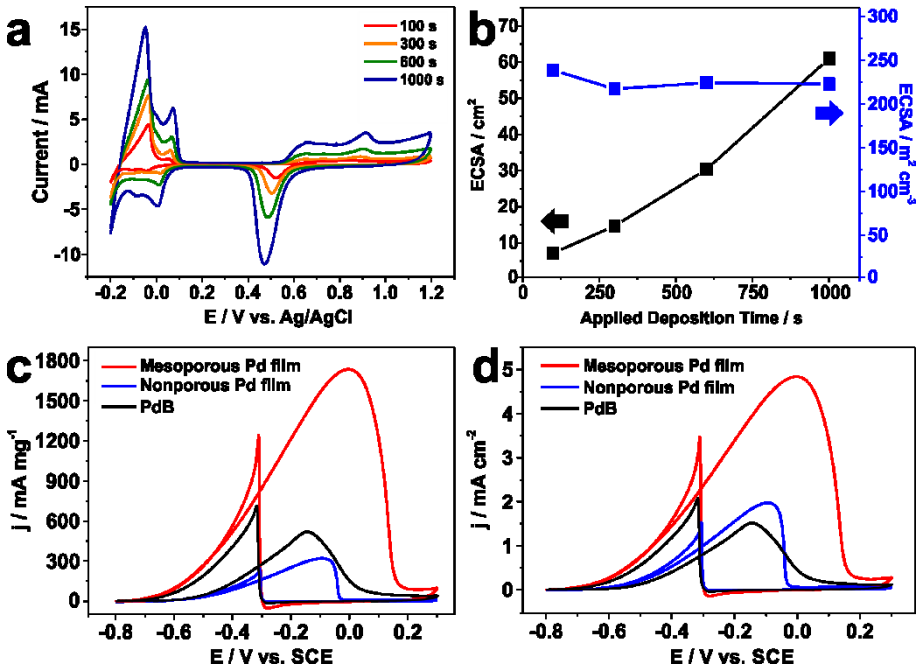

Figure 2.18. (a) CV curves in 0.5 M H_2SO_4 of the mesoporous Pd films prepared by various applied deposition time (100, 300, 600 and 1000 s). (b) Relation between the thickness of mesoporous Pd films towards electrochemical active surface area (ECSA) and volume-normalized ECSA. (c) Pd mass-normalized and (d) ECSA-normalized CV curves of

mesoporous Pd film, nonporous Pd film and commercial PdB in 1 M KOH containing 1 M C_2H_5OH. All the CV curves were obtained at a scan rate of 50 mVs^{-1}.

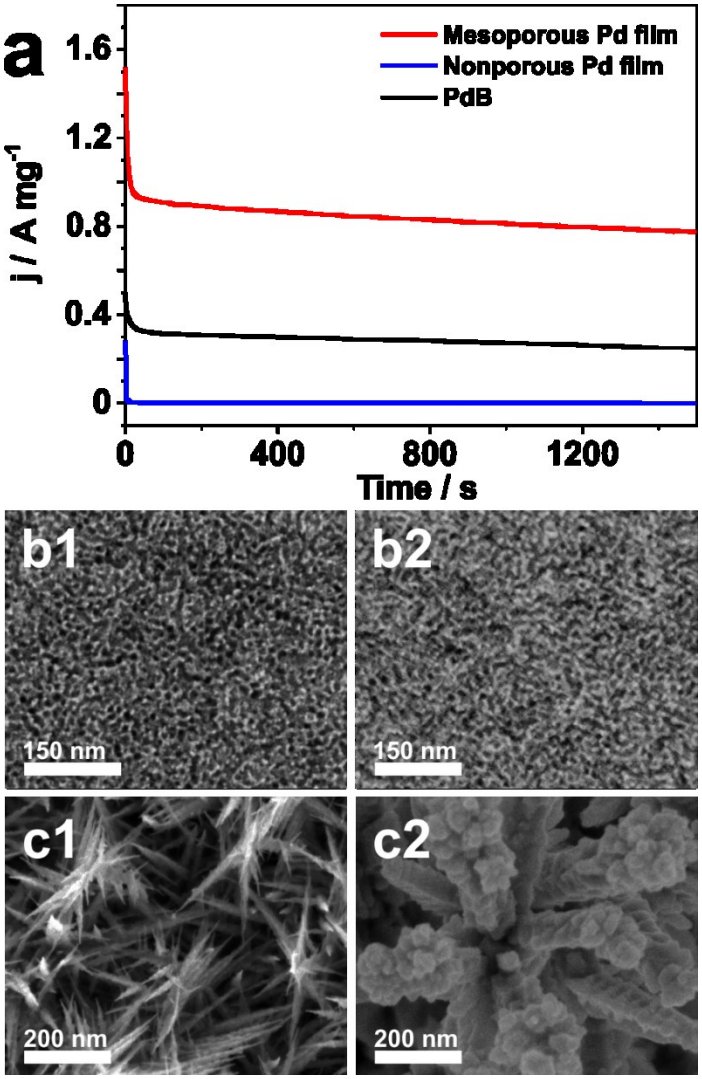

Figure 2.19. (a) Amperometric *i-t* curve of mesoporous Pd film, nonporous Pd film and PdB for the catalytic stability test at potential of -0.3 V for 1500 s. (b-c) SEM images of (b) mesoporous Pd film and (c) nonporous Pd films before and after the stability test.

Pd is well known as a most promising composition in catalyzing the fuel molecules oxidation reaction in alkaline solution even in comparison to Pt. To check the potential application of the as-prepared mesoporous Pd films, ethanol oxidation reaction was selected as a model reaction. For comparison, mesoporous Pd film and nonporous Pd film (as shown in **Figure 2.12a**) with same deposition time of 100 s, and Pd black (abbreviated as PdB) were selected and studied in electrolyte of 1.0 M KOH containing 1.0 M C_2H_5OH. The CV curves recorded at scan rate of 50 mV s^{-1} are shown in **Figure 2.18c**. The CV

curves of Pd films in forward scan showed different current peak position compared to that of commercial PdB. This uncommon shape can be ascribed to the effect of the use of gold substrate as a working electrode instead of glassy carbon electrode (GCE). Without any doubt, the mesoporous Pd film showed best mass-normalized activity of 1735.00 mA mg^{-1}, which is 5.4 and 2.4 times higher than that of nonporous Pd film (320.9 mA mg^{-1}) and PdB (710.6 mA mg^{-1}), respectively (**Figure 2.18c**). Even when the CV curves were normalized by the respective ECSA of the samples, mesoporous Pd film sample exhibit remarkable peak current density compared to both nonporous Pd film and PdB. The superior catalytic activity is ascribed to the exposure of the active surface. The catalytic stability was then evaluated by amperometric *i-t* method at potential of -0.3 V (*vs*. Hg/HgO) for 1500 s. The results showed that the mesoporous Pd film retained more stable than that of nonporous Pd film and the PdB (**Figure 2.19a**). SEM images were taken for the mesoporous Pd film and nonporous Pd film after the stability test. The mesoporous Pd film sample can retain their pores structure meanwhile the nonporous Pd film undergo the changes of their structure after the stability test (**Figure 2.19b-c**). The features of accessible pores structure both on the surface and inside the mesoporous Pd film are believed lead to the enhancement of electrocatalytic activity. All the studies indicate that the mesoporous Pd film exposes larger active surface area and the exposed surfaces are more accessible than other samples.

2.1.5. Conclusions

In this chapter, I successfully prepared the mesoporous Pd films which possess abundant accessible active sites for electrocatalytic application such as electrooxidation of ethanol. SANS data showed that that the Pluronic P123 micelles formed via self-assembly are not altered by the addition of the metal precursor. The UV-Vis spectroscopy investigation on the electrolyte solution consists of the P123 micelles and metal precursor was confirmed the interaction between head moiety of the micelles with metal ions, both $[PdCl_4]^{2-}$ and $[Pd(H_2O)_4]^{2+}$. Mesoporous structure film was deposited onto the substrate surface as the metal ions were attracted and in turn reduced by potential which applied during the electrodeposition process. The morphological study observed by SEM shows that the pores were formed over the film and having the average pore diameter size of 10.9 nm. Cross-

sectional observation of the film by TEM also shows continuous pores from the bottom to the top of the film. The crystallinity, crystal phase and electronic coordination state of the Pd film was confirmed by HRTEM, XRD and XPS, respectively. The optimized surfactant concentration and applied deposition potential are the key factors to govern the formation of homogenous and well-distributed pores in the entire of the film. Electrodeposition of mesoporous metal film by using nonionic surfactant has the advantage of easy template removal. Some ionic surfactants require organic or other harmful compound to remove the micelles templates effectively. The preparation of this pure crystalline Pd film open the opportunity for another metals and alloys and can be beneficial to fabricate microfuel cells as on-chip power source device.

2.1.6. References

[1] M. Davis, *Nature* **2002**, *417*, 813–821.

[2] P. Innocenzi, L. Malfatti, *Chem. Soc. Rev.* **2013**, *42*, 4198–4216.

[3] S. Shao, H. Wu, S. Wang, Q. Hong, R. Koehn, T. Wua, W. -F. Rao, *J. Mater. Chem. C* **2015**, *3*, 10819–10829.

[4] B. Bastakoti, S. Ishihara, S. -Y. Leo, K. Ariga, K. -W. Wu, Y. Yamauchi, *Langmuir* **2014**, *30*, 651–659.

[5] J. Martens, J. Jammaer, S. Bajpe, A. Aerts, Y. Lorgouilloux, C. Kirschhock, *Microporous and Mesoporous Materials* **2011**, *140*, 2–8.

[6] H. Wang, L. Wang, T. Sato, Y. Sakamoto, S. Tominaka, K. Miyasaka, N. Miyamoto, Y. Nemoto, O. Terasaki, Y. Yamauchi, *Chem. Mater.* **2012**, *24*, 1591−1598.

[7] S. Fu, C. Zhu, J. Song, M. H. Engelhard, H. Xia, D. Du, Y. Lin, *ACS Appl. Mater. Interfaces* **2016**, *8 (51)*, 35213–35218.

[8] E. A. Franceschini, M. M. Bruno, F. J. Williams, F. A. Viva, H. R. Corti, *ACS Appl. Mater. Interfaces* **2013**, *5 (21)*, 10437–10444.

[9] T. Sun, C. Zhang, J. Chen, Y. Yan, A. A. Zakhidov, R. H. Baughman, L. Xu, *J. Mater. Chem. A* **2015**, *3*, 11367-11375.

[10] C. Li, B. Jiang, N. Miyamoto, J. H. Kim, V. Malgras, Y. Yamauchi, *J. Am. Chem. Soc.* **2015***, 137 (36),* 11558–11561.

[11] M. Hao, S. Wu, H. Zhou, W. Ye, X. Wei, X. Wang, Z. Chen, S. Li, *J. Mater. Sci.* **2016**, *51,* 2420–2426.

[12] S. Abate, G. Giorgianni, S. Gentiluomo, G. Centi, S. Perathoner, *ChemSusChem* **2015**, *8*, 3805–3814.

[13] A. Fukuoka, H. Araki, J. Kimura, Y. Sakamoto, T. Higuchi, N. Sugimoto, S. Inagaki, M. Ichikawa, *J. Mater. Chem.* **2004**, *14*, 752–756.

[14] C. Du, M. Chen, W. Wang, G. Yin, *ACS Appl. Mater. Interfaces* **2011**, 3, 105–109.

[15] W. -C. Li, T. Balk, *Materials* **2009**, *2*, 2496–2509.

[16] S. Tominaka, T. Hayashi, Y. Nakamura, T. Osaka, *J. Mater. Chem.* **2010**, *20*, 7175–7182.

[17] G. Denuault, C. Milhano, D. Pletcher, *Phys. Chem. Chem. Phys.* **2005**, *7*, 3545–3551.

[18] N. A. A. Abass, G. Denuault, D. Pletcher, *Phys. Chem. Chem. Phys.* **2014**, *16*, 4892–4899.

[19] K. S. Choi, E. W. McFarland, G. D. Stucky, *Adv. Mater.* **2003,** *15*, 2018–2021.

[20] Y. Song, Y. Yang, C. J. Medforth, E. Pereira, A. K. Singh, H. Xu, Y. Jiang, C. J. Brinker, F. Swol, J. A. Shelnutt, *J. Am. Chem. Soc.* **2004**, *126 (2)*, 635–645.

[21] F. Wang, C. Li, L. -D. Sun, C. -H. Xu, J. Wang, J. C. Yu, C. -H. Yan, *Angew. Chem. Int. Ed.* **2012**, *51*: 4872–4876.

[22] B. Jiang, C. Li, V. Malgras, M. Imura, S. Tominaka, Y. Yamauchi, *Chem. Sci.* **2016**, *7*, 1575-1581.

[23] L. Sun, H. Wang, K. Eid, L. Wang, *Sci. Tech. Adv. Mater.* **2016**, *17:1*, 58–62.

[24] Z. -Y. Shih, C. -W. Wang, G. Xu, H. -T. Chang, *J. Mater. Chem. A* **2013**, *1*, 4774–4778.

[25] C. Li, T. Sato, Y. Yamauchi, *Chem. Commun.* **2014**, *50*, 11753–11756.

[26] A. M. Kalekar, K. K. K. Sharma, M. N. Luwang, G. K. Sharma, *RSC Adv.* **2016**, *6*, 11911–11920.

[27] S. A. Bagshaw, E. Prouze, T. J. Pinnavaia, *Science* **1995**, *269*, 1242–1244.

[28] G. Calleja, D. R. Serrano, R. Sanz, P. Pizarro, A. Garcia, *Ind. Eng. Chem. Res.* **2004**, *43 (10)*, 2485–2492.

[29] Q. Fan, J. Liu, Y. Yu, S. Zuo, *RSC Adv*. **2014**, *4 (106)*, 61877−61883.

[30] (a) A. Sokolova, J. Christofordis, A. Eltobaji, J. Barnes, F. Darmann, A. E. Whitten, L. de Campo, *Neutron News* **2016**, *27*, 9-13. (b) O. Arnold, J. C. Bilheux, J. M. Borreguero, A. Buts, S. I. Campbell, L. Chapon, M. Doucet, N. Draper, R. F. Leal,

M. A. Gigg, V. E. Lynch, A. Markvardsen, D. J. Mikkelson, R. L. Mikkelson, R. Miller, K. Palmen, P. Parker, G. Passos, T. G. Perring, P. F. Peterson, S. Ren, M. A. Reuter, A. T. Savici, J. W. Taylor, R. J. Taylor, R. Tolchenov, W. Zhou, J. Zikovsky, *Nucl. Instrum. Methods Phys. Res. A*, **2006**, *764*, 156-166.

[31] Y. Yamauchi, M. Sawada, A. Sugiyama, T. Osaka, Y. Sakka, K. Kuroda, *J. Mater. Chem.* **2006**, *16*, 3693–3700.

[32] (a) L. I. Elding, L. F. Olsson, *J. Phys. Chem.* **1978**, *82*, 69-74. (b) R. J. Deeth, L. I. Elding, Inorg. *Chem.* **1996**, *35*, 5019-5026. (c) K. Mech, P. Zabinski, R. Kowalik, K. Fitzner, *J. Electrochem. Soc.* **2013**, *160*, H770-H774. (d) A. Podborska, M. Wojnicki, *J. Molecular Structure* **2017**, *1128*, 117-122.

[33] Y. Liu, S. H. Chen, J. S. Huang, *Macromolecules* **1998**, *31*, 2236–2244.

[34] S. R. Kline, *J Appl. Cryst* **2006**, *39*, 895–900.

[35] P. Alexandridis, J. F. Holzwarth, T. A. Hatton, *Macromolecules* **1994**, *27 (9)*, 2414–242.

[36] (a) C. M. Shen, X. G. Zhang, H. L. Li, *Applied Surface Science* **2005**, *240*, *34–41*. (b) S. N. A. Malek, Y. Mohd, *Int. J. Electrochem. Sci.* **2017**, *12*, 1561 – 1571.

[37] G. S. Attard, J. M. Corker, C. G. Göltner, S. Henke, R. H. Templer, *Angew. Chem. Int. Ed. Engl.* **1997**, *36*, 1315–1317.

[38] R. G. Ehl, A. Ihde, *Journal of Chemical Education* **1954**, *31*, 226–232.

[39] F. Kadirgan, B. Beden, J. M. Leger, C. Lamy, *J. Electroanal. Chem* **1981**, *125*, 89–103.

2.2. Pore-Expanded Mesoporous Pd Films Using PS-*b*-PEO

2.2.1. Introduction

Porous materials offer excellent functionalities for a wide variety of applications, such as wastewater remediation, biomedical/drug delivery, and catalysis.[1-5] Soft-templating methods provide a facile approach for the preparation of mesoporous materials as they are simpler to perform and require fewer synthetic steps.[6-8] The pore size and structure of these materials can be tuned by considering the assembly of surfactants or block copolymer micelles in the reaction solution. In particular, large-sized micelle assembly can facilitate the formation of open pores of the materials. However, the large-sized porous materials are still limited to carbon, silica, metal oxides, and organosilicates. At present, there are relatively few literatures on the preparation of large-sized mesoporous metallic materials by soft-templating methods.[9-13] Metallic materials, especially noble metals, with large-sized open pores are expected to possess enhanced performance towards many important applications, including electrocatalysis.[14,15] Therefore, the fabrication of large-sized mesoporous noble metal materials through soft-templating technique remains a big challenge to overcome.

Among noble metals, platinum (Pt) is known as the most catalytically active element. However, its scarcity in nature hinders its practical use, thus many researchers are now seeking to reduce the usage of Pt-based catalysts or to replace them altogether with cheaper materials. As the second most catalytically active element, palladium (Pd) is more abundant and possesses a similar structure as Pt. As such, it has a great potential to replace or substitute Pt in various catalytic reactions.[16-18] Based on previous studies, Pd has been shown to display excellent catalytic performance towards the oxidation of hydrogen or liquid fuels and show high selectivity towards the hydrogenation of acetylene.[19,20]

Several works have been reported on the preparation of large-sized mesoporous metals from polymeric micelle assembly. Mesoporous Pd, both particles and films, have also been reported, however the pore size was limited to 2-10 nm.[21-24] Furthermore, these works relied on the use of cationic and non-ionic surfactants with relatively short chain lengths. Block copolymer with a relatively large chain length (higher molecular weight)

can form micelles in solution with an average diameter of over 10 nm. The selection of suitable hydrophobic moiety of the block copolymer is critical for ensuring stable interactions between the block copolymer and the Pd ion complexes in water, which in turn, will assist the formation of large-sized mesoporous Pd architectures.

Herein, I report the preparation of mesoporous Pd films *via* a facile polymeric micelle-assisted electrochemical deposition method. Pd films with a variety of large sized pores can be achieved by utilizing block copolymers with different molecular weight. The electrolyte solution consists of Pd precursor and micelles dissolved in a mixture of tetrahydrofuran (THF), ethanol, hydrochloric acid, and water. In such reaction system, THF promotes dissolution of the block copolymer into free unimers in the solution. The subsequent additions of ethanol and water induce the micellization of the block copolymers. The as-prepared mesoporous Pd films deposited from the electrolyte solution containing $PS_{(5000)}$-*b*-$PEO_{(2200)}$, $PS_{(18000)}$-*b*-$PEO_{(7500)}$, and $PS_{(63000)}$-*b*-$PEO_{(26000)}$ are denoted as meso Pd-2.2, meso Pd-7.5, and meso Pd-26, respectively (the molecular weight for each block is shown in parenthesis). To probe the electrocatalytic performance of the obtained mesoporous Pd films, ethanol oxidation was selected as the model reaction. The electrocatalytic test reveals that the as-obtained mesoporous Pd films display superior electrocatalytic activity for ethanol oxidation, owing to the large surface-active area, open accessible pores, and stable mesoporous structure.

2.2.2. Experimental Section

Materials

Block copolymers, polystyrene-*b*-poly(ethylene oxide) with three different molecular weights, were purchased from Polymer Source. Tetrahydrofuran (THF), palladium(II) chloride, and ethanol were received from Nacalai Tesque, Inc. Hydrochloric acid, sulfuric acid, and potassium hydroxide were purchased from Wako Chemicals. All the chemicals were used without prior treatment. The double distilled water was obtained through a water purification system Merck Milli-Q®.

Synthesis of Mesoporous Pd Films

The electrochemical deposition of mesoporous Pd films was carried out in the electrochemical cells containing the electrolyte solutions with three standard electrodes. At

first, the electrolyte solutions were prepared by dissolving the 4 mg of block copolymers in THF through sonication for 5 minutes. The amount of THF was different for each block copolymer, *i.e.* 0.08 mL, 0.6 mL, and 1.6 mL for $PS_{(5000)}$-*b*-$PEO_{(2200)}$, $PS_{(18000)}$-*b*-$PEO_{(7500)}$, and $PS_{(63000)}$-*b*-$PEO_{(26000)}$, respectively. Ethanol (1.5 mL) was then added into the above solutions, followed by the addition of 0.08 mL of 2 M HCl along with distilled water to make the total volume of each electrolyte solution to be 3.75 mL. Finally, 0.25 mL of 80 mM $PdCl_2$ aqueous solution was added into each electrolyte solution. The electrodes for electrochemical deposition consisted of a gold-coated silicon substrate, Ag/AgCl, and Pt wire as the working, reference, and counter electrodes, respectively. The working electrode had a dimension of 0.3 cm x 1.5 cm with a deposition area of 0.3 cm × 0.6 cm (0.18 cm^2). The electrochemical deposition from each different block copolymer-containing electrolyte solution was carried out by the amperometric *i-t* technique using electrochemical station CHI 842B model (CH Instrument, USA) at constant applied potentials of 0.0 V for 600, 1200, and 1800 s. Template removal was subsequently carried out by first rinsing the films with distilled water followed by blowing under nitrogen gas flow and finally, immersion in THF for overnight. The obtained samples electrodeposited from the electrolyte solution containing $PS_{(5000)}$-*b*-$PEO_{(2200)}$, $PS_{(18000)}$-*b*-$PEO_{(7500)}$, and $PS_{(63000)}$-*b*-$PEO_{(26000)}$ were denoted as meso Pd-2.2, meso Pd-7.5, and meso Pd-26, respectively.

Characterizations

Scanning electron microscopy (SEM) images of the deposited Pd films were obtained using a Hitachi FESEM SU-82300 microscope operated at an accelerating voltage of 5 kV. Transmission electron microscopy (TEM) was carried out using a JEOL JEM-2100F microscope operated at an accelerating voltage of 200 kV. The ultraviolet-visible (UV-Vis) spectra of the aqueous electrolyte solution used for electrochemical deposition were obtained with a JASCO V-7200. Low- and wide-angle X-ray diffraction (XRD) patterns of the as-deposited Pd films were obtained by Rigaku SmartLab XRD with Cu Kα radiation. X-ray photoelectron spectroscopy (XPS) was carried out using a PHI Quantera SXM (ULVAC-PHI) with Al Kα radiation to determine the composition and electronic coordination state of the as-prepared Pd films. All XPS spectra were calibrated to the C 1*s* peak at 285.0 eV. To determine the mass of the deposited Pd on the final mesoporous Pd films, inductively coupled plasma optical emission spectroscopy (ICP-OES) was carried out using a 720 ICP-OES.

Electrochemical Measurement

All electrochemical measurements were conducted with a CHI 842B electrochemical analyzer (CHI Instruments, USA). A conventional three-electrode set up was employed to carry out the electrochemical measurements. A gold-coated silicon wafer substrate further coated with the Pd films, a Pt wire and Ag/AgCl or SCE electrodes were employed as the working, counter and reference electrodes, respectively. The geometric area of the deposited Pd films on the gold-coated silicon wafer working electrode was 0.3 cm × 0.6 cm. As for the electrochemical measurement of the commercially available Pd black (denoted as PdB), a glassy carbon electrode (GCE) with a diameter of 0.3 cm was used as the working electrode. Prior to the PdB surface coating, the GCE was polished with 1.0 and 0.05 μm alumina powder, rinsed with deionized water and dried under nitrogen gas flow. Then, 5.0 mg of PdB was coated on the surface of the GCE. After drying under atmospheric conditions, a Nafion® solution (5.0 μL, 0.5 wt%) was subsequently coated on the GCE surface and dried at room temperature before further electrochemical measurements. Cyclic voltammograms were recorded in a 0.5 M H_2SO_4 electrolyte at a scan rate of 50 mV s^{-1} between -0.2 and +1.2 V (*vs.* Ag/AgCl). The electrocatalytic performance towards the ethanol oxidation reaction was recorded in 1.0 M KOH containing 1.0 M C_2H_5OH in the potential range from -0.8 to 0.3 V (vs. SCE). Amperometric *i-t* curves were recorded at a potential of -0.1 V (vs. SCE) for 1,500 s in 1.0 M KOH containing 1.0 M C_2H_5OH to study the stability test.

2.2.3. Characterization of Pore-Expanded Mesoporous Pd Films

The block copolymer, PS-*b*-PEO, is comprised of two segments, *i.e.* polystyrene and polyethylene oxide which have hydrophobic and hydrophilic behaviors, respectively. PS-*b*-PEO easily dissolves in THF to become a free unimer. The addition of an ethanol-water mixture induces the transformation of free unimer into micelles, as indicated by the presence of Tyndall effect which can be observed visually (**Figure 2.20**). The PS and PEO blocks act as the hydrophobic moiety (core) and hydrophilic moiety (shell) of the micelles, respectively.[25] The TEM images presented in **Figure 2.21** reveal that spherical micelles

with average micelle sizes of 15.5, 28.8, and 33.6 nm were formed from block copolymers $PS_{(5000)}$-*b*-$PEO_{(2200)}$, $PS_{(18000)}$-*b*-$PEO_{(7500)}$, and $PS_{(63000)}$-*b*-$PEO_{(26000)}$, respectively.

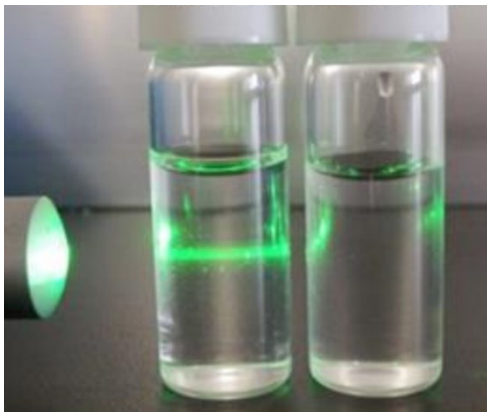

Figure 2.20 Photograph of the Tyndall effect showing the light scattering phenomenon in the presence of micelles. The addition of an ethanol-water mixture induces the transformation of free unimer (right side) into micelles (left side).

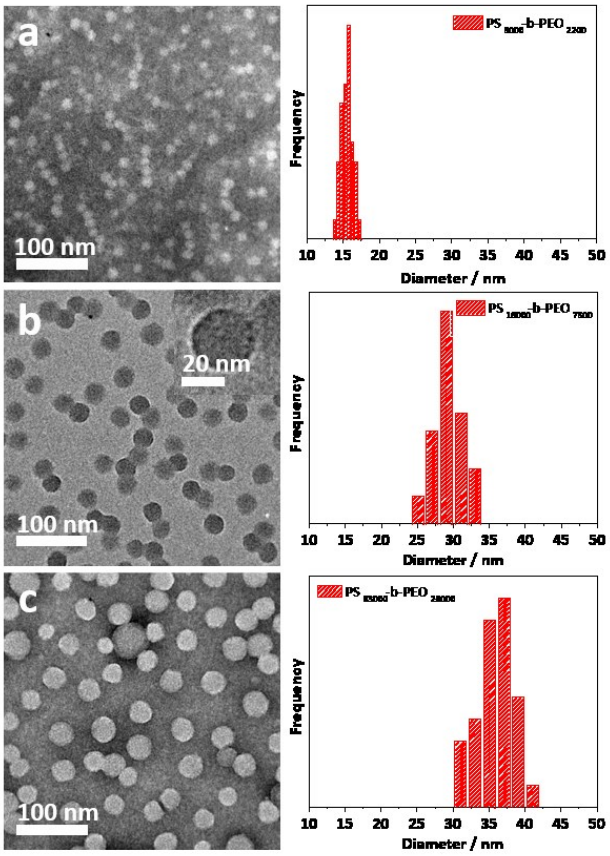

Figure 2.21 TEM images (left) and diameter histogram (right) of the spherical micelles made from (a) $PS_{(5000)}$-*b*-$PEO_{(2200)}$, (b) $PS_{(18000)}$-*b*-$PEO_{(7500)}$, and (c) $PS_{(63000)}$-*b*-$PEO_{(26000)}$. The micelles were stained with 1.0 wt% phosphotungstic acid. In some parts, staining

agents are adsorbed on the PEO micelle surface thus shown as a corona, as indicated on the inset in panel b (left).

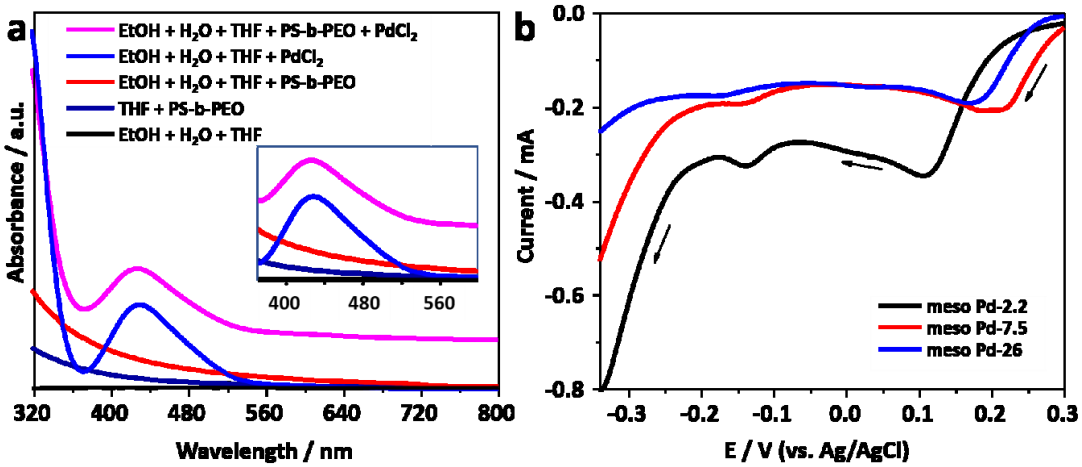

Figure 2.22 (a) UV-visible absorption spectra recorded from the various solutions. (b) Linear sweep voltammetry (LSV) curves obtained from the electrolyte solution for electrochemical deposition of mesoporous Pd films at a scan rate of 10 mV s^{-1}. Black arrows indicate the scan direction.

A previous report has suggested that the incorporation of metal precursors into the micellar solution would not destroy the micelles structure.[24] The metal precursor is transformed into water-coordinated metal ion complexes after its addition into the micellar solution. UV-visible spectroscopy was employed to observe the interactions between water-coordinated metal ion complexes with the shells of the micelles (**Figure 2.22**). Initially, UV-visible absorption spectrum was recorded from the $PdCl_2$ aqueous solution. The absorption peak centered at around 425 nm with a tail on the low energy side is assigned to *d-d* transition in the Pd(II) complexes (inset **Figure 2.22**). The spectrum indicates the presence of $[PdCl_{4-x}(H_2O)_x]^{(-2+x)}$ (where *x* varies from 0 to 4) complex species which were formed as a result of the ligand exchange reaction between coordinated Cl^- ion and water molecules in aqueous media.[26,27] The charge on the complexes, accordingly, change from 2- to 2+ with the increase in the number of water molecules (from 0 to 4) entering the coordination sphere of Pd^{2+} ions.[28] The hyperchromic effect was observed in the UV-visible absorption spectrum of the solution containing micelles and $PdCl_2$. The spectrum is shifted upward without any changes on the absorption peaks (**Figure 2.22**). The hyperchromic effect observed in the UV-visible absorption spectra can be attributed

to the existence of interactions between water-coordinated Pd ions with the shells of the micelles. Such interactions were previously suggested to occur through hydrogen bonding.[29]

The mesoporous Pd films with different pore sizes were obtained by applying deposition potential to conductive substrates (working electrodes). The applied deposition potential of the Pd films was determined by carefully carrying out negative scan linear sweep voltammetry (LSV) at a slow scan rate from the electrolyte solution containing polymers with different molecular weight (**Figure 2.22**). The LSV curve clearly shows that the reduction potential of Pd(II) into Pd(0) occurs clearly. The plateau region of the LSV plot was observed at around 0.0 V and hence, this potential was selected as the applied potential for the deposition of mesoporous Pd films. A previous study has demonstrated that at a higher applied deposition potential (more positive), the reduction rate of metal ions became slower which may repel the micelles.[30] On the contrary, at a lower applied deposition potential (more negative), the reduction rate became faster, which may break down the structure of the micelles.[24,31]

As discussed above, the water-coordinated metal ion complexes are thought to interact with the shells of the micelles through hydrogen bonding. The formation of the mesoporous Pd films can be described as follows. When the electrical current generated by the potentiostat (using the amperometric *i-t* technique) passed through the working electrode, it attracted the metal ion complexes along with the micelles to the working electrode. The charge of metal ion complexes varies from -2 to +2 which are important for the assembly and interaction with the micelle domains. Notice that the water-rich metal complexes are positively charged and attracted by the micelles. The negatively charged Cl^--rich metal complexes are attracted by the positively charged water-rich complexes through electrostatic interactions, thus enhancing the Pd(II) species content in and around the micelles during the electrodeposition of Pd(0). The electrical current enabled the reduction of Pd(II) ions into Pd(0) metallic state. The number of reduced Pd ions (the deposited Pd) is associated with the charge passing through the working electrode to the electrolyte solution. Subsequently, the Pd metal constructed the pore walls which enveloped the micelles as the electrical current passed through the working electrode. To ensure complete removal of the polymeric templates, the deposited films were immersed in THF for overnight and Pd metallic framework films with mesoporous structures remained on the substrate (**Scheme 2.2**).

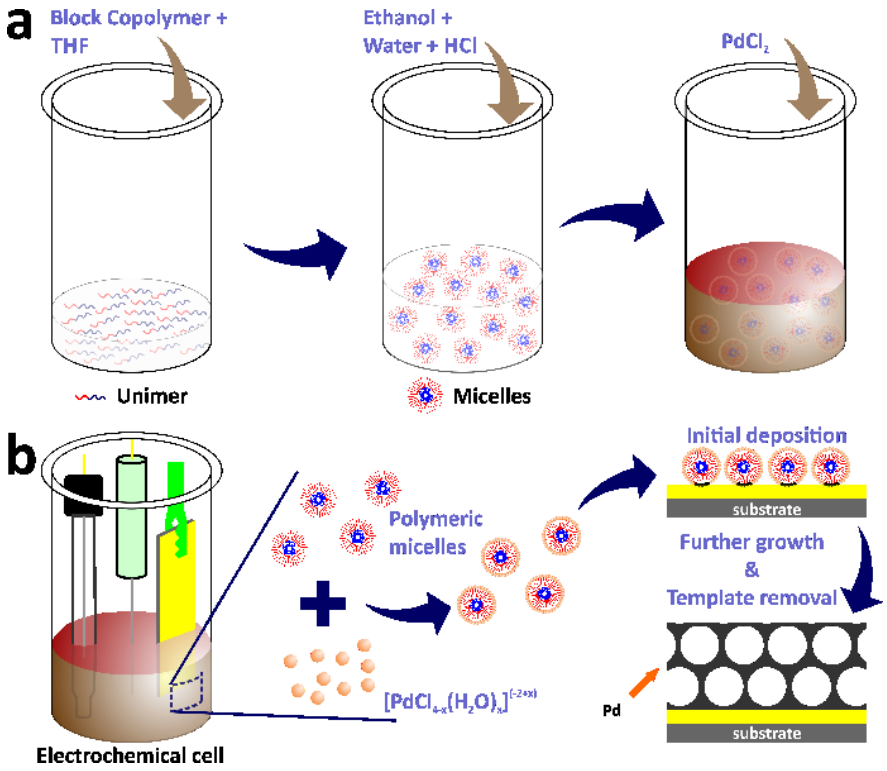

Scheme 2.2 (a) Illustration of the electrolyte preparation for electrochemical deposition. (b) Schematic illustration for the electrochemical deposition of mesoporous Pd films assisted by polymeric micelles.

The morphology of the as-prepared films was characterized by SEM (**Figure 2.23**). Both top-view and cross-sectional observations reveal that the spherical pores are formed continuously throughout the entire films arranged in a cage-type manner (**Figure 2.23a1-c2**). Moreover, from the top-view SEM images, the average pore sizes of meso Pd-2.2, meso Pd-7.5, and meso Pd-26 were statistically calculated from more than 100 pores and can be estimated to be 14, 25, and 41 nm, respectively (**Figure 2.23a3-c3**). Furthermore, the contrast difference in the high-angle annular dark-field scanning TEM (HAADF-STEM) images indicates the porous nature of the films, the pores were constructed from the substrate surface to the top films surface and suggests that the pore walls are well-interconnected (**Figure 2.24**). The high-resolution TEM (HR-TEM) images depicted in **Figure 2.25a1-c1** clearly reveal the existence of mesopores in each film, as indicated by the yellow circles. In contrast, no porous structure is observed in the film deposited in the absence of polymeric micelles under similar electrodeposition conditions (**Figure 2.26**). This observation suggests that the spherical micelles present in the electrolyte solution play an important role in the formation of mesoporous Pd films.

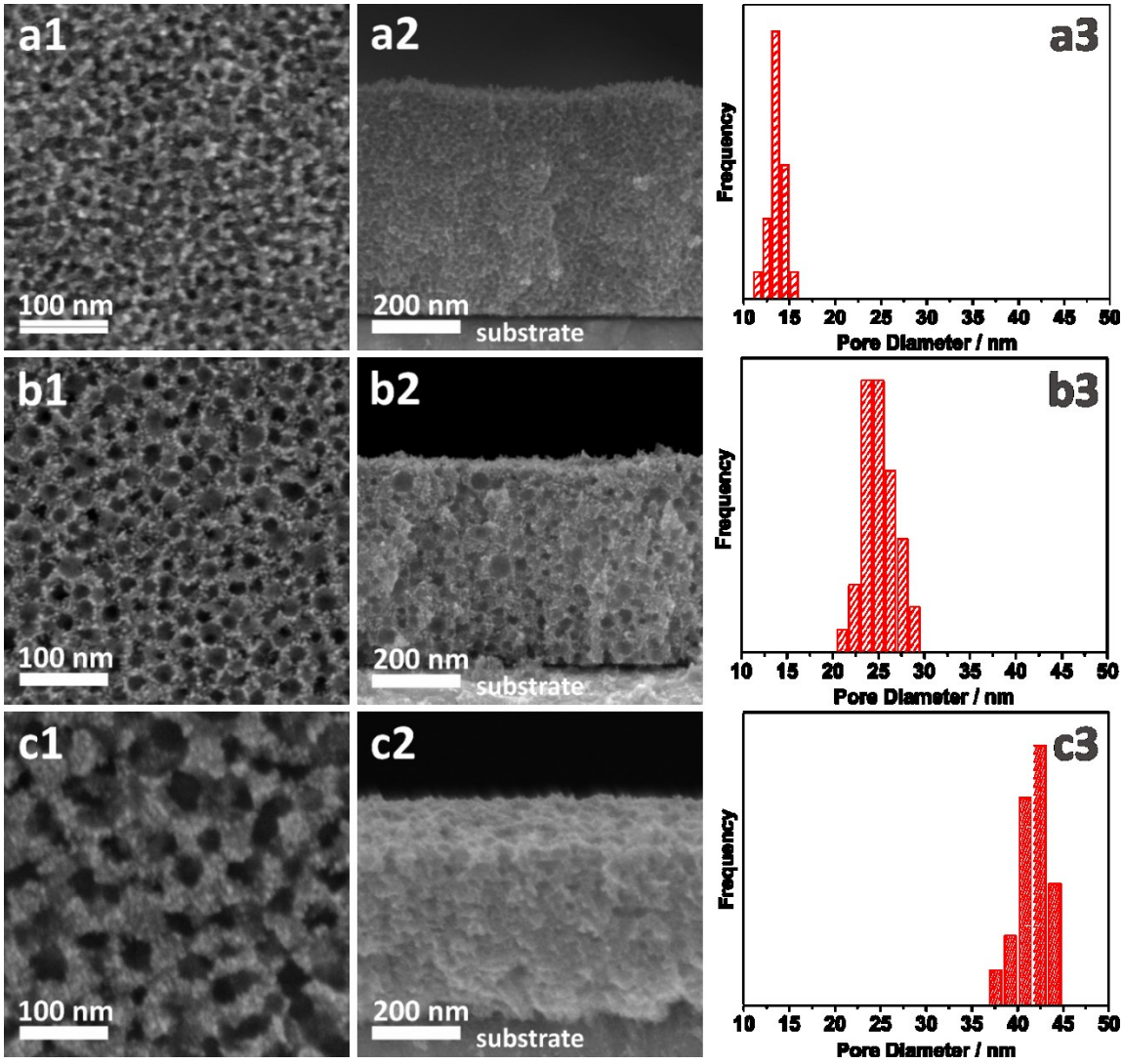

Figure 2.23 (a1-c1) Top-view, (a2-c2) cross-sectional SEM images, and (a3-c3) pore size distribution histogram of (a) meso Pd-2.2, (b) meso Pd-7.5, and (c) meso Pd-26. The pore size distributions are statistically calculated from the top-view SEM images.

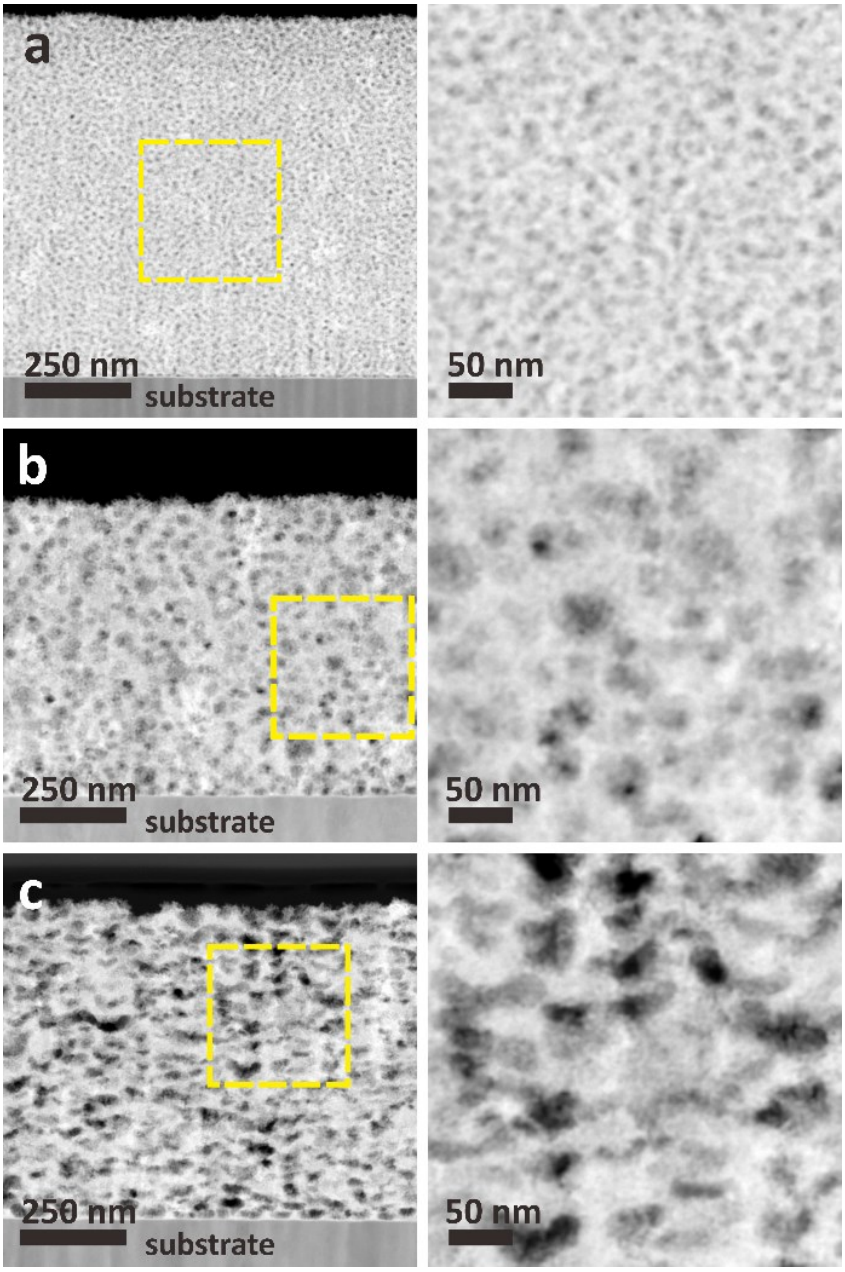

Figure 2.24. Cross-section HAADF-STEM images of (a) meso Pd-2.2, (b) meso Pd-7.5, and (c) meso Pd-26. The images on the right panel are the enlarged images of dashed rectangle area on the left panel.

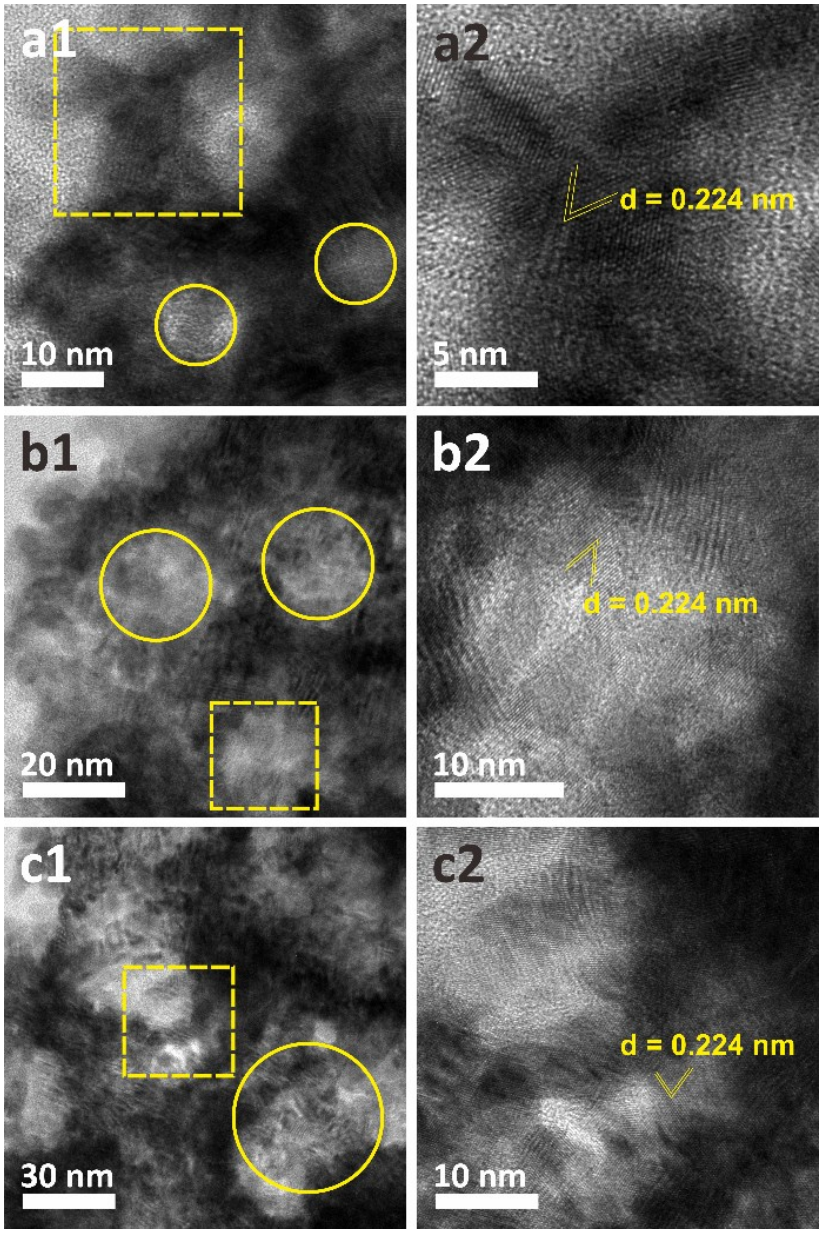

Figure 2.25. HR-TEM images of (a) meso Pd-2.2, (b) meso Pd-7.5, and (c) meso Pd-26 films. The panels (a2-c2) are the enlarged HR-TEM images of dashed rectangle area in panels (a1-c1). Yellow circles in panels (a1-c1) indicate the mesopores formed on the deposited films.

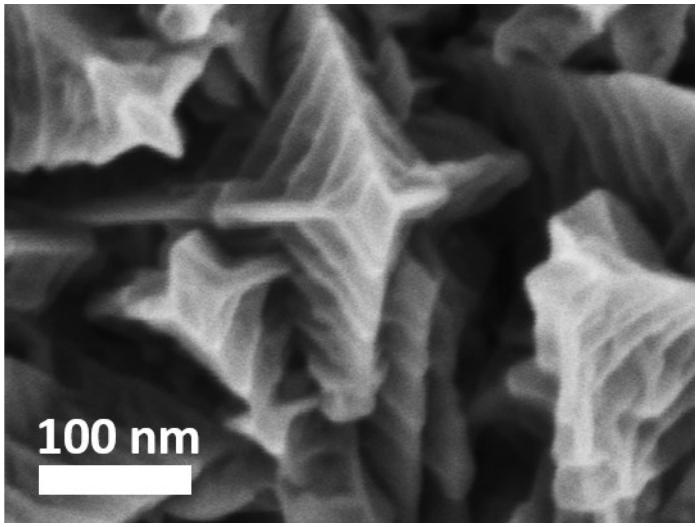

Figure 2.26. SEM image of the non-porous Pd film obtained in the absence of block copolymer PS-*b*-PEO using the same electrochemical deposition process.

Thin film X-ray diffractometer was utilized to examine the crystalline phase of these films (**Figure 2.27**). The diffraction patterns of the films with different pore sizes show diffraction peaks located at 40.18°, 46.72°, 68.16°, 82.18° and 86.82°, which can be assigned to the (111), (200), (220), (311) and (222) diffraction planes of Pd with a face-centered cubic (*fcc*) structure, respectively (JCPDS Card No. 05-0681). The crystallite sizes of the meso Pd-2.2, meso Pd-7.5, and meso Pd-26 were estimated using Scherrer equation to be 5.78, 5.99, 6.29 nm, respectively. The lattice structures of the three-representative mesoporous Pd films were observed by HR-TEM, as depicted in **Figure 2.25a2-c2**. Typical lattice fringes with a constant *d*-spacing of 0.224 nm, corresponding to (111) lattice plane of *fcc* Pd crystal are observed, which is in good agreement with the XRD examination. **Figure 2.27c** displays the X-ray photoemission spectroscopy (XPS) survey spectra recorded from meso Pd-2.2, meso Pd-7.5, and meso Pd-26 films. The high-resolution Pd 3*d* spectrum clearly shows the presence of doublet peaks at 336 eV and 341 eV which can be indexed to metallic Pd $3d_{5/2}$ and Pd $3d_{3/2,}$ respectively (**Figure 2.27d**). However, the PdO peak was not observed indicating that these films were composed of pure metallic Pd.

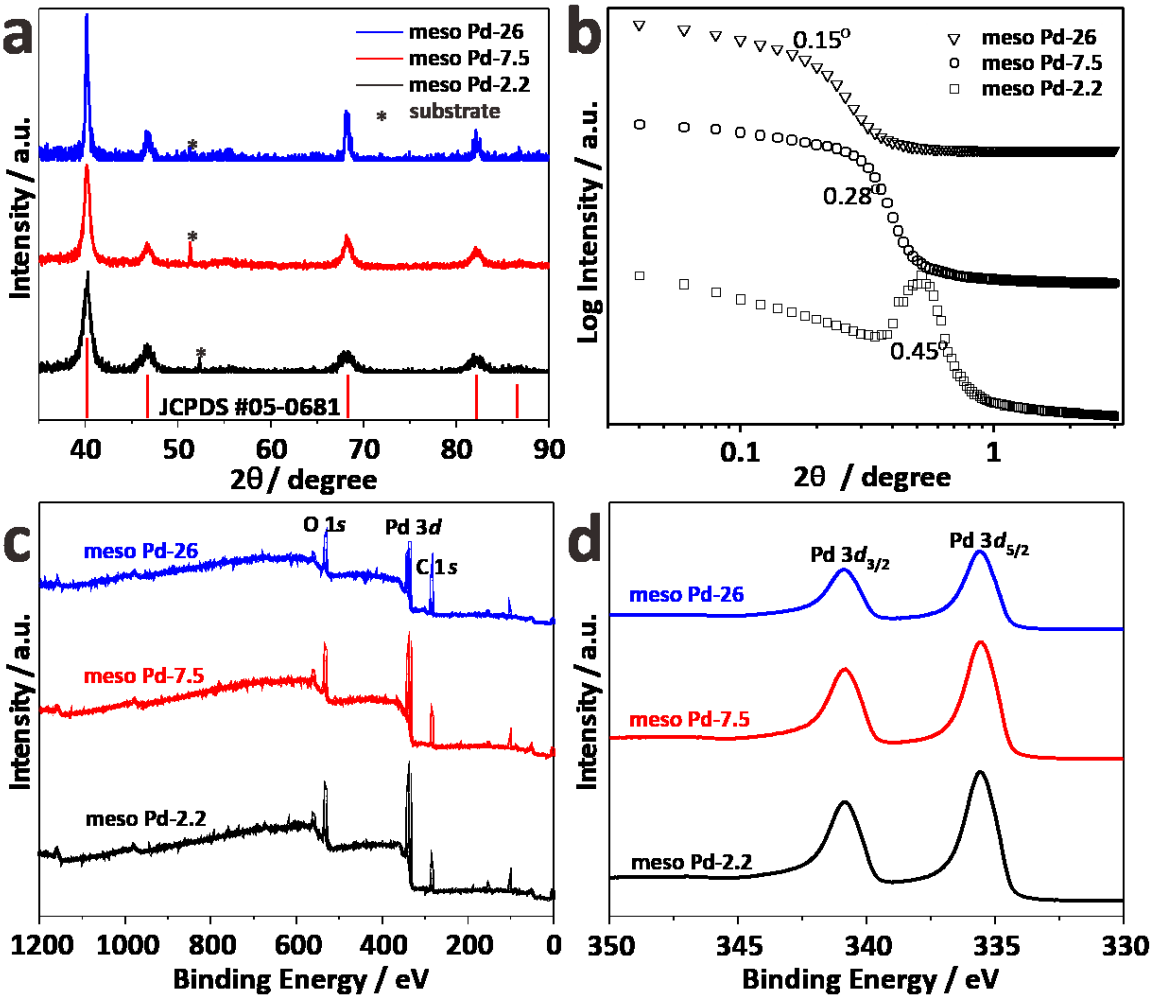

Figure 2.27 (a) Wide-angle and (b) low-angle XRD patterns of the as-prepared mesoporous Pd films. (c) Survey and (b) high-resolution Pd 3*d* X-ray photoemission spectra recorded from meso Pd-2.2, meso Pd-7.5, and meso Pd-26 films.

Low-angle XRD is a useful technique for characterizing the *d*-spacing of well-ordered materials. For ordered mesoporous materials, the *d*-spacing which resulted from low-angle XRD measurement is commonly ascribed to the average distance between adjacent pores. **Figure 2.27b** shows the low-angle diffraction pattern recorded from meso Pd-2.2, meso Pd-7.5, and meso Pd-26. All the diffraction patterns exhibit peaks centered at 0.44°, 0.28°, and 0.15° for meso Pd-2.2, meso Pd-7.5, and meso Pd-26, respectively. The pore-to-pore distance can then be estimated to be 20.1, 31.6, and 58.9 nm for meso Pd-2.2, meso Pd-7.5, and meso Pd-26, respectively. These values are in good agreement with the average pore size and pore wall thickness estimated from TEM and SEM images, respectively. According to the estimated average pore-to-pore distance and the pore wall

thickness, I modeled the pore arrangement in 1,000,000 nm^3 (100 × 100 × 100 nm) and further estimated the surface area ratio of the pore/void region for the mesoporous films with three different pore sizes (**Figure 2.28**). By assuming that the volumetric dimensions of the deposited layer among the three films are identical, the ratio of Pd surface area of meso Pd-2.2, meso Pd-7.5, and meso Pd-26 is estimated to be 4 : 3 : 2.

Figure 2.28 Modeled pore arrangement and geometry of meso Pd-2.2, meso Pd-7.5, and meso Pd-26 for validating the calculation of the Pd surface area inside the films. To make these models, the pore sizes and the wall thicknesses were fixed to be 14 nm and 6 nm (for meso Pd-2.2), 25 nm and 6 nm (for meso Pd-7.5), 41 nm and 18 nm (for meso Pd-26), respectively.

2.2.4. Electrocatalytic Activity of Pore-Expanded Mesoporous Pd Films

An electrochemical approach was employed to estimate the electrochemical active surface area (ECSA) of each mesoporous Pd film by carrying out the cyclic voltammetry (CV) in 0.5 M H_2SO_4 electrolyte from -0.2 to +1.2 V (vs. Ag/AgCl) at a scan rate of 50 mV s^{-1} (**Figure 2.29a**). The CV curves show the typical hydrogen and oxygen adsorption/desorption features. The ECSA was estimated by calculating the oxide reduction charge assuming that the conversion factor for an oxide monolayer reduction was 420 μC cm^{-2} on the smooth surface of Pd.[32] The ECSA values are 41.49, 32.27, and 21.75 cm^2 for meso Pd-2.2, meso Pd-7.5, and meso Pd-26 films with the same film thickness (~ 500 nm), respectively, and these values closely match the surface area ratio of the films with three different average pore sizes estimated from the model (**Figure 2.28**). Clearly,

meso Pd-2.2 has the largest ECSA since its pore size is relatively smaller than those of meso Pd-7.5 and meso Pd-26, implying that larger mesopores lead to smaller ECSA. When the ECSA is normalized with the respective deposited Pd mass, the mass-normalized ECSA for meso Pd-26 has a larger value (90.61 $m^2 g^{-1}$) than those of meso Pd-2.2 (40.28 $m^2 g^{-1}$) and meso Pd-7.5 (33.92 $m^2 g^{-1}$). This mass-normalized ECSA values of mesoporous Pd films are obviously higher than those of non-porous Pd films (11.38 $m^2 g^{-1}$) and commercially available Pd black, abbreviated as PdB (14.52 $m^2 g^{-1}$). The ECSA of meso Pd-26 linearly increases with the increase of film thickness (**Figure 2.29b**, black line). Even when the ECSA values of meso Pd-26 films with various thickness are divided by their respective geometric volume, the volume-normalized ECSA values are relatively similar (**Figure 2.29b**, blue line), indicating that the large surface area derived from the mesoporous structure inside the film is fully accessible.

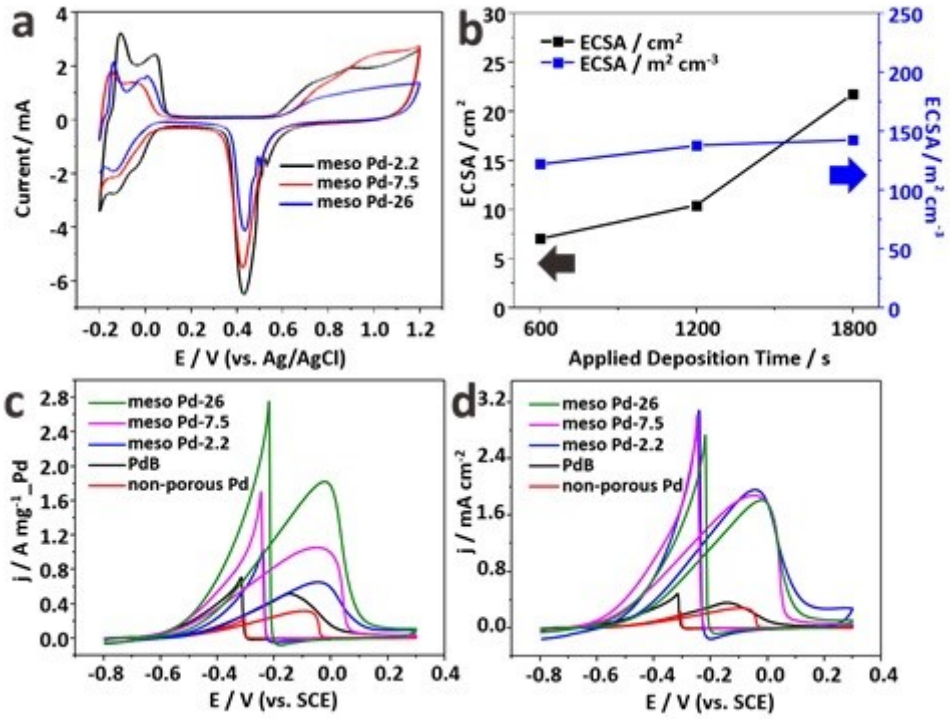

Figure 2.29 (a) Cyclic voltammetry (CV) recorded in 0.5 M H_2SO_4 at a scan rate of 50 mV s^{-1} of meso Pd-2.2 and meso Pd-26 films prepared by applied deposition of 1800 s. (b) The relationship between the film thickness of meso Pd-26 films with the electrochemical active surface area (ECSA; black line) and the volume-normalized ECSA (blue line). (c) Pd mass-normalized and (d) ECSA-normalized CV curves of meso Pd-2.2, meso Pd-7.5, meso Pd-26, non-porous Pd films, and PdB in 1.0 M KOH containing 1.0 M C_2H_5OH at a scan rate of 50 mV s^{-1}.

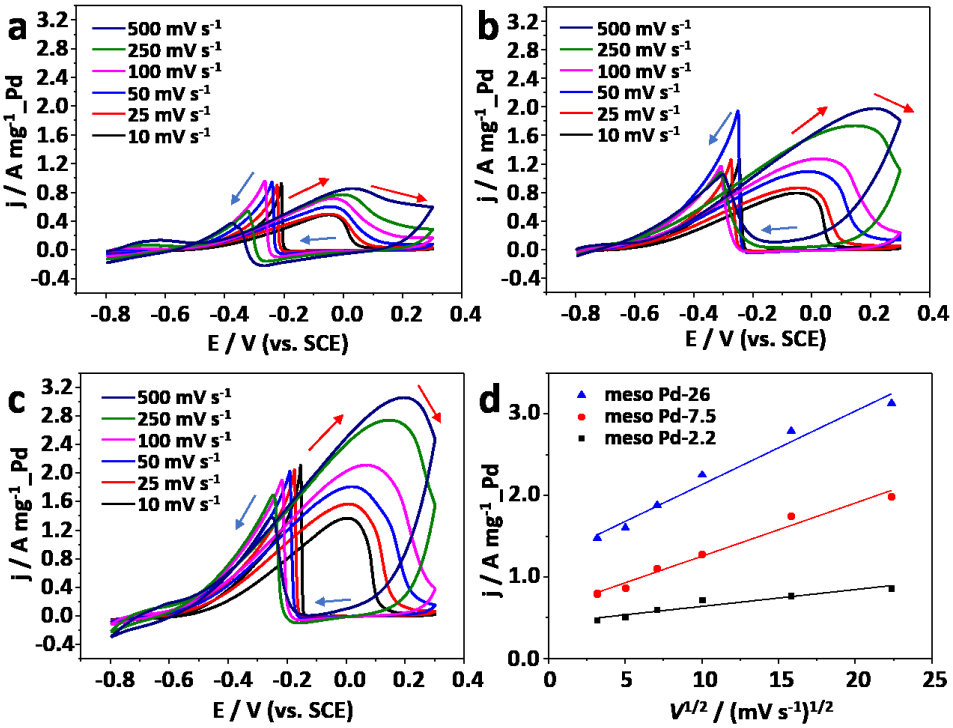

Figure 2.30. (a-c) Cyclic voltammetry of (a) meso Pd-2.2 films, (b) meso Pd-7.5 films, and (c) meso Pd-26 films in 1.0 M KOH containing 1.0 M C_2H_5OH at various scan rate (10, 25, 50, 100, 250 and 500 mV s^{-1}). (d) Forward oxidation peak current density (mass activity) as a function of the square root of the scan rate for meso Pd-2.2, meso Pd-7.5, and meso Pd-26 films. The red and blue arrows in the panel a-c indicates positive and negative scan direction, respectively.

Electrooxidation of small organic molecules by noble metal catalysts is an important reaction in electrochemical energy conversion devices, such as direct alcohol fuel cells.[33] The anodes on such devices typically require highly active and stable catalysts to ensure their good performance and durability towards poisoning reaction intermediate products, such as carbon monoxide (CO), as well as deformation of the surface morphology.[34] In this chapter, we carried out electrocatalytic tests of the meso Pd-2.2, meso Pd-7.5, and meso Pd-26 films towards ethanol oxidation reaction (EOR) as the model reaction. For the performance comparison, non-porous Pd films and commercial PdB were also tested for electrocatalytic EOR. The CV curves were recorded in 1.0 M KOH containing 1.0 M C_2H_5OH at a scan rate of 50 mV s^{-1} in the potential window of -0.8 V - +0.3 V (vs. SCE). All the mass-normalized CV curves clearly show the characteristic of ethanol oxidation peaks in the forward and backward scans (**Figure 2.29c**). The peak

current density (mass-activity) of meso Pd-26 films in positive sweep (1.82 A mg^{-1}_Pd) is larger than those of non-porous Pd films (0.32 A mg^{-1}_Pd), PdB (0.52 A mg^{-1}_Pd), and other mesoporous Pd films samples (meso Pd-2.2 and meso Pd-7.5). In addition, the surface area-normalized cyclic voltammetry shows that the mesoporous Pd films with different average pore size possessed a similar specific activity (**Figure 2.29d**). This implies that the stepped and kinked atomic arrangement of the porous structures is really affecting the electrocatalytic activity of the catalyst.[35]

On the other hand, the large-sized pores provide a better mass transport for the reactants and products from and to the electrolyte. The advantage of large-sized pores of meso Pd-26 films was investigated by carrying out the additional CVs towards ethanol oxidation at a various scan rate (**Figure 2.30a-c)**. The diffusion characteristics of the guest molecule species can be indicated by the relationship between a series of square root scan rate and the mass activity obtained from the CVs of mesoporous Pd films with three kinds of pore sizes at the respective scan rate.[36] The plot slope of forward oxidation peak current densities towards square root of the scan rate of the meso Pd-26 films was larger than those of meso Pd-2.2 and meso Pd-7.5 films (**Figure 2.30d**). This phenomenon suggesting that the diffusion efficiency of ethanol molecules inside the large-sized mesoporous is higher than the relatively smaller pores films structures.[37] Large-sized and open pores features on the meso Pd-26 films shows an improved transport for reactant and products. To assess the electrocatalytic stability, a chronoamperometry test was carried out in 1 M KOH containing 1.0 M C_2H_5OH at a constant potential of -0.1 V (vs. SCE) for 1500 s (**Figure 2.31a**). The current density of meso Pd-26 remains higher than those of non-porous Pd films and PdB even after a long run of stability test. The superior stability of meso Pd-26 can be attributed to the mesoporous architectures which are beneficial for preventing aggregation or morphological deformation of the catalyst (**Figure 2.31b,c**).[38]

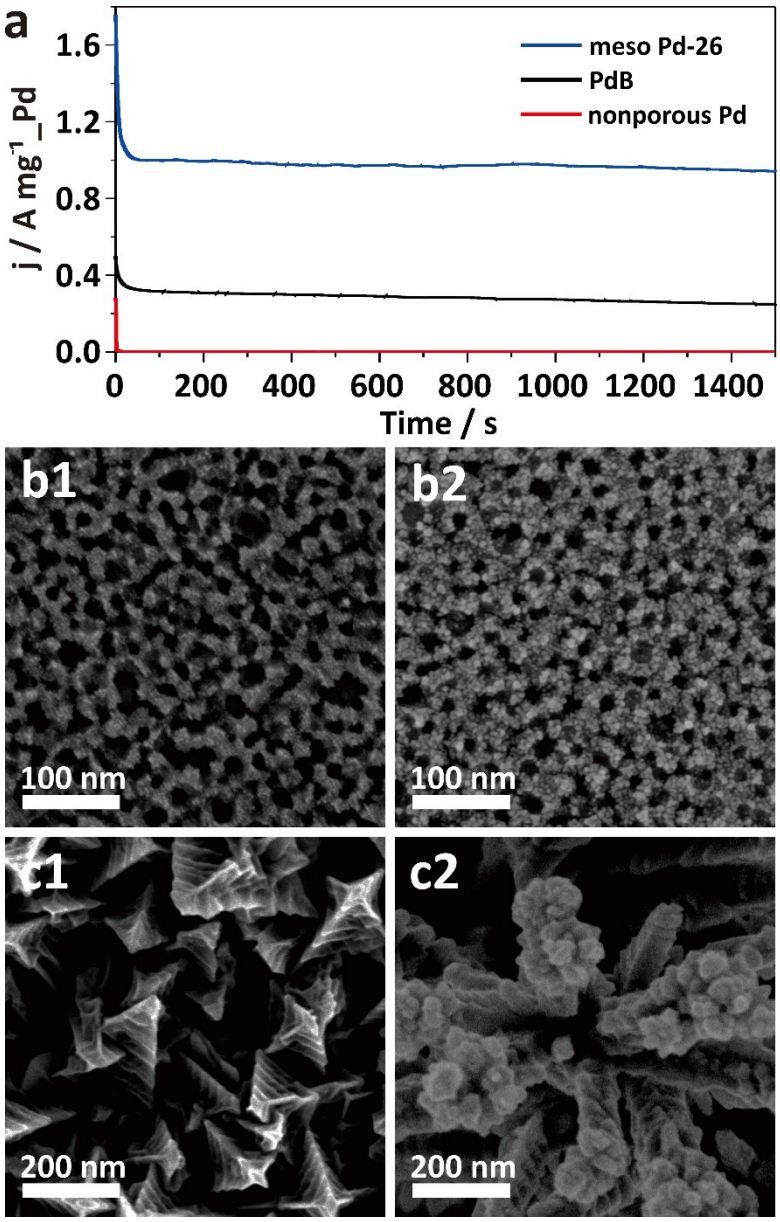

Figure 2.31 (a) Amperometric *i-t* curves at a constant potential of -0.1 V (vs. SCE) for 1500 s in 1.0 M KOH containing 1.0 M C_2H_5OH of non-porous Pd films, commercial PdB, and meso Pd-26 films. SEM images of the (b) meso Pd-26 films and (c) non-porous Pd film obtained in the absence of block copolymer PS-*b*-PEO (b1, c1) before and (b2, c2) after the stability test.

2.2.5. Conclusions

I have prepared continuous mesoporous Pd films with tunable pore size from polymeric micelle assembly through an electrochemical deposition route. The micelles play a critical

role on the formation of the mesoporous structure and the size of the micelles is highly dependent on the molecular weight of the block copolymer, which also determines the pore size of the obtained films. The mesoporous architectures of the as-prepared Pd films lead to enhanced electrocatalytic activity and stability compared to non-porous Pd films and commercial PdB for ethanol oxidation reaction. The proposed approach can be extended to synthesize a wide range of mesoporous films with metallic frameworks for various electrocatalytic applications.

2.2.6. References

[1] J. Tao, J. Xiong, C. Jiao, D. Zhang, H. Lin and Y. Chen, *ACS Sustainable Chem. Eng.*, 2016, **4**, 60.

[2] M. Manzano and M. Vallet-Regi, *J. Mater. Chem.*, 2010, **20**, 5593.

[3] Y. Li, N. Li, W. Pan, Z. Yu, L. Yang and B. Tang, *ACS Appl. Mater. Interfaces,* 2017, **9**, 2123.

[4] C. Perego and R. Milini, *Chem. Soc. Rev.,* 2013, **42**, 3956.

[5] J. Wei, Z. Sun, W. Luo, Y. Li, A. A. Elzatahry, A. M. Al-Enizi, Y. Deng and D. Zhao, *J. Am. Chem. Soc.,* 2017, **139**, 1706.

[6] J. Fan, C. Yu, J. Lei, Q. Zhang, T. Li, B. Tu, W. Zhou and D. Zhao, *J. Am. Chem. Soc.,* 2005, **127**, 10794.

[7] Y. Yamauchi and K. Kuroda, *Chem. Asian J.,* 2008, **3**, 664.

[8] Walcarius, A.; Sibottier, E.; Etienne, M.; Ghanbaja, J. *Nat. Mater.* 2007, **6**, 602.

[9] Y. Yamauchi, A. Sugiyama, R. Ryoichi Morimoto, A. Takai and K. Kuroda, *Angew. Chem. Int. Ed.*, 2008, **47**, 5371.

[10] C. Li, Ö. Dag, T. D. Dao, T. Nagao, Y. Sakamoto, T. Kimura, O. Terasaki and Y. Yamauchi, *Nat. Commun.,* 2015, **6**, 6608.

[11] B. Jiang, C. Li, J. Tang, T. Takei, J. H. Kim, Y. Ide, J. Henzie, S. Tominaka and Y. Yamauchi, *Angew. Chem. Int. Ed.*, 2016, **128**, 10191.

[12] A. S. Nugraha, C. Li, B. Jiang, M. Iqbal, S. M. Alshehri, T. Ahamad, V. Malgras, Y. Yamauchi and T. Asahi, *ChemElectroChem,* 2017, **4**, 2571.

[13] D. Baba, C. Li, V. Malgras, B. Jiang, H. R. Alamri, Z. A. Alothman, M. S. A. Hossain, Y. Yamauchi and T. Asahi, *Chem. Asian J.*, 2017, **12**, 2467.

[14] C. Li, H. Tan, J. Lin, X. Luo, S. Wang, J. You, Y.-M. Kang, Y. Bando, Y. Yamauchi and J. Kim, *Nano Today*, 2018, **21**, 91.

[15] C. Li, M. Iqbal, J. Lin, X. Luo, B. Jiang, V. Malgras, K. C.-W. Wu, J. Kim, and Y. Yamauchi, *Acc. Chem. Res.,* 2018, **51**, 1764.

[16] E. Antolini, *Energy Environ. Sci.,* 2009, **2**, 915.

[17] E. Antolini, S. C. Zignani, S. F. Santos and E. R. Gonzalez, *Electrochim. Acta,* 2011, **56**, 2299.

[18] B. D. Adams and A. Chen, *Mater. Today,* 2011, **14**, 282.

[19] A. Chen, and C. Ostrom, *Chem. Rev.,* 2015, **115,** 11999.

[20] M. Armbrüster, M. Behrens, F. Cinquini, K. Föttinger, Y. Grin, A. Haghofer, B. Klötzer, A. Knop-Gericke, H. Lorenz, A. Ota, S. Penner, J. Prinz, C. Rameshan. Z. Révay, D. Rosenthal, G. Rupprechter, P. Sautet, R. Schlögl, L. Shao, L. Szentmiklósi, D. Teschner, D. Torres, R. Wagner, R. Widmer and G. Wowsnick, *ChemCatChem*, 2012, **4**, 1048.

[21] C. Li, T. Sato and Y. Yamauchi, *Chem. Commun.,* 2014, **50**, 11753.

[22] C. Li, B. Jiang, N. Miyamoto, J. H. Kim, V. Malgras and Y. Yamauchi, *J. Am. Chem. Soc.,* 2015, **137**, 11558.

[23] L. Zhang, J. Zhang, Z. Jiang, S. Xie, M. Jin, X. Han, Q. Kuang, Z. Xie and L. Zheng, *J. Mater. Chem*., 2011, **21**, 9620.

[24] M. Iqbal, C. Li, K. Wood, B. Jiang, T. Takei, Ö.Dag, D. Baba, A. S. Nugraha, T. Asahi, A. E. Whitten, M. S. A. Hossain, V. Malgras, and Y. Yamauchi, *Chem. Mater.,* 2017, **29**, 6405.

[25] K. Yu and A. Eisenberg, *Macromolecules,* 1998, **31**, 3509.

[26] L. I. Elding and L. F. Olsson, *J. Phys. Chem.,* 1978, **82**, 69.

[27] R. J. Deeth and L. I. Elding, *Inorg. Chem.,* 1996, **35**, 5019.

[28] K. Mech, P. Zabinski, R. Kowalik and K. Fitzner, *J. Electrochem. Soc.,* 2013, **160**, H770.

[29] C. Albayrak, A. M. Soylu and Ö.Dag, *Langmuir,* 2008, **24**, 10592.

[30] G. S. Attard, J. M. Corker, C. G. Göltner, S. Henke and R. H. Templer, *Angew. Chem. Int. Ed. Engl.,* 1997, **36**, 1315.

[31] J. M. Elliott, G. S. Attard, P. N. Bartlett, N. R. B. Coleman, D. A. S. Merckel and J. R. Owen, *Chem. Mater.*, 1999, **11**, 3602.

[32] F. Kadirgan, B. Beden, J. M. Leger and C. Lamy, *J. Electroanal. Chem,* 1981, **125**, 89.

[33] B. Cai, S. Henning, J. Herranz, T. J. Schmidt, A. Eychmüller, *Adv. Energy Mater*., 2017, **7**, 1700548.

[34] J. C. Meier, I. Katsounaros, C. Galeano, H. J. Bongard, A. A. Topalov, A. Kotska, A. Karschin, F. Schüth and K. J. J. Mayrhofer, *Energy Environ. Sci.,* 2012, **5**, 9319.

[35] L. P. Ford, P. Blowers and R. I. Masel, *J. Vac. Sci, Technol. A* 1999, **17**, 1705-1709.

[36] Y. Noh, Y. Kim, S. Lee, E. J. Lim, J. G. Kim, M. S. Choi, M. H. Seo, W. B. Kim, *Nanoscale*, 2015, **7**, 9438-9442.

[37] D. Wen, A. -K. Herrmann, L. Borchardt, F. Simon, W. Liu, S. Kaskel and A. Eychmüller, *J. Am. Chem. Soc.*, 2014, **136**, 2727.

[38] C. Zhu, D. Du, A. Eychmüller and Y. Lin, *Chem. Rev.,* 2015, **115**, 8896.

Chapter 3

3. Mesoporous PdCu Films with Vertically Aligned Mesochannels

3.1. Introduction

Mesoporous materials are promising platform for many applications, such as catalysis, energy conversion and storage, sensing, drug delivery, and adsorber.[1-4] In particular, mesoporous metals films have the potential to enhance the oxidation reactions of small molecules and oxygen reduction reactions by combining high catalytic activity and high surface area.[5-7] Mesoporous metal films with ordered mesochannels promoting the transport of guest molecule species are still challenging to design and fabricate. Especially, a well-ordered perpendicular mesochannels structure is expected to provide short migration distances for the reactant and products and increase the diffusion rate of guest molecule species.[8-10] However, the possible compositions are very limited to metal oxides and carbons.

So far, common approaches to fabricate mesoporous metal films have relied on hard-templating methods.[11,12] Unfortunately, these techniques require much effort to grow the metallic frameworks or metallic nanoparticles on the templates while maintaining both the mesostructure and the morphology. Metallic films with uniform mesopores can be fabricated through liquid crystals-[13,14] or micelles-assisted electrodeposition[15-18], yielding pores with a mean size within the range of 2-25 nm. Mesoporous Au, Pt, and Pd films have been reported to showcase better performance towards electrooxidation reaction.[15,17-18] Soft-templating methods are more favorable due to their simplicity; they can be summed up in only two steps: direct grow of the metallic framework and template removal.

As the second most active noble metal-based electrocatalyst (after Pt), the abundance of Pd makes it more suitable for further commercialization for low-temperature fuel cells, such as direct alcohol fuel cells (DAFCs).[19,20] Unfortunately, generation of intermediate products during the electrooxidation reaction of small molecules leads to poisoning effect which generally limits the activity and stability of Pd-based catalysts.[21] Alloying Pd with a second metal (such as Pt, Au, Ir, *etc*.) is effective in reducing the adsorption of intermediate reaction products onto the catalyst surface.[22-24] Cu is another secondary component from 3*d* transition metals which also has the potential to provide a cost-effective materials while enhancing catalytic activity and stability of Pd-based electrocatalysts. Both experimental and theoretical study reveal strong Cu-Pd interactions and the capability of bimetallic PdCu alloy to resist contamination.[25-27] However, the

fabrication of bimetallic PdCu alloy films with ordered mesochannels has been never reported.

Herein, I combine the advantages of both the *bimetallic alloy* and the *perpendicular mesochannels structure*, which not only lead to enhance electrocatalytic activity and stability, but also to increase the diffusion rate of guest molecule species. Although the previous study reported vertical orientation of mesochannels in mesoporous Pd films using cationic surfactants[17], in the present study I extended this concept to other types of surfactants to apply mesoporous alloy systems. I successfully prepared the PdCu films with mesochannels vertically-aligned on the substrate by simple nonionic surfactant (Pluronic P123) micelles-assisted electrodeposition from aqueous electrolyte solutions. The electrocatalytic activity as-deposited films were studied towards ethanol oxidation as the model reaction. The synthesis of mesoporous PdCu films was carried out based on electrochemical deposition technique from nonionic micellar solution (**Scheme 3.1**).

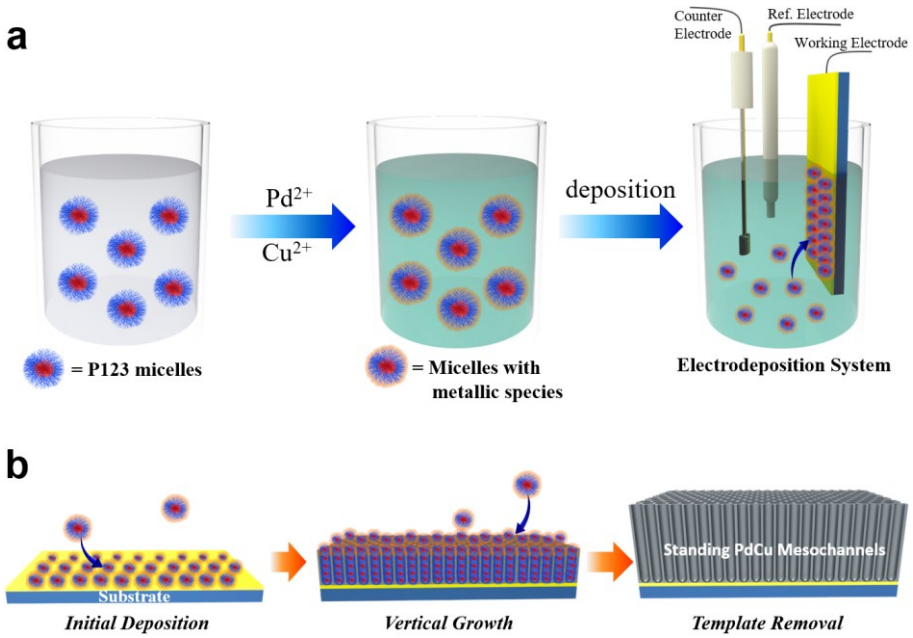

Scheme 3.1 Scheme illustrating the formation mechanism of vertically-aligned mesochannel PdCu films. (a) Micelle formation and 3-electrodes system for electrocdeposition system. (b) Growth of PdCu vertical mesochannels by micelles decorated with Pd and Cu metal species.

3.2. Experimental Section

3.2.1. Materials

Pluronic P123 and palladium black (PdB) were obtained from Sigma-Aldrich (USA). Ethanol and sulfuric acid were purchased from Nacalai Co. (Japan). Palladium(II) chloride, copper(II) sulfate and potassium hydroxide was obtained from Wako Chemicals (Japan). All the chemicals were used without any prior treatment. Double distilled water with specific resistivity of 18.2 MΩ cm was provided by Merck Milli-Q® water purification system.

3.2.2. Synthesis of Mesoporous PdCu Films with Vertically Aligned Mesochannels

All potential values in this chapter are reported (*vs*. Ag/AgCl), unless specified. Electrochemical deposition of mesoporous PdCu films was conducted utilizing an electrochemical station (CHI 842B electrochemical analyzer, CHI Instruments, USA). The conventional three-electrode system was employed: Au-coated Si wafer substrate (3 mm x 15 mm), Ag/AgCl electrode and Pt wire were used as the working, reference and counter electrode, respectively. Firstly, 80 mM $PdCl_2$ solution and 80 mM $CuSO_4$ solution were prepared as stock solutions for preparation of the electrolytes (It is noted that a few drops of 2 M HCl solution were added to avoid the precipitation.). The electrolyte solutions consisted of a nonionic micellar solution prepared by dissolving 2.0 wt% P123 (cmc 0.18 wt% at 293K) along with the metal precursors in water. The total concentration of the metal precursors was fixed to 40 mM. To optimize the system, various Pd:Cu molar ratios (90:10, 80:20, 70:30, 60:40, and 50:50) and deposition times (50, 100, 150, and 200 s) were tested, while the applied deposition potential was fixed at -0.4 V. To remove the soft-templates, the as-deposited mesoporous PdCu films were rinsed thoroughly with double distilled water and dried under nitrogen gas flow. The obtained films were kept for further characterizations and electrochemical measurements. Mesoporous Pd films (without Cu) and nonporous PdCu films (without P123) were also fabricated for comparison.

3.2.3. Characterizations

The morphology of the mesoporous PdCu films was examined by field emission scanning electron microscopy (FESEM; Hitachi SU-8230 at accelerating voltage of 5 kV). Transmission electron microscope (TEM), high-resolution TEM (HRTEM), high-angle

angular dark-field (HAADF) images and energy dispersive X-ray (EDX) mapping were obtained with a JEOL JEM-2100F at an accelerating voltage of 200 kV. Wide-angle X-ray diffraction (XRD) pattern were acquired with a Rigaku SmartLab XRD equipped with Cu Kα X-ray source. 2D profile grazing-incidence small-angle X-ray scattering (GI-SAXS) was collected with a Rigaku NANO-Viewer (Microfocus rotating anode; Cu Kα radiation; 40 kV, 30 mA) equipped with a camera length of 680 mm. Ultraviolet-visible (UV-Vis) absorption spectroscopy of the electrolyte solutions was performed by a JASCO V-7200. The surface elemental composition and electronic coordination state of the as-prepared PdCu films were analyzed by X-ray photoelectron spectroscopy (XPS; PHI Quantera SXM; ULVAC-PHI; Al Kα radiation). All XPS spectra were calibrated to the C1s peak at 285.0 eV. To gather information about molar ratio on the final PdCu films product, inductively coupled plasma optical emission spectroscopy (ICP-OES) was carried out on a Hitachi model SPS3520UV-DD.

3.2.4. Electrochemical Measurement

All the electrochemical measurements were recorded on a CHI 842B electrochemical analyzer (CH Instrument, USA) with standard three-electrode system. As-deposited PdCu films on Au-coated Si substrate was employed as the working electrode. The Ag/AgCl electrode and standard calomel electrode (SCE) were used as the reference electrode in acidic medium and basic medium electrolyte, respectively. A Pt wire was utilized as the counter electrode. Cyclic voltammograms (CV) were recorded in 0.5 M H_2SO_4 electrolyte at a scan rate of 50 mVs^{-1} between -0.2 and +1.2 V. The electrocatalytic performance toward ethanol oxidation reaction was recorded in 1.0 M KOH containing 1.0 M C_2H_5OH in the potential range from -0.8 to 0.3 V (*vs*. SCE). All the CV measurements were repeated 3 times for each sample. Amperometric *i-t* curves were recorded at a fixed potential of -0.2 V (*vs*. SCE) for 1,200 s in 1.0 M KOH containing 1.0 M C_2H_5OH to study the stability. Other working electrodes were prepared for performance comparison: mesoporous Pd and nonporous PdCu films deposited on Au-coated Si substrate and commercial palladium black (PdB). 5 μL of 1 mg mL^{-1} PdB was drop-cast on a polished glassy carbon electrode (GCE) followed by coating with Nafion® resin solution and dried in atmospheric ambient prior to electrochemical measurement.

3.3. Characterization of Mesoporous PdCu Films with Vertically Aligned Mesochannels

The conventional three-electrode system was employed: Au-coated Si wafer substrate, Ag/AgCl electrode and Pt wire were used as the working, reference and counter electrode, respectively. The electrolyte solution consisted of a nonionic micellar solution prepared by dissolving 2.0 wt% P123 (cmc 0.18 wt% at 293K) along with the metal precursors ($PdCl_2$ and $CuSO_4$) in double distilled water. To optimize the system, various Pd:Cu molar ratios (90:10, 80:20, 70:30, 60:40, and 50:50) and deposition times (50, 100, 150, and 200 s) were tested, while the applied deposition potential was fixed at -0.4 V. To remove the soft-templates, the as-deposited mesoporous PdCu films were rinsed thoroughly with double distilled water and dried under nitrogen gas flow. For comparison, mesoporous Pd films (without Cu) and nonporous PdCu films (without P123) were also fabricated (**Figure 3.1**).

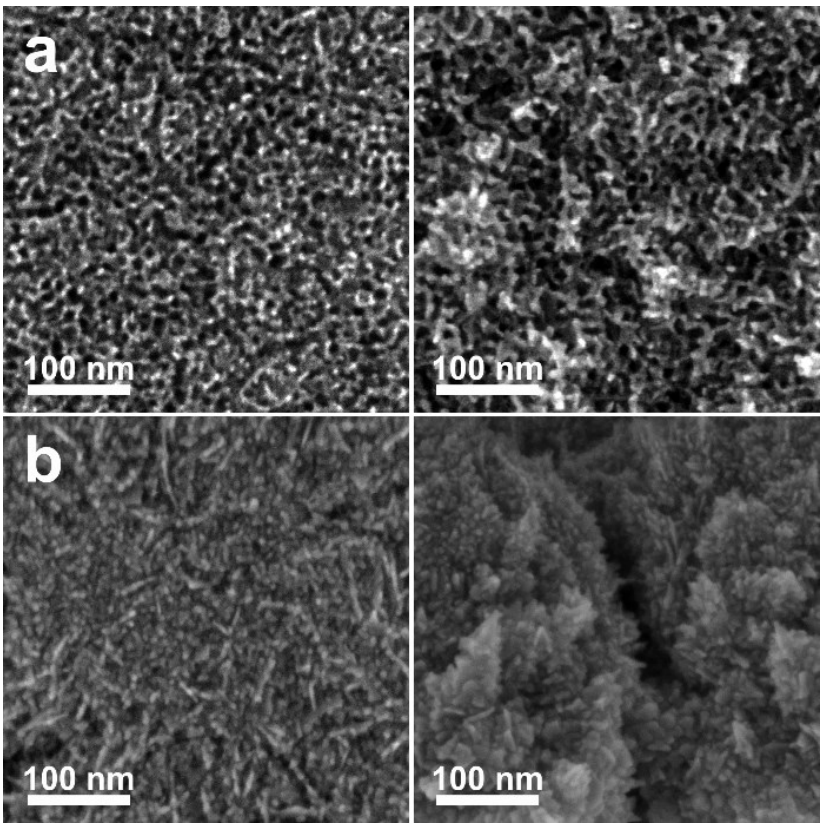

Figure 3.1 Top-view (left) and cross-sectional (right) SEM images of (a) mesoporous Pd films and (b) nonporous $Pd_{81}Cu_{19}$ films.

According to scattering data obtained by SANS, it was proved that the nonionic surfactant Pluronic P123 formed spherical-shaped micelles in water with an average diameter *ca*. 13 nm (**Figure 3.2**).[16] The micelle core consisted of a hydrophobic moiety (PPO block) and its shell of a hydrophilic moiety (PEO block). Even after addition of metal precursors, the average diameter of the spherical-shaped micelles did not change significantly. To study the interactions between solvent, micelles, and metal precursors interaction, optical absorption spectroscopy was carried out on various aqueous solutions (**Figure 3.3**). The UV-Vis absorption study showed the existence of two metal-aqua complexes: $[Cu(H_2O)_x]^{2+}$ ions and $[PdCl_{4-x}(H_2O)_x]^{(-2+x)}$ ions where which the Cl^- ions are exchanged with the water molecules. These water-coordinated Pd and Cu ions in the electrolyte solutions were interacted with the PEO groups of micelles through hydrogen bonding.

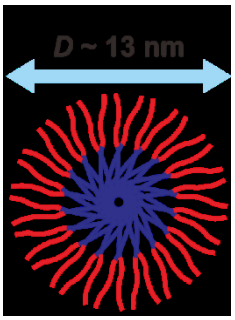

Figure 3.2 Schematic model representing P123 micelles in water.

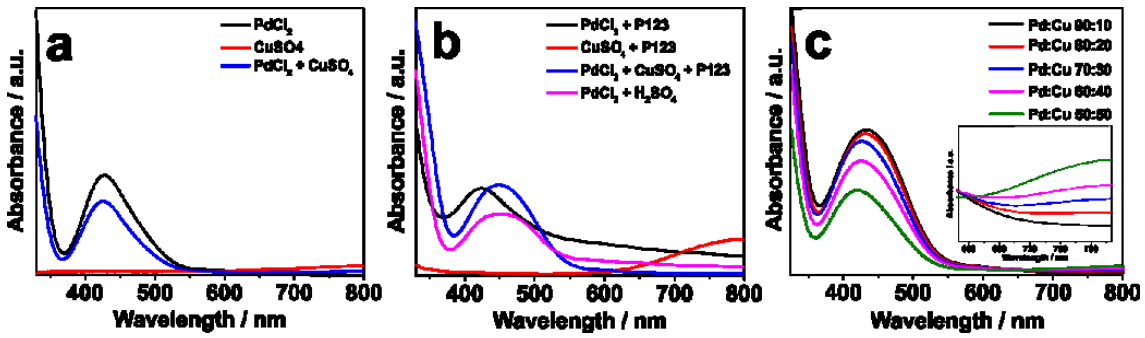

Figure 3.3 UV-Vis absorption spectra of the (a) aqueous solutions containing $PdCl_2$, $CuSO_4$ and $PdCl_2 + CuSO_4$, (b) aqueous solution containing $PdCl_2$, $CuSO_4$ and $PdCl_2 + CuSO_4$ with P123, and $PdCl_2$ with the addition of an acid, and (c) aqueous solutions containing $PdCl_2$ and $CuSO_4$ with P123 at various Pd:Cu molar ratios. Inset on panel (c) shows the increasing absorption around 800 nm as the Cu content is increased.

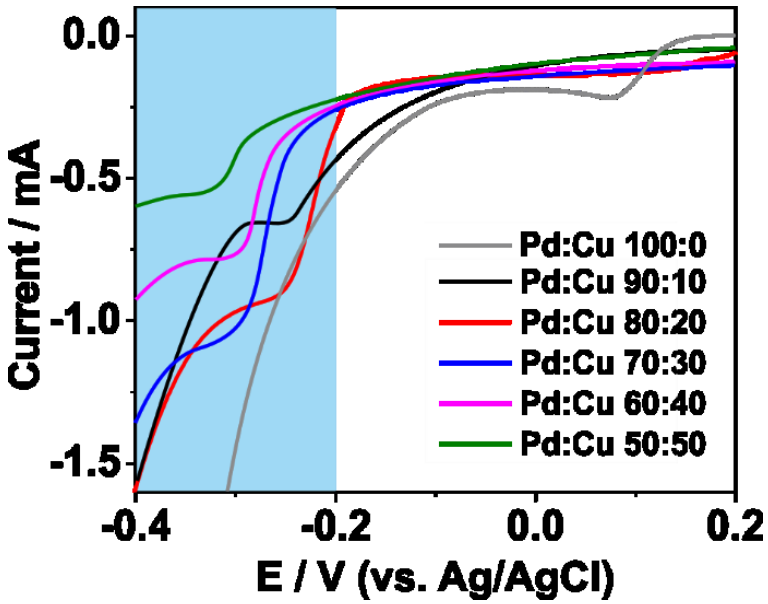

Figure 3.4 LSV curves with the Au-coated Si substrate as the working electrode (geometrical area of 0.18 cm^2) recorded at a scan rate of 10 mV s^{-1} from electrolyte solutions containing micelles and various Pd:Cu precursors molar ratios. The precursors concentration in the electrolyte solutions were fixed at 40 mM.

The potential applied during the electrodeposition of mesoporous PdCu films was determined after studying the reduction potential of Pd and Cu ions in the electrolyte solution by linear sweeping voltammetry (LSV) (**Figure 3.4**). In the previous chapter, it was found that the reduction potential to carry out the reduction of Pd ions into Pd(0) in an electrolyte solution containing micelles was around 0.0 V.[16] In accordance to the LSV plot in **Figure 3.4**, the reduction of Pd and Cu ions into PdCu alloys started at *ca*. -0.2 V. The formation of hydrogen bubbles was observed beyond -0.4 V. The electrodeposition of PdCu films was then carried out at -0.2 V, -0.3 V, and -0.4 V to ensure the reduction of both Pd and Cu precursor, as well as to avoid detrimental effects caused by the generation of hydrogen bubbles on the film structure. The optimal deposition voltage was selected after observing the morphology of the films from cross-sectional and top scanning electron microscope (SEM) images and grazing-incidence small angle X-ray scattering (GI-SAXS) (**Figure 3.5**). The SEM images reveal that carrying out the deposition at -0.4 V leads to a smooth and uniform structure (**Figure 3.6a-b**), unlike the films deposited at -0.2 and -0.3V (**Figure 3.5**). The 2D scattering profiles of the films deposited at -0.2 V and -0.3 V show half ring pattern, which indicates that the pores were randomly packed, while clear spots could be observed on the left and right side of the beam for the film deposited at -0.4 V, indicating a well-ordered mesochannels vertically-aligned on the substrate (The detailed

discussion on the obtained GI-SAXS spots is given in a later section.).[28,29] Cross-sectional TEM and HAADF-STEM images of mesoporous the $Pd_{81}Cu_{19}$ film show that all the mesochannels are standing on the substrate (**Figure 3.6c-d**).

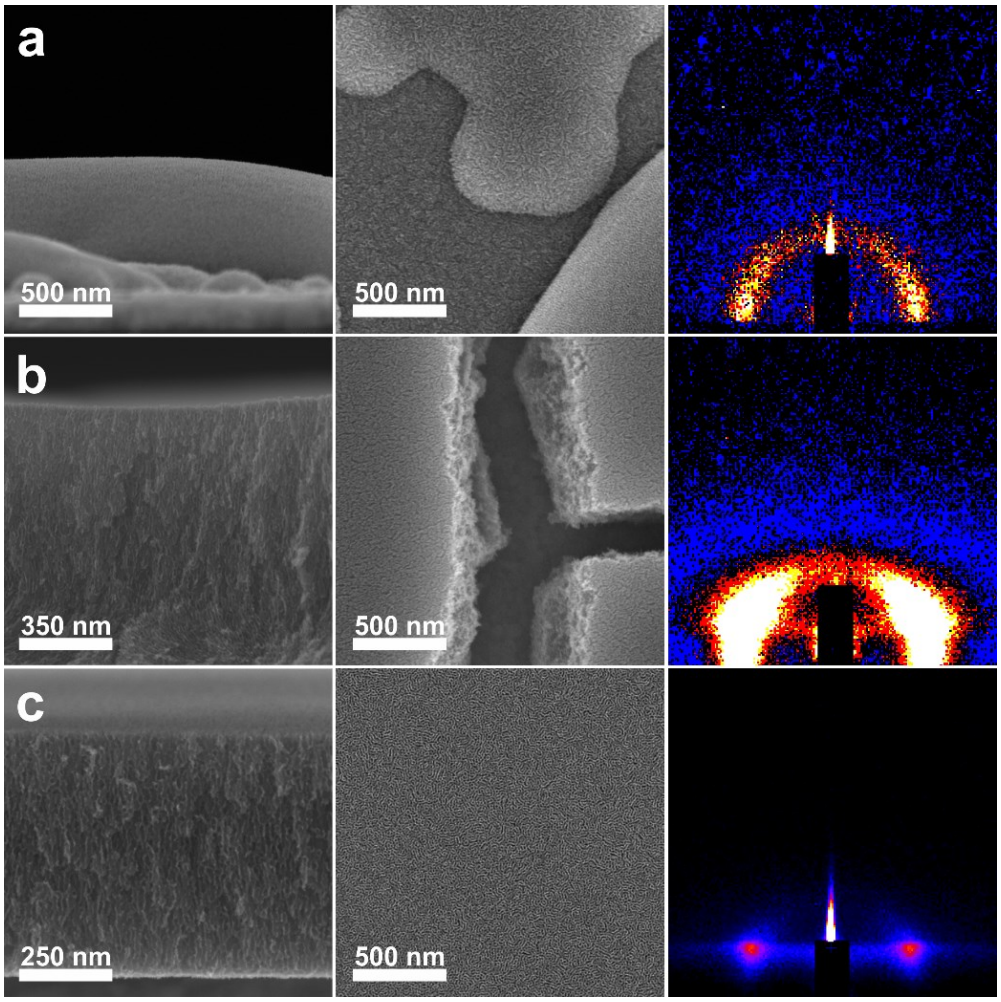

Figure 3.5 Cross-sectional (left panel), low-magnification top-view SEM images (center panel) and corresponding 2D profile GI-SAXS pattern (right panel) of the mesoporous $Pd_{81}Cu_{19}$ films deposited at (a) -0.2 V, (b) -0.3 V, and (c) -0.4 V, respectively.

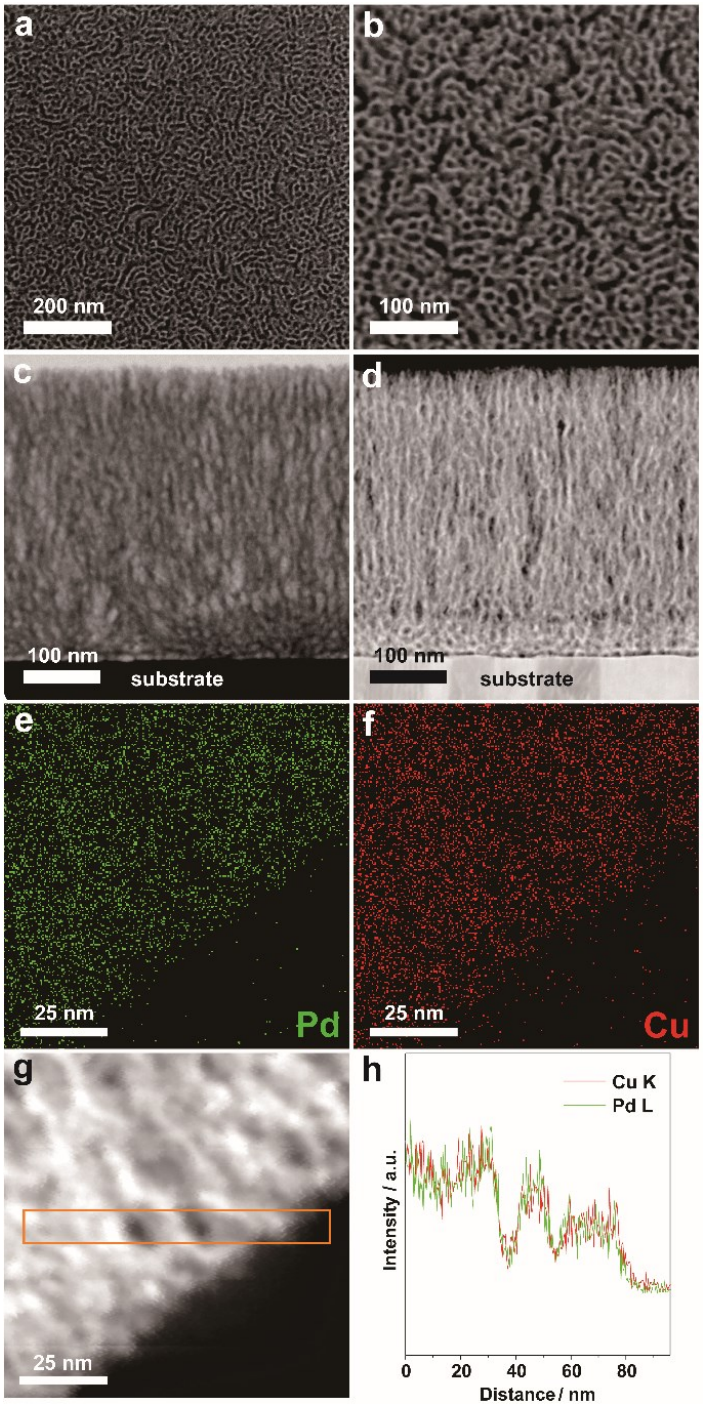

Figure 3.6 (a, b) Top view SEM images with different magnifications, (c) TEM and (d) HAADF-STEM cross-sectional images of the mesoporous $Pd_{81}Cu_{19}$ film with mesochannels aligned perpendicularly to the substrate. (e, f) Elemental mapping images, (g) HAADF-STEM image, and (h) line-scanning compositional profile of the mesoporous $Pd_{49}Cu_{51}$ films from the rectangle area indicated in (g).

Table 3.1. Summary of Pd and Cu molar ratio in both the precursor electrolytes and the films. Inductively coupled plasma optical emission spectroscopy (ICP-OES) was utilized to measure accurately the mass of Pd and Cu in the final films.

Sample	Molar Ratio of Pd:Cu in the Electrolyte Solution	Molar Ratio of Pd:Cu on the Deposited Films
$Pd_{91}Cu_9$	90:10	91:9
$Pd_{81}Cu_{19}$	80:20	81:19
$Pd_{71}Cu_{29}$	70:30	71:29
$Pd_{59}Cu_{41}$	60:40	59:41
$Pd_{49}Cu_{51}$	50:50	49:51

My method enables a simple and accurate approach to tune the metal composition of the final film, which was found to closely match the initial precursor molar ratio (**Table 3.1**). Mesoporous PdCu films deposited at -0.4 V were synthesized with different Pd:Cu molar ratios. According to ICP-OES results, the samples designated as Pd_xCu_{100-x}, where x and 100-x correspond to the percentage of Pd and Cu, respectively. It is worth mentioning that the film thickness can simply be tuned by changing the deposition time without affecting the integrity of the mesoporous structure (**Figure 3.7**). The top-view of the mesoporous Pd_xCu_{100-x} films observed by SEM reveal pores distributed uniformly through the entire surface (**Figure 3.6a-b, Figure 3.8**). The average pore size, statistically calculated from over than 100 pores, was found to range between 7 and 9 nm. GI-SAXS was further employed to characterize the pore ordering and periodicity of the films with various Pd:Cu ratios. The half ring (halo) observed on the 2D scattering profile of the pure Pd film indicates the existence of isotropic periodicity, while the two spots observed for the alloyed films suggest that the mesochannels are aligned perpendicularly to the substrate (**Figure 3.9**).[28,29] Samples showing spots overlapping with a pseudo-half ring consist of aligned channels with a mild degree of isotropy. Since mass transport is expected to be favored in well-aligned mesochannels, electrocatalytic activity should decrease as the degree of isotropy is increased. The converted 2D scattering (in-plane) profiles of each mesoporous Pd_xCu_{100-x} films samples showed a distinct peak located between q = 0.4 and 0.5 nm^{-1} (**Figure 3.9**). Although all the mesochannels in the alloyed films are vertically aligned, the in-plane ordering is not perfectly arranged. Therefore, the resulting pore-to-pore distance can be roughly estimated from the d values of the in-plane spots. The pore-to-pore distance are 12.4, 12.4, 12.6, 13.0, and 13.3 nm for $Pd_{91}Cu_9$, $Pd_{81}Cu_{19}$, $Pd_{71}Cu_{29}$,

$Pd_{59}Cu_{41}$, and $Pd_{49}Cu_{51}$, respectively. These values are matched with the top-surface SEM images (**Figure 3.8**).

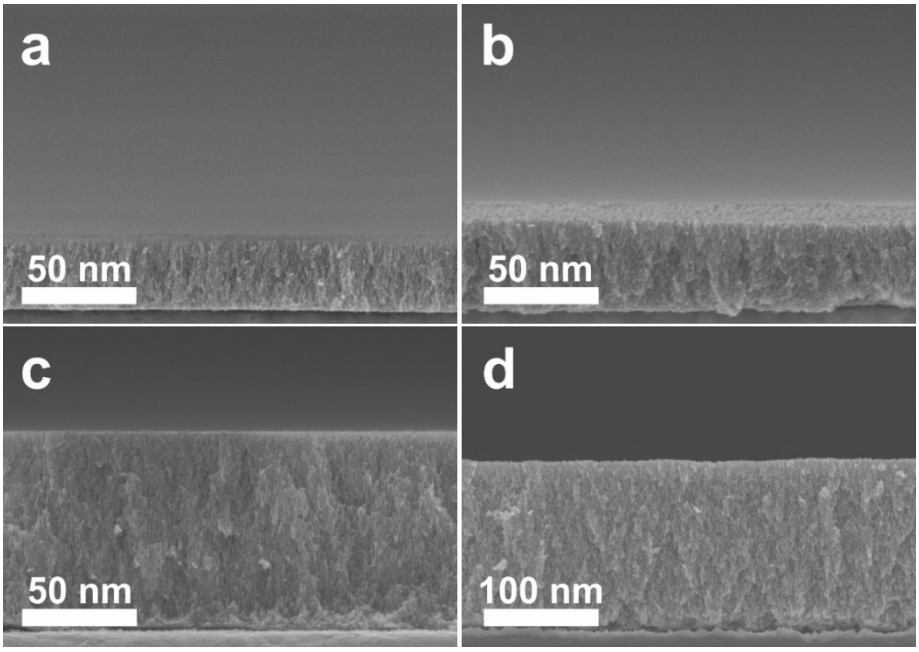

Figure 3.7 Cross-sectional SEM images of mesoporous $Pd_{81}Cu_{19}$ films deposited with various deposition times: (a) 50 s, (b) 100 s, (c) 200 s, and (d) 400 s.

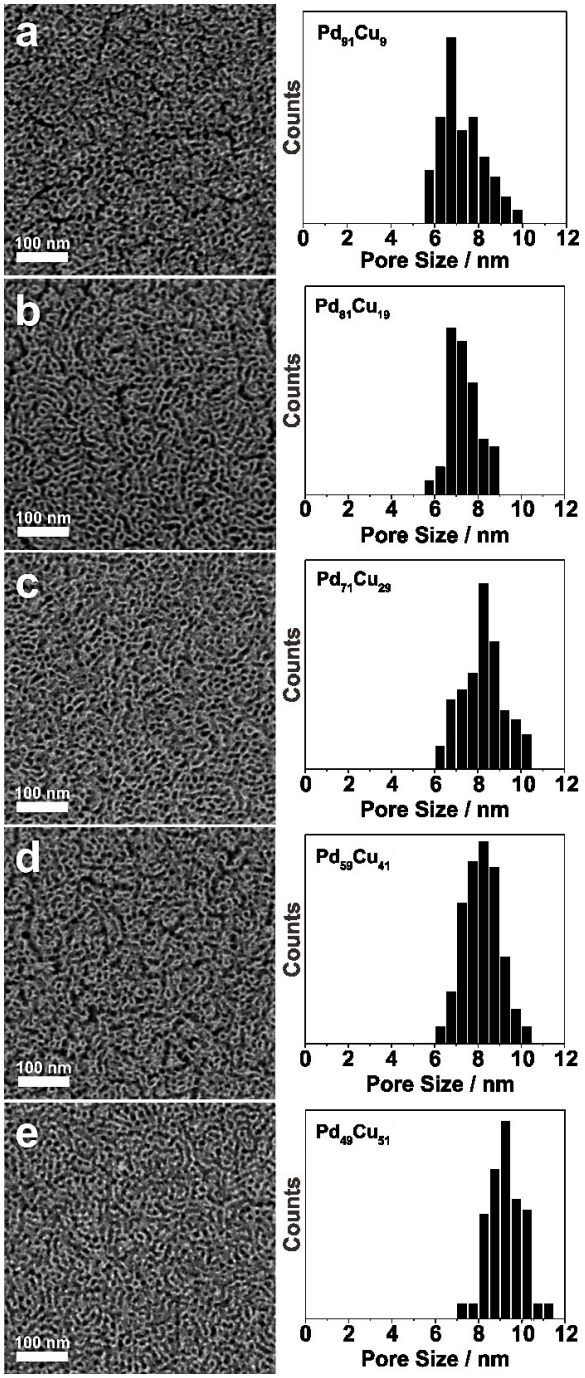

Figure 3.8 Top view SEM images (left) and pore size distribution histogram (right) of the mesoporous (a) $Pd_{91}Cu_9$, (b) $Pd_{81}Cu_{19}$, (c) $Pd_{71}Cu_{29}$, (d) $Pd_{59}Cu_{41}$, and (e) $Pd_{49}Cu_{51}$ films.

In light of these results, I propose the following mechanism for the formation of mesochannels in the PdCu films: The hydrophobic moiety of P123 in the electrolyte solution maintains the stability of the micelles, while the hydrophilic moiety can solvate or attract the metal ion complex species through hydrogen-bonding (-CH_2CH_2O-…H_2O-Cu(II) or -CH_2CH_2O-…H_2O-Pd(II)) and electrostatic interactions. Notice also that the pH of the solution is around 2 that means the SO_4^{2-} ion is protonated, HSO_4^- ion, that is chaotropic and further enhances the micellization of P123 (increases the micelle concentration in the media). Since the charge of the Pd(II) complexes vary from 2- to 2+ with increasing water in the coordination sphere and also the Cu^{2+} ion coordination sphere is water, the presence of coordinated water is important for the assembly and also for interaction of metal ions with the ethylene oxide domains for accumulating metal ions (Pd(II) as well as Cu(II)) in and around the micelles. When a potential is applied on the Au-coated Si substrate (working electrode), the generated electromotive force attracts the Pd(II)/Cu(II) complex ions (along with the micelles) towards the working electrode, where they are reduced to their metallic state. As a summary, the water-rich complex are positively charged and attracted by the micelles and therefore the negatively charged Cl^--rich (Pd(II)) complexes are attracted by the positively charged water-rich complexes through electrostatic interactions to enhance the Pd(II) and Cu(II) species in and around the micelles for electrodeposition of Pd(0) and Cu(0). The basis for the reductive and transformative reaction is the current, which passed through the working electrode.[30] Note that the applied deposition potential in this chapter was -0.4 V *vs.* Ag/AgCl. The standard reduction potentials of $[PdCl_4]^{2-}$/Pd and Cu^{2+}/Cu are 0.591 and 0.342 V *vs*. SHE, respectively.[31] The PdCu alloy films are electrochemically deposited on the substrate and the mesochannels form around the micelles, as shown in **Scheme 3.1**.

During the metallic growth, the spherical micelles fuse together to form cylindrical micelles, hence leading to the assembly of mesochannels aligned perpendicularly to the substrate. In general, the fusion of spherical triblock copolymer micelles into rod-like micelles is affected by the temperature and the quality of the solvent (*i.e.*, addition of ethanol, acid, and salts).[32] In some cases, the spherical-to-rod micelles transition can be observed by adjusting the polymer-to-precursors ratio.[33] However, in the present study, the sphere-to-rod micelles transition does not seem to be affected by these factors. As shown in **Figure 3.5**, the quality of the mesoporous structures is mostly affected by the deposition potential. At low voltage (slow deposition rate), the micelles tend to remain spherical. Therefore, it is assumed that the fusion of spherical micelles into rod-like micelles occurs

at faster deposition rate (-0.4 V). In addition, the hydrophobicity of the substrate is expected to suppress any possible interactions with the hydrophilic moiety of the micelles, thus accommodating the growth of the mesochannels along the vertical direction.[28,29] The Pd-Cu alloy state in the framework were confirmed by X-ray diffraction (XRD) patterns, X-ray photoelectron spectroscopy (XPS), and elemental mapping (**Figures 3.10-3.13, Table 3.1**). The Pd and Cu elements are spread throughout the metallic pore walls, as confirmed by energy dispersive X-ray (EDX) elemental mapping and line-scanning compositional profile (**Figure 3.6e-h**).

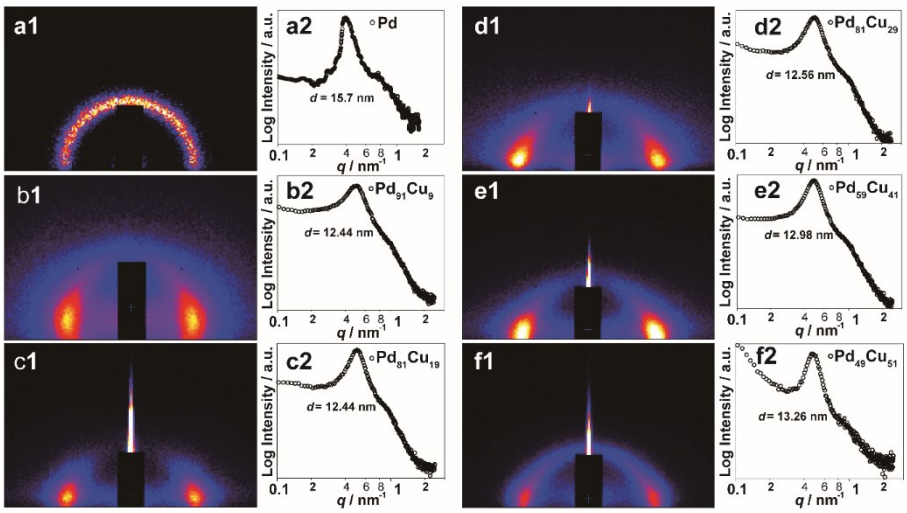

Figure 3.9 (a1-f1) 2D scattering profiles and (a2-f2) in-plane converted profiles of the mesoporous Pd_xCu_{100-x} films obtained by GI-SAXS.

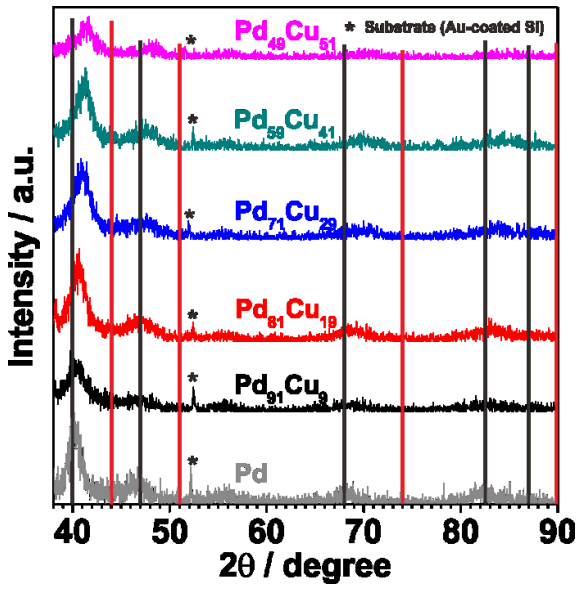

Figure 3.10 Diffraction patterns of the mesoporous Pd_xCu_{100-x} films.

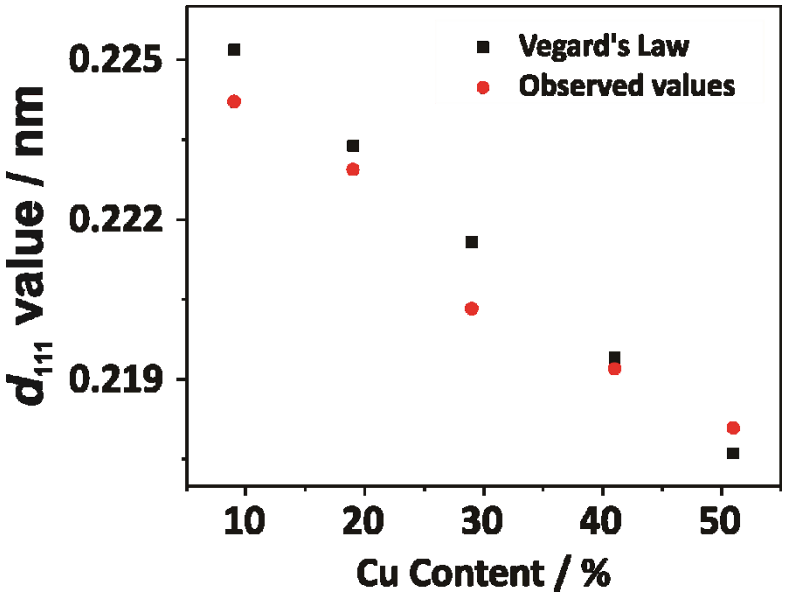

Figure 3.11 Relationship between the Cu content in the as-deposited films and the *d*-spacings according to the Vegard's Law and the XRD diffraction patterns.

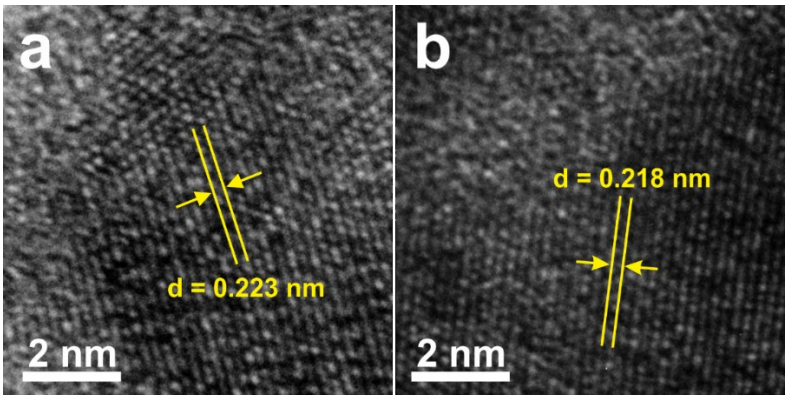

Figure 3.12 HRTEM images of the mesoporous (a) $Pd_{81}Cu_{19}$ and (b) $Pd_{49}Cu_{51}$ films.

Notes for Figure 3.10-3.12 and Table 3.1:

X-ray diffraction (XRD) patterns highlight the presence of a single-phase metallic PdCu alloy (**Figure 3.10**). The four main peaks observed can be assigned to the (111), (200), (220), and (311) diffraction planes of the *fcc* PdCu. Importantly, the first diffraction peak of Pd_xCu_{100-x}, corresponding to the (111) plane, is gradually shifted towards larger angle as the Cu content is increased. This implies that substituting Pd for Cu atoms with smaller nuclei tends to shrink the average unit cell volume. It was found that the lattice parameter of the PdCu alloy has a close-to-linear dependence on the concentration of the constituent

elements, which agrees well with the expected Vegard's law (**Figure 3.11**). The metallic pore walls consist of alloyed PdCu nanocrystals with sizes estimated between 3.6-5.5 nm according to the Scherrer equation, which agrees with the high resolution TEM (HRTEM) observations (**Table 3.1** and **Figure 3.12**). The Pd and Cu elements are spread throughout the metallic pore walls, as confirmed by energy dispersive X-ray (EDX) elemental mapping and line-scanning compositional profile (**Figure 3.6e-h**).

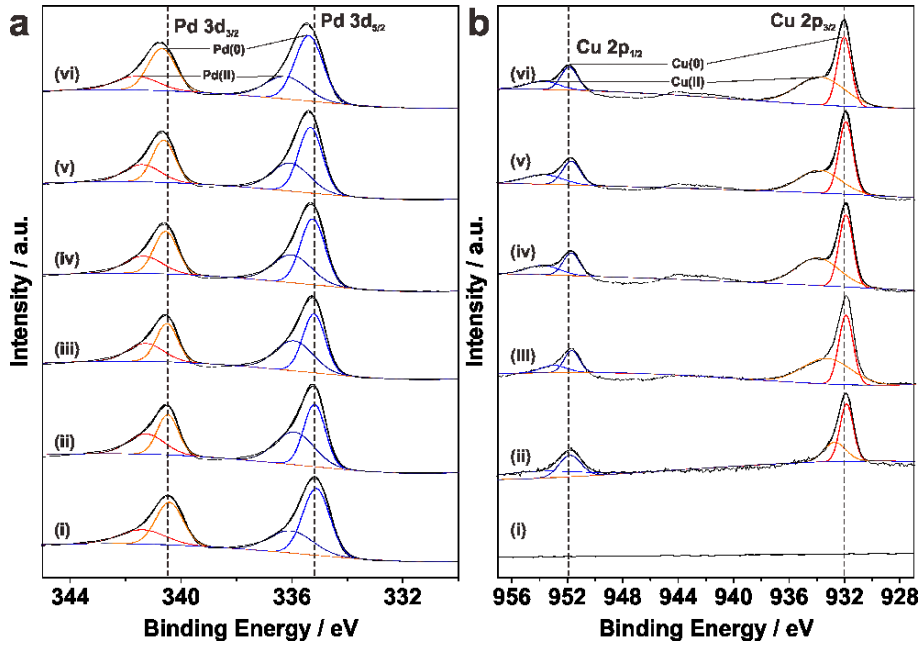

Figure 3.13 High resolution (a) Pd 3d and (b) Cu 2p XPS spectra of the (i) mesoporous Pd, (ii) $Pd_{91}Cu_9$, (iii) $Pd_{81}Cu_{19}$, (iv) $Pd_{71}Cu_{29}$, (v) $Pd_{59}Cu_{41}$, and (vi) $Pd_{49}Cu_{51}$ films.

Notes for Figure 3.13:

Investigating the oxidation states present in an alloy, *e.g.* using X-ray photoelectron spectroscopy (XPS), is critical in order to determine the interactions between each constituent. **Figure 3.13** shows the high-resolution Pd 3*d* and Cu 2*p* XPS spectra of the mesoporous Pd_xCu_{100-x} films. Core-levels Pd 3*d* and Cu 2*p* spectra from all samples comprised of two main doublets. The Pd $3d_{5/2}$ and Pd$3d_{3/2}$ peaks are shifted towards higher binding energy as the Cu content increases. The two peaks centered at around 932 eV and 952 eV belong to Cu $2p_{3/2}$ and Cu $2p_{1/2}$, respectively (**Figure 3.13b**). These results suggest that charge transfer occurs from Cu to Pd, thus shifting their respective *d*-band centers and enabling different properties related to the oxidation of fuel molecules, such as the adsorption of intermediate reaction products on the catalyst surface.

3.4. Electrocatalytic Activity of Mesoporous PdCu Films with Vertically Aligned Mesochannels

The electrochemical active surface area (ECSA) of Pd-based electrocatalysts can be estimated by cyclic voltammetry (CV) and CO-stripping experiment (**Figures 3.14-3.15** and **Table 3.2**). The catalyst films were studied for the electrooxidation reaction of ethanol molecules. On the Pd mass-normalized CV curve of the mesoporous alloyed films shown in **Figure 3.16a**, the clear anodic peaks observed in the forward scan are a signature of the oxidation of chemisorbed ethanol.[34] The $Pd_{81}Cu_{19}$ film did not only show superior mass-normalized peak current density (2.77 A mg^{-1}) compared to the other alloyed films, but also compared to the three control and benchmark samples: mesoporous Pd films (1.75 A mg^{-1}), nonporous $Pd_{81}Cu_{19}$ films (1.01 A mg^{-1}), and PdB (0.71 A mg^{-1}) (**Figure 3.16a**). Even when normalized by their respective surface area, the mesoporous $Pd_{81}Cu_{19}$ film still exhibited the highest peak current density among the all (**Figure 3.16b**). The onset potential of the mesoporous $Pd_{81}Cu_{19}$ film measured by linear sweep voltammetry (LSV) was more negative than the control and benchmark samples (**Figure 3.17**), showcasing the importance of both the bimetallic synergy and the aligned mesochannels in enhancing ethanol oxidation activity.

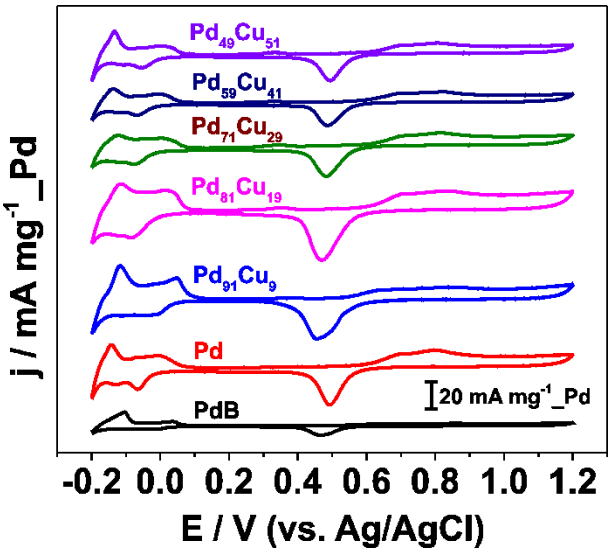

Figure 3.14 CV curves of PdB, mesoporous Pd and Pd_xCu_{100-x} films in 0.5 M H_2SO_4 obtained at a scan rate of 50 mVs^{-1}.

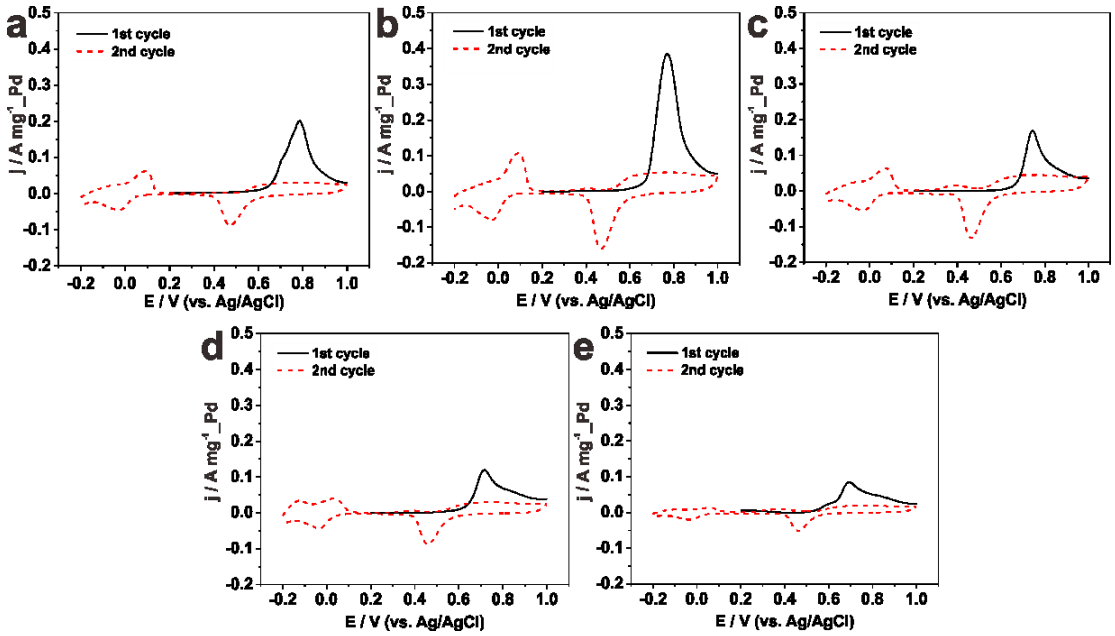

Figure 3.15 1st and 2nd cycle CO-stripping voltammetry of mesoporous (a) $Pd_{91}Cu_9$ (b) $Pd_{81}Cu_{19}$, (c) $Pd_{71}Cu_{29}$, (d) $Pd_{59}Cu_{41}$, and (e) $Pd_{49}Cu_{51}$ films in 0.5 M H_2SO_4 at a scan rate of 50 mVs^{-1}.

Table 3.2 Electrochemical Surface-Active Area (ECSA) of mesoporous Pd_xCu_{100-x} films investigated from oxide monolayer reduction and CO-stripping experiment.

Sample	ECSA (m^2g^{-1})	
	Oxide Monolayer Reduction	CO-Stripping
$Pd_{91}Cu_9$	35.07	36.13
$Pd_{81}Cu_{19}$	58.76	60.67
$Pd_{71}Cu_{29}$	32.99	29.57
$Pd_{59}Cu_{41}$	20.67	27.40
$Pd_{49}Cu_{51}$	20.57	27.20

Notes for Figure 3.14-3.15 and Table 3.2:

The electrochemical active surface area (ECSA) of Pd-based electrocatalysts can be estimated by cyclic voltammetry (CV), after integrating the area under the region assigned to PdO reduction in H_2SO_4 and by CO-stripping experiment. Typical CV obtained from all the samples in 0.5 M H_2SO_4 at a scan rate of 50 mVs^{-1} shows a pair of hydrogen adsorption-desorption peaks between -0.2 and 0.1 V (**Figure 3.14**). After integrating the PdO reduction

region, located between 0.4 V and 0.6 V, and assuming that the conversion factor for the reduction of an oxide monolayer is 420 μCcm^{-2} on a smooth Pd surface, the ECSA of the mesoporous Pd, $Pd_{91}Cu_9$, $Pd_{81}Cu_{19}$, $Pd_{71}Cu_{29}$, $Pd_{59}Cu_{41}$, and $Pd_{49}Cu_{51}$ films are estimated to be 37.85, 35.07, 58.76, 32.99, 20.67, and 20.57 m^2g^{-1}, respectively. For comparison, the ECSA value for the commercial PdB nanoparticles found in the literatures lies between 6.88–24.2 m^2g^{-1}. Similarly, the ECSA calculated from CO-stripping experiments for mesoporous $Pd_{91}Cu_9$, $Pd_{81}Cu_{19}$, $Pd_{71}Cu_{29}$, $Pd_{59}Cu_{41}$, and $Pd_{49}Cu_{51}$ films are 36.13, 60.67, 29.57, 27.40, and 27.20 m^2g^{-1}, respectively (**Figure 3.15**). Because of its high ECSA, the mesoporous $Pd_{81}Cu_{19}$ film is further selected to perform electrocatalytic activity test towards the oxidation of small molecules.

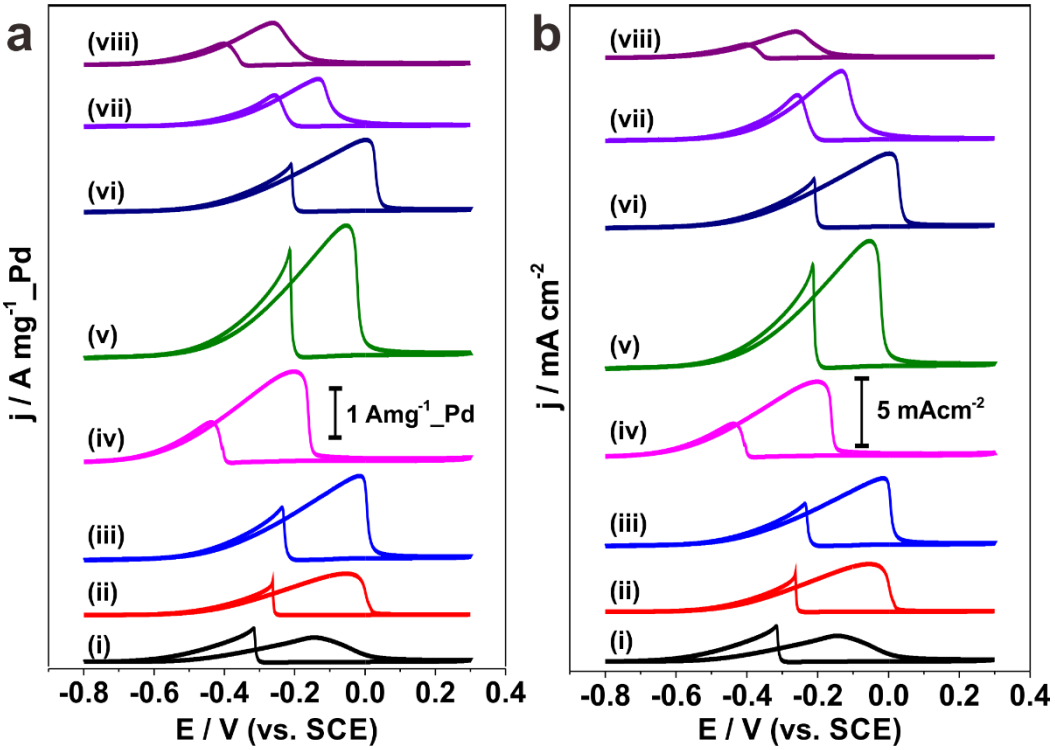

Figure 3.16 (a) Pd mass-normalized and (b) ECSA-normalized CV curves of (i) PdB, (ii) nonporous $Pd_{81}Cu_{19}$ films, mesoporous (iii) Pd, (iv) $Pd_{91}Cu_9$, (v) $Pd_{81}Cu_{19}$, (vi) $Pd_{71}Cu_{29}$, (vii) $Pd_{59}Cu_{41}$, (viii) $Pd_{49}Cu_{51}$ films in 1.0 M KOH containing 1.0 M C_2H_5OH at a scan rate of 50 mVs^{-1}.

The stability of the electrocatalyst is an important factor for ethanol oxidation reaction. Therefore, the mesoporous $Pd_{81}Cu_{19}$ films and control samples were examined for stability test. The $Pd_{81}Cu_{19}$ film revealed superior catalytic stability when investigated by amperometric *i-t* technique at a constant potential of -0.2 V (*vs*. SCE) for 1,200 s (**Figure**

3.18). The feature of standing mesochannels of $Pd_{81}Cu_{19}$ films was also investigated by carrying out cyclic voltammetry towards ethanol oxidation at a various scan rate (**Figure 3.19a-c**). From the parameters extracted from the CVs of mesoporous Pd with cage-type mesopores, mesoporous $Pd_{81}Cu_{19}$ with vertically oriented mesochannels and nonporous $Pd_{81}Cu_{19}$ films at various scan rates, the relationship between a series of square root scan rate and the mass activity obtained at the respective scan rates can indicate the diffusion characteristics of the guest molecule species.[35] The plot gradient of forward oxidation peak current densities towards square root of the scan rate of the mesoporous $Pd_{81}Cu_{19}$ films was larger than those of mesoporous Pd and nonporous $Pd_{81}Cu_{19}$ films (**Figure 3.19d**). This phenomenon suggesting that the diffusion efficiency of ethanol molecules inside the standing mesochannels is higher than cage-type pores and nonporous films structures.[36-39] Mesochannels feature on the mesoporous $Pd_{81}Cu_{12}$ films shows an improved transport for reactant and products.

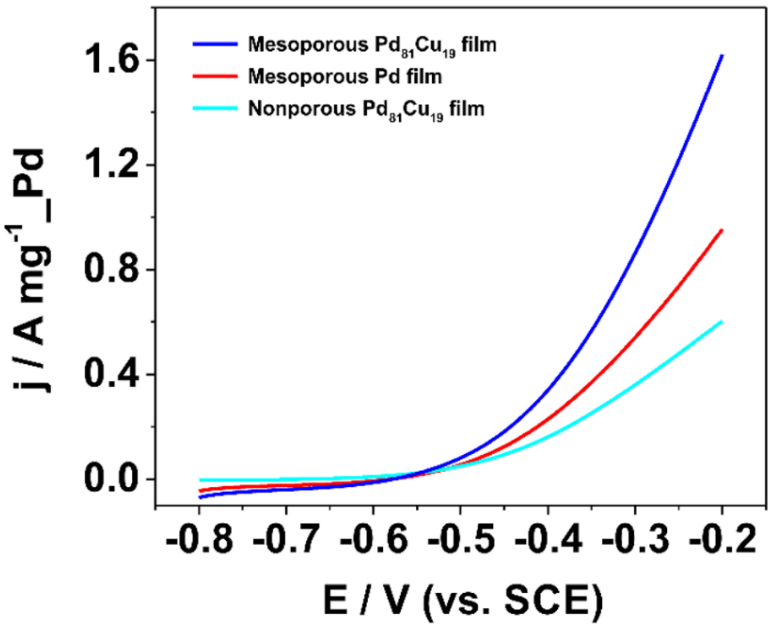

Figure 3.17 Pd mass-normalized LSV measurement of the mesoporous $Pd_{81}Cu_{19}$, mesoporous Pd and nonporous $Pd_{81}Cu_{19}$ films in 1.0 M KOH containing 1.0 M C_2H_5OH. The curves were obtained at a scan rate of 50 mVs^{-1}**.** All the tested film electrode has the same geometrical area (0.18 cm^2).

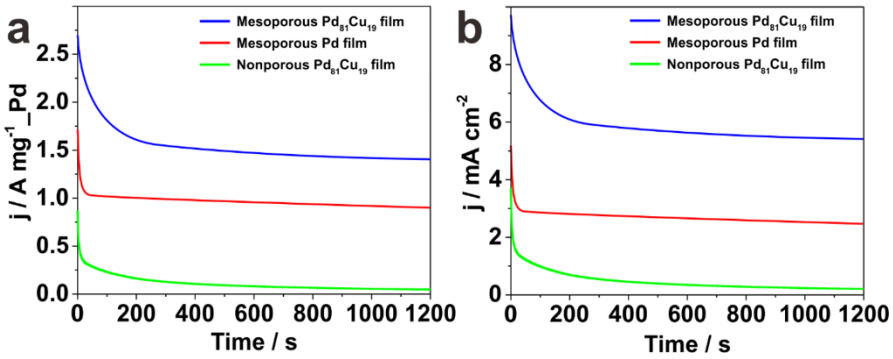

Figure 3.18 (a) Pd mass-normalized and (b) ECSA-normalized amperometric *i-t* curves of the mesoporous $Pd_{81}Cu_{19}$, mesoporous Pd and nonporous $Pd_{81}Cu_{19}$ films in 1.0 M KOH containing 1.0 M C_2H_5OH for 1,200 s at constant potential of -0.2 V (*vs*. SCE).

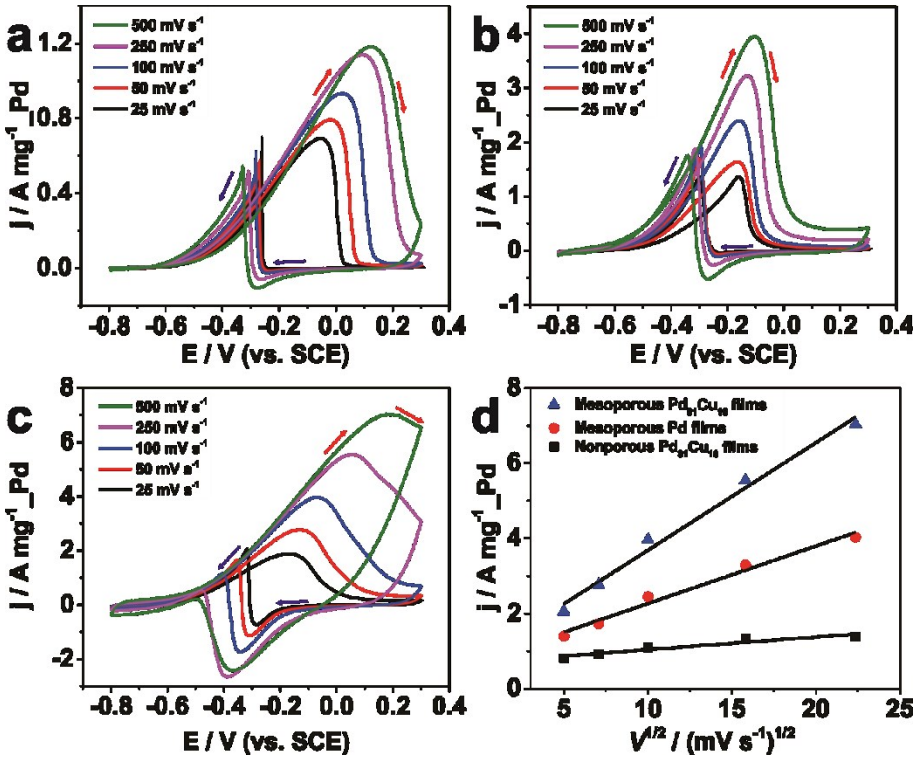

Figure 3.19. (a-c) Cyclic voltammetry of (a) nonporous $Pd_{81}Cu_{19}$, (b) mesoporous Pd, and (c) mesoporous $Pd_{81}Cu_{19}$ films in 1.0 M KOH containing 1.0 M C_2H_5OH at various scan rate (25, 50, 100, 250 and 500 mV s^{-1}). (d) Forward oxidation peak current density (mass activity) as a function of the square root of the scan rate for nonporous $Pd_{81}Cu_{19}$, mesoporous Pd, and mesoporous $Pd_{81}Cu_{19}$ films. The red and blue arrows in the panel a-c indicates positive and negative scan direction, respectively.

3.5. Conclusions

In this chapter, mesoporous PdCu films with mesochannels structure have been successfully synthesized by surfactant micelles-assisted electrodeposition. The mesoporous structure has the highest degree of vertical alignment, as evidenced by GI-SAXS characterization, thus promoting the accessibility of the surface-active sites and lowering reactant diffusion resistance. Also, the presence of Cu atoms in the bimetallic system reduces the capability of the surface to accommodate poisoning products from intermediate reactions. The concept of soft-templating electrodeposition of mesoporous metallic alloy films is still at its early stage and already demonstrates promising outputs, such as for direct alcohol fuel cells devices. In the broader context, the soft-templating approach can be addressed to prepare a newly kind family of the mesoporous, hollow, and mesochannels metal nanostructures.[40-43]

3.6. References

[1] K. Ariga, A. Vinu, Y. Yamauchi, Q. Ji, J. P. Hill, *Bull. Chem. Soc. Jpn*. **2012**, *85*, 1-32.

[2] T. Wagner, S. Haffer, C. Weinberger, D. Klaus, M. Tiemann, *Chem. Soc. Rev.* **2013**, *42*, 4036-4053.

[3] M. Hartman, *Chem. Mater.* **2005**, *17*, 4577-4593.

[4] Z. Wu, D. Zhao, *Chem. Commun.* **2011**, *47*, 3332-3338.

[5] Y. Yamauchi, K. Kuroda, *Chem. Asian J.* **2008**, *3*, 664-676.

[6] G. S. Attard, P. N. Bartlett, N. R. B. Coleman, J. M. Elliott, J. R. Owen, J. H. Wang, *Science* **1997**, *278*, 838-840.

[7] V. Malgras, H. Ataee-Esfahani, H. Wang, B. Jiang, C. Li, K. C. -W. Wu, J. H. Kim, Y. Yamauchi, Y. *Adv Mater*. **2016**, *28*, 993-1010.

[8] Z. Teng, G. Zheng, Y. Dou, W. Li, C. Mou, X. Zhang, A. M. Asiri, D. Zhao, *Angew. Chem. Int. Ed.* **2012**, *51*, 2173-2177.

[9] A. Walcarius, E. Sibottier, M. Etienne, J. Ghanbaja, *Nat. Mater.* **2007**, *6*, 602-608.

[10] M. -L. Lin, C. -C. Huang, M. -Y. Lo, C. -Y. Mou, *J. Phys. Chem*. **2008**, *112*, 867-873.

[11] D. Wang, W. L. Zhou, B. F. McCaughy, J. E. Hampsey, X. Ji, Y. B. Jiang, H. Xu, J. Tang, R. H. Schmehl, C. O'Connor, C. J. Brinker, Y. Liu, *Adv. Mater*. **2003**, *15*, 130-133.

[12] D. Wang, H. Luo, R. Kou, M. P. Gil, S. Xiao, V. O. Golub, Z. Yang, C. J. Brinker, Y. A. Lu, *Angew. Chem. Int. Ed.* **2004**, *43*, 6169-6173.

[13] P. N. Bartlett, B. Gollas, S. Guerin, J. Marwan, *Phys. Chem. Chem. Phys*. **2002**, *4*, 3835-3842.

[14] A. H. Whitehead, J. M. Elliott, J. R. Owen, G. S. Attard, *Chem. Commun*. **1999**, 331-332.

[15] H. Wang, L. Wang, T. Sato, Y. Sakamoto, S. Tominaka, K. Miyasaka, N. Miyamoto, Y. Nemoto, O. Terasaki, Y. Yamauchi, *Chem. Mater.* **2012**, *24*, 1591-1598.

[16] M. Iqbal, C. Li, K. Wood, B. Jiang, T. Takei, Ö. Dag, D. Baba, A. S. Nugraha, T. Asahi, A. E. Whitten, M. S. A. Hossain, V. Malgras, Y. Yamauchi, *Chem. Mater.* **2017**, *29*, 6405-6413.

[17] C. Li, B. Jiang, N. Miyamoto, J. H. Kim, V. Malgras, Y. Yamauchi, *J. Am. Chem. Soc*., **2015**, *137*, 11558–11561.

[18] C. Li, Ö. Dag, T. D. Dao, T. Nagao, Y. Sakamoto, T. Kimura, O. Terasaki, Y. Yamauchi, *Nat. Commun*. **2015**, 6, 6608.

[19] C. Bianchini, P. K. Shen, *Chem. Rev.* **2009**, *109*, 4183-4206.

[20] F. Ksar, L. Ramos, B. Keita, L. Nadjo, P. Beaunier, H. Remita, *Chem. Mater.* **2009**, *21*, 3677-3683.

[21] A. Chen, C. Ostrom, *Chem. Rev.* **2015**, *115*, 11999-12044.

[22] E. Antolini, *Energy Environ. Sci.* **2009**, *2*, 915-931.

[23] Z. Yin, L. Lin, D. Ma, *Catal. Sci. Technol.* **2014**, *4*, 4116-4128.

[24] A. Wang, X. He, X. Lu, H. Xu, Y. Tong, G. Li, *Angew. Chem. Int. Ed.* **2015**, *54*, 3669-3673.

[25] B. Hammer, J. K. Nørskov, *Adv. Catal.* **2000**, *45*, 71-129.

[26] A. A. B. Padama, A. P. S. Cristobal, J. D. Ocon, W. A. Diño, H. Kasai, *J. Phys. Chem. C.* **2017**, *121*, 17818-17826.

[27] K. Jiang, P. Wang, S. Guo, X. Zhang, X. Shen, G. Lu, D. Su, X. Huang, *Angew. Chem. Int. Ed.* **2016**, *55*, 9030-9035.

[28] V. R. Koganti, D. Dunphy, V. Gowrishanker, M. D. McGehee, X. Li, J. Wang, S. E. Rankin, *Nano Lett*. **2006**, *6*, 2567-2570.

[29] V. R. Koganti, S. E. Rankin, *J. Phys. Chem. B*. **2005**, *109*, 3279-3283.

[30] K. Choi, E. W. McFarland, G. D. Stucky, *Adv. Mat.* **2003**, *15*, 2018-2021.

[31] C. Xu, Y. Zhang, L. Wang, L. Xu, X. Bian, H. Ma, Y. Ding, *Chem. Mater.* **2009**, *21*, 3110-3116.

[32] A. G. Denkova, E. Mendes, M. Coppens, *J. Phys. Chem. B* **2009**, *113*, 989-996.

[33] W. Luo, T. Zhao, Y. Li, J. Wei, P. Xu, X. Li, Y. Wang, W. Zhang, A. A. Elzatahry, A. Alghamdi, Y. Deng, L. Wang, W. Jiang, Y. Liu, B. Kong, D. Zhao, *J. Am. Chem. Soc.* **2016**, *138*, 12586-12595.

[34] Z. X. Liang, T. S. Zhao, J. B. Xu, L. D. Zhu, *Electrochim. Acta* **2009**, *54*, 2203-2208.

[35] Y. Noh, Y. Kim, S. Lee, E. J. Lim, J. G. Kim, M. S. Choi, M. H. Seo, W. B. Kim, *Nanoscale* **2015**, *7*, 9438-9442.

[36] L. Tang, Y. Wang, Y. Li, H. Feng, J. Lu, J. Li, *Adv. Funct. Mater.* **2009**, *19*, 2782.

[37] L. Dong, R. R. S. Gari, Z. Li, M. M. Craig, S. Hou, *Carbon* **2010**, *48*, 781.

[38] D. Wen, A. -K. Herrmann, L. Borchardt, F. Simon, W. Liu, S. Kaskel, A. Eychmüller, *J. Am. Chem. Soc.* **2014**, *136*, 2727.

[39] E. A. Franceschini, M. M. Bruno, F. J. Williams, F. A. Viva, H. R. Corti, *ACS Appl. Mater. Interfaces* **2013**, *5*, 10437.

[40] H. You, F. Zhang, Z. Liu, J. Fang, *ACS Catal.* **2014**, *9*, 2829.

[41] H. You, J. Fang, *Nano Today* **2016**, *11*, 145.

[42] L. Zhang, J. Li, H. You, C. Ma, S. Lan, Z. Wu, J. Zeng, F. Tian, J. Fang, *Small* **2017**, *14*, 1702565.

[43] J. Fang, L. Zhang, J. Li, L. Lu, C. Ma, S. Cheng, Z. Li, Q. Xiong, H. A. You, *Nat. Commun.* **2018**, *9*, 521.

Chapter 4

4. Three-Dimensional Superbranched PdCu

4.1. Introduction

Precise control over structures of noble-metal nanomaterials has sparked extensive research to find highly active electrocatalysts for the electrocatalytic reactions.[1-4] The catalytic performance of a noble-metal nanomaterial is generally recognized to be dependent on its surface structures and composition.[5-8] Well-defined nanocrystals in shapes such as spheres,[9,10] cubes,[11,12] and octahedra[13-15] have been well developed to enhance the catalytic activity and the noble-metal utilization efficiency. A previous study demonstrated that Pt cubic and octahedral nanocages enclosed by {100} and {111} facets exhibit distinctive catalytic activities towards the oxygen reduction reaction due to the high dispersion of the active atoms.[16] Until now, the nanocrystals with specific shapes and structures have been limited to isolated ones, not nanocrystals in well-patterned networks. These isolated nanoparticles, unfortunately, suffer from big limitations in terms of catalytic stability and thermal stability, because they easily undergo structural transformation under detrimental corrosive catalytic conditions, thus resulting in undesirable performance loss.[17-19] This has created a new challenge, whether it will be able to design a more stable architecture (*e.g.,* three-dimensional (3D) structure) with controlled facets exposed that can greatly improve the stability and activity.

Nanoscale self-assembly has been employed to manipulate nanocrystals to create two-dimensional (2D) or 3D arrangements (e.g., superlattices) by carefully tailoring the interactions between the nanocrystals.[20-22] This approach, however, requires complicated operations and tends to be rather slow. To extend the utility of the self-assembly approach and make it versatile, combining it with the bottom-up approach is more attractive. The direct assembly of the tiny nanocrystals during their growth process is expected to produce unique nanoarchitectures with controlled facets and better catalytic activity and stability. Nevertheless, it has been extremely difficult to realize such nanoarchitectures.

In this chapter, I have demonstrated an effective wet-chemical method for the production of 3D super-branched PdCu nanoarchitectures with particular crystal facets. The obtained 3D nanostructures contain over a dozen one-dimensional (1D) sub-branches, which are constructed by direct assembly of tiny octahedral nanocrystals. To the best of my knowledge, this is the first example of facet-controlled super-branched alloy structures. The 3D super-branched PdCu nanoarchitectures were synthesized by the reduction of palladium acetylacetonate ($Pd(acac)_2$) and copper chloride in a mixed solvent of

dimethylformamide (DMF) and ethanol. Hexadecyl-pyridinium chloride (HDPC) and polyvinyl pyrrolidone (PVP) and $W(CO)_6$ as the shape-directing agent were also mixed in (**Scheme 4.1**). After all the chemicals were completely dissolved under vigorous stirring, the mixed solution was then transferred to a Teflon-lined stainless-steel autoclave and solvothermally treated at 180 °C for 30 min. The resultant products were then collected through consecutive washings in ethanol using centrifugation.

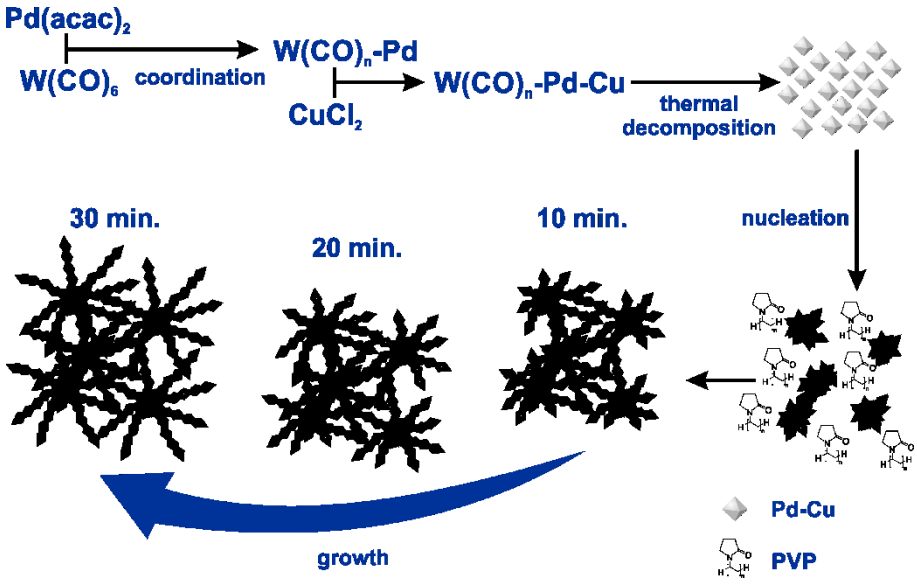

Scheme 4.1 Schematic illustration of the preparation of 3D super-branched PdCu alloy nanostructures. In the present study, tungsten carbonyl ($W(CO)_6$), which can be initially decomposed into metallic W and CO molecules at a relatively low temperature, has an essential role in the facet controls. The initially formed metallic tungsten (W) is replaced by and directs the formation of tiny Pd nanocrystals, and then the released CO molecules are specifically adsorbed on the {111} facets of the tiny Pd nanocrystals and direct the formation of nano-octahedra.

4.2. Experimental Section

4.2.1. Materials

Palladium(II) acetylacetonate ($Pd(acac)_2$), copper(II) chloride ($CuCl_2$), tungsten hexacarbonyl ($W(CO)_6$), and hexadecyl-pyridinium chloride (HDPC) were purchased from

Sigma-Aldrich. Polyvinyl pyrrolidone (PVP) was purchased from Nacalai Co. All chemicals were used without any prior treatment.

4.2.2. Synthesis of Three-Dimensional Superbranched PdCu

100 mg HDPC was dissolved in a mixture of DMF (10.0 mL) and ethanol (2.0 mL) under stirring. Then, 25 mg of PVP was added into the reaction solution, which was followed by adding 8 mg of $Pd(acac)_2$, 50 mg of $W(CO)_6$, and 8 mg of $CuCl_2$ under vigorous stirring. After stirring for another 30 min and sonication for 5 min, the mixed solution was then transferred to a Teflon-lined stainless steel autoclave and solvothermally treated at 180°C for 30 min. The resultant colloid from the solvothermal reaction was then collected through consecutive washings in ethanol using centrifugation and sonication several times. The 3D Pd nanostructure was prepared by the same procedure without adding $CuCl_2$ in the reaction solution.

4.2.3. Characterizations

Scanning electron microscope (SEM) images were obtained using a Hitachi high-resolution SEM (HR-SEM) SU8000 microscope at an accelerating voltage of 5 kV. Transmission electron microscope (TEM), high-resolution TEM (HRTEM), and high-angle annular dark-field scanning TEM (HAADF-STEM) images, as well as elemental mapping, were collected using a JEOL JEM-2100F microscope at an accelerating voltage of 200 kV. Fourier transform infrared spectra of reaction solutions with various compositions were examined with a Thermoscientific Nicolet 4700 instrument. X-ray diffraction (XRD) on a RIGAKU Smartlab diffractometer was employed to obtain wide-angle X-ray diffraction patterns with Cu Kα radiation. X-ray photoelectron spectroscopy (XPS) spectra were obtained on a JEOL JPS-9010TR with Mg Kα radiation at room temperature, and all the spectra were calibrated to C 1s (286.0 eV) as reference.

4.2.4. Electrochemical Measurement

All electrochemical measurements were recorded using a CHI 842B electrochemical analyzer (CH Instruments, USA). A conventional three-electrode set-up was employed to carry out the electrochemical measurements. Glassy carbon electrode (GCE, 3 mm in diameter), coated by the electrocatalysts, platinum wire, and Ag/AgCl electrode were employed as the working, counter, and reference electrodes, respectively. Prior to the

surface coating, the GCE was polished with 1.0 and 0.05 μm alumina powder, rinsed with deionized water, and dried under nitrogen gas flow. Then, 5.0 μg of the as-prepared 3D super-branched PdCu alloy (denoted sample i), 3D Pd (sample ii) or commercially available Pd black (sample iii) suspension was coated on the surface of the GCE. After drying under atmospheric conditions, a Nafion® solution (5.0 μL, 0.5 wt%) was subsequently coated on the GCE surface and dried at room temperature before further electrochemical measurements.

In order to obtain a clean catalyst surface prior to the electrochemical investigations, the modified GCE was treated electrochemically by applying –0.2 V to 1.5 V (vs. Ag/AgCl) for 100 cycles at a scan rate of 50 mV s^{-1}. Cyclic voltammograms were recorded in 0.5 M H_2SO_4 electrolyte at a scan rate of 50 mV s^{-1} in the potential range from –0.2 to 1.2 V. The electrocatalytic performance towards the formic acid oxidation reaction was recorded in 0.5 M H_2SO_4 containing 0.5 M HCOOH. All potential values were referenced to an Ag/AgCl (saturated KCl) electrode.

4.3. Characterization of Three-Dimensional Superbranched PdCu

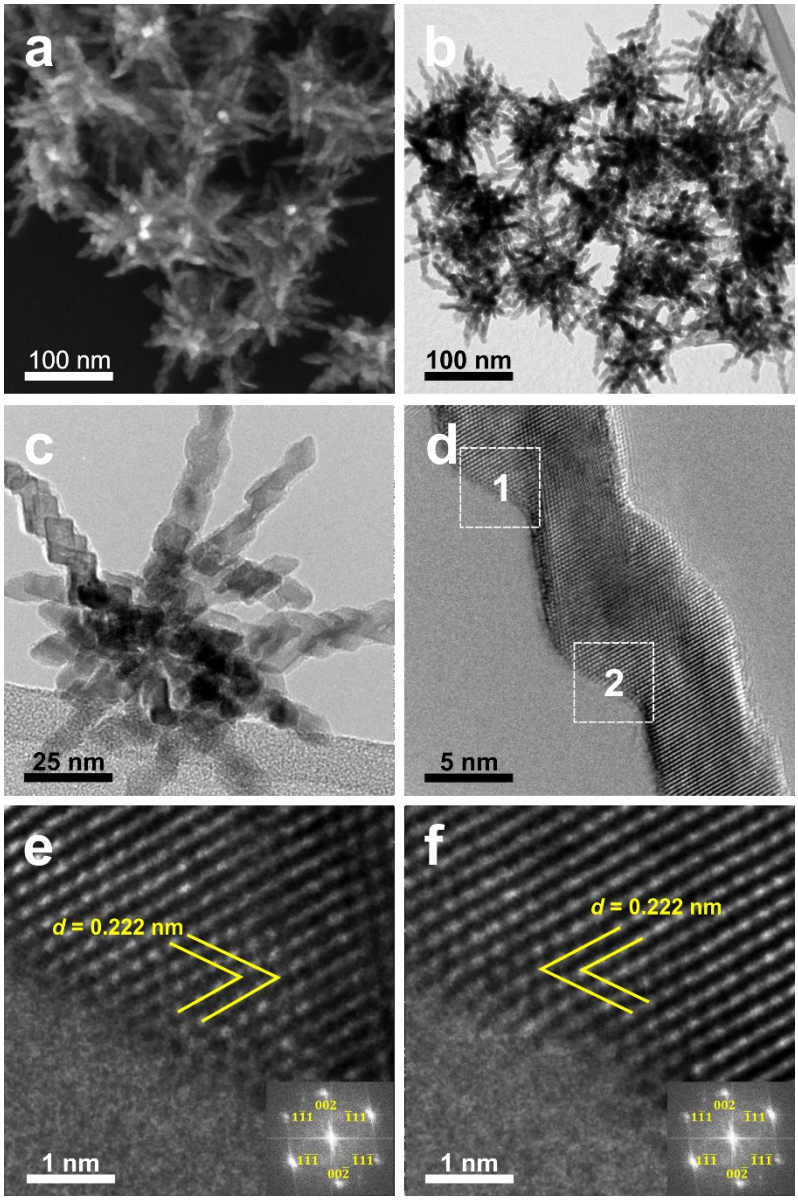

Figure 4.1 (a) Typical SEM and (b, c) TEM images of the 3D super-branched PdCu alloy nanostructures, (d) HRTEM image of a single PdCu branch, (e, f) HRTEM images of the edges of the surfaces derived from the rectangular areas marked in panel (d), respectively. The corresponding FFT patterns are shown as insets in panels (e) and (f).

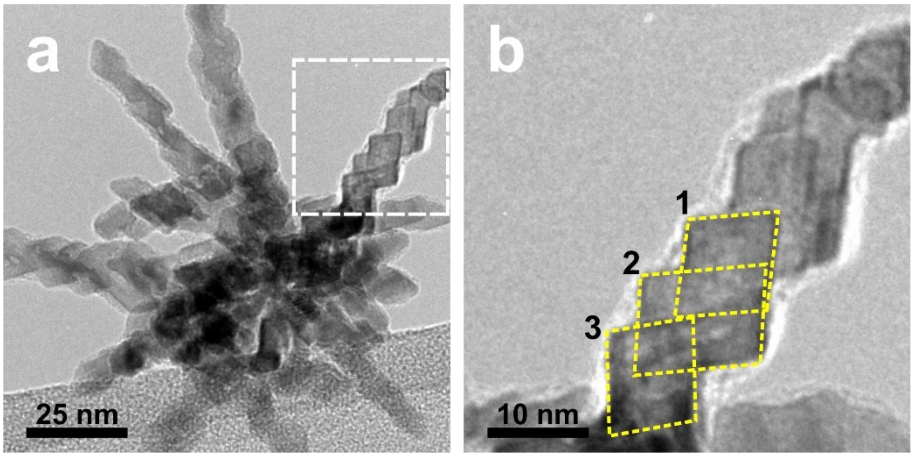

Figure 4.2 a) TEM image of the 3D super-branched PdCu alloy nanostructure. b) High magnification TEM image derived from the rectangular area marked in panel (a). Yellow marks in panel (b) represent octahedral structures which assembled into a branch.

The structures of the obtained product were studied by scanning electron microscopy (SEM) and transmission electron microscopy (TEM), respectively. The representative SEM images clearly show that the obtained products are highly branched 3D nanostructures. No by-products, such as non-branched particles or bulks, were observed (**Figure 4.1a**). Under TEM observation, it is obvious that the aggregations forming the nanobranches are uniform in particle size and structure. The nanobranches radiate from the same center in various directions to form 3D interconnected structures (**Figure 4.1b**). Insights into the morphology by TEM further prove that each 3D branched structure consists of 10-20 subunits. The diameters and lengths of the nanowires are in the range of 8-10 nm and ~80 nm, respectively (**Figure 4.1c**). In contrast to the smooth surfaces usually observed in assembled structures of 1D nanobranches, the branches of my 3D super-branched PdCu nanostructures are composed of many small-sized nano-octahedra (**Figure 4.2**). This feature is an indication of the unique manner of growth, rather than the direct type of growth reported in the previous studies.[36]

Detailed investigations on the compositions of the obtained product were then carried out by wide-angle X-ray diffraction (XRD). In comparison to the standard diffraction patterns of Pd or Cu, all the diffraction peaks of the products show obvious shifts and lie between them. The diffraction peaks observed at 40.5°, 47.1°, 68.9°, 83.4°, and 87.8° can be assigned to the (111), (200), (220), (311), and (222) diffraction planes of face-centered cubic (*fcc*) PdCu alloy, respectively (**Figure 4.3a**). No other diffraction peaks were observed, suggesting the formation of a single-phase PdCu alloy. The electronic

structure was analyzed by X-ray photoelectron spectroscopy (XPS). The XPS spectra of the Pd 3d and Cu 2p regions are displayed in **Figure 4.4**. The doublet peaks with binding energy of 335.6 and 340.8 eV can be assigned to the metallic Pd $3d_{5/2}$ and Pd $3d_{3/2}$ states (**Figure 4.4a**), whereas the peaks at 932.0 and 952.0 eV can be ascribed to the metallic Cu $2p_{3/2}$ and Cu $2p_{1/2}$ states (**Figure 4.4b**). The slight shift in binding energy of the PdCu relative to pure Pd (Pd $3d_{5/2}$: 335.0 eV) and pure Cu (Cu $2p_{3/2}$: 932.6 eV) indicates the electronic interactions between Pd and Cu. The surface molar ratio of Pd:Cu calculated from the XPS spectra is 15:1, which is consistent with the results confirmed by energy dispersive spectroscopy (EDS) and inductively coupled plasma – atomic emission spectroscopy (ICP-AES). The consistent molar ratio between Pd and Cu implies that the Pd and Cu are uniformly distributed inside the structures.

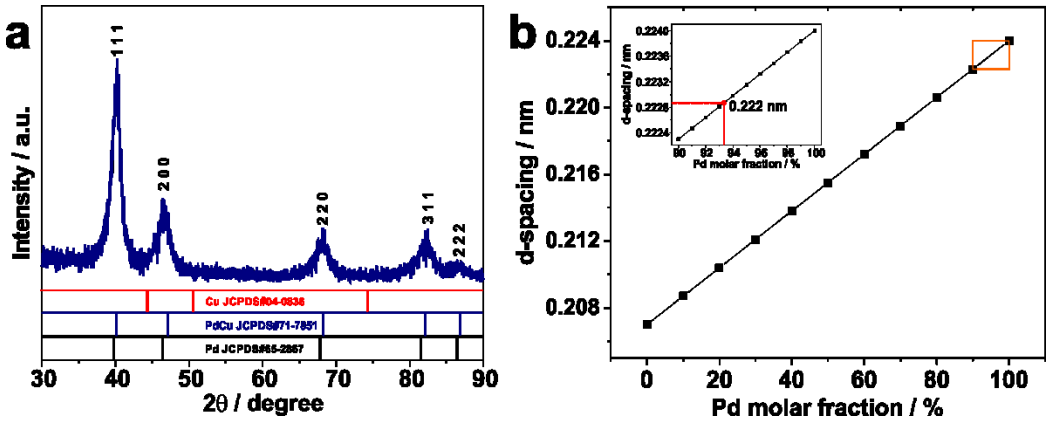

Figure 4.3 (a) XRD pattern of the obtained 3D super-branched PdCu nanostructures. (b) The relationship between the (111) lattice spacing and the Cu molar fraction in a PdCu alloy. The corresponding lattice spacing is indicated (inset) for the PdCu alloy with a molar ratio of Pd:Cu = 15:1.

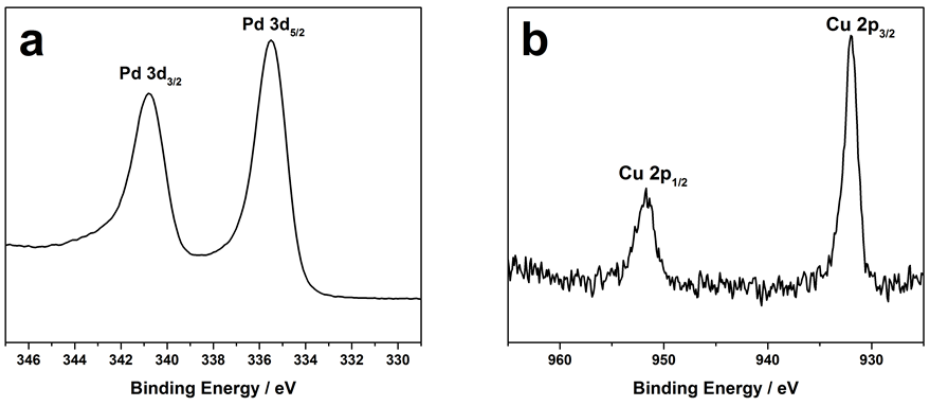

Figure 4.4 XPS spectra of (a) Pd 3d and (b) Cu 2p.

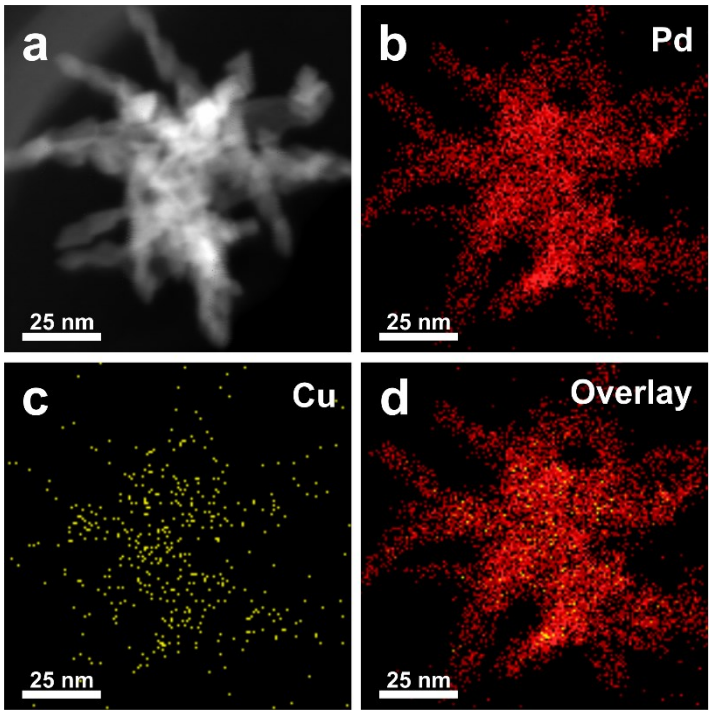

Figure 4.5 (a) STEM image and (b-d) elemental mapping of an individual 3D super-branched PdCu nanoparticle.

To study the crystallinity, high-resolution TEM (HRTEM) was further conducted on the sub-branches, as shown in **Figure 4.1d**. The HRTEM observations revealed continuous fringes running through the 1D branches, suggesting the monocrystallinity of the branches (**Figure 4.1d**). The lattice spacing of 0.222 nm lies between the (111) lattice spacing of pure Pd (0.223 nm) and that of Cu (0.208 nm), supporting the formation of a PdCu alloy. The fast Fourier transform (FFT) patterns of the atomic lattice fringes were identical, as displayed in the insets of **Figure 4.1e** and **4.1f**, further showing the single crystalline nature of the PdCu nanobranches. The (111) lattice spacing calculated from the (111) diffraction peak of the XRD pattern was 0.222 nm, which agrees well with the HRTEM result and the value estimated based on Vegard's law (**Figure 4.3b**). All these results definitely confirmed the formation of PdCu alloy in a 3D super-branched structure.

The high-angle annular dark-field scanning TEM (HAADF-STEM) and energy-dispersive spectroscopy (EDS) mapping analyses in **Figure 4.5** further confirmed the uniform distribution of Pd and Cu elements throughout the 3D structure. Also, the EDS

results gave a molar ratio between Pd and Cu of 15:1, which is in accordance with the ICP-AES data. The composition ratio, however, deviates from the feeding molar ratio. Due to the relatively low redox potential for Cu^{2+} species (Cu^{2+}/Cu = 0.34 V *vs.* Standard Hydrogen Electrode (SHE)) relative to that for the Pd precursor (Pd^{2+}/Pd = 0.91 V *vs.* SHE), the reduction of Cu^{2+} is more difficult than that of Pd^{2+} in the present study. Therefore, a tiny amount of Cu was realized in the final products, even with an equal feeding amount. It is also important to note that no W was detected in the obtained products, despite $W(CO)_6$ being used in the synthesis.

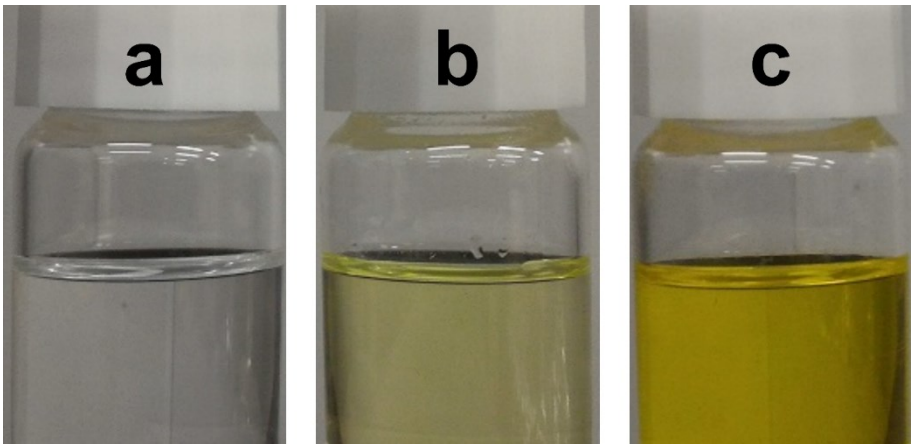

Figure 4.6 Photographs of the reaction solutions with different compositions: (a) solvent (clear), (b) solvent and metal precursors (light transparent yellow), and (c) solvent, metal precursors, and tungsten hexacarbonyl (darker transparent yellow).

Although the structure directing effects of surfactants and additives have been demonstrated before, the 3D super-branched PdCu structure assembled from nano-octahedra has never been previously realized. This unique 3D super-branched structure motivated us to gain a deeper understanding of the formation mechanism. Additives that can selectively adsorb on the crystal surfaces are generally used to assist the shape-controlled synthesis of nanocrystals. For instance, several types of metal ions, such as Fe, Cu, and Ag ions, have been used to tune the nanostructure of Au, Pt, and AuPd.[37-40] Also, $W(CO)_6$ has also been used for the shape-control of various materials, including hollow Pd/Pt single crystalline nanocubes,[41] Pt_3Ni nanopolyhedra,[42] and Ni nanosheets.[43] In the present study, $W(CO)_6$ was selected to shape the growth of the PdCu nanocrystals. The $W(CO)_6$ directly decomposed into metallic W and carbon monoxide (CO). Subsequently, the W could help to rapidly reduce $Pd(acac)_2$ to Pd atoms (*i.e.*, seeds) in the early stage of the nucleation. This process is very fast and can take place even at room temperature.[42]

The solution color of the $Pd(acac)_2$ changed from light-yellow to dark-yellow when it was mixed with the $W(CO)_6$ (**Figure 4.6**). At the this stage, the thus-formed CO molecules will strongly adsorb on the basal {111} planes of the initially formed Pd seeds to prevent growth along the <111> direction, which is responsible for the formation of octahedral nanocrystals.[44] (**Figure 4.7**). The reactions taking place at the initial stage were further confirmed by the Fourier transform infrared (FTIR) spectrum, as shown in **Figure 4.7a**. As clearly observed from the FTIR plots, the newly formed peak that appears after mixing the $Pd(acac)_2$ and $W(CO)_6$ is attributable to the CO adsorption on the Pd {111} surfaces (**Figure 4.7b**).[45,46] As the galvanic replacement reaction goes on, the resultant W cations may accumulate in a relatively high concentration, which slows down the subsequent metallic Pd particle growth, thus favoring the formation of a PdCu alloy in my study. Without the addition of $W(CO)_6$, only irregularly-shaped crystal aggregations were obtained as the final products (**Figure 4.8**), further illuminating the crystal-directing effect of the $W(CO)_6$. The influence of other additives is also critical (**Figures 4.9-4.11**).

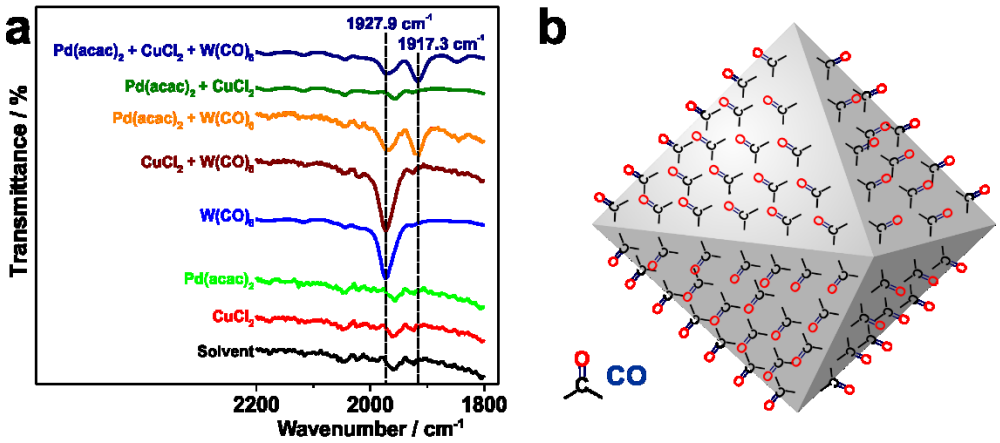

Figure 4.7 a) FTIR spectra of various mixtures. b) Drawing of the structure of a nano-octahedron with CO molecules on the {111} facets.

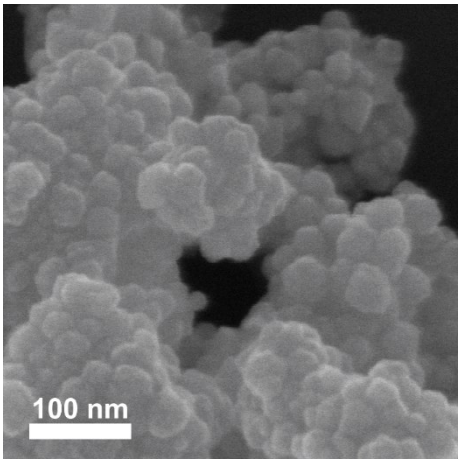

Figure 4.8 SEM image of sample prepared in the absence of $W(CO)_6$, while the other reaction parameters were kept the same as in the typical experimental conditions.

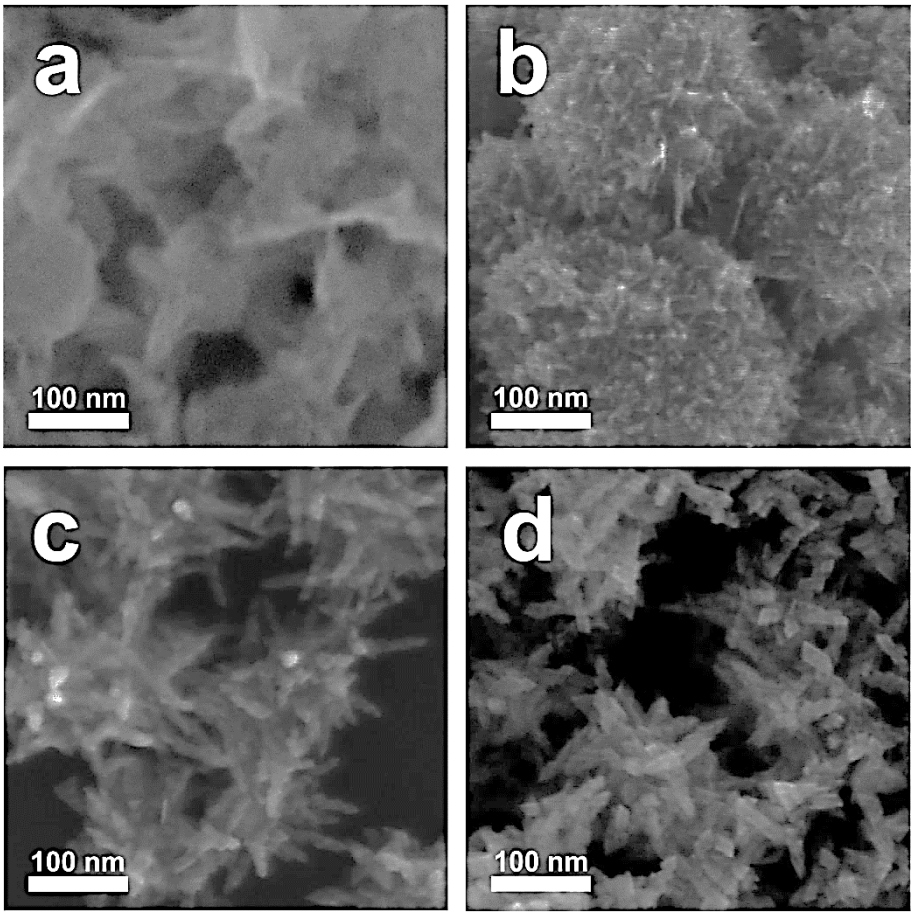

Figure 4.9 SEM images of the samples prepared by using various amounts of HDPC: (a) 0 mg, (b) 50 mg, (c) 100 mg, and (d) 200 mg, respectively.

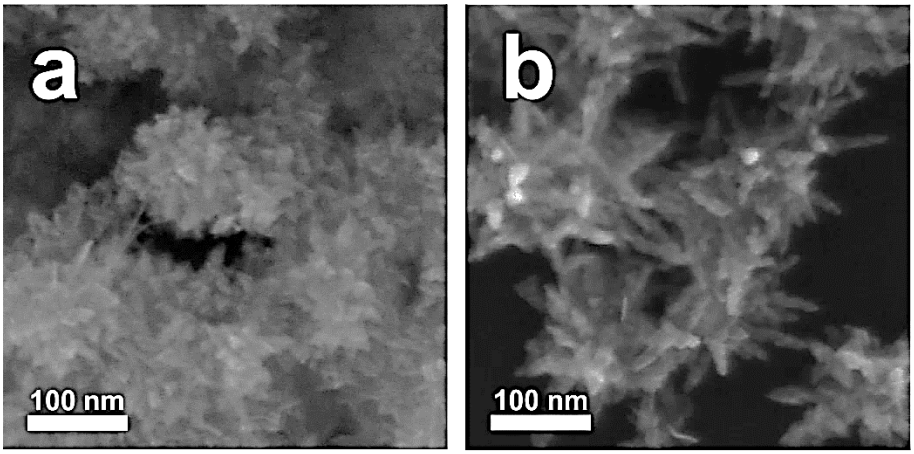

Figure 4.10 SEM images of the samples prepared in the (a) absence and (b) presence of 25 mg PVP.

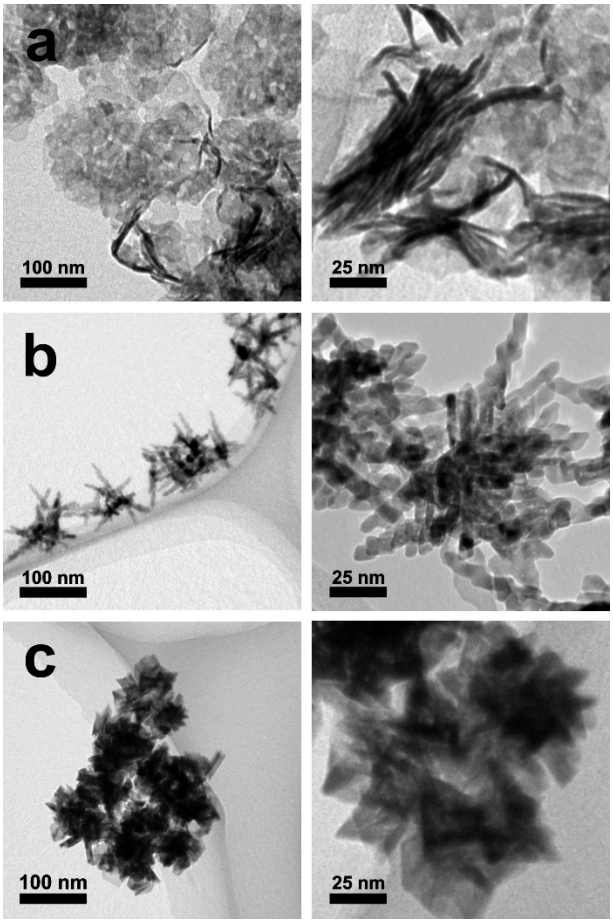

Figure 4.11 TEM images at (left) low and (right) high magnification of the products obtained by using different solvent compositions: (a) 8 mL DMF + 4 mL ethanol, (b) 10 mL DMF + 2 mL ethanol, and (c) 12 mL DMF, respectively.

Without the addition of HDPC, the products gave an irregular structure without any branches (**Figure 4.9a**). Only irregular large aggregations composed of short branches

were obtained when a small amount of HDPC (50 mg) was used in the reaction system (**Figure 4.9b**). When the amount of HDPC was increased to 100 mg, the desired 3D PdCu structures were formed. Further increasing the amount of HDPC (200 mg) resulted in the formation of 3D PdCu structures composed of short arms (**Figure 4.9d**). All of these results suggest that the interconnected 3D structures are likely to be formed only in the presence of HDPC. In a similar way as in previous reports, the PVP used in the present study not only serves as a protective agent against serious aggregation of the nanobranches, but also directs the assembly of the nano-octahedra into nanobranches (**Figure 4.10**).

An optimized ratio of the solvent pair, DMF and ethanol, is the key to enabling the assembly of the octahedral nanocrystals in the present system. It was confirmed that neither DMF nor ethanol alone would lead to the formation of 3D super-branched structures, and an optimized ratio of DMF:C_2H_5OH was evidenced at a volume ratio of 10:2 (**Figure 4.11**). When a lower ratio of DMF to ethanol was used, 2D nanosheets were preferred, because the mixed solution probably has a relatively low surface tension of the reaction solution (**Figure 4.11a**). With increasing the amount of DMF, the surface tension increased and triggered the assembly of the nano-octahedra into the 3D super-branched structures (**Figure 4.11b**). Serious aggregations of the crystals were produced, however, when only DMF was fed (**Figure 4.11c**).

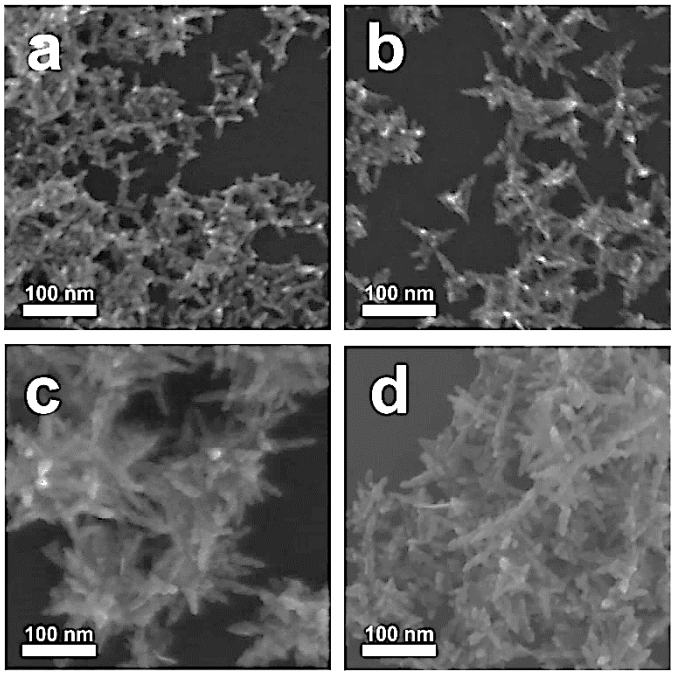

Figure 4.12 Typical TEM images of the PdCu nanostructures (NSs) obtained after various reaction intervals: (a) 10 min, (b) 20 min, (c) 30 min, and (d) 120 min, respectively.

The time-dependent morphological changes are important to illuminate the manner of growth of the 3D super-branched PdCu nanostructures. It is clear that the 3D structure can be well recognized even after a reaction time of 10 min (**Figure 4.12a**). Further increasing the reaction time (*i.e.*, 20 min, 30 min, and 120 min) not only increased the number of 1D branches, but also resulted in increased length of the branches (**Figure 4.12b-d**). These results demonstrate that the initially formed Pd nanocrystals formed the centers of the 3D nanostructures. After the initial process, the simultaneous reduction of Pd and Cu took place on the Pd seeds with the assistance of the CO molecules formed during the synthesis.

4.4. Electrocatalytic Activity of Three-Dimensional Superbranched PdCu

The catalytic performance of catalysts greatly depends on their electrochemical surface area (ECSA). Therefore, the ECSA of the obtained 3D super-branched PdCu nanostructures was studied by using cyclic voltammetry (CV). For comparison, 3D Pd (**Figure 4.14**) and commercially available Pd black (abbreviated as PdB) was also studied as a reference under the same conditions. Typical CV curves obtained in 0.5 M H_2SO_4 are shown in **Figure 4.13a**. The ECSA of Pt is usually calculated on the basis of the hydrogen adsorption/desorption charge.[47] The ECSA estimation for Pd-based materials, however, is still under debate.[48,49] In the present study, the oxide reduction charge is used for calculating the ECSA values because the hydrogen can penetrate into the Pd lattice.[50] The ECSA values of the 3D super-branched PdCu structures, 3D Pd and PdB are 38.08 $m^2 g^{-1}$, 33.00 $m^2 g^{-1}$and 14.53 $m^2 g^{-1}$, respectively. By theoretically calculating the external surface areas of general nanowires with smooth surfaces, the dependence of the surface area on the diameter is plotted in **Figure 4.15**. The surface area of my 3D super-branched PdCu alloy is in the range of the statistical results for nanowires 8-10 nm in diameter.

Pd is well known for its superior catalytic activity towards the oxidation reaction of small organic molecules, especially formic acid. Therefore, the electrocatalytic oxidation of formic acid was selected as a probe reaction to evaluate the activity and stability of the unique 3D super-branched PdCu alloy. The typical CV curves of formic acid oxidation were acquired in 0.5 M H_2SO_4 containing 0.5 M HCOOH electrolyte at a

scan rate of 50 mV s^{-1}. The mass activity of the 3D super-branched PdCu alloy exhibited a larger current density (808 mA mg^{-1}_Pd) than that of 3D Pd and PdB catalyst (330 mA mg^{-1}_Pd and 267 mA mg^{-1}_Pd, respectively) (**Figure 4.13b**). Even when the activity was normalized by the ECSA, my catalyst still showed enhanced specific activity (**Figure 4.13c**). A comparison of the transient current density of formic acid oxidation at 0.3 V on the 3D super-branched PdCu alloy, 3D Pd and on the PdB catalyst shows that my sample exhibits higher current density than that of 3D Pd and PdB (**Figure 4.13d**). The superior performance of the as-prepared 3D super-branched PdCu alloy should probably be ascribed to the unique branched structures and the improved electronic properties provided by the alloyed structure.[51] The surface area and mass activity of the 3D super-branched PdCu alloy in comparison with other reported Pd-based electrocatalyst materials are summarized in **Table 4.1.**

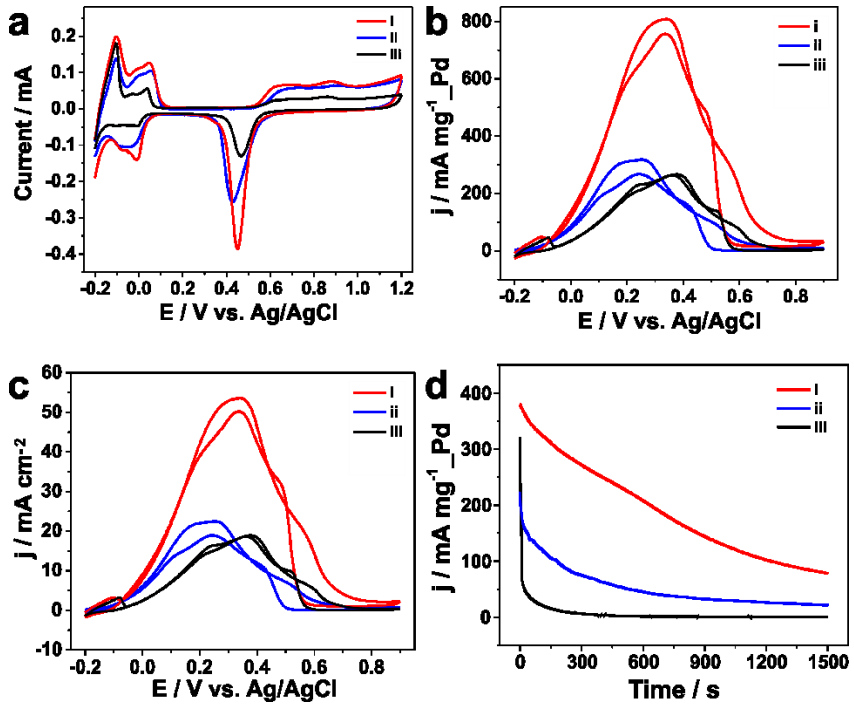

Figure 4.13 (a) CV curves in 0.5 M H_2SO_4 of the (i) 3D super-branched PdCu alloy nanostructures, (ii) 3D Pd and (iii) PdB, respectively. (b) Mass-normalized and (c) ECSA-normalized CV curves, and (d) chronoamperometric curves for formic acid oxidation catalyzed by (i) 3D super-branched PdCu alloy nanostructures, (ii) 3D Pd and (iii) PdB, respectively, in 0.5 M H_2SO_4 containing 0.5 M HCOOH. All the CV curves were obtained at a scan rate of 50 mV s^{-1}. The chronoamperometric measurements were carried out at a constant potential of 0.3 V.

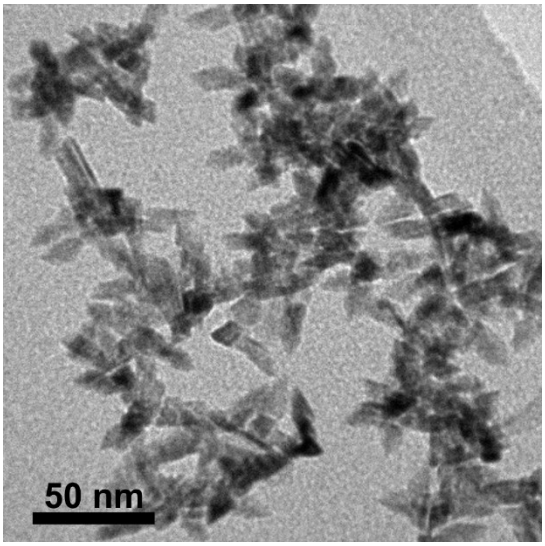

Figure 4.14 Typical TEM image of the 3D branched Pd nanostructures prepared under the typical condition without addition of Cu precursor.

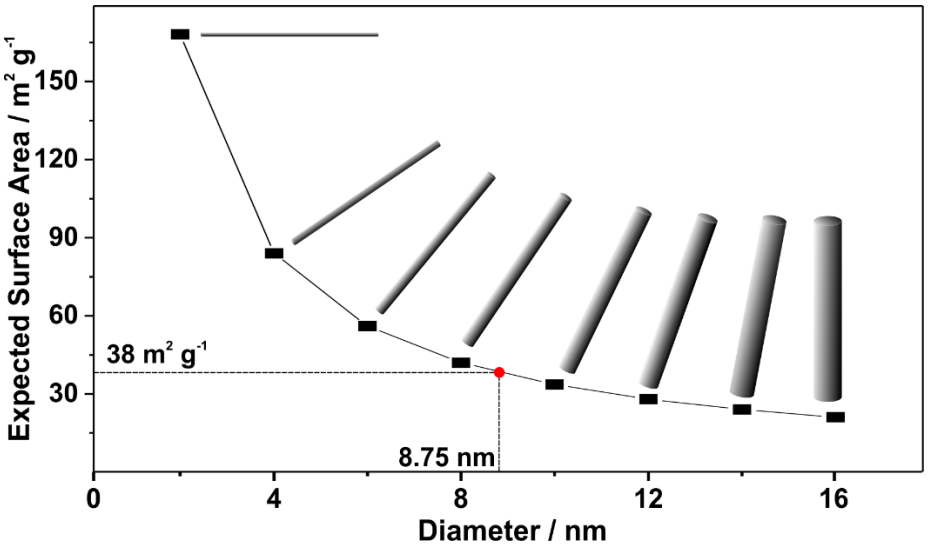

Figure 4.15 Surface area dependence on the diameter of nanowires with smooth surfaces. The corresponding diameter of a surface area that is the same as for the 3D super-branched PdCu alloy is indicated.

4.5. Conclusions

In summary, I have demonstrated a facile approach to the preparation of 3D super-branched PdCu structures. The essential aspects of the ingenious synthesis lie in the combination of

control through the surface-directing agent and the solvent properties. The CO molecules released from $W(CO)_6$ decomposition were selectively adsorbed on the {111} facets of the initial nanoseeds, which exclusively grew into nano-octahedra and were assembled into 1D nanobranches due to a precise control of the solvent properties. The present success not only indicates the simultaneous assembly of the nanocrystals during their growth process, but also paves the way to the preparation of well-organized 3D materials with superior electrocatalytic activity and stability.

4.6. References

[1] X. Huang, Z. Zhao, L. Cao, Y. Chen, E. Zhu, Z. Lin, M. Li, A. Yan, A. Zettl, Y. M. Wang, X. Duan, T. Mueller and Y. Huang, Science, 2015, **348**, 1230-1234.

[2] G. Chen, Y. Zhao, G. Fu, P. N. Duchesne, L. Gu, Y. Zheng, X. Weng, M. Chen, P. Zhang, C.-W. Pao, J.-F. Lee and N. Zheng, Science, 2014, **344**, 495-499.

[3] N. Tian, Z.-Y. Zhou, S.-G. Sun, Y. Ding and Z. L. Wang, Science, 2007, **316**, 732-735.

[4] S. Zhang, S. Guo, H. Zhu, D. Su and S. Sun, J. Am. Chem. Soc., 2012, **134**, 5060-5063.

[5] L. Bu, J. Ding, S. Guo, X. Zhang, D. Su, X. Zhu, J. Yao, J. Guo, G. Lu and X. Huang, Adv. Mater., 2015, **27**, 7204-7212.

[6] Y. Wu, D. Wang, G. Zhou, R. Yu, C. Chen and Y. Li, J. Am. Chem. Soc., 2014, **136**, 11594-11597.

[7] V. Malgras, H. Ataee-Esfahani, H. Wang, B. Jiang, C. Li, K. C.-W. Wu, J. H. Kim and Y. Yamauchi, Adv. Mater., 2016, **28**, 993-1010.

[8] B. T. Sneed, C. N. Brodsky, C.-H. Kuo, L. K. Lamontagne, Y. Jiang, Y. Wang, F. Tao, W. Huang and C.-K. Tsung, J. Am. Chem. Soc., 2013, **135**, 14691-14700.

[9] M. Yang, Q. Cai, C. Liu, R. Wu, D. Sun, Y. Chen, Y. Tang and T. Lu, J. Mater. Chem. A, 2014, **2**, 13778-13742.

[10] L. Zhang, F. Hou and Y. Tan, Chem. Commun., 2012, **48**, 7152-7154.

[11] W. Niu, W. Zhang, S. Firdoz and X. Lu, Chem. Mater., 2014, **26**, 2180-2186.

[12] J. Zhang, C. Feng, Y. Deng, L. Liu, Y. Wu, B. Shen, C. Zhong and W. Hu, Chem. Mater., 2014, **26**, 1213-1218.

[13] M. Wang, L. Wang, H. Li, W. Du, M. U. Khan, S. Zhao, C. Ma, Z. Li and J. Zeng, J. Am. Chem. Soc., 2015, **137**, 14027-14030.

[14] H. Zhang, M. Jin, J. Wang, M. J. Kim, D. Yang and Y. Xia, J. Am. Chem. Soc., 2011, **133**, 19432-19441.

[15] A.-X. Yin, X.-Q. Min, Y.-W. Zhang and C.-H. Yan, J. Am. Chem. Soc., 2011, **133**, 3816-3819.

[16] L. Zhang, L. T. Roling, X. Wang, M. Vara, M. Chi, J. Liu, S.-I. Choi, J. Park, J. A. Herron, Z. Xie, M. Mavrikakis and Y. Xia, Science, 2015, **349**, 412-416.

[17] C. Li, T. Sato and Y. Yamauchi, Angew. Chem., Int. Ed., 2013, **52**, 8050-8053.

[18] B. Jiang, C. Li, V. Malgras, Y. Bando and Y. Yamauchi, Chem. Commun., 2016, **52**, 1186-1189.

[19] L. Bu, S. Guo, X. Zhang, X. Shen, D. Su, G. Lu, X. Zhu, J. Yao, J. Guo and X. Huang, Nat. Commun., 2016, **7**, 11850.

[20] X. Hong, C. Tan, J. Liu, J. Yang, X.-J. Wu, Z. Fan, Z. Luo, J. Chen, X. Zhang, B. Chen and H. Zhang, J. Am. Chem. Soc., 2015, **137**, 1444-1447.

[21] Y. H. Lee, W. Shi, H. K. Lee, R. Jiang, I. Y. Phang, Y. Cui, L. Isa, Y. Yang, J. Wang, S. Li and X. Y. Ling, Nat. Commun., 2015, **6**, 6990.

[22] D. V. Talapin, E. V. Shevchenko, M. I. Bodnarchuk, X. Ye, J. Chen and C. B. Murray, Nature, 2009, **461**, 964-967.

[23] A. Morozan, B. Jousselme and S. Palacin, Energy Environ. Sci., 2011, **4**, 1238.

[24] A. D. Banadaki and A. Kajbafvala, Journal of Nanomaterials, 2014, 1-28.

[25] C. Xu, Y. Zhang, L. Wang, L. Xu, W. Bian, H. Ma, and Y. Ding, Chem. Mater., 2009, **21**, 3110-3116.

[26] Y. C. Yeh, H. M. Chen, R. S. Liu, K. Asakura, M. Y. Lo, Y. M. Peng, T. S. Chan and J. F. Lee, Chem. Mater., 2009, **21**, 4030-4036.

[27] D.C. Martínez-Casillasa, G. Vázquez-Huertaa, J.F. Pérez-Roblesb and O. Solorza-Feria, Journal of Power Sources, 2011, **196**, 4468-4474.

[28] J. L. Haan, K. M. Stafford, R. D. Morgan and R. I. Masel, Electrochimica Acta, 2010, **55**, 2477-2481.

[29] X. Wang, Y. Tang, Y. Gao, T. Lu, Journal of Power Sources, 2008, **175**, 784-788.

[30] R. Wang, S. Liao, S. Ji, Journal of Power Sources, 2008, **180**, 205-208.

[31] A. R.J. Kucernak, K.F. Fahy and V. N. N. Sundaram, Catalysis Today, 2016, **262**, 48-56.

[32] V. Stamenkovic, B. S. Mun, K. J. J. Mayrhofer, P. N. Ross, N. M. Markovic, J. Rossmeisl, J. Greeley and J. K. Norskov, Angew. Chem., Int. Ed., 2006, **45**, 2897-2901.

[33] R. C. Sekol, X. Li, P. Cohen, G. Doubek, M. Carmo, A. D. Taylor, Applied Catalysis B: Environmental, 2013, **138-139**, 285- 293.

[34] B. Jiang, C. Li, M. Imura, J. Tang and Y. Yamauchi, Adv. Sci., 2015, **2**, 1500112.

[35] B. Jiang, C. Li, V. Malgras and Y. Yamauchi, J. Mater. Chem. A, 2015, **3**, 18053.

[36] B. Y. Xia, H. B. Wu, N. Li, Y. Yan, X. W. Lou and X. Wang, Angew. Chem., Int. Ed., 2015, **54**, 3797-3801.

[37] F. Lu, Y. Zhang, L. Zhang, Y. Zhang, J. X. Wang, R. R. Adzic, E. A. Stach and O. Gang, J. Am. Chem. Soc., 2011, **133**, 18074-18077.

[38] J. Chen, T. Herricks and Y. Xia, Angew. Chem., Int. Ed., 2005, **44**, 2589-2592.

[39] H. Song, F. Kim, S. Connor, G. A. Somorjai and P. Yang, J. Phys. Chem. B, 2005, **109**, 188-193.

[40] L. Zhang, J. Zhang, Q. Kuang, S. Xie, Z. Jiang, Z. Xie and L. Zheng, J. Am. Chem. Soc., 2011, **133**, 17114-17117.

[41] X. Huang, H. Zhang, C. Guo, Z. Zhou and N. Zheng, Angew. Chem., Int. Ed., 2009, **48**, 4808-4812.

[42] J. Zhang, H. Yang, J. Fang and S. Zhou, Nano Lett., 2010, **10**, 638-644.

[43] Z. Wang, Y. Chen, D. Zeng, Q. Zhang and D.-L. Peng, CrystEngComm, 2016, **18**, 1295-1301.

[44] X. Huang, S. Tang, X. Mu, Y. Dai, G. Chen, Z. Zhou, F. Ruan, Z. Yang and N. Zheng, Nat. Nanotech., 2011, **6**, 28-32.

[45] J. Lu, K.-B. Low, Y. Lei, J. A. Libera, A. Nicholls, P. C. Stair and J. W. Elam, Nat. Commun., 2014, **5**, 3264.

[46] X. Xia, L. Figueroa-Cosme, J. Tao, H.-C. Peng, G. Niu, Y. Zhu and Y. Xia, J. Am. Chem. Soc., 2014, **136**, 10878-10881.

[47] B. Jiang, C. Li, J. Tang, T. Takei, J. H. Kim, Y. Ide, J. Henzie, S. Tominaka and Y. Yamauchi, Angew. Chem., Int. Ed., 2016, DOI: 10.1002/anie.201603967.

[48] C. Li, B. Jiang, N. Miyamoto, J. H. Kim, V. Malgras and Y. Yamauchi, J. Am. Chem. Soc., 2015, **137**, 11558-11561.

[49] S. Tominaka and T. Osaka, Adv. Phys. Chem., 2011, **2011**, 821916 (13 pages).

[50] G. Li, H. Kobayashi, S. Dekura, R. Ikeda, Y. Kubota, K. Kato, M. Takata, T. Yamamoto, S. Matsumura and H. Kitagawa, J. Am. Chem. Soc., 2014, **136**, 10222-10225.

[51] Q. S. Chen, Z. N. Xu, S. Y. Peng, Y. M. Chen, D. W. Lv, Z. Q. Wang, J. Sun and G. C. Guo, J. Power Sources, 2015, **282**, 471.

Chapter 5

5. Tethered Mesoporous Pd Nanoparticles on Functionalized Reduced Graphene Oxide

5.1. Introduction

Noble metal nanoparticles are ubiquitous in modern applications of catalysis spanning electrocatalysis to organic catalysis.[1-5] The scarcity of these materials has motivated work to enhance the utilization efficiency of the material by increasing surface area, engineering the activity and selectivity of active sites, and increasing stability.[6-8] The fruits of these efforts are particularly true in the case of platinum (Pt), which is still used in diverse applications despite its scarcity.[9,10] Palladium (Pd) is not quite as active as Pt but it is a cheaper and more Earth abundant element.[11,12] Efforts to enhance the performance of Pd-based electrocatalysts to the level of Pt have been pursued.[13-19] For example, Wen *et al* prepared Pd-based electrocatalysts with relatively good performance by controlling particle size.[17] The shape of the nanoparticle also determines performance, and creating Pd nanoparticles with high-index facets that expose atoms with low coordination is a viable strategy.[20] These methods succeed to the extent that they can manipulate the exterior of the particle. Yamauchi's group is developing methods to manipulate the interior space and exterior of particles by controlling porosity. These mesoporous Pd nanoparticles have large active surface areas to catalyze chemical reactions.[18]

On the other hand, carbonaceous materials such as carbon black, nanotubes and nanofibers are widely used as supports structures for noble metal nanoparticle electrocatalysts.[21-24] But the amorphous nature of many carbonaceous materials minimizes the conductivity of the carbon-nanoparticle system and affects durability.[25] More promising are two-dimensional (2D) materials such as graphene which have better chemical stability and better conductivity to serve as catalyst supports.[26-28] However, graphene is difficult to use in solution-based synthetic methods because of strong Van der Waals forces between adjacent carbon sheets. Graphene oxide (GO) is a variant of graphene that can be well dispersed in polar solvents, particularly water, because it has hydroxide or epoxide defects bound to some of the carbon atoms, in addition to some carboxy, carbonyl, phenol, lactose and quinone groups at the sheet edges.[29] But the electrical conductivity of the GO is less than graphene, limiting its use in high performance hybrid electrocatalyst materials. However, GO can be partially reduced (so-called 'rGO'), restoring some electrical conductivity while maintaining its dispersibility in polar solvents.[30] In this chapter, I modified the GO surface with block copolymer Pluronic F127 and reduced the GO with hydrazine. The F127-modified rGO (FrGO) served as a support

to grow three-dimensional (3D) mesoporous Pd nanoparticles with good electronic contact with the rGO surface. This new mesoporous Pd-rGO hybrid materials has much better electrochemical active surface area, catalytic activity and stability in electrooxidation reactions compared to state-of-the-art Pd/C catalysts presently used in industry.

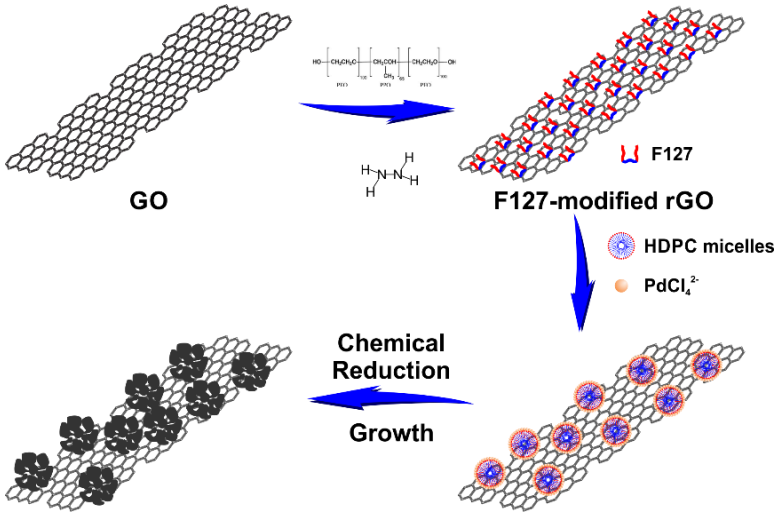

Scheme 5.1 An illustration showing the reduction of GO and its surface modification with F127 polymer. Addition of Pd precursors and a reducing agent resulted in growth of mesoporous Pd nanoparticles on the F127-modified rGO (FrGO) surface.

5.2. Experimental Section

5.2.1. Materials

Graphene oxide (GO, 4 mg mL^{-1} dispersion in water), Brij 58, Pluronic F127, Pluronic P123 and hexadecylpyridinium chloride (HDPC) were obtained from Sigma Aldrich. Hydrazine and ascorbic acid were purchased from Wako Chemicals. Sodium tetrachloropalladate was purchased from Nacalai Tesque, Inc. All chemicals were used without further purification.

5.2.2. Synthesis of Tethered Mesoporous Pd Nanopartciels on Functionalized Reduced Graphene Oxide

192 mg of Pluronic F127 was added to 20 mL of GO suspension (0.25 mg mL^{-1}) and stirred at room temperature for 12 h. Then a small amount of hydrazine (16.8 μL) was added to

the F127-GO solution and heated at 95ºC for 1 h to convert the GO into rGO. Finally, the F127-modified rGO (denoted as FrGO) was collected by centrifugation and re-dispersed in water. The concentration of FrGO was diluted to 2 mg mL^{-1}. Next, 20 mg of HDPC was added to 1 mL of the 2 mg mL^{-1} FrGO suspension. Additional F127 (0.8 mL of 2.0 wt% F127 in water) was added to the solution and stirred for 2 h. To generate the tethered mesoporous Pd nanoparticles, 0.1 mL of 40 mM sodium tetrachloropalladate in water was added to the solution. Then 0.2 mL of 100 mM ascorbic acid in water was added to reduce the Pd precursor at 50ºC for 10 h in a water bath. After the reaction was complete, the FrGO supported mesoporous Pd nanoparticles (denoted as FrGO-Pd) were collected by centrifugation and washed several times in ethanol. **Scheme 5.1** illustrates the full procedure for initial modification of GO to formation of rGO and the subsequent growth of mesoporous Pd nanoparticles on the F127-modified rGO surface. The Pd loading mass on the FrGO support is 19.6% as measured by inductively coupled plasma optical emission spectrometer (ICP-OES).

5.2.3. Characterizations

The morphology of the samples was observed by field emission scanning electron microscopy (FE-SEM) using a Hitachi SU-8000 operating at 5kV. Transmission electron microscopy (TEM) imaging was conducted using a JEOL JEM 2100F at 200kV. FT-IR and Raman spectra were recorded by Thermoscientific Nicolet 4700 and Horiba-Jovin Yvon T64000, respectively. The mesostructural characteristics of the sample were characterized by small-angle X-ray scattering (SAXS) Rigaku MicroMax-007HF with High-Intensity Microfocus Rotating Anode X-Ray Generator, while X-ray diffraction patterns were collected with a Rigaku, Altima III, Rint 2000. X-ray photoelectron spectroscopy (XPS) spectra were obtained on a PHI Quantera SXM (ULVAC-PHI) with Al Kα radiation source at room temperature, and all the spectra were calibrated to the C1s (285.0 eV) peak which served as a reference. The loading mass of Pd on FrGO support was characterized with a Thermo IRIS Advantage ICP-OES.

5.2.4. Electrochemical Measurement

All electrochemical measurements were carried out with a CHI 842B electrochemical analyzer (CH Instruments, USA) using a standard three-electrode set-up. The three-electrode cell consisted of a 3-mm diameter glassy carbon electrode (GCE), a Pt wire, and

an Ag/AgCl electrode, which served as the working, counter, and reference electrodes, respectively. The surface of the GCE initially prepared by polishing it with diamond and alumina powder, then rinsing it with deionized water, and drying it under nitrogen (N_2) gas flow. Then the surface of the GCE was coated with either 5.0 μg of the FrGO-Pd sample or commercially available 10wt% Pd loaded activated carbon (denoted as Pd/C). After drying in air, a Nafion® solution (5.0 μL, 0.5 wt%) was applied to the GCE surface and dried at room temperature before electrochemical characterization. In order to obtain a clean catalyst surface prior to the electrochemical investigations, the GCE was treated electrochemically by applying -0.2 V to 1.5 V (*vs.* Ag/AgCl) for 100 cycles at a scan rate of 500 mV s^{-1}. Cyclic voltammograms were recorded in 0.5 M H_2SO_4 electrolyte at a scan rate of 50 mV s^{-1} in the potential range from -0.2 to 1.2 V. The electrocatalytic performance towards the formic acid oxidation reaction was recorded in 0.5 M H_2SO_4 containing 0.5 M HCOOH at a scan rate of 50 mV s^{-1} in the potential range from -0.2 to 0.9 V. Amperometric *i-t* curves were recorded in 0.5 M H_2SO_4 containing 0.5 M HCOOH at potential of 0.3 V for 1500 s. All potential values were referenced to an Ag/AgCl reference electrode.

5.3. Characterization of Tethered Mesoporous Pd Nanopartciels on Functionalized Reduced Graphene Oxide

The morphology of the mesoporous Pd nanoparticles on FrGO was observed by scanning electron microscopy (SEM) and transmission electron microscopy (TEM) (**Figure 5.1** and **5.2a**). The deposited mesoporous Pd nanoparticles are spherical with an average diameter of 34 nm, and are well distributed on the rGO surface without any agglomeration (**Figure 5.2**). In contrast, rGO unmodified with F127 created severely agglomerated Pd nanoparticles (**Figure 5.2b**). This observation proves that the modification of rGO surface by F127 is essential to form well-dispersed Pd nanoparticles on rGO (the role of F127 will be discussed later). A single mesoporous Pd nanoparticle was observed by high-angle annular dark-field scanning TEM (HAADF-STEM), showing that the mesoporous structure extends throughout the Pd particle (**Figure 5.1b**). High-resolution TEM (HR-TEM) was also employed to show that the Pd nanoparticle had a very rough fractal-like surface which is preferable for electrocatalysis (**Figure 5.1c**).[20] The HR-TEM image also

shows lattice fringes that correspond to the (111) planes of Pd and appear throughout the particle (**Figure 5.1d**).

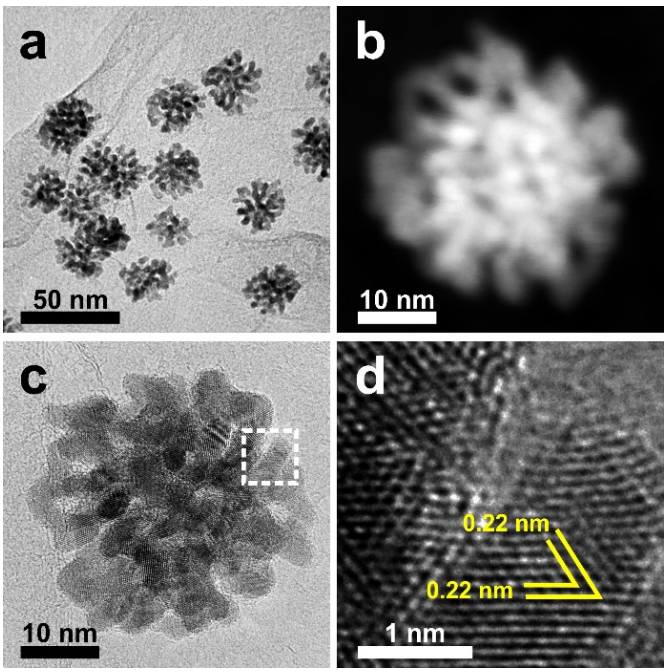

Figure 5.1 (a) TEM image, (b) HAADF-STEM image and (c) high resolution (HR) TEM image of mesoporous Pd nanoparticles on FrGO. (d) HR-TEM image from the square area marked on panel (c).

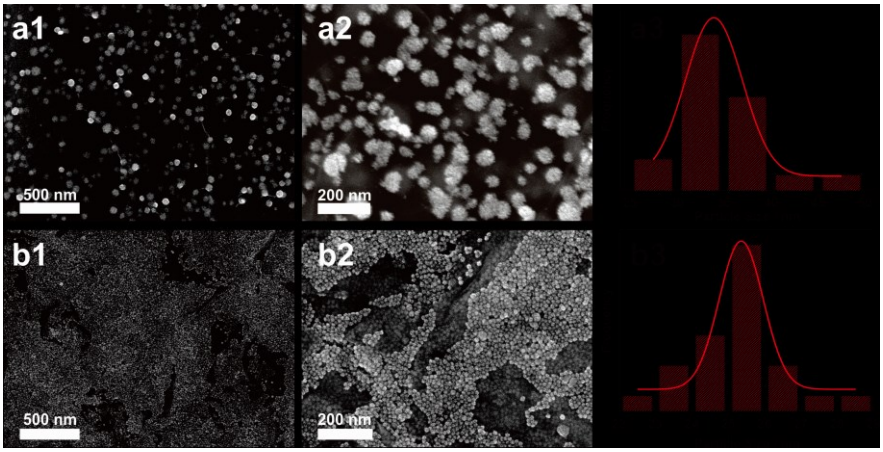

Figure 5.2 SEM images and particles size distribution of (a) mesoporous Pd nanoparticles loaded on FrGO and (b) mesoporous Pd nanoparticles loaded on rGO without modification by F127, respectively.

The fractal ("rough") surface structure and the porosity of the Pd mesoprous nanoparticle interior were characterized with small-angle X-ray scattering (SAXS).

According to the Porod's law ($I(q) \propto q^{-(6-Ds)}$ where D_s denotes the surface fractal dimension), the slope of $I(q)$ *vs*. q in the high q region ($0.2 < q < 1.0$) enables the determination of particle surface.[31] If the slope in high q region decays as -4 ($D_s = 2$), the particles can be considered as smooth and hard spheres. Rough surface with fractal-like qualities requires $2 < D_s \leq 3$. The SAXS profile plot of the FrGO-Pd sample between q = 0.2 to 1.0 has a slope corresponding to q^{-3} ($D_s = 3$) which shows the particles are very rough and fractal-like (**Figure 5.3a**).[32] In addition, a broad peak at q = 1.5 indicates mesostructural periodicity.

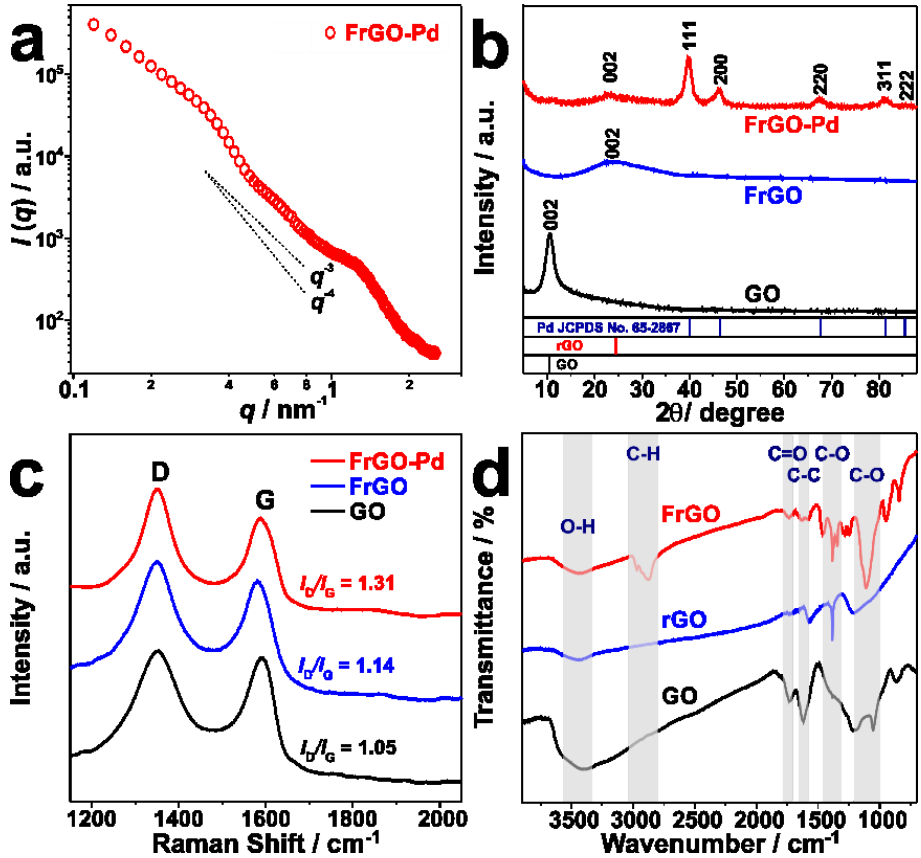

Figure 5.3 (a) Small-angle X-ray scattering (SAXS) profile of FrGO-Pd. (b) Wide-angle XRD patterns and (c) Raman spectra of GO, FrGO, and FrGO-Pd. (d) FT-IR spectra of GO, rGO, and FrGO.

The interior space of the mesoporous Pd nanoparticles on F127-modified rGO forms as follows.[18] HDPC forms micelles in the aqueous solution because its concentration is well above its critical micelle concentration (CMC). The metal precursor (Na_2PdCl_4) is dissociated by water to create metal anions, $[PdCl_4]^{2-}$. At the early stages, the metal anions $[PdCl_4]^{2-}$ interact strongly with positively charged HDP^+. This interaction was

confirmed from UV-vis absorption spectra recorded from the mixture solution of HDPC and Na_2PdCl_4 because a new absorption peak was observed at 300 nm (**Figure 5.4**). When the deposition process starts, small Pd clusters (*i.e.* nuclei) are generated on the FrGO surface. As the particle grows, the cationic surfactant directs the Pd species to form a continuous mesoporous structure. (**Scheme 5.1**).

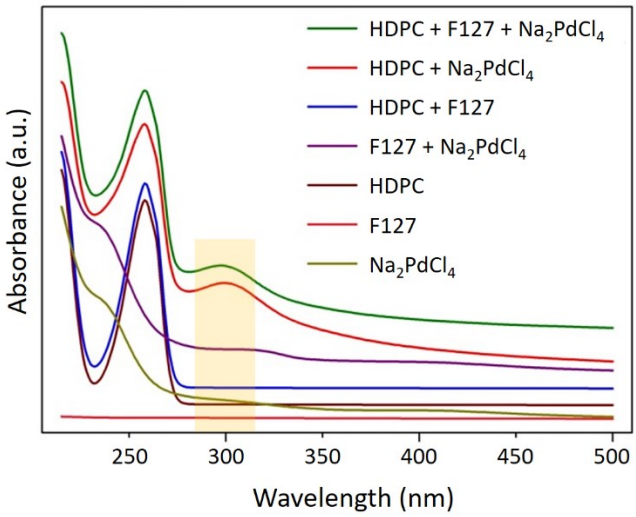

Figure 5.4 Ultraviolet-visible (UV-vis) absorption spectra of various reaction precursors. Reproduced with permission [Y. Yamauchi *et al.*, *Chem. Commun.* 2014, **50**, 11753-11756].

X-ray diffraction (XRD) measurements were carried out for GO, FrGO, and FrGO-Pd. The XRD pattern of GO has a sharp peak at $2\theta = 10.6^{o}$ ($d = 0.79$ nm) which matches the (002) diffraction plane of GO sheets (**Figure 5.3b**). The reduction of GO causes the diffraction peak to shift to $2\theta = 25.0^{o}$ ($d = 0.36$ nm), matching the (002) diffraction plane of rGO.[33] The FrGO has an even smaller interlayer distance, suggesting that some hydroxyl and carboxyl groups are removed during chemical reduction.[34] In the case of the FrGO-Pd sample, besides the (002)-plane rGO diffraction peak at 25.0°, peaks at 40.2°, 46.4°, 67.5°, 81.4° and 85.5° match the (111), (200), (220), (311) and (222) diffraction planes of face-centered cubic (*fcc*) Pd (JCPDS No. 65-2867). Thea average crystallite size of Pd was around 5.49 nm as calculated by Scherrer equation from the first X-ray diffraction peak. This structural data clearly demonstrates that reduction of GO and formation of Pd nanoparticles occurred.

To bolster my explanation of the process to reduce GO into rGO, Raman measurements were recorded on GO, FrGO, and FrGO-Pd samples (**Figure 5.3c**). Raman

spectroscopy is a powerful tool to characterize the structures of carbon materials because defects in the graphite lattice scatter at ~1352 cm^{-1} (the so-called D band), while the E_{2g} mode for sp^2-bonded carbon lattice has a distinct scattering peak at 1591 cm^{-1} (the so-called G band).[34,35] The ratio between *D* and *G* band intensities (I_D/I_G) corresponds to the degree of defects in the graphene network and is inversely correlated with graphitization degree.[36] From **Figure 5.3c**, it was clear that the I_D/I_G value of FrGO and FrGO-Pd samples is higher than GO. This is logical because FrGO and FrGO-Pd will have more defects in the sp^2-bonded carbon lattice compared to GO, hence they have smaller sp^2 domains.[26] In addition, the position of the G band for FrGO is shifted to a higher frequency compared to GO (from 1591 cm^{-1} to 1579 cm^{-1}). This measurement suggests that the FrGO could undergo the graphitic "self-healing" during the reduction process and reflects the successful reduction of GO into rGO as well as restoration of its electrical conductivity.[37]

The role of F127 to modify the rGO surface can be explained more clearly with additional control experiments. I tested other nonionic surfactants, *i.e.* Brij 58 and Pluronic P123 instead of F127 to modify the rGO under the same synthetic conditions. After mixing these surfactants with GO in aqueous solution for 12 hours, a small amount of hydrazine was added and the solution was heated up at 95ºC for 1 hour with mild stirring (further details are located in the experimental section). The reduction of GO enhances electrical conductivity, which is desirable for hybrid carbon/metallic electrocatalyst materials. In the case of Brij 58 and P123 system, the rGO was less dispersed in aqueous solution, which is not good for growing well-dispersed Pd particles on rGO in the solution phase synthesis.[30] **Figure 5.4** shows the three mixtures after the reduction of Pd precursor. Only F127-modified rGO successfully maintained the good dispersion of rGO in an aqueous solution.

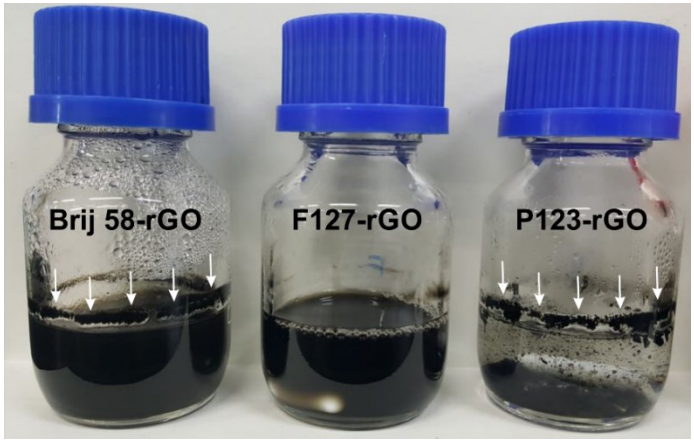

Figure 5.4 Photographs of reaction solutions after reduction and modification of GO by various nonionic surfactants. The white arrows indicate the precipitates of rGO and demonstrate that Brij 58 and P123 are not good at dispersing rGO in the aqueous solution.

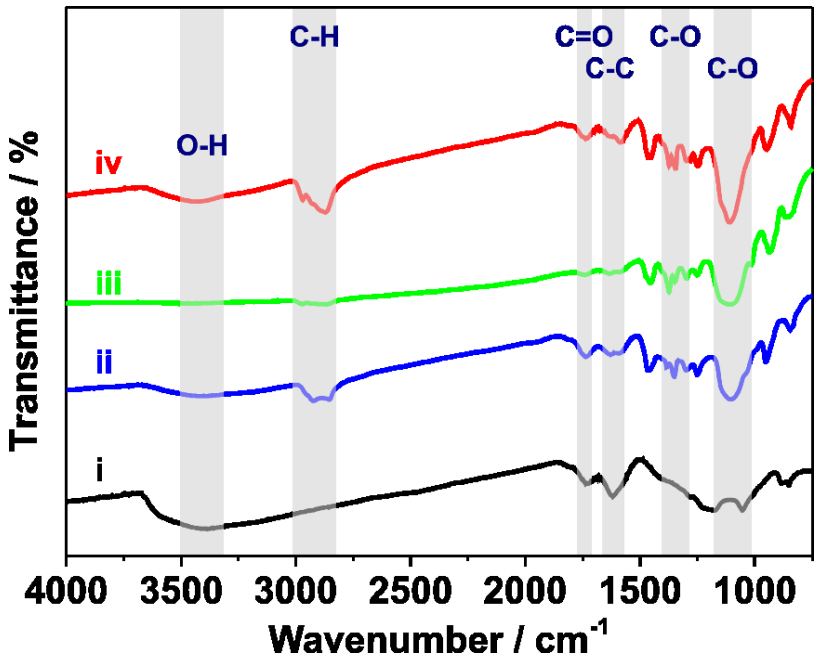

Figure 5.5 FT-IR spectra of (i) GO, (ii) Brij 58-modified rGO, (iii) P123-modified rGO, and (iv) F127-modified rGO (FrGO).

The FT-IR spectra were recorded for GO, rGO and surfactant-modified rGO (*i.e.*, Brij 58-, P123-, and F127-modified rGO) to investigate the functional groups on each sample (**Figure 5.3d** and **5.5**). The GO sample had a peak at 3386 cm^{-1}, which matches the O-H stretch. There were also peaks at 1735, 1617, 1174 and 1052 cm^{-1} which are assigned to C=O (carbonyl/carboxy), C=C (aromatics), C-O (epoxy) and C-O (alkoxy) of GO, respectively. The O-H stretching vibration peak also appears on the surfactant-modified

rGO but it is weaker indicating the rGO will be less soluble in aqueous solutions.[38] Meanwhile, the FT-IR spectra of surfactant-modified GO had new peaks at 2969 and 2869 cm^{-1}, corresponding to C-H asymmetric stretching vibrations (**Figure 5.5**). Interestingly, these new peaks observed on FrGO are more intense than rGO modified with P123 and Brij 58 surfactants. The C-H functional group presumably come from the hydrophilic moiety of the F127 which is utilized to modify the rGO and enhance the dispersion of rGO in aqueous solution. F127 is a block copolymer PEO_{100}-PPO_{70}-PEO_{100} where the EO block is hydrophilic and the PO block is hydrophobic. According to the previous reports, the PO blocks of F127 strongly adsorb and anchor to the rGO surface while the EO blocks form "buoys" which together provide exceptional stability.[39, 40] P123 and Brij 58 also have EO segments (each polymer segment has 20 units of EO block) but unfortunately their length was likely not sufficient to form the anchor-buoy structure and prevent the interaction with other rGO sheets. The combination of fortuitous interactions between F127 and GO and the accompanying the reduction process of GO into modified rGO resulted in exceptional dispersions in aqueous solutions. Additionally, the anchor-buoy type configuration should also assist in the initial attachment Pd seeds and help catalyze the growth of mesoporous Pd nanoparticles on the surface of the FrGO (**Figure 5.2**).

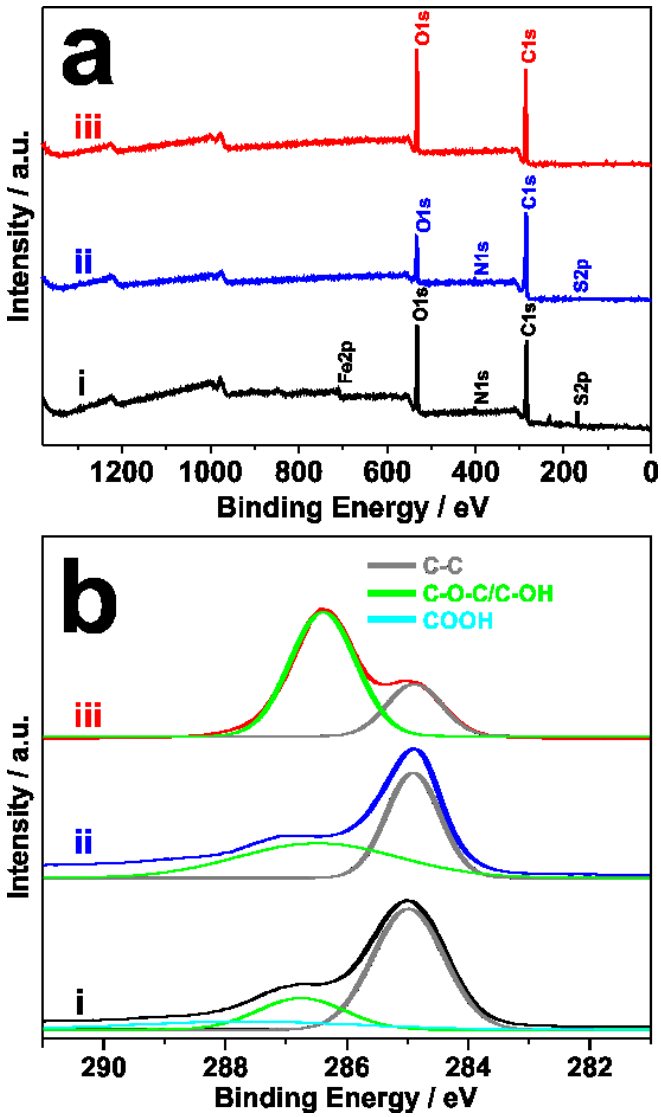

Figure 5.6 (a) Survey XPS spectra and (b) C 1*s* spectra for (i) GO, (ii) rGO and (iii) FrGO, respectively.

Table 5.1 Atomic ratios on GO, rGO and FrGO samples calculated using the XPS data.

Sample	C 1*s*	N 1*s*	O 1*s*	S 2*p*	Fe 2*p*
GO	62.00%	2.30%	30.00%	4.10%	1.60%
rGO	79.50%	1.10%	19.30%	0.10%	--
FrGO	71.70%	--	28.30%	--	--

X-ray photoelectron spectroscopy (XPS) was carried out on GO, rGO, and FrGO to further examine the differences in surface structure. The survey XPS spectra of GO has distinct peaks at ~285 and ~532 eV which can be assigned as C-1*s* and O-1*s*, respectively (**Figure 5.6a**). Impurities such as Fe, N and S were also found in the GO and rGO samples. **Table 5.1** shows a summary of the atomic percentages of C-1*s*, N-1*s*, O-1*s*, S-2*p*, and Fe-

2*p* for GO, rGO and FrGO. Impurities were not completely removed in the rGO. The high-resolution C-1*s* spectra for GO, rGO and FrGO can be deconvoluted to show different carbon moieties (**Figure 5.6b**). The GO sample has three peaks corresponding to sp^2-/sp^3-bonded carbon, epoxy/hydroxy groups (C-O-C/C-OH) and carboxyl groups (-COOH) (Note: Because the binding energy of epoxy and hydroxy groups are similar, here I dealt with two contributions as one combined peak.).[35] Meanwhile, only two peaks were obvious in the rGO and FrGO samples. These peaks correspond to sp^2-/sp^3-bonded carbon, epoxy/hydroxy groups (C-O-C/C-OH). The dramatic increase in the peak representing the epoxy/hydroxy groups is caused by the ethylene oxide (EO) block of F127 on the rGO surface, supporting previous FT-IR measurement that showing that F127 is on the rGO surface. From the difference of C/O atomic ratio, the degree of reduction of the surfaces can be roughly calculated.[34] The C/O atomic ratio of rGO and FrGO is 4.1 and 2.5, respectively, which is higher than GO (2.0). The lower C/O ratio of FrGO compared to rGO is due to adsorbed F127 (with C/O ratio of 2.13) polymer.

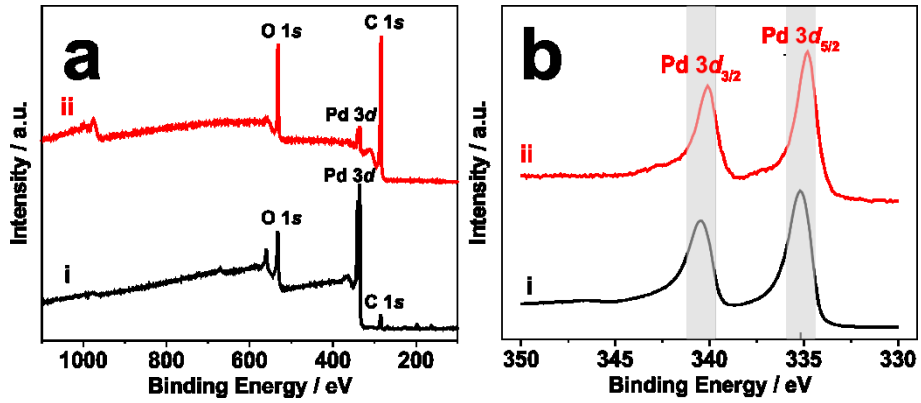

Figure 5.7 (a) Survey XPS spectra and (b) high-resolution Pd 3*d* XPS spectra of (i) mesoporous Pd nanoparticles without rGO support and (ii) FrGO-Pd.

Figure 5.7a shows the XPS spectra for mesoporous Pd versus FrGO-Pd. Three distinct peaks were observed in the XPS survey spectra at ~285, ~335 and ~532 eV which correspond to C-1*s*, Pd-3*d* and O-1*s*, respectively. High-resolution Pd-3*d* spectra for the FrGO-Pd sample had peaks at 334.8 and 340.1 eV, which match Pd-3$d_{5/2}$ and Pd-3$d_{3/2}$, respectively (**Figure 5.7b**). Interestingly, the Pd-3*d* peaks of FrGO-Pd are slightly shifted to lower binding energies compared to the Pd-3*d* peaks of mesoporous Pd nanoparticles without rGO (335.2 eV to 334.8 eV and 340.5 eV to 340.1 eV for Pd-3$d_{5/2}$ and Pd-3$d_{3/2}$, respectively). This lower binding energy of the Pd electronic state in FrGO-Pd suggests

there is additional of valence electron charge.[41] In the present study, I assume that the rGO donated an electron to the Pd atoms, promoting stronger interaction between the nanoparticle and substrate.[42]

5.4. Electrocatalytic Activity of Tethered Mesoporous Pd Nanopartciels on Functionalized Reduced Graphene Oxide

Pd is more Earth abundant than Pt and is a promising candidate for its replacement in electrocatalytic reactions. However, in general Pd catalysts do not exceed the performance of Pt electrocatalysts in fuel cell applications.[11,12] I examined the potential of FrGO-Pd in the electrooxidation of formic acid. For comparison, commercially-available Pd nanoparticles supported on activated carbon (10 wt%; abbreviated as Pd/C) were selected as a benchmark catalyst (**Figure 5.8**). The cyclic voltammetric (CV) measurement was employed using 0.5 M H_2SO_4 electrolyte at potentials between -0.2 and 1.2 V *vs.* Ag/AgCl to study the electrochemically active surface area (ECSA) of the FrGO-Pd and Pd/C samples. ECSA value not only provides information about the active sites available on the catalyst but also the available conductive path to deliver electrons to the electrode surface.[43] The CV curves show typical hydrogen desorption and surface oxide reduction peak pairs located at approximately -0.1 (positive scan) and +0.5 V (negative scan) *vs.* Ag/AgCl, respectively (**Figure 5.9a**). The ECSAs were estimated by calculating the hydrogen desorption charge after double-layer correction assuming that the conversion factor for a hydrogen monolayer is 240 μC cm^{-2}.[43-46] The ECSA value for FrGO-Pd was 85.89 m^2 g^{-1} which is 2.9 times higher than that of Pd/C (29.43 m^2 g^{-1}), even exceeding the highest ECSA values of similar Pd nanoparticles[18] and other graphene/rGO-supported Pd electrocatalyst materials previously reported in the literature (**Table 5.2**). The improvement of active sites of the FrGO sample can be attributed to the rough features of the Pd nanoparticles. In addition, the modified rGO support provides more accessible conductive path for the transfer of charged ion on the electrode surface.[47]

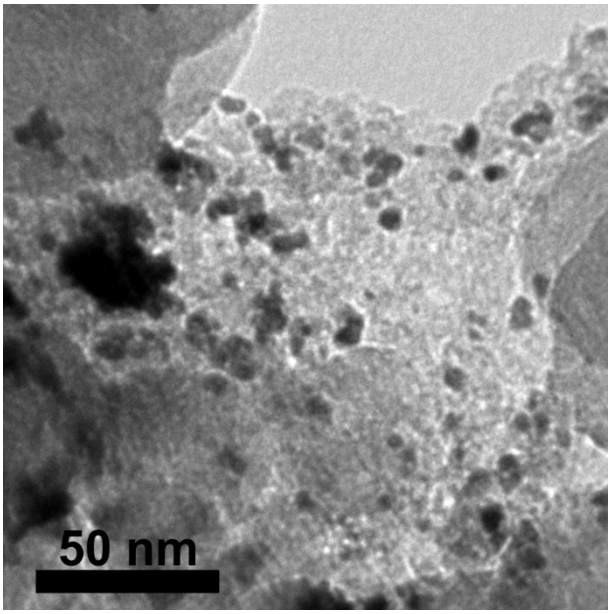

Figure 5.8 TEM image of commercially-available Pd/C electrocatalyst.

To compare the performance of FrGO-Pd and Pd/C in catalyzing oxidation of formic acid, the CV curves were recorded in 0.5 M H_2SO_4 electrolyte containing 0.5 M HCOOH at scan rate of 50 mV s^{-1} in the potential range from -0.2 to 0.9 V. The CV curves are normalized by respective mass and ECSA to obtain mass activity and specific activity (**Figure 5.9b-c**). Obviously, FrGO-Pd sample has significantly larger mass activity (1,752.2 mA mg^{-1}_Pd) compared to Pd/C (376.8 mA mg^{-1}_Pd). The highest mass activity of similar mesoporous Pd nanoparticles without modified rGO support under identical CV conditions was 735.6 mA mg^{-1} Pd.[18] Even when normalized by the ECSA, the FrGO-Pd sample exhibited a specific activity 1.6-times higher than commercial Pd/C. Using the rGO as the support prevented agglomeration of mesoporous Pd nanoparticles, thereby helping to maintain its high surface area. The ECSA and electrocatalytic activities of the FrGO-Pd are greater than other carbon supported Pd-based electrocatalyst materials reported by other groups (**Table 5.2**). Furthermore, the stability test of electrocatalyst was carried out by chonoamperometry in 0.5M H_2SO_4 electrolyte containing 0.5 M HCOOH at fixed potential of 0.3 V *vs*. Ag/AgCl for 1500 s (**Figure 5.9d**). The FrGO-Pd sample shows better stability than commercial Pd/C sample. These electrochemical results demonstrate a synergistic interaction between the mesoporous Pd nanoparticles and rGO to generate catalytic performance that is greater than the sum of its component parts.

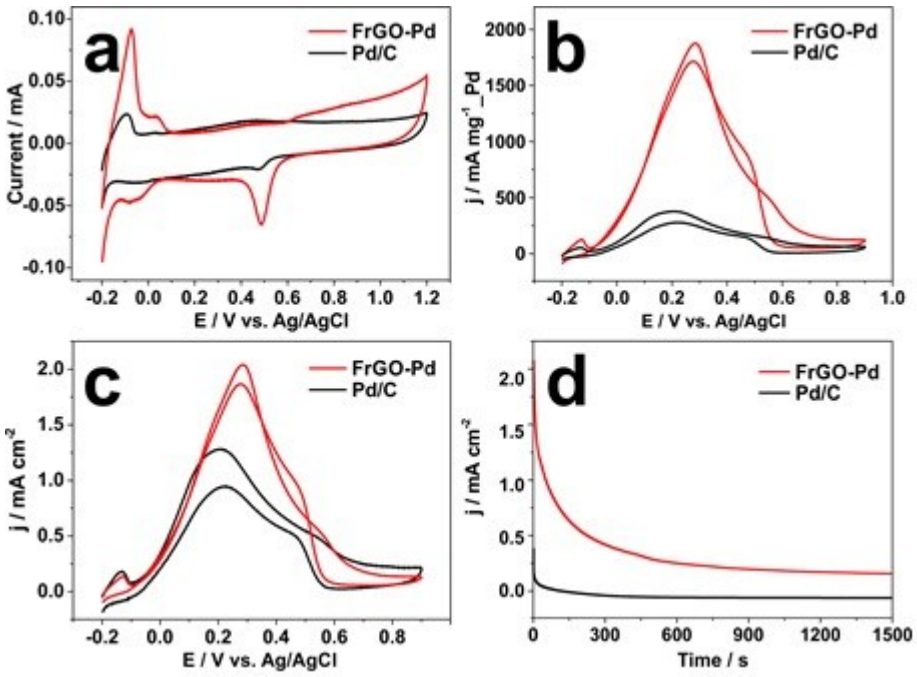

Figure 5.9. (a) CV curves of FrGO-Pd and Pd/C samples in 0.5 M H_2SO_4 electrolyte at a scan rate of 50 mV s^{-1} in the potential range from -0.2 to 1.2 V. (b) Mass-normalized and (c) ECSA-normalized CV curves of FrGO-Pd and Pd/C in 0.5 M H_2SO_4 containing 0.5 M HCOOH at a scan rate of 50 mV s^{-1} in the potential range from -0.2 to 0.9 V on the first CV cycle. (d) ECSA-normalized amperometric *i-t* curve of FrGO-Pd and Pd/C samples in 0.5 M H_2SO_4 containing 0.5 M HCOOH at potential of 0.3 V for 1,500 s. All the applied potentials are referenced to a Ag/AgCl reference electrode.

Table 5.2 A comparison of the surface area and mass activity of my FrGO-Pd sample versus other graphene-supported Pd electrocatalyst materials previously reported in the literature.

Sample Name	Surface Area ($m^2 g^{-1}$)	Condition	Scan rate ($mV s^{-1}$)	Mass Activity ($mA mg^{-1}$_Pd)	Ref.
FrGO-Pd	85.69	0.5 M H_2SO_4 + 0.5 M HCOOH	50	1,752.2	This chapter
La_2O_3 promoted Pd/rGO	57.80	0.25 M H_2SO_4 + 1.0 M HCOOH	50	986.42	[48]
rGO supported Pd nanoparticles	41.8	0.5 M H_2SO_4 + 0.5 M HCOOH	50	902	[49]
Pd nanoparticles on graphitic carbon nitride-modified rGO	107.5	0.5 M H_2SO_4 + 0.5 M HCOOH	50	1,610	[50]
Pd nanoparticles on rGO-tungsten carbide composite	81.22	0.5 M H_2SO_4 + 1.0 M HCOOH	20	-	[51]
Pd/PW_{12}/rGO Composite	-	0.5 M H_2SO_4 + 1.0 M HCOOH	50	955	[52]
Pd nanoparticles on graphene	-	0.25 M H_2SO_4 + 0.25 M HCOOH	50	7	[53]
Pd with graphene/carbon black binary carbon supports	13.24 cm^2	0.5 M H_2SO_4 + 0.5 M HCOOH	10	102.14	[54]
Graphene nanosheets support Pd nanodendrites	38.6	0.25 M H_2SO_4 + 0.25 M HCOOH	50	9.86	[55]

5.5. Conclusions

Three-dimensional mesoporous Pd nanoparticles supported on surfactant-modified rGO were prepared with a simple solution phase process. Uniformly sized spherical Pd nanoparticles with mesoporous structure were grown on the surfactant-modified rGO surface. Compared to other nonionic surfactants tested, Pluronic F127 enhanced the solubility enhancement of rGO in the aqueous solution due the existence of particular functionalities. XPS and XRD measurements both demonstrate the successful formation of

hybrid rGO and Pd nanoparticles where the Pd nanoparticles were tethered to the F127-modified rGO surface. The hybrid FrGO-Pd has a promising potential for catalyzing the oxidation of formic acid molecules in acidic medium. In electrocatalytic measurements the hybrid FrGO-Pd exhibited superior active surface area, specific activity as well as stability compared to the commercial Pd/C catalysts. These results demonstrate that higher performing electrocatalysts are feasible by employing hybrid structures of metallic nanoparticles tethered to rGO.

5.6. References

[1] M. B. Gawande, A. Goswami, T. Asefa, H. Guo, A. V. Biradar, D. L. Peng, R. Zboril and R. S. Varma, *Chem. Soc. Rev.* 2015, **44**, 7540-7590.

[2] J. Bai, C. L. Fang, Z. H. Liu and Y. Chen, *Nanoscale*, 2016, **8**, 2875-2880.

[3] S. Sui, X. Wang, X. Zhou, Y. Su, S. Riffat and C. J. Liu, *J. Mater. Chem. A*, 2017, **5**, 1808-1825.

[4] Z. Fan and H. Zhang, *Chem. Soc. Rev.*, 2016, **45**, 63-82.

[5] S. Sadjadi and M. M. Heravi, *RSC Adv.*, 2016, **6**, 88588-88624.

[6] M. H. Sun, S. Z. Huang, L. H. Chen, Y. Li, X. Y. Yang, Z. Y. Yuan and B. L. Su, *Chem. Soc. Rev.*, 2016, **45**, 3479-3563.

[7] Y. W. Lee, E. T. Hwang, D. H. Kwak and K. W. Park, *Catal. Sci. Technol.*, 2016, **6**, 569-576.

[8] X. Yu, F. Luo and Z. Yang, *RSC Adv.*, 2016, **6**, 98861-98866.

[9] G. A. Somorjai and Y. Li, *Introduction to Surface Chemistry and Catalysis (2nd Edition)*, John Wiley & Sons, New Jersey, 2010.

[10] M. A. Abbas and J. H. Bang, *Chem. Mater*., 2015, **27**, 7218–7235.

[11] A. Chen and C. Ostrom, *Chem. Rev.*, 2015, **115**, 11999–12044.

[12] A. Morozan, B. Jousselme and S. Palacin, *Energy Environ. Sci.*, 2011, **4**, 1238-1254.

[13] C. Bianchini and P. K. Shen, *Chem. Rev.,* 2009, **109**, 4183–4206.

[14] F. Wang, C. Li, L. D. Sun, C. H. Xu, J. Wang, J. C. Yu, and C. H. Yan, *Angew. Chem. Int. Ed.*, 2011, **51**, 4872-4876.

[15] C. Koenigsmann, E. Sutter, T. A. Chiesa, R. R. Adzic and S. S. Wong, *Nano Lett.*, 2012, **12**, 2013–2020.

[16] W. Liu, A. K. Herrmann, D. Geiger, L. Borchardt, F. Simon, S. Kaskel, N. Gaponik and A. Eychmuller, *Angew. Chem. Int. Ed.*, 2012, **51**, 5743-5747.

[17] C. Wen, Z. Li, C. Cao, Y. Wang, P. Guo and X. Zhao, *RSC Adv*., 2016, **6**, 91991-91998.

[18] C. Li, T. Sato and Y. Yamauchi, *Chem. Commun.*, 2014, **50**, 11753-11756.

[19] M. Iqbal, C. Li, J. H. Kim, S. M. Alshehri, T. Nakayama and Y. Yamauchi, *Chem. Eur. J.*, 2016, **22**, 51-56.

[20] J. Pal and T. Pal, *Nanoscale*, 2015, **7**, 14159-14190.

[21] D. S. Su, S. Perathoner and G. Centi, *Chem. Rev.*, 2013, **113**, 5782–5816.

[22] Y. Holade, N. E. Sahin, K. Servat, T. W. Napporn and K. B. Kokoh, *Catalysts*, 2015, **5**, 310-348.

[23] G. Darabdhara, P. K. Boruah, P. Borthakur, N. Hussain, M. R. Das, T. Ahamad, S. M. Alshehri, V. Malgras, K. C.-W. Wu and Y. Yamauchi, *Nanoscale*, 2016, **8**, 8276.

[24] S. Dutta, A. Bhaumik and K. C.-W. Wu, *Energy Environ. Sci.*, 2014, **7**, 3574.

[25] L. Castanheira, L. Dubau, M. Mermoux, G. Berthome, N. Caque, E. Rossinot, M. Chatenet, and F. Maillard, *ACS Catal.*, 2014, **4**, 2258-2267.

[26] S. Stankovich, D. A. Dikin, R. D. Piner, K. A. Kohlhaas, A. Kleinhammes, Y. Jia, Y. Wu, S. T. Nguyen and R. S. Ruoff, *Carbon*, 2007, **45**, 1558-1565.

[27] M. Liu, R. Zhang and W. Chen, *Chem. Rev.*, 2014, **114**, 5117-5160.

[28] A. Ambrosi, C. K. Chua, A. Bonanni and M. Pumera, *Chem. Rev*., 2014, **114**, 7150-7188.

[29] D. Chen, H. Feng and J. Li, *Chem. Rev.*, 2012, **112**, 6027-6053.

[30] C. K. Chua and M. Pumera, *Chem. Soc. Rev.*, 2014, **43**, 291-312.

[31] T. Li, A. J. Senesi and B. Lee, *Chem. Rev.*, 2016, **116**, 11128−11180.

[32] J. Teixeira, *J. Appl. Crystallogr.*, 1988, **21**, 781-785.

[33] H. Feng, R. Cheng, X. Zhao, X. Duan and J. Li, *Nat. Commun*., 2013, **1539**, 1-7.

[34] N. A. Kumar, S. Gambarelli, F. Duclairoir, G. Bidan and L. Dubois, *J. Mater. Chem. A*, 2013, **1**, 2789–2794.

[35] D. Yang, A. Velamakanni, G. Bozoklu, S. Park, M. Stoller, R. D. Piner, S. Stankovich, I. Jung, D. A. Field, C. A. Ventrice Jr. And R. S. Ruoff, *Carbon*, 2009, **47**, 145-152.

[36] P. T. Araujo, M. Terrones and M. S. Dresselhaus, *Mater. Today*, 2012, **15**, 98-109.

[37] K. N. Kudin, B. Ozbas, H. C. Schniepp, R. K. Prud'homme, I. A. Aksay and R. Car, *Nano Lett*., 2008, **8**, 36-41.

[38] V. Georgakilas, J. N. Tiwari, K. C. Kemp, J. A. Perman, A. B. Bourlinos, K. S. Kim and R. Zboril, *Chem. Rev*., 2016, **116**, 5464−5519.

[39] Q. Ke, Y. Liu, H. Liu, Y. Zhang, Y. Hu and J. Wang, *RSC Adv.* 2014, **4**, 26398–26406.

[40] Y. Yan, L. Piao, S. H. Kim, W. Li, and H. Zhou, *RSC Adv*. 2015, **5**, 40199–40204.

[41] E. G. Espino, G. Hu, A. Shchukarev and T. Wagberg, *J. Am. Chem. Soc*., 2014, **136**, 6626-6633.

[42] Z. Liu, Y. Feng, X. Wu, K. Huang, S. Feng, X. Dong, Y. Yang and B. Zhao, *RSC Adv*., 2016, **6**, 98708-98716.

[43] Y. S. Dong, S. C. Min, T. Hao, H. Wei, Z. X. Gang and G. H. Jun, *Chin. Phys. B*, 2011, **20**, 113301.

[44] L. B. Sheridan, Y. G. Kim, B. R. Perdue, K. Jagannathan, J. L. Stickney and D. B. Robinson, *J. Phys. Chem. C*, 2013, **117**, 15728-15740.

[45] J. Zhao, Z. Liu, H. Li, W. Hu, C. Zhao, P. Zhao, and D. Shi, *Langmuir*, 2015, **31**, 2576-2583.

[46] H. Ali, F. K. Kanodarwala, I. Majeed, J. A. Stride and M. A. Nadeem, *ACS Appl. Mater. Interfaces*, 2016, **8**, 32581−3259.

[47] Y. J. Wang, N. Zhao, B. Fang, H. Li, X. T. Bi and H. Wang, *Chem. Rev.* 2015, **115**, 3433–3467.

[48] H. Ali, F. K. Kanodarwala, I. Majeed, J. A. Stride and M. A. Nadeem, *ACS Appl. Mater. Interfaces*, 2016, **8**, 32581−3259.

[49] X. Gao, F. Li, Y. Li, S. Li, Y. Chen, Y and J. M. Lee, *Journal of Power Sources*, 2015**, 280**, 491-498.

[50] W. Zhang, H. Huang, F. Li, K. Deng and X. Wang, *J. Mater. Chem. A*, 2014, **2**, 19084-19094.

[51] M. Shi, W. Liu, D. Zhao, Y. Chu and C. Ma, *J. Solid State Electrochem.*, 2014, **18**, 1923-1932.

[52] X. Zhang, X. Wang, L. Le, A. Ma, and S. Lin, *J. Electrochem. Soc.*, 2016, **163**, F71-F78.

[53] S. Yang, C. Shen, Y. Tian, X. Zhang and H. J. Gao, *Nanoscale*, 2014, **6**, 13154–13162.

[54] M. Lv, W. Li, H. Liu, W. Wen, G. Dong, J. Liu and K. Peng, *Chinese J. Catal.*, 2017**, 38**, 939–947.

[55] Y. S. Dong and C. Lin, *Chin. Phys. B*, 2015, **24**, 118104.

Chapter 6

6. PdCu Mesoporous Nanospheres

6.1. Introduction

The electronic and physiochemical properties of noble metal nanoparticles depend on their size, shape, exposed crystallographic facets and alloy compositions. Colloidal synthetic methods used to generate noble metal nanoparticles have drawn huge attention due to their simplicity, high yields, and effectiveness.[1-4] Both theoretical and experimental studies show that the surface structure affects the electronic properties of catalysts and their active sites.[5-8] Various kinds of ultra-small metal nanocatalysts with well-defined shapes (*e.g.*, cube, tetrahedral, octahedral, and dodecahedral shapes) have been developed and they possess high performance in various catalytic reactions.[9-12] However, the these tiny nanocatalysts are particularly vulnerable to dissolution or aggregation which leads to performance degradation.[13]

Palladium (Pd) metal is a highly active catalyst for many heterogenous chemical reactions including the oxidation of hydrogen and small organic molecules, hydrogenation of acetylene, and various coupling reactions.[14-17] Pd belongs to the same group as platinum (Pt) and has a similar face-centered cubic (*fcc*) crystal structures. But Pd is relatively more abundant in nature than Pt, and Pd has the potential to promote a less- or non-Pt based nanocatalyst which could result in a more economically viable catalyst material.[18,19] Combining Pd with cheaper metals such as Ni, Co, Cu is a viable strategy to reduce the need for noble-metals and can also enhance the activity of the catalyst and improve its stability against poisoning effects.[20,21] Both previous theoretical and experimental studies show that a good interaction of the noble-metal with the second element in an alloy nanocatalyst could enhance the electronic properties resulting in the improvement of catalytic activity and stability.[22-24] Despite the great success of controlled synthesis of ultrasmall Pd nanocatalyst with various sizes and morphologies, an efficient one-pot approach to prepare well-organized three-dimensional (3D) Pd alloys structures with the abundant of active sites remains a great challenge.[25]

Herein, I describe a method to create 3D spherical palladium-copper (PdCu) alloy nanoparticles with an open porous network and uniform morphology using PS-*b*-PEO block copolymers micelles as pore directing agents and sacrificial tempates (**Scheme 1**). The micelles were dissolved with Pd and Cu precursor in a mixture of tetrahydrofuran (THF), water, sulfuric acid, and ascorbic acid. In such a reaction system, THF promotes dissolution of the block copolymer into free unimer in the solution. The subsequent

additions of water induce the micellization of the block copolymer. The ethanol oxidation reaction (EOR) was used as a model reaction to evaluate the electrocatalytic performance of the obtained PdCu MNs versus commercil palladium black catalyst. The electrocatalytic test revealed that the PdCu MNs displayed superior electrocatalytic activity for the EOR, owing to the large surface-active area, open accessible pores, and stable 3D spherical structure.

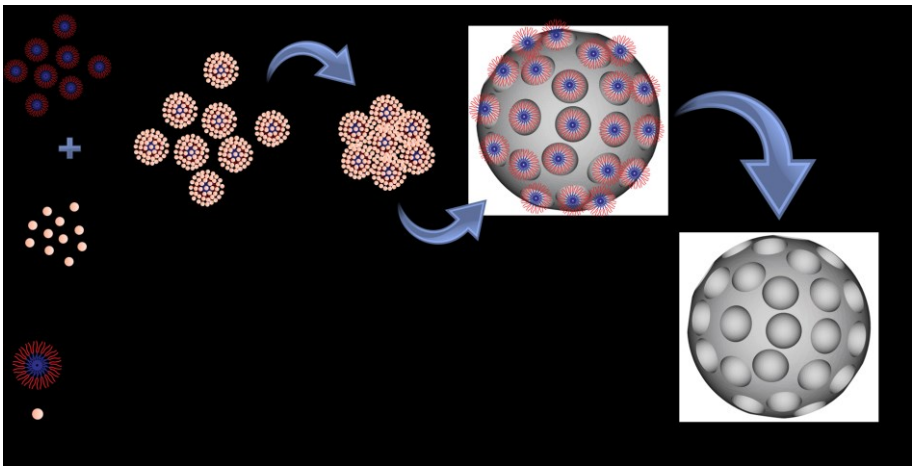

Scheme 6.1. Illustration of the formation mechanism of PdCu mesoporous nanospheres via micelles-assembly assisted chemical reduction approach.

6.2. Experimental Section

6.2.1. Materials

Block copolymer poly(styrene)-*b*-poly(ethylene oxide) ($PS_{(5000)}$-*b*-$PEO_{(2200)}$) was purchased from Polymer Source, Inc., Canada. Palladium(II) chloride ($PdCl_2$), hydrochloric acid (HCl, 35%), ethanol (C_2H_5OH), potassium hydroxide (KOH, 1 M), sulfuric acid (H_2SO_4), and ascorbic acid (AA) were obtained from Nacalai Tesque, Japan. Copper(II) sulfate ($CuSO_4$) and tetrahydrofuran (THF) were purchased from Wako Chemicals, Japan. Palladium black (PdB) and Nafion® resin solution (~5% in a mixture of lower aliphatic alcohol and water) were obtained from Sigma Aldrich. All chemicals were used as is without further purification. Deionized (DI) water used in the experiment was obtained through a water purification system Merck Milli-Q®.

6.2.2. Synthesis of PdCu Mesoporous Nanospheres

All of the methods used to prepare mesoporous nanospheres were performed via chemical reduction in solution. In a typical synthesis, 4 mg of $PS_{(5000)}$-*b*-$PEO_{(2200)}$ was dissolved by sonication in 80 μL THF. Subsequently, 0.49 mL of DI water was added to induce the micellization of the polymer. Then palladium (80 mM) and copper (80 mM) precursor solutions (0.25 mL in total) were added to the micellar solution followed by the addition of 1 mL of 0.1 M AA and 180 μL of 2 M H_2SO_4. The molar ratio of Pd and Cu precursor solutions was fixed at 1:9, 1:1, and 9:1. The solution was then allowed to sit on the oil bath at 80 ^oC for 2 h. After 2 h, the solution turns into dark color and was cooled down into room temperature then washed with THF to remove the polymers and centrifuged consecutively several times (at 14,000 rpm for 10 min for each cycle). The washed samples were then dissolved in DI water and kept for further characterization and electrochemical measurement.

6.2.3. Synthesis of Pd Mesoporous Nanospheres

The preparation of pure Pd MNs was identical with the preparation of PdCu MNs except for the addition of the copper precursor solution.

6.2.4. Characterizations

The morphology of the PdCu MNs was examined by field emission scanning electron microscopy (FESEM; Hitachi SU-8230 at accelerating voltage of 5 kV). Transmission electron microscope (TEM), high-resolution TEM (HR-TEM), high-angle annular dark-field (HAADF) images and energy dispersive X-ray (EDX) mapping were obtained with a JEOL JEM-2100F at an accelerating voltage of 200 kV. Wide-angle X-ray diffraction (XRD) pattern was acquired with a Rigaku RINT Ultima III equipped with a Cu Kα X-ray source. Ultraviolet-visible (UV-Vis) absorption spectroscopy of the electrolyte solutions was performed by a JASCO V-7200.

6.2.5. Electrochemical Measurement

All electrochemical measurements were recorded using a CHI 842B electrochemical analyzer (CH Instruments, USA). A conventional three-electrode set-up was employed to carry out the electrochemical measurements. A glassy carbon electrode (GCE, 3 mm in diameter) was used as the working electrode by coating it with the electrocatalysts. Prior

to the coating step, the GCE was polished with 1.0 and 0.05 μm diameter alumina powder, rinsed with deionized water, and dried under a flow of nitrogen gas. Then 5.0 μg of the as-prepared PdCu 1:9 MNs (denoted sample i), PdCu 1:1 MNs (sample ii), PdCu 9:1 MNs (sample iii), Pd MNs (sample iv) or commercially available Pd black (sample v) suspension was coated on the surface of the GCE. After drying under atmospheric conditions, a Nafion® solution (5.0 μL, 0.5 wt%) was subsequently coated on the GCE surface and dried at room temperature before further electrochemical measurements. A platinum wire and Ag/AgCl (or standard calomel, SCE) electrode were employed as the counter and reference electrodes, respectively. In order to obtain a clean catalyst surface prior to the electrochemical investigations, the modified GCE was treated electrochemically by applying –0.2 V to 1.5 V (*vs.* Ag/AgCl) for 100 cycles at a scan rate of 500 mV s^{-1}. Cyclic voltammograms were recorded in 0.5 M H_2SO_4 electrolyte at a scan rate of 50 mV s^{-1} over a potential range spanning –0.2 to 1.2 V (*vs*. Ag/AgCl). The ethanol oxidation reaction (EOR) was used to test the electrocatalytic performance of the MNs. These electrocatalytic measurements were recorded in 1.0 M KOH containing 1.0 M C_2H_5OH over a potential range of -0.8 to 0.3 V (*vs*. SCE). All the CV measurements were repeated 3 times for each sample. Amperometric *i-t* curves were recorded to study the stability of the catalysts at a fixed potential of -0.2 V (*vs*. SCE) for 1,000 s in 1.0 M KOH containing 1.0 M C_2H_5OH.

6.3. Characterization of PdCu Mesoporous Nanospheres

The as-prepared sample morphologies were examined by SEM and TEM (**Figures 6.1** and **6.2**). All the samples were spherical, with an average diameter of 83.7 nm, 101.9 nm, and 109.5 nm for PdCu 1:9 MNs, PdCu 1:1 MNs, and PdCu 9:1 MNs, respectively (**Figure 6.1**). The diameters of the particles were calculated by averaging ~100 particles. Higher magnification SEM and HR-TEM images revealed that each spherical particle with riddled with well-defined ~10-nm diameter mesopores with interconnected pore walls (**Figures 6.1a2-c2** and **2a-c**). The contrast difference in the TEM and HAADF-STEM images of the PdCu MNs shows that the pores are uniformly distributed throughout the exterior and interior spaces of the nanospheres (**Figures 6.2a, b** and **6.3**). This interconnected porous network is expected to expose a large proportion of the surface area of the metal to the outside environment and generate abundant sites for catalytic applications. Both stepped

and kinked atomic arrangements can be clearly observed in HR-TEM images focused on the edges of the nanospheres (**Figure 6.2d**). The HR-TEM image in **Figure 6.2d** has continuous fringes running throughout the nanosphere subunit, with a lattice spacing of d = 0.221 nm which matches the approximate spacing of the (111) crystal plane of an alloyed PdCu *fcc* structure. This effect is most clear in the fast Fourier transform (FFT) pattern of the atomic lattice fringe (**Figure 6.2d, inset**).

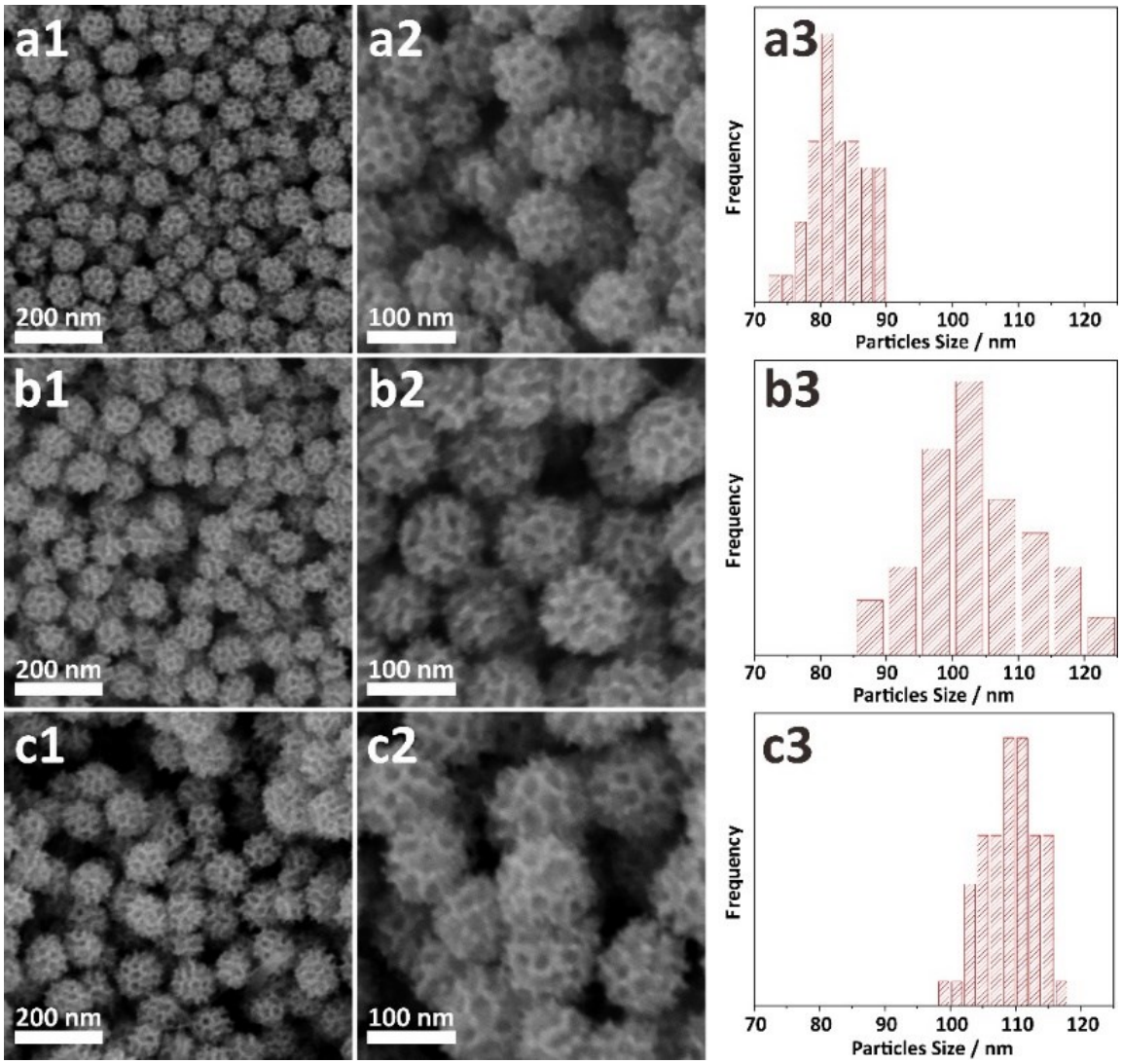

Figure 6.1 (a1-c1) Low and (a2-c2) high-magnification SEM and (a3-c3) the corresponding particles size distribution of (a) PdCu 1:9 MNs, (b) PdCu 1:1 MNs, and (c) PdCu 9:1 MNs.

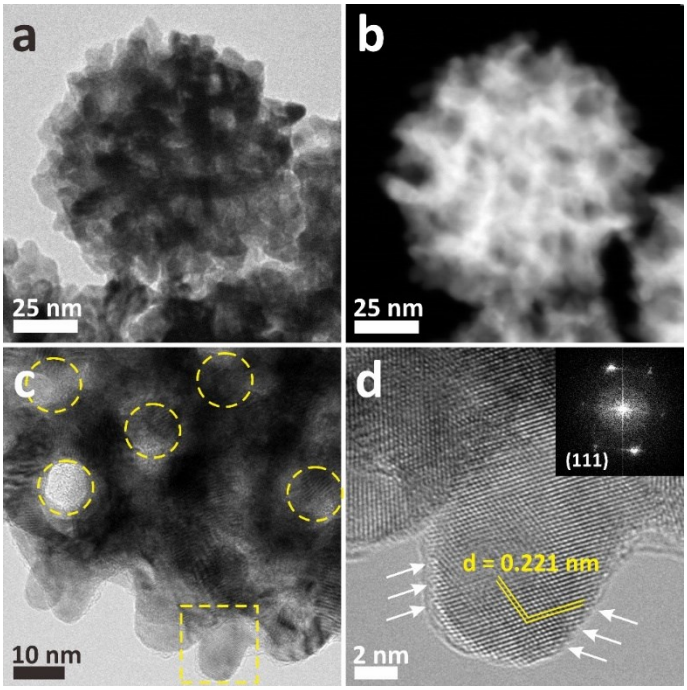

Figure 6.2 (a) TEM, (b) HAADF-STEM, (c) low and (d) high-magnification HR-TEM of PdCu 1:1 MNs. The yellow dashed circles in panel (c) represent the pores formed on a single nanosphere. Panel (d) is the enlarged area marked by yellow dashed square in panel (c). The white arrows in panel (d) highlight the stepped and kinked atomic arrangement on the edge of the nanosphere. The inset in panel (d) depicts the corresponding FFT pattern.

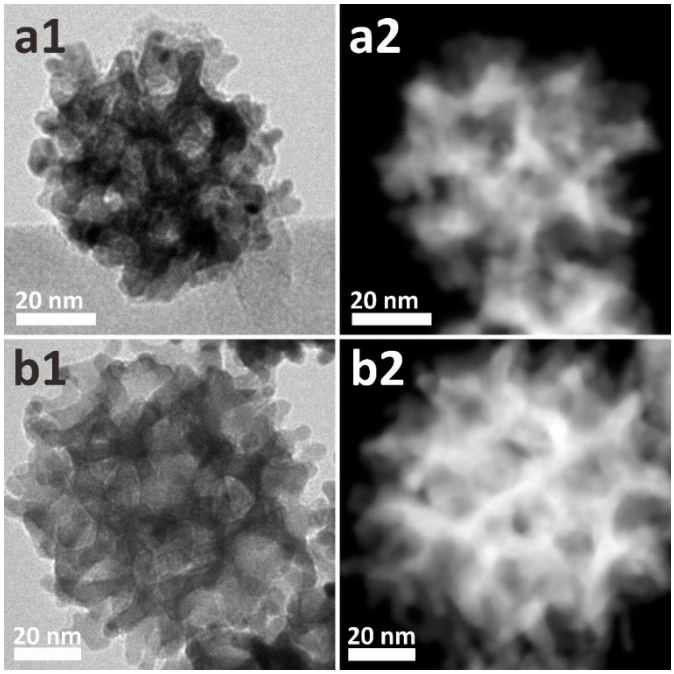

Figure 6.3 (a1,b1) TEM and (a2,b2) HAADF-STEM of (a) PdCu 1:9 MNs and (b) PdCu 9:1 MNs.

To confirm the compositions of the as-prepared nanospheres, the detailed investigations were carried out with XRD and EDX (**Figure 6.4a** and **6.5**). In comparison to the standard diffraction patterns of neat Pd or Cu, all the diffraction patterns of the PdCu MN samples have subtle deviations in angle. The diffraction peaks observed can be assigned to the (111), (200), (220), (311), and (222) diffraction planes of *fcc* PdCu alloy, respectively (**Figure 3a**).[26] No other diffraction peaks were observed, suggesting the formation of a single-phase PdCu alloy. Vegard's law allows us to predict the *d*-spacing of each alloy sample based on composition: 0.220 nm, 0.218 nm, and 0.224 nm for PdCu 1:9 MNs, PdCu 1:1 MNs, and PdCu 9:1 MNs, respectively. Although the initial molar ratio of Pd and Cu was fixed at 1:9, 1:1, and 9:1, it was predicted that the molar ratios of the final products were slightly different. In metallic alloy synthesis *via* chemical reduction methods, the deposition of the constituent metals typically occur through a co-deposition process. The standard reduction potential for Cu^{2+} species (Cu^{2+}/Cu=0.34 V vs. standard hydrogen electrode (SHE)) is ~3-times lower than the Pd species (Pd^{2+}/Pd=0.91 V vs. SHE), hence the reduction of Cu^{2+} is expected to be more difficult than Pd^{2+} in the present study. According to EDX, the molar ratios of Pd and Cu in the 1:9, 1:1 and 9:1 MN samples were 0.65:0.35, 0.72:0.28, and 0.92:0.08, respectively. The elemental mapping with scanning TEM-EDX shows that Pd and Cu were well-distributed throughout the nanospheres (**Figure 6.4b-d** and **6.6**).

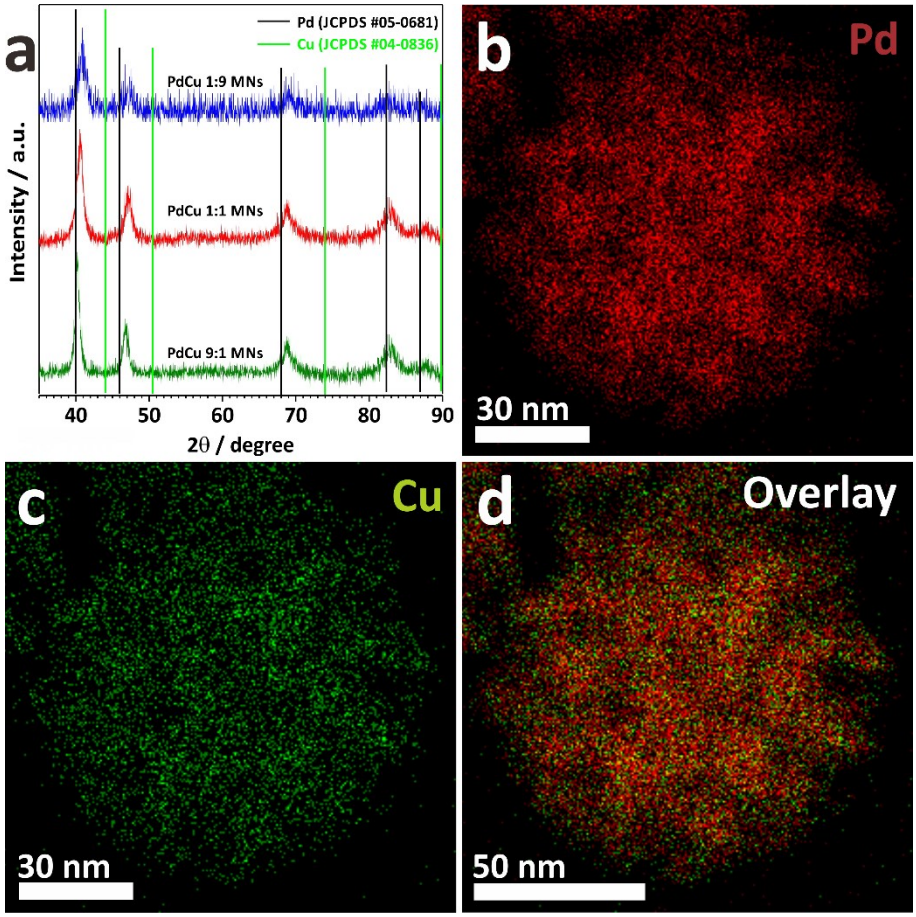

Figure 6.4 (a) Wide-angle XRD of PdCu 1:9 MNs, PdCu 1:1 MNs, and PdCu 9:1 MNs. Elemental mapping of (b) Pd, (c) Cu, and (d) overlay of a single PdCu 1:1 mesoporous nanosphere.

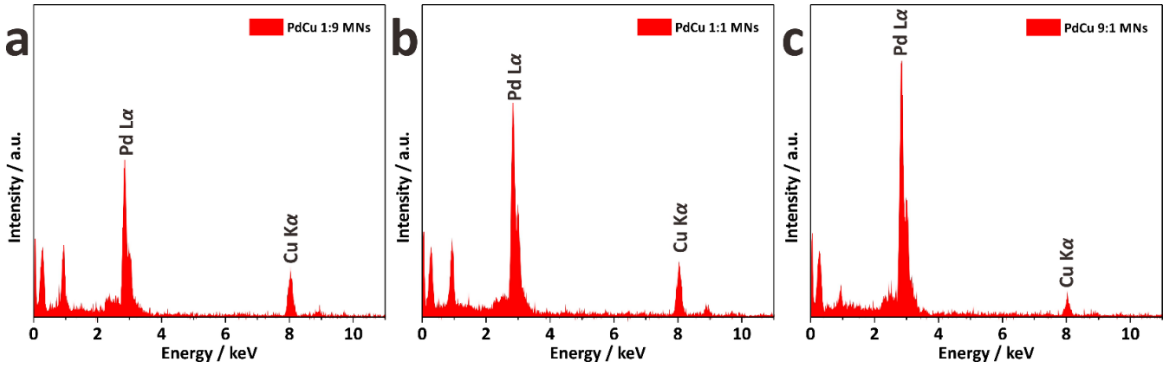

Figure 6.5 EDX spectra of (a) PdCu 1:9 MNs, (b) PdCu 1:1 MNs, and (c) PdCu 9:1 MNs.

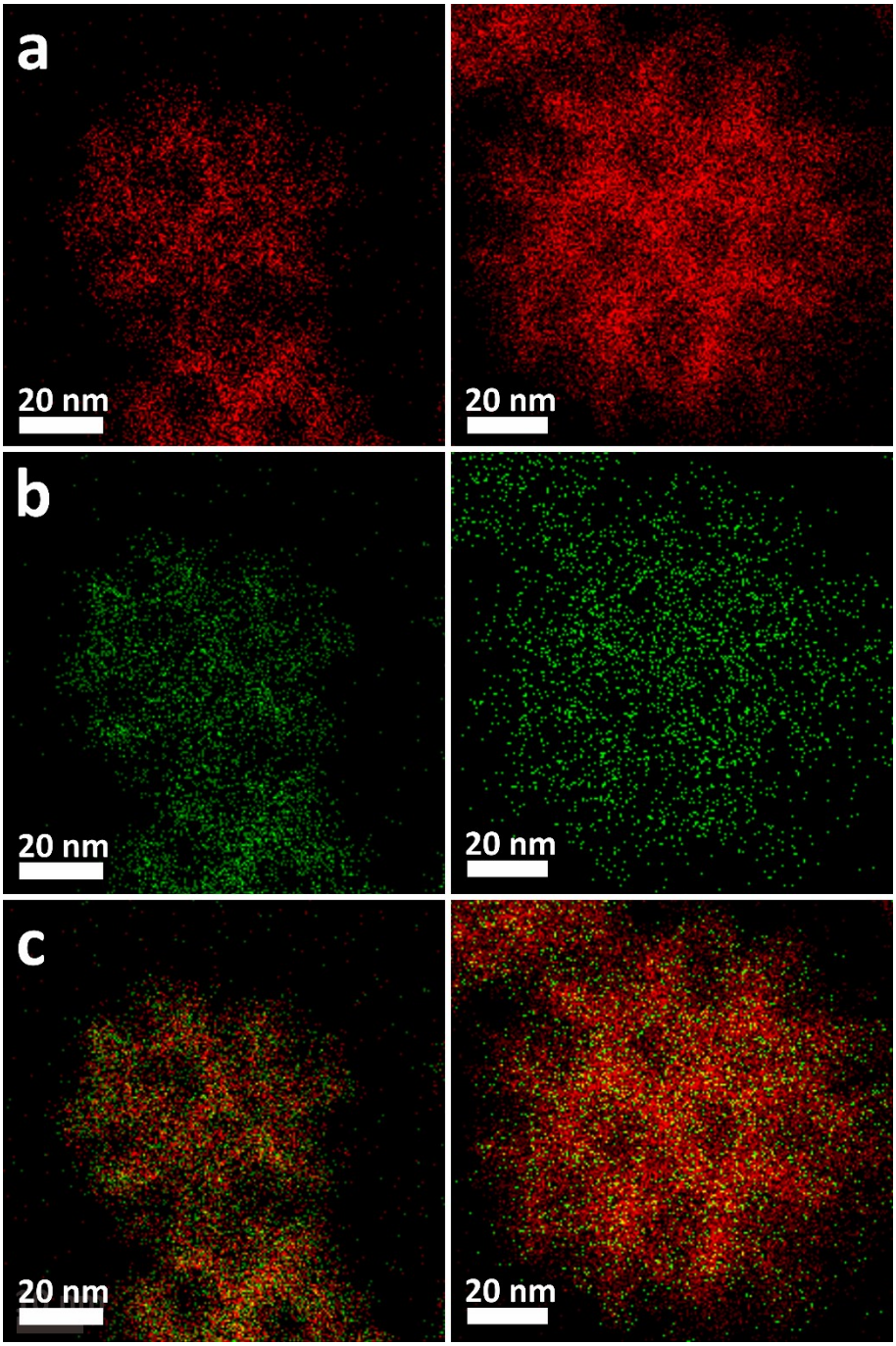

Figure 6.6 Elemental mapping of (a) Pd, (b) Cu, and (c) overlay of a single PdCu 1:9 MNs (left panel) and PdCu 9:1 MNs (right).

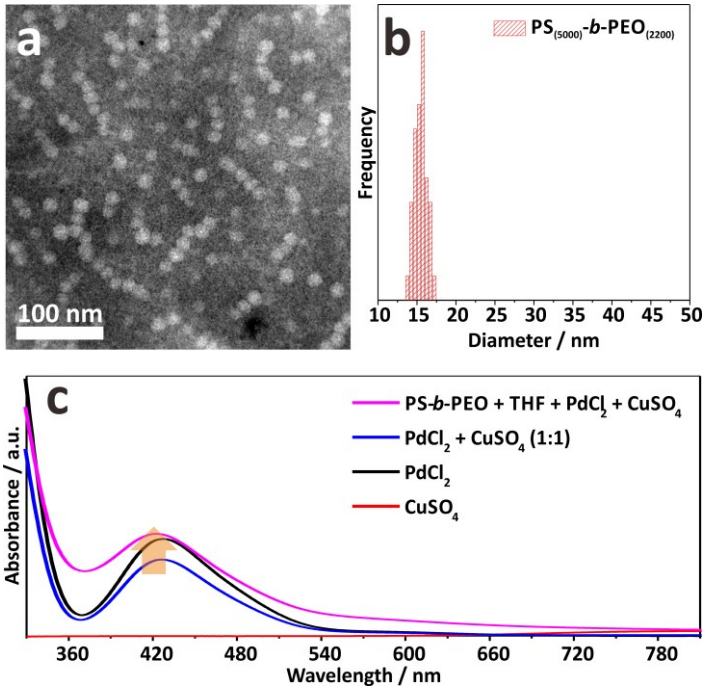

Figure 6.7 (a) TEM images and (b) diameter histogram of the spherical micelles made from $PS_{(5000)}$-*b*-$PEO_{(2200)}$. The micelles were stained with 1.0 wt% phosphotungstic acid. (c) UV-visible (UV-vis) spectra of various aqueous solutions.

PS-*b*-PEO is an amphiphilic surfactant composed of a hydrophilic PS subunit and a hydrophilic PEO subunit. Dissolution of PS-*b*-PEO in a mixture of THF and water induced the formation of spherical micelles with an average diameter of ~15 nm (**Figure 6.7a-b**). The TEM observation revealed that the micelles have a uniform shape and size. In addition, the spherical micelles were not aggregated. Upon the addition of metal precursor solutions, the micelle structures maintained their shape (data not shown). The UV-visible (UV-vis) absorption spectra were recorded for neat $PdCl_2$ and $CuSO_4$ solutions, a mixed solution of $PdCl_2$ and $CuSO_4$, and a solution containing the micelles and both metal precursors (**Figure 6.7c**). The absorption peaks centered at 425 nm and 800 nm match the *d-d* transitions of Pd(II) complexes and Cu(II) complexes, respectively.[27,28] Those absorption peaks were observed in solutions consisting of both metal precursors. Interestingly, the absorption spectrum of the micelles mixed with metal precursors exhibited a hyperchromic effect; the absorption spectra shifted to the higher absorbance value. This phenomenon implies that there is an interaction between the metal ion complexes with the micelles. The outer surface of micelles solvates the metal ion complexes and binds them through hydrogen bonding.[29] A previous study revealed that the charge of the metal ion complexes in the aqueous media varies from 2- to 2+ according to the number of water molecules in its coordination

sphere.[30] The water-rich complexes are positively charged and attracted by the micelles, whereas the negatively charged complexes are attracted by the positively charged water-rich complexes through electrostatic interactions to enrich the Pd(II) and Cu(II) species in and around the micelles.[31] Therefore, the micelles and metal ion complexes construction were stable due to the synergistic interaction between negatively and positively charged metal ion complexes presented in the aqueous medium.

Additional reactions were carried out with different reaction times to evaluate how the PdCu MNs form in solution. Ascorbic acid serves as the reducing agent to nucleate the metal nanoparticles and grow the metal around the micelles to form discrete MNs. **Figure 6.8** shows the SEM images of the PdCu 1:1 MNs prepared at a various reaction times: 5, 15, 30, 120, and 240 minutes. The average diameter of these particles was 67.8, 82.2, 96.5, 101.9, and 102.4 nm, respectively. The rate of growth decreased after ~30 min and halted beyond 240 min under typical synthesis conditions. After nucleation (<5min) the growth phase is relatively slow and enables the Pd and Cu atoms to grow via templated co-deposition on the pore walls. The presence of sulfuric acid was also necessary in order to control the reaction. I performed the reaction without sulfuric acid (2M H_2SO_4 = 0 uL) and with ~1.6-times more sulfuric acid (2M H_2SO_4 = 280 uL) used in the previous reactions. In the reaction without H_2SO_4 the metal was reduced almost instantly by the ascorbic acid. The reaction was heated for 240 min and the resulting sample was composed of large PdCu structures with random pores (**Figure 6.9a**). The reaction with additional H_2SO_4 (~1.6-times) proceeded more slowly and the resulting particles were smaller than the earlier samples (**Figure 6.9b**). It is worth noting that other synthesis methods using ascorbic acid as the reducing agent for metals frequently use a hard acid to increase the redox potential of ascorbic acid.[32] This ostensibly slows the kinetics of the reaction and modulates which metals can be reduced by the ascorbic acid. H_2SO_4 likely functions similarly in my method and prohibits the nucleation of Cu NPs while still enabling Pd nucleation. I replaced H_2SO_4 (pKa = -3) with equal amounts of 2M hydrochloric acid (HCl; pKa = -6) and 2M nitric acid (HNO_3; pKa = -6) and obtained irregular structures (**Figure 6.10**). So, the pKa of the acid (i.e. $[H^+]$) may play a role here, although counter anions could also play a role too.

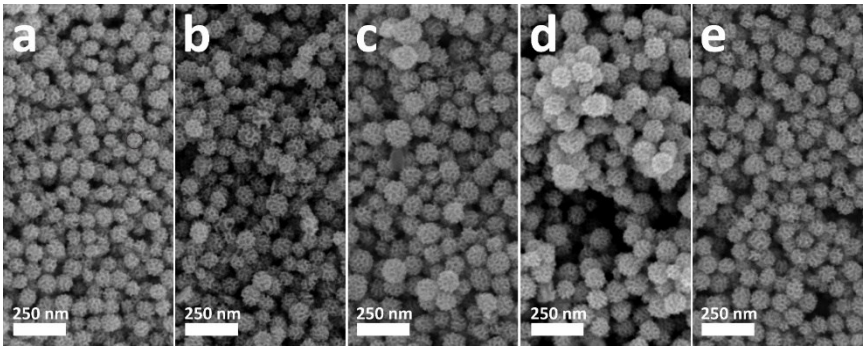

Figure 6.8 SEM images of PdCu MNs prepared by the typical condition with various reaction time: (a) 5 min, (b) 15 min, (c) 30 min, (d) 120 min, and (e) 240 min.

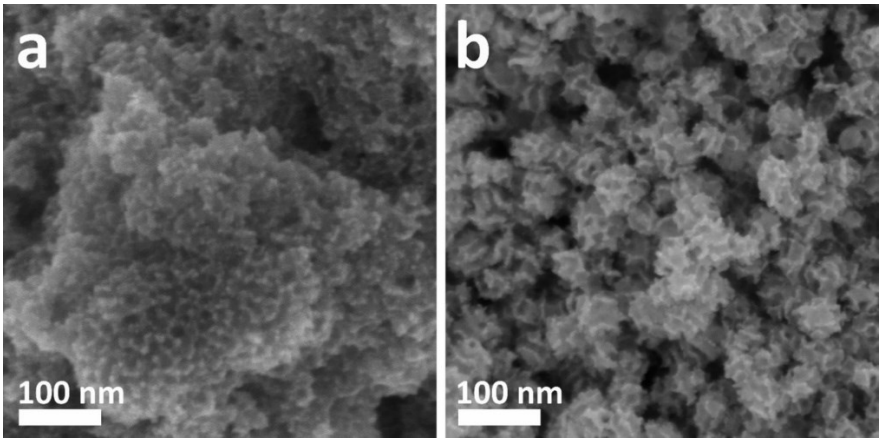

Figure 6.9 SEM images of the products prepared by the typical synthesis condition (PdCu 1:1), but (a) without H_2SO_4 and (b) with 280 μL H_2SO_4 in the reaction solution. Both reactions were collected after 240 minutes.

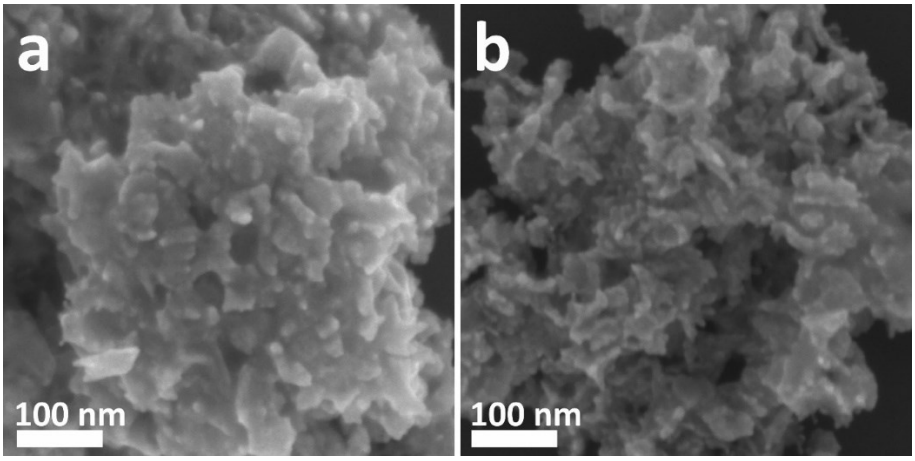

Figure 6.10 SEM images of the products prepared by the typical synthesis condition (PdCu 1:1), except the use of (a) HCl and (b) HNO_3 instead of H_2SO_4. Both reactions were collected after 240 minutes.

6.4. Electrocatalytic Activity of PdCu Mesoporous Nanospheres

Three-dimensional mesoporous metallic nanospheres are expected to possess the abundant exposed active sites due to the surface roughness and high density of stepped and kinked atomic arrangements. Therefore, PdCu MNs are believed to exhibit superior electrochemically active surface areas (ECSA) which will improve the overall catalytic performance. The ECSAs of the PdCu MNs were characterized with cyclic voltammetry (CV). For comparison, Pd MNs (which was prepared under the same condition to the PdCu MNs without feeding Cu precursor, **Figure 6.11a**) and commercially available Pd black (abbreviated as PdB; **Figure 6.11b**) were also studied as a reference under the same ECSA measurement conditions. Typical CV curves obtained in 0.5 M H_2SO_4 are shown in **Figure 6.12a**. In the present study, the oxide reduction charge is used for calculating the ECSA values because the hydrogen can penetrate the Pd lattice.[33] The ECSA estimated by calculating the oxide reduction charge assuming that the conversion factor for an oxide monolayer reduction was 420 μC cm^{-2} on the smooth surface of Pd. The ECSA values of the PdCu 1:9 MNs, PdCu 1:1 MNs, PdCu 9:1 MNs, and Pd MNs are estimated to be 33.57 m^2 g^{-1}, 70.20 m^2 g^{-1}, 44.82 m^2 g^{-1}, and 38.20 m^2 g^{-1}, respectively. The ECSA of MNs were about 2-4 times higher than that of commercial PdB (15.63 m^2 g^{-1}) due to the higher density of active sites.

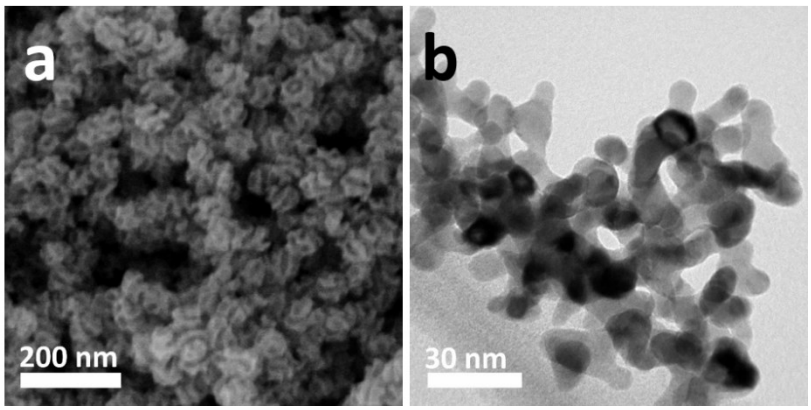

Figure 6.11 (a) SEM image of Pd MNs prepared by the typical synthetic condition (without feeding the Cu precursor) and (b) TEM image of commercially available Pd black (PdB).

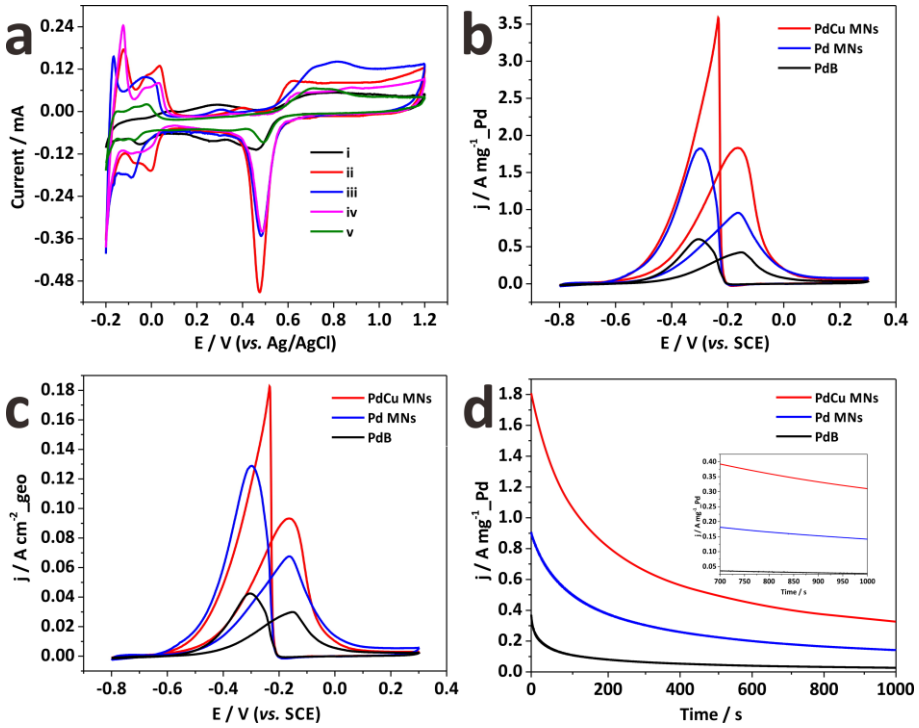

Figure 6.12 (a) CV curves in 0.5 M H_2SO_4 of the (i) PdCu 1:9 MNs, (ii) PdCu 1:1 MNs, (iii) PdCu 9:1 MNs, (iv) Pd MNs, and (v) PdB, respectively. (b) Mass-normalized and (c) geometrical area-normalized CV curves, and (d) chronoamperometric curves for ethanol oxidation catalyzed by PdCu MNs, Pd MNs, and PdB, respectively, in 1.0 M KOH containing 1.0 M C_2H_5OH. All the CV curves were obtained at a scan rate of 50 mV s^{-1}. The chronoamperometric measurements were carried out at a constant potential of −0.2 V (*vs.* SCE). Inset in panel (d) highlights the different current density of the samples after a long period of the stability test.

Pd is well known for its superior catalytic activity towards the oxidation of small organic molecules including ethanol. Therefore, the electrocatalytic oxidation of ethanol was selected as a model reaction to evaluate the activity and stability of the PdCu MNs. As the typical sample, the PdCu MNs with the initial Pd and Cu molar ratio of 1:1 were selected for the additional experiments. Typical CV curves of ethanol oxidation were acquired in 1.0 M KOH containing 1.0 M C_2H_5OH electrolyte at a scan rate of 50 mV s^{-1}. The mass activity of the PdCu MNs exhibited a larger current density (1.83 A mg^{-1}_Pd) than Pd MNs (0.96 Amg^{-1}_Pd), and PdB (0.42 A mg^{-1}_Pd) catalysts (**Figure 6.12b**). Even when the activity was normalized to the working electrode geometrical area, the PdCu MN

catalyst still had a higher specific activity (**Figure 6.12c**). The activity improvement of the alloyed Pd with Cu can be ascribed to the modulated d-band center, which weakens the bonding of intermediate species such as CO molecules to the surface of th alloy.[34] However, on the catalyst with a larger amount of Cu (PdCu 1:9 MNs), the ECSA and catalytic activity were smaller due to the lack of Pd atoms serving as active sites. A comparison of the current density of ethanol oxidation at −0.2 V on the PdCu MNs, Pd MNs, and PdB catalysts show that the PdCu MNs sample had a higher current density than the other Pd MNs in addition to PdB (**Figure 6.12d**). Alloying with the secondary metals is usually effective in enhancing the stability of the catalysts. Therefore, the superior performance of the as-prepared PdCu MNs is ascribed to the improved electronic properties provided by the alloyed structure as well as the unique mesoporous network.

6.5. Conclusions

I demonstrated a simple method to generate mesoporous PdCu nanospheres. The PdCu MNs form by nucleating the precursors on sacrificial polymer micelle templates to form porous nanoparticles. The reaction is relatively slow and occurred over the course of ~240 minutes, enabling both the Pd and Cu to create a uniform mesoporous alloy. The important aspects of the synthesis are the assembly of the polymeric micelles, and the reducing power of the ascorbic acid which depended on the addition of acid. The amount of Cu on the final product was lower than the initial Pd and Cu molar ratios due in part to the lower standard reduction potential of Cu compared to Pd. Both Pd and Cu are co-deposited on these nuclei resulting in an alloyed structure. H_2SO_4 increases the reduction potential of ascorbic acid which creates a mild growth rate to enable the generation of uniform mesoporous nanospheres. The optimum enhanced ECSA and activity towards ethanol oxidation reaction was achieved by the PdCu with 1:1 initial molar ratio. The introduction of Cu atoms weakens the adsorption of intermediate reaction species on the catalyst surface, thus the introduction of some Cu enhances both catalytic activity and stability.

6.6. References

[1] H. You, S. Yang, B. Ding, H. Yang, *Chem. Soc. Rev.* **2013**, *42*, 2880-2904.

[2] L. Zhang, Y. Xia, *Adv. Mater.* **2014**, *26*, 2600–2606.

[3] Y. Xia, X. Xia, H. -C. Peng, *J. Am. Chem. Soc.* **2015**, *137*, 7947−7966.

[4] B. Cai, S. Henning, J. Herranz, T. J. Schmidt, A. Eychmüller, *Adv. Energy Mater.* **2017**, *7*, 1700548.

[5] M. Shao, T. Yu, J. H. Odell, M. Jin, Y. Xia, *Chem. Commun.* **2011**, *47*, 6566–6568.

[6] J. Solla-Gullón, F. J. Vidal-Iglesias, J. M. Feliu, *Annu. Rep. Sect. C: Phys. Chem.* **2011**, *107*, 263.

[7] P. Suchomel, L. Kvitek, R. Prucek, A. Panacek, A. Halder, S. Vajda, R. Zboril, *Sci. Rep.* **2018**, *8*, 4589 (1-10).

[8] M. Crespo-Quesada, A. Yarulin, M. Jin, Y. Xia, L. Kiwi-Minsker, *J. Am. Chem. Soc.* **2011**, *133*, 12787–12794.

[9] L. Zhang, W. Niu, G. Xu, *Nanoscale* **2011**, *3*, 678–682.

[10] Y. Zhang, M. Wang, E. Zhu, Y. Zheng, Y. Huang, X. Huang, *Nano Lett.* **2015**, *15*, 7519-7525.

[11] X. -Y. Ma, Y. Chen, H. Wang, Q. -X. Li, W. -F. Lin, and W. -B. Cai, *Chem. Commun.,* **2018**, *54*, 2562-2565.

[12] J. Pal, T. Pal, *Nanoscale* **2015**, *7*, 14159-14190.

[13] Y. Li, Q. Liu, W. Shen, *Dalton Trans.* **2011**, *40*, 5811-5826.

[14] E. Antolini, *Energy Environ. Sci.* **2009**, *2*, 915.

[15] A. Chen, C. Ostrom, *Chem. Rev.* **2015**, *115*, 11999.

[16] M. Armbrüster, M. Behrens, F. Cinquini, K. Föttinger, Y. Grin, A. Haghofer, B. Klötzer, A. Knop-Gericke, H. Lorenz, A. Ota, S. Penner, J. Prinz, C. Rameshan. Z. Révay, D. Rosenthal, G. Rupprechter, P. Sautet, R. Schlögl, L. Shao, L. Szentmiklósi, D. Teschner, D. Torres, R. Wagner, R. Widmer, G. Wowsnick, *ChemCatChem* **2012**, *4*, 1048.

[17] L. Liu, A. Corma, *Chem. Rev.* **2018**, *118*, 4981.

[18] E. Antolini, S. C. Zignani, S. F. Santos, E. R. Gonzalez, *Electrochim. Acta*, **2011**, *56*, 2299.

[19] B. D. Adams, A. Chen, *Mater. Today*, **2011**, *14*, 282.

[20] J. Xue, G. Han, W. Ye, Y. Sang, H. Li, P. Guo, X. S. Zhao, *ACS Appl. Mater. Interfaces* **2016**, *8*, 34497.

[21] X. Li, X. Wang, M. Liu, H. Liu, Q. Chen, Y. Yin, M. Jin, *Nano Res.* **2018**, *11*, 780.

[22] M. Mavrikakis, B. Hammer, J. K. Nørskov, *Phys. Rev. Lett.* **1998**, *81*, 2819-2822.

[23] N. Lopez, J. K. Nørskov, *Surf. Sci.* **2001**, *477*, 59.

[24] A. K. Singh, Q. Xu, *ChemCatChem* **2013**, *5*, 652.

[25] H. -L. Liu, F. Nosheen, X. Wang, *Chem. Soc. Rev.* **2015**, *44*, 3056-3078.

[26] H. Liu, R. R. Adzic, S. S. Wong, *ACS Appl. Mater. Interfaces* **2015**, *7*, 26145-26157.

[27] L. I. Elding, L. F. Olsson, *J. Phys. Chem.* **1978**, *82*, 69-74.

[28] P. S. Salmon, G. W. Neilson, J. E. Enderby, *J. Phys. C: Solid State Phys.* **1988**, *21*, 1335-1349.

[29] C. Albayrak, A. M. Soylu, Ö.Dag, *Langmuir*, **2008**, *24*, 10592.

[30] K. Mech, P. Zabinski, R. Kowalik, K. Fitzner, *J. Electrochem. Soc.* **2013**, *160*, H770.

[31] M. Iqbal, C. Li, K. Wood, B. Jiang, T. Takei, Ö.Dag, D. Baba, A. S. Nugraha, T. Asahi, A. E. Whitten, M. S. A. Hossain, V. Malgras, Y. Yamauchi, *Chem. Mater.* **2017**, *29*, 6405.

[32] J. -H. Lee, K. J. Gibson, G. Chen, Y. Weizmann, *Nat. Commun.* **2015**, *6*, 7571.

[33] F. Kadirgan, B. Beden, J. M. Leger, C. Lamy, *J. Electroanal. Chem* **1981**, *125*, 89.

[34] J. Fan, S. Yu, K. Qi, C. Liu, L. Zhang, H. Zhang, X. Cui, W. Zheng, *J. Mater. Chem. A* **2018**, *6*, 8531.

Chapter 7

7. General Conclusions and Future Perspective

7.1. General Conclusions

The successful fabrication of Pd-based nanoarchitectures by solution-phase chemical reduction and electrochemical deposition methods toward the development of cost-effective and high-performance catalysts have been achieved. By designing Pd nanoarchitectures with specifically exposed facets and controlled morphology, Pd nanocatalysts with outstanding catalytic performance for some catalytic reactions can be achieved. Furthermore, by combining Pd with non-noble elements and/or support materials can enhance its catalytic performance and stability toward corrosion and harsh reaction conditions.

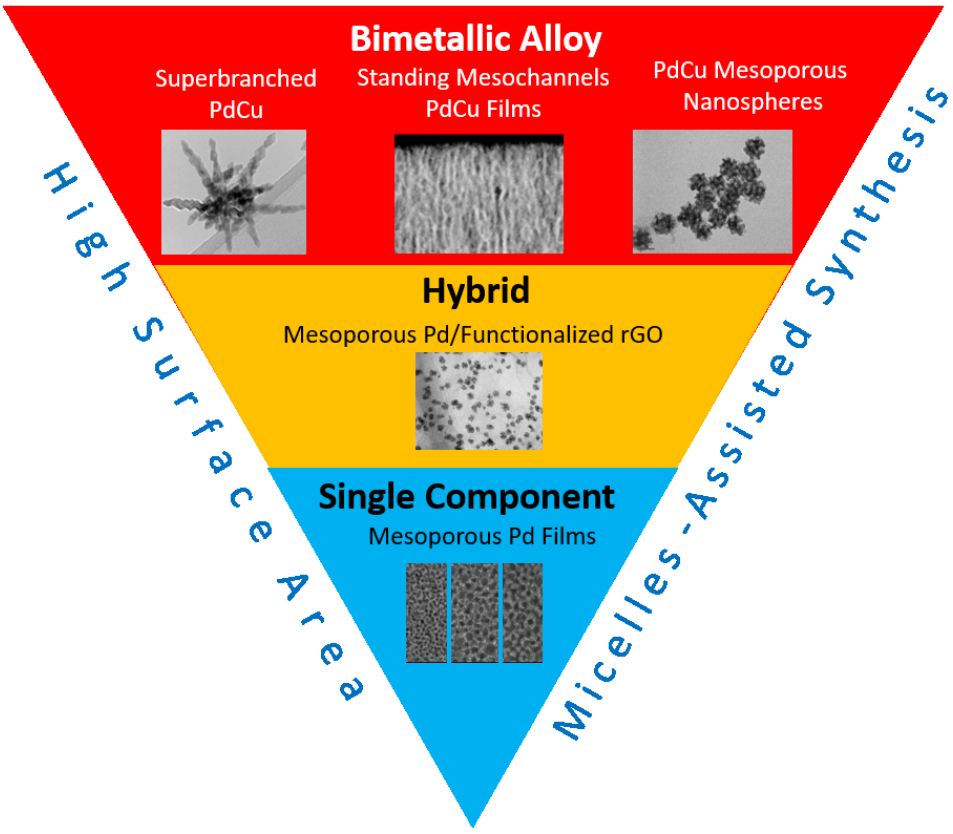

Figure 7.1. Summary of the PhD projects.

As an overview, these PhD thesis projects focused on the preparation of the new nanoarchitectures of Pd and PdCu alloys via a facile method and produce a high yield through the assistance of micelles assembly (**Figure 7.1**). The prepared products have a high surface area which is necessary for the surface reaction applications such as catalysis.

The proposed synthetical approach have been applied either for the preparation of nanoarchitectured films or particles of Pd and PdCu alloy. Furthermore, the synthetic approaches have been extended to prepare the hybrid of mesoporous Pd nanoparticles and functionalized reduced graphene oxide to provide a highly efficient electrocatalyst materials.

7.1.1. Electrodeposition of Metallic Films with Large-Sized Pores and Vertical Oriented Mesochannels

This thesis reveals that non-ionic surfactants (block copolymers) can interact with dissolved metal ions to form complexes in solution. These interactions form the essence of the micelle assembly technique. The concentrations and molecular weights of the templates are crucial in creating a suitable environment for the growth of the desired final structures. A non-ionic surfactant, triblock copolymer P123, was used as a pore-directing agent and dissolved altogether with the Pd precursors as the electrolyte solution for the electrodeposition. From small-angle neutron scattering (SANS) data, it was found that spherical P123 micelles, with an average diameter of ~14 nm, were formed in the electrolyte, and the addition of Pd ions did not significantly modify their structure, which was the essence of the micelle assembly approach. The electrodeposition co-deposits micelles and Pd precursors on the surface of the working electrode. This is works because the water-coordinated species favorably interacted with the ethylene oxide moiety of the micelles through hydrogen bonding to effectively drive the Pd(II) species toward the working electrode surface. After the Pd deposition, the template can be removed to reveal uniformly sized mesopores over the entire of film, with an average pore diameter of 10.9 nm.

To expand the pore sizes, a high molecular-weight block copolymer, polystyrene-*block*-poly(ethylene oxide) (PS-*b*-PEO), was selected as another pore-directing agent. TEM observation clearly showed the formation of PS-*b*-PEO micelles. By varying the molecular weights of the block copolymers, the average pore sizes of the Pd films could be tuned from 13 nm to 40 nm. Cross-sectional TEM observations showed mesopores spanning continuously from the bottom to the top of the films. The optimized micelle concentrations, solvent compositions, and the applied deposition potentials are very significant key factors that govern the formation of homogeneous and well-distributed mesopores over the entire film. This approach of combining electrochemistry with colloidal

and coordination chemistry is widely applicable to other promising metals and alloyed electrocatalysts.

7.1.2. Hybridization of Catalytically Active Materials and Support Materials with High Surface Area

Based on the project described in Chapter 5, the cationic surfactant hexadecylpyridinium chloride (HPDC) can forms micelles in aqueous solutions above its critical micelle concentration (CMC). The metal precursor (Na_2PdCl_4) dissociated in water to create metal-containing anions, $[PdCl_4]^{2-}$. The metal anions $[PdCl_4]^{2-}$ interacted strongly with positively charged HDP^+. As the particles grow, the cationic surfactant directed the Pd species to form continuous mesoporous structures. The functionalized reduced graphene oxide (FrGO) sheets served as the catalyst support material and were obtained by a mild reduction process using GO in the presence of non-ionic surfactant F127. The 'anchor-buoy' type configuration of F127 assisted in the initial attachment of Pd seeds and helped further growth of mesoporous Pd nanoparticles on the surface of the FrGO. The resulting FrGO-Pd hybrid structure efficiently catalyzed the oxidation of formic acid molecules in an acidic environment. These results demonstrate that high-performance electrocatalysts can be designed by employing hybrid structures of metallic mesoporous with nanoparticles a high surface area tethered to FrGO.

7.1.3. Optimizing Mesoporous and Nanoarchitectured Pd through Alloying with Cu

The presence of Cu atoms in the Pd alloy bimetallic system reduces the capability of the catalyst surface to accommodate poisoning products from intermediate reactions. To achieve such bimetallic system, a one-pot synthesis with utilized micelles assembly had been carried out. This PhD project successfully prepared the three-dimensional superbranched PdCu and PdCu mesoporous nanospheres.

For the synthesis of superbranched PdCu, the reaction solution consisted of the shape-directing agent, capping agent, and metal precursors. To control the growth of the PdCu facets, tungsten hexacarbonyl ($W(CO)_6$) was added to the reaction solution. The decomposed carbonyl molecules from $W(CO)_6$ adsorbed on the {111} facets of tiny PdCu nanocrystals, restricting the growth of tiny octahedral nanocrystals along the lateral

direction. The present success not only indicates the simultaneous assembly of the nanocrystals during their growth process but also paves the way to prepare the well-organized 3D Pd-alloy structures with superior electrocatalytic activity and stability.

For the the synthesis of PdCu mesoporous nanospheres, a solution containing tetrahydrofuran (THF) and diblock copolymer PS_{5000}-*b*-PEO_{2200} was mixed with water to induce the formation of polymeric micelles. The further addition of metal precursors created the aqua-complexes which interacted with the PEO moieties of the micelles through hydrogen bonding. The Cu ions were co-reduced with the Pd ions by the assistance of a mild reducing agent, ascorbic acid. After the initial nucleation, the particles grew and finally enveloped the micelle templates. The obtained mesoporous PdCu spheres showed high surface area, superior electrocatalytic activity, and stability in comparison to commercially available Pd catalysts. This approach can be extended to prepare various kinds of large-sized mesoporous metallic spheres.

7.2. Future Perspective

In the future, the synthetic strategies in this thesis can be extended to prepare various kinds of three-dimensional Pd-based materials or even other metallic materials. To avoid the risk of dissolution, Ostwald ripening and aggregation associated with 0D nanoparticles, higher dimensional Pd nanoarchitectures (1D to 3D) are generally preferred. Furthermore, they can provide better electron and mass transport, greater abundance of low-coordinated atoms and hierarchical porous structure, leading to higher catalytic activity.

Despite some success, there are still some limitations with respect to the solution-phase synthesis. Traces of additives and surfactants involved in the reaction should be completely removed from the final product or they will lower the catalytic performance. Post-synthetic cleaning by ozone treatment or high-temperature heating are usually necessary to ensure complete removal of unwanted elements or organic compounds from the product. In the case of supported Pd nanocatalysts, the combination of 2D or 3D Pd nanoarchitectures or hybrids (intermetallics/alloys) with support materials has rarely been reported in the literatures. The synergistic effect of the support material to enhance the charge transfer (and dispersion of the active catalyst) and the abundance of active sites offered by 2D or 3D nanoarchitectures are expected to produce significantly higher performance than supported 0D nanoparticles.

From economical viewpoint, the price of Pd has increased steadily over the past two years. However, the Pd resource on earth is at least fifty times larger than Pt and hence, Pd can still partially be used to reduce the heavy demand for Pt catalyst. The combination of Pd with non-noble elements, such as transition metals, is expected to provide cost-effective catalysts with similar or higher catalytic activity than pure Pt or Pd catalyst. Furthermore, to improve the feasibility of Pd-based catalysts toward real-life catalytic applications, more efforts into development of facile, greener and scalable synthetic methods should be carried out in the future.

List of Achievements

Original Papers

1. Three-Dimensional Super-Branched PdCu Nanoarchitectures Exposed on Controlled Crystal Facets, *Chemistry - A European Journal*, **2017**, 23, 51-56 (3 January 2017)
   Muhammad Iqbal, Cuiling Li, Jung Ho Kim, Saad M. Alshehri, Tsuruo Nakayama, Yusuke Yamauchi

2. Continuous Mesoporous Pd Films by Electrochemical Deposition in Nonionic Micellar Solution, *Chemistry of Materials,* **2017**, 29, 6405-6413 (17 July 2017)
   Muhammad Iqbal, Cuiling Li, Kathleen Wood, Bo Jiang, Toshiaki Takei, Ömer Dag, Daisuke Baba, Asep Sugih Nugraha, Toru Asahi, Andrew E Whitten, Md Shahriar A Hossain, Victor Malgras, Yusuke Yamauchi

3. Tethering Mesoporous Pd Nanoparticles to Reduced Graphene Oxide Sheets Forms Highly Efficient Electrooxidation Catalysts, *Journal of Materials Chemistry A*, **2017**, 5, 21249-21256 (24 August 2017)
   Muhammad Iqbal, Cuiling Li, Bo Jiang, Md Shahriar A Hossain, Md Tofazzal Islam, Joel Henzie, Yusuke Yamauchi

4. Electrochemical Deposition: An Advanced Approach for Templated Synthesis of Nanoporous Metal Architectures, *Account of Chemical Research,* **2018**, 51, 1765-1773 (9 July 2018)
   Cuiling Li, Muhammad Iqbal, Jianjian Lin, Xiliang Luo, Bo Jiang, Victor Malgras, Kevin C-W Wu, Jeonghun Kim, Yusuke Yamauchi

5. Standing Mesochannels: Mesoporous PdCu Films with Vertically-Aligned Mesochannels from Nonionic Micellar Solutions, *ACS Applied Materials and Interface*, **2018**, 10, 40623-40630 (14 November 2018)
   Muhammad Iqbal, Bo Jiang, Cuiling Li, Ömer Dag, Victor Malgras, Brian Yuliarto, Jeonghun Kim, Yusuke Yamauchi

6. Chemical Design of Palladium-Based Nanoarchitectures for Catalytic Applications, *Small*, **2019,** DOI: 10.1002/smll.201804378 (11 January 2019)
   Muhammad Iqbal, Yusuf Valentino Kaneti, Jeonghun Kim, Brian Yuliarto, Yong-Mook Kang, Yoshio Bando, Yoshiyuki Sugahara, Yusuke Yamauchi

7. Block-Copolymer-Assisted Electrochemical Synthesis of Mesoporous Gold Electrodes: Towards a Non-Enzymatic Glucose Sensor, *ChemElectroChem,* **2017**, *4*, 2571-2576 (28 June 2017)
   Asep Sugih Nugraha, Cuiling Li, Jiang Bo, Muhammad Iqbal, Saad M. Alshehri, Tansir Ahamad, Victor Malgras, Yusuke Yamauchi, Toru Asahi

8. Mesoporous Bimetallic RhCu Alloy Nanospheres Using a Sophisticated Soft-Templating Strategy, *Chemistry of Materials*, **2018**, 30, 428-435 (10 January 2018)
   Bo Jiang, Kenya Kani, Muhammad Iqbal, Hideki Abe, Tatsuo Kimura, Md Shahriar A Hossain, Oruganti Anjaneyulu, Joel Henzie, Yusuke Yamauchi

9. Nafion®-Coated Mesoporous Pd Film Toward Remarkably Enhanced Detection of Lactic Acid, *RSC Advances*, **2018**, 8, 10446-10449 (14 March 2018)
   Daisuke Baba, Asep Sugih Nugraha, Muhammad Iqbal, Jiang Bo, Cuiling Li, Abdulmohsen Ali Alshehri, Jungmok You, Victor Malgras, Yusuke Yamauchi, Toru Asahi

10. Electrochemical Synthesis of Mesoporous Au-Cu Alloy Films with Vertically Oriented Mesochannels Using Block Copolymer Micelles, *ACS Applied Materials and Interfaces*, **2018**, 10, 23783-23791 (2 July 2018)
    Asep Sugih Nugraha, Victor Malgras, Muhammad Iqbal, Bo Jiang, Cuiling Li, Yoshio Bando, Abdulmohsen Alshehri, Jeonghun Kim, Yusuke Yamauchi, Toru Asahi

11. Trimetallic Mesoporous AuCuNi Electrocatalysts with Controlled Compositions Using Block Copolymer Micelles as Templates, *Small Methods*, **2018**, 2, 1800283 (11 December 2018)
    Asep Sugih Nugraha, Victor Malgras, Jeonghun Kim, Jiang Bo, Cuiling Li, Muhammad Iqbal, Yusuke Yamauchi, Toru Asahi

Acknowledgment

I would like to express my acknowledgment and appreciation to my supervisor, Prof. Yusuke Yamauchi for his invaluable advice and guidance during my PhD study.

I am deeply grateful to Prof. Yoshiyuki Sugahara, Prof Yoshio Bando, Prof. Toru Asahi, and Dr. Joel Henzie for their helpful comments.

I gratefully thank Dr. Cuiling Li, Dr. Bo Jiang, Dr. Yusuf Valentino Kaneti, Dr. Victor Malgras, and Dr. Jeonghun Kim for their continuous encouragements and helpful supports.

I wish to thank all my friends and lab-mates, especially Mr. Yuichiro Kamachi, Ms. Kimiko Takai, Dr. Mohamed B. Zakaria, Dr. Yunqi Li, Dr. Tang Jing, Dr. Peng Mei, Dr. Christine Young, Mr. Daisuke Baba, Mr. Kenya Kani, Mr. Shunsuke Tanaka, Mr. Haibo Tan, Miss. Yanna Guo, Ms. Azhar A. Salman, Mr. Asep Sugih Nugraha and Mr. Indra Saptiama for their support and assistance on my study.

I would like to thank the staff of the Center for Science and Engineering at Waseda University for their assistance and their time during my PhD study.

I thank all administrative, especially Ms. Naoko Kaneta, Ms. Shinobu Oishi, and Ms. Monika Ostrowska; and technical staff at International Center for Materials Nanoarchitectonics (MANA), National Institute for Materials Science (NIMS) for their support.

The financial support from Indonesia Endowment Fund for Education (LPDP) is highly appreciated.

I want to especially thank my wife, Dr. Nuri Trianti, my daughter, Syifa Fathiya Khairunnisa, and my parents whose unconditional love and support helped me during these years to pursue my goals.

February 2019

Muhammad Iqbal